Geometric and scale effects on energy absorption of structural composites

Zhang, Chi. C.

Geometric and Scale Effects on Energy Absorption of Structural Composites

By

Chi. C. Zhang

A thesis submitted for the degree of Doctor of Philosophy in the

School of Engineering and Materials Science

Faculty of Science and Engineering

Queen Mary College, University of London

Acknowledgements

This thesis summarizes the work I have carried out during my Ph.D. studies with the composites research group in Queen Mary College, University of London. I was very lucky that I was offered great support from a number of people during this period. Without their help, this Ph.D. thesis would not become a reality.

Foremost, I would like to record my gratitude to my supervisor, Prof. Paul Hogg, for his guidance in both academic and moral. His vision, discipline and intelligent effort reformed my working attitude and thinking. During these years, Paul demonstrated an admirable way of exploring science with independence, free thinking, personal responsibility and mutual trust. This experience for me is an invaluable treasure, and it has much more meaning than this study itself.

I would like to extend my sincere gratitude to Dr. Silvano Cauchi-Savona and Mr. Alan Leong for suggestion and moral support from the initial to the final level of this research. I am greatly indebted to Prof. Ton Peijs and Dr. James Busfield, who gave special attention and support. Great thanks to all the technicians and officers in the School of Engineering and Materials Science, especially Mr Bill Godwin, Mr Colin Langdown, Mr John Caulfield and Mr Mick Willis, without whom I would have had a much harder time. Many thanks to other colleagues in the department for their support, in particular Manabu Kuwata, Choothum Jeenjitkaew, Kyriakos Berketis, Wei Tu, Mohamed El-Habti, Philip Gabriel, Praveen Kumar and Nutthanun Suphadon (Mark) for their enjoyable conversations.

I am very grateful to the Department of Trade and Industry (UK) as well as our School of Engineering and Materials Science for financially supporting this work. I am also grateful to Carr Reinforcement, BTI Europe, Sigmatex, Advanced Composites Group, Scott Bader, Reichhold and Huntsman Corporation for supplying materials.

Last but not least, I am extremely grateful for the encouragement from my family – my parents and my wife. They always supported me spiritually and practically for completing this work, no matter at good time or difficult time. I also would like give thanks to my little angel, my daughter, who brings lots and lots of joy as well as wonderment into my research and my life.

Für meine liebe Tochter

献给我心爱的女儿

Esther

德馨

Table of Contents

Abbreviations and Acronyms .... **xix**

Abstract .... **xx**

Chapter 1. Introduction **1**

1.1. Background and motivation *1*

1.2. Aim and objectives *3*

Chapter 2. Literature Review **4**

2.1. Crushing mechanisms of composites *4*

2.1.1. Structural instability and buckling 4

2.1.2. Composite failure modes 6

2.1.2.1. Transverse shearing (fragmentation) 7

2.1.2.2. Lamina bending (splaying) 8

2.1.2.3. Brittle fracturing 8

2.1.2.4. Local buckling (folding) 8

2.1.3. Trigger mechanisms 9

2.1.4. Energy absorption in progressive crushing mode 12

2.1.4.1. Crushing process 12

2.1.4.2. Evaluation of crushing energy 13

2.1.4.3. Energy absorbing mechanisms 14

2.2. Factors of controlling energy absorption capability of composites *15*

2.2.1. Effect of material properties 15

2.2.1.1. Fibre types 15

2.2.1.2. Matrix systems 18

2.2.1.3. Fibre architecture 21

- *Stacking sequence* 21
- *Fibre orientation* 23

2.2.1.4. Fibre volume fraction 25

2.2.2. Effect of fracture toughness 27

2.2.2.1. Energy analysis 27

2.2.2.2. Local stresses 29

2.2.2.3. Modes of crack surface displacement 31

2.2.2.4. Effect of stitching 32

2.2.3. Effects of crushing strain rate ... 34
2.2.3.1. Higher strain rates increase energy absorption capability ... 35
2.2.3.2. Higher strain rates decrease energy absorption capability ... 37
2.2.4. Effects of structural geometries ... 38
2.2.4.1. Cones ... 38
2.2.4.2. Tubes ... 39
2.2.4.3. Beams ... 43
2.2.4.4. Plates ... 44
2.2.4.5. Energy absorption in sandwich panels ... 44
2.3. Robust design experiments ... 48
2.3.1. Classification of factors ... 48
2.3.2. The design of experiments process ... 49
2.3.3. Orthogonal array, loss function and signal-to-noise ratio ... 50
2.3.3.1. Orthogonal arrays ... 51
2.3.3.2. Quality loss functions ... 52
2.3.3.3. Signal-to-noise (S/N) ratio ... 54
2.4. Analysis methods used in Robust Design ... 55
2.4.1. The Response Table ... 56
2.4.2. Analysis of Variance (ANOVA) ... 57
2.4.2.1. Equations for calculating ANOVA ... 57
2.4.2.2. F-ratio and F-test ... 60
2.4.2.3. Percent contribution, P% ... 61
2.4.2.4. The ANOVA summary table and pooling techniques ... 62
2.4.2.5. Alpha and beta mistakes ... 63
2.4.3. Estimated mean and confidence intervals in confirmation experiment ... 64
Chapter 3. Experimental Techniques ... 67
3.1. Experimental stages ... 67
3.2. Materials ... 69
3.2.1. Fabrics ... 69
3.2.2. Resins ... 69
3.2.3. Description of laminate orientations ... 71
3.3. Manufacture of composite panels ... 72
3.4. Experimental methods and their specimens ... 73
3.4.1. Crushing test ... 73
3.4.1.1. Crushing test for plates ... 73
3.4.1.2. Crushing test for composite structures ... 74
3.4.2. Fracture toughness test ... 75
3.4.2.1. Mode-I testing – Double cantilever beam (DCB) ... 75

3.4.2.2. Methods of identifying delamination initiation 78
i. Visual observation (VIS) 78
ii. Deviation from linearity (NL) 78
iii. 5% offset/maximum load (5%/Max) 78
3.4.2.3. Mode-II testing – 4-point bend end-notched flexure (4-ENF) 78
3.4.3. Flexure test 81
3.4.4. Tensile specimen 82
3.4.5. Finite element method (FEM) 83
3.4.6. Density measurement 85

Chapter 4. Intersecting Square Cell and Buckling 86

4.1. Intersecting square cell 86
4.1.1. Specimen preparation 86
4.1.2. Comparison between single-cell and multi-cell specimens 88
4.1.3. Crushing response of intersecting square cells 89
4.1.4. Comparisons between intersecting square cells and plates 90

4.2. Critical buckling analysis 97
4.2.1. Buckling of isotropic plate 98
4.2.2. Buckling of anisotropic plate: Theory and Abaqus FEMs 100
4.2.3. Comparison of critical buckling of plates with tubes and ISCs 102

4.3. Effects of critical buckling stress on crushing performance 105
4.3.1. Buckling issues in composite plates during crushing 106
4.3.2. Buckling issues in intersecting square cells during crushing 106

4.4. Summary 107

Chapter 5. Geometric Cells 109

5.1. Specimens 109
5.1.1. Geometric characteristics 109
5.1.2. Materials and laminate properties 111
5.1.3. Stitching parameters 113

5.2. Crushing stages and periods 115

5.3. Crushing results 119

5.4. Sustained structural efficiency (SSE) 126

5.5. Summary 131

Chapter 6. Flexural Properties 133

6.1. Flexure testing samples 133

6.2. Flexure testing results 135

6.3. Discussion ... *138*
6.3.1. Comparisons between flexural modulus and SEA data ... 138
6.3.2. Relationship between SEA and flexural rigidity ... 143
6.3.3. Effects of matrix ... 147
6.4. Summary ... *150*

Chapter 7. Fracture Toughness ... 151

7.1. Fracture toughness tests: DCB and 4-ENF ... *151*
7.1.1. DCB testing samples and testing results ... 152
7.1.2. ENF testing samples and testing results ... 156
7.1.3. Comparison between stitched and unstitched samples ... 158
7.1.3.1. Stitching influences on Mode-I fracture toughness ... 159
7.1.3.2. Stitching influences on Mode-II fracture toughness ... 163
7.2. Effect of resin toughness on DCB and 4-ENF tests ... *165*
7.3. Discussion on the relation between fracture toughness and SEA ... *166*
7.4. Summary ... *173*

Chapter 8. Optimization Process ... 177

8.1. Sample configurations ... *177*
8.1.1. Modification of cross-sectional geometry ... 177
8.1.2. Manufacturing process ... 179
8.1.3. Selection of control factors and levels ... 181
8.1.3.1. Trigger system ... 181
8.1.3.2. Fabric type and orientation ... 183
8.1.3.3. Matrix system ... 183
8.1.3.4. Beam web length ... 184
8.1.3.5. Stitching gap on beam webs ... 184
8.1.3.6. Crushing speed (crushing strain rate) ... 186
8.1.4. Selection of orthogonal array ... 186
8.2. Results of Robust Design ... *190*
8.2.1. Response Tables ... 190
8.2.2. ANOVA method ... 192
8.2.3. Confirmation experiment ... 195
8.3. Summary ... *196*

Chapter 9. Discussion ... 197

9.1. Failure mechanism of intersecting square cells ... *197*
9.2. Failure mechanism of three geometric cells ... *201*

9.2.1. Effect of the content of 0° fibres 204
9.2.2. Failure mechanism map for three geometric cells 208

9.3. Failure mechanism of modified geometric cells 211

9.4. Comparisons of failure mechanisms for all samples 211

9.5. Prediction of energy absorption capacities of composites panels 218
9.5.1. Crushing properties of the panel type structure with thickness of 50mm 219
9.5.2. Crushing properties of the panel type structure with various thickness 219

Chapter 10. Conclusions 224

Appendix 1. Classical laminate theory and buckling 226

A1.1. Basic conceptions of orthotropic elasticity 226

A1.2. Elastic properties of a unidirectional lamina 229

A1.3. Elastic properties of multi-directional laminates 232

A1.4. Buckling of composite plates - Minimum Potential Energy 235

A1.5. Flexural modulus of a thin laminate 239

Appendix 2. F-ratio tables 241

References 242

List of Figures

Figure 2.1 Sketches of different cross-sectional profile of tubes (left) and variation of failure mode with height and corner radius (right) [11] ... 5

Figure 2.2 Energy absorption in two different crushing failure modes [13] ... 6

Figure 2.3 Crushing modes of continuous fibre-reinforced composite tubes [14] ... 7

Figure 2.4 Schematic representation of formation of progressive failure mode (splaying mode) crush zone based on microscopic examination of polished sections [15] ... 9

Figure 2.5 Schematic sketch of typical crushing triggers: Steeple and notch [17, 22] ... 10

Figure 2.6 Comparison of crushing results between notch and steeple triggers [17] ... 10

Figure 2.7 Effect of trigger configuration and laminate lay-up on the energy absorption capability and crushing efficiency [18] ... 11

Figure 2.8 Typical plot of splaying crushing mode with steeple trigger: (1) first peak; (2) second peak; (3) drop after initial split; and (4) specific sustained crushing stress [16] ... 12

Figure 2.9 schematic sketch of cross-sectional area for the typical composite laminate during crushing and different energy absorption mechanisms [24] ... 14

Figure 2.10 Specific energies and crushing stress comparisons of PEEK matrix composite tubes with different fibres [12] ... 16

Figure 2.11 Effect of stacking sequence on energy absorbing capability of [±45] tubes [14] ... 17

Figure 2.12 Comparison of SEA as a function of preform architecture [27] ... 17

Figure 2.13 Energy absorption of composite tubes reinforced by random fibre mat in three different thermosetting resins [28] ... 19

Figure 2.14 Effects of processing conditions on SEA of composite tubes [28] ... 19

Figure 2.15 Energy absorption perform on different dimensions for composite plates with various fibre orientations: closed symbols represent polyester matrix laminates, while open symbols represent the equivalent laminate with an epoxy matrix [16] ... 20

Figure 2.16 Specific energies of carbon fibre reinforced thermoplastic composite tubes [12] ... 21

Figure 2.17 Schematic cross section of baseline, ply-level, and sublaminate-level scaled composite plates with steeple trigger [17] ... 22

Figure 2.18 Comparison of specific sustained crushing stress for composite plates made of Carbon/PEEK, Carbon/Epoxy, and Carbon/Kevlar® Epoxy with different triggers [17] ... 23

Figure 2.19 Effect of fibre orientations (±θ) on SEA for tubes and plates [15, 30, 31] 24

Figure 2.20 Effect of fibre orientation [0/±θ] on SEA for circular tubes [32] 25

Figure 2.21 Influence of fibre volume fraction on energy absorption capability of carbon/epoxy composite tubes [14] 27

Figure 2.22 General loading on a body of thickness *B* and crack length *a* [35] 28

Figure 2.23 Schematic sketch of local stresses at the crack tip: (a) the coordinate system used; (b) the stress σ as a function of *r* at the crack tip [35] 29

Figure 2.24 the three modes of crack surface displacement 31

Figure 2.25 Effects of Mode-I (left) and Mode-II (right) fracture toughness properties on the SEA of composite plates. Square and triangle symbols refer to quadriaxial and triaxial laminates, respectively [24]. 32

Figure 2.26 Illustrations of the various stitch types used to reinforce laminates [39] 33

Figure 2.27 Scanning electron micrographs showing a stitch bridging an interlaminar crack (left) and a broken Kevlar® thread partially pulled from a Mode-I fracture surface [41] 34

Figure 2.28 Effects of crushing speed on Kevlar/epoxy tubes [48] 36

Figure 2.29 Effects of crushing speed on carbon/epoxy tubes [48] 36

Figure 2.30 Comparison of specific energies of quasi-static and dynamic tested plates: carbon/PEEK (left) and carbon/epoxy (right), with different triggers [47] 37

Figure 2.31 Effects of D/t (inner diameter/wall thickness) ratio on the energy absorption of $[\pm45]_n$ carbon/epoxy (left) and Kevlar/epoxy (right) circular tubes [57] 40

Figure 2.32 Effects of w/t (tube width/wall thickness) ratio on the energy absorption of $[\pm45]_n$ carbon/epoxy (left) and Kevlar/epoxy (right) square tubes [84]. 40

Figure 2.33 Effects of corner radius of composite tubes on energy absorption [85]. 41

Figure 2.34 Pictures of finished composite tube specimens with triggering [60] 41

Figure 2.35 Specific energy absorption of composite tubes with different geometrical shapes: top) thickness of tubes = 1mm; bottom) thickness of tubes = 2mm [60] 42

Figure 2.36 Dimensions of a typical sandwich beam 45

Figure 2.37 Core types in sandwich sacrificial panels 46

Figure 2.38 The perspective view of a typical egg-box [4] 46

Figure 2.39 Block diagram of a product / process: P Diagram 49

Figure 2.40 Phases and steps in Robust design 50

Figure 2.41 Quadratic loss functions: 1) nominal-is-best; 2) smaller-the-better; 3) larger-the-better ... 53

Figure 3.1 Outline of experimental work of present research ... 68

Figure 3.2 Schematic sketch of SCRIMP setup ... 72

Figure 3.3 Illustration of the crushing test for simply-supported plates [2] ... 74

Figure 3.4 Image of the crush rig as used in this research ... 75

Figure 3.5 Dimensions and configuration of the DCB specimen ... 76

Figure 3.6 Determination of Δ (left) for DCB test, and $\partial C/\partial a$ (right) for ENF test ... 77

Figure 3.7 The load-displacement trace from DCB tests can follow three typical patterns: a) brittle matrix, b) tough matrix, and c) unstable crack growth [90] ... 79

Figure 3.8 Dimensions and configuration of the 4-ENF specimen ... 80

Figure 3.9 Schematic sketch of the flexure test ... 81

Figure 3.10 Schematic sketch of the tensile test ... 83

Figure 4.1 Schematic sketch of machined plate and intersecting square cell ... 87

Figure 4.2 Comparison of crushing stress vs. displacement curve between single-cell tube and multi-cell specimens ... 88

Figure 4.3 Typical stages in the crushing process of intersecting square cell ... 89

Figure 4.4 Schematic sketches of typical crushing process of intersecting square cell ... 90

Figure 4.5 Photographs of the sections of crushed $[\pm45/(90,0)]_{2S}$ laminates for plate (top-left, [16]) and intersecting square cell (bottom & right) ... 91

Figure 4.6 Comparison of intersecting square cells and simply-supported plates (For plates, D/h ratio = KES/h ratio, see Table 4.2.) ... 92

Figure 4.7 Comparison of intersecting square cells and simply-supported plates in further details (For plates, D/h ratio = KES/h ratio, see Table 4.2.) ... 92

Figure 4.8 Comparison of specific energy absorption vs. displacement curve between intersecting square cells and simply-supported plate for $[PW600]_6$ laminate ... 94

Figure 4.9 Schematic sketches of sample failure modes illustrating the difference between simply-supported composite plate and intersecting square cell. ... 95

Figure 4.10 Photographs of crushed samples: $[\pm45/PW600]_{2S}$ (top) and $[PW400]_{12}$ (bottom) ... 97

Figure 4.11 Influence of boundary conditions and a/b ratio on the buckling coefficients of isotropic plates subjected to in-plane compressive loading [10] ... 99

Figure 4.12 Classical theory and ABAQUS simulations for simply-supported plate with lay-ups of $[90/0]_{3S}$, $[90/0]_{2S}$, and $[90/0]_S$, where m is the number of half-waves. ... 100

Figure 4.13 Boundary conditions (vertical edges) and loading conditions on different Geometric FEMs ... 103

Figure 4.14 Buckling analysis of intersecting plate, simply-supported plate, and square tube: top and bottom boundaries are simply-supported 103

Figure 4.15 Buckling analysis of intersecting plate, simply-supported plate, and square tube: top and bottom boundaries are freely-supported 104

Figure 4.16 Relationship between critical buckling stress and crushing stress 105

Figure 4.17 Photographs of crushed composites plates having a $[\pm 45/0]_{2S}$ orientation and stitched by Kevlar® yarns in a transverse orientation [2] 106

Figure 4.18 Photographs of crushed $[PW600]_8$ sample (F1541a_ISC) 107

Figure 5.1 Geometric dimensions of the cross-sectional area (half) for three transition geometries: a) rectangular; b) circular; C) hexagonal 110

Figure 5.2 photographs of modified samples with three different transition geometries 113

Figure 5.3 Cross-sectional area of modified lock stitched laminate 114

Figure 5.4 Effects of stitching on the SEA of triaxial $[90/0_2]_S$ laminate of C-cells 114

Figure 5.5 A typical SCS/displacement curve with three distinct stages 115

Figure 5.6 Schematic representation of the trigger of 90-degree-fibre initiated at stage I 116

Figure 5.7 Photographs of modified geometric cells under unstable crushing: (a), (b) and (c); and stable crushing: (d) 117

Figure 5.8 SEA values of all modified geometric cells in every crushing period of 10mm 118

Figure 5.9 Normalized SEA of all modified geometric cells in every crushing period of 10mm 119

Figure 5.10 Crushing responses of geometric cells made of biaxial fabrics during three different crushing periods 122

Figure 5.11 Crushing responses of the geometric cells that are composed of triaxial fabrics during three crushing periods 123

Figure 5.12 Crushing responses of geometric cells that are composed of quadriaxial fabrics during three different crushing periods 123

Figure 5.13 Crushing responses of biaxial cells during three different crushing periods 124

Figure 5.14 Crushing responses of triaxial cells during three different crushing periods 125

Figure 5.15 Actual energy absorption capacity of all geometric transition cells 127

Figure 5.16 Potential energy absorption capacity of all geometric transition cells 128

Figure 5.17 Sustained structural efficiency of all geometric transition cells 129

Figure 5.18 Comparisons between geometric cells (actual crushing data), and intersecting square cells as well as simply-supported plates 132

Figure 6.1 Picture of a typical flexural testing sample with a stitching line in the middle 133

Figure 6.2 Comparisons of flexural strength and bending modulus 136

Figure 6.3 Schematic sketch of determination of strain energy density at flexural strength 136

Figure 6.4 Results of strain energy density at flexural strength... 137

Figure 6.5 Comparison of 0° fibres locations in three-point bending: 0° in inner layers (left) and 0° in outer layers (right)... 137

Figure 6.6 The relationships between potential energy absorption capability, flexural modulus and weight fraction of 0° fibres for biaxial laminates... 139

Figure 6.7 The relationships between potential energy absorption capability, flexural modulus and weight fraction of 0° fibres for triaxial laminates 139

Figure 6.8 Potential energy absorption capability vs. flexural modulus for all laminates grouped according to lay-ups 140

Figure 6.9 Data comparison of different geometries on SEA – flexural modulus curve 141

Figure 6.10 Data comparison of different lay-ups on SEA – E*(t/P) curve 142

Figure 6.11 Data comparison of different geometrical shapes on SEA – E*(t/P) curve...................... 143

Figure 6.12 Schematic sketch of bending fronds... 144

Figure 6.13 Transition map of crushing forms for geometric cells.. 146

Figure 6.14 Effects of resin systems on triaxial ($[90/0_2]_S$) flexure samples....................................... 147

Figure 6.15 Comparisons between theoretical prediction and experiment results on flexural samples made of different resin types.. 148

Figure 6.16 Schematic sketches of an unstitched flexural specimen (left) and a stitched flexural specimen (right) showing the locations of bending damages [114] 149

Figure 7.1 DCB sample (tested) without stiffener 153

Figure 7.2 DCB sample (tested) with stiffener 153

Figure 7.3 Determination of the average $G_{IC\text{-}prop}$ values on typical R-curves of Left) F1676_DCB unstitched $[0_3/\pm45$^$\mp45/0_3]$/Polyester; Right) 1681_DCB, stitched $[0_3/90^{\wedge}0_4]$/Polyester. 155

Figure 7.4 DCB sample (tested) bonded with stiffener 156

Figure 7.5 Photograph of crack propagation in a typical $[0_3/90$^$0_4]$ DCB sample 159

Figure 7.6 Photograph of crack propagation in a typical $[0_3/90$^$0_4]$ DCB sample 160

Figure 7.7 R-curves for DCB testing of stitched and unstitched samples... 160

Figure 7.8 Load-displacement curves for DCB testing of stitched and unstitched samples 161

Figure 7.9 Comparison of results calculated by the different methods for DCB samples 162

Figure 7.10 Load-displacement curves for stitched and unstitched [0_3/±45^0_4] samples 163

Figure 7.11 R-curves for 4-ENF testing of stitched and unstitched samples 164

Figure 7.12 Comparison of results calculated by the different methods for DCB samples 164

Figure 7.13 Comparison of different resin systems on stitched DCB samples 165

Figure 7.14 Comparison of different resin systems on stitched 4-ENF samples 166

Figure 7.15 Energy absorption mechanisms referring to Mode-I and Mode-II failures at the flat sides and core section of a typical geometric cell (F1655_C, $[\pm 45/0]_S$) 167

Figure 7.16 Percentages of energy absorption caused by Mode-I and Mode-II failures for geometric cells within the ideal crushing process 170

Figure 7.17 Comparisons between energy absorption capacity of C-cells and the energy fraction absorbed by Mode-I and Mode-II delaminations. 172

Figure 7.18 Comparisons between energy absorption capacity of H-cells and the energy fraction absorbed by Mode-I and Mode-II delaminations. 172

Figure 7.19 Comparisons between energy absorption capacity of S-cells and the energy fraction absorbed by Mode-I and Mode-II delaminations. 173

Figure 7.20 Comparison of all DCB testing results 174

Figure 7.21 Comparison of all 4-ENF testing results 175

Figure 8.1 Schematic sketch of the cross-sectional area of modified cell 178

Figure 8.2 Comparisons of crushing results between modified cell and other cells 178

Figure 8.3 Manufacturing process of side-stitched crushing sample 180

Figure 8.4 Demonstration of the trigger which is made by ply drop-off 182

Figure 8.5 Comparisons of typical crushing behaviour between the samples triggered by lateral fibres and the samples triggered by ply drop-off chamfer 182

Figure 8.6 Six factors which indicated on a typical crushing sample for the Robust Design 186

Figure 8.7 Response graph of SEA results for mean values (Error deviation = CI_1; confidence level = 95%) 191

Figure 8.8 Response graph of SEA results for S/N ratios (Error deviation = CI_1; confidence level = 95%) 192

Figure 8.9 Percentage contributions of factors for the ANOVA of mean values 194

Figure 8.10 Percentage contributions of factors for the ANOVA of S/N ratios 194

Figure 9.1 SEA vs. separation width/thickness (SD/h) for all intersecting square cells 197

Figure 9.2 SEA vs. separation width/thickness (SD/h) for all intersecting square cells which were categorized by the fibre architecture 198

Figure 9.3 Photographs of intersecting square cells during crushing: $[\pm 45/0_3]_{2S}$ (F1564_ISC top), $[PW400]_{10}$ (F1537_ISC, bottom left) and $[\pm 45/PW600]_{2S}$ (F1567_ISC, bottom right) 199

Figure 9.4 Photographs of crushed $[\pm 45/(90,0)]_{2S}$ sample (F1535_ISC) 200

Figure 9.5 Schematic sketch of crushing forms 202

Figure 9.6 Potential energy absorption capability of biaxial cells affected by the weight proportion of longitudinal 0° fibres. 204

Figure 9.7 Potential energy absorption capability of triaxial cells affected by the weight proportion of longitudinal 0° fibres 205

Figure 9.8 Photographs of crushed [0/90/0] C-cells (left), S-cells (middle) and H-cells (right)........ 206

Figure 9.9 Photographs of crushed $[90/0_2]_S$ C-cells (left), S-cells (middle) and H-cells (right) 206

Figure 9.10 Effect of the content of 0° fibres on crushing performance and flexural modulus 207

Figure 9.11 Potential energy absorption capacity vs. P/t ratio of all modified cells 208

Figure 9.12 Schematic sketch of crushing mechanisms in the core section of [PW400/0]S cells 209

Figure 9.13 SEA vs. perimeter/thickness (P/t) ratio for all geometric cells basing on actual energy absorption data 210

Figure 9.14 The distribution of crushing mechanisms for composite laminate (date for plates are obtained from Ref [16, 116]). 212

Figure 9.15 Comparison between plates and all geometric cells that investigated in this research 213

Figure 9.16 SEA vs. D/t ratio for both plates and geometric cells showing the general behaviour of the data 214

Figure 9.17 Summary the relationship between crushing behaviour and geometric and scale effects for structural composites 217

Figure 9.18 Schematic sketches of panel type energy absorbers for different composite cells 218

Figure 9.19 Geometric and scale effects on SEA levels for all samples measured in this research: SEA vs. normalized panel weight. 221

Figure 9.20 3D view of normalized crushing data. 222

Figure 9.21 Side views of normalized crushing data corresponding to Figure 9.20. 223

Figure A10.1. Control element in an elastic body 227

Figure A10.2. $x_1 - x_2$ plane of symmetry 228

Figure A10.3. Unidirectional lamina is loaded along principal material direction 229

Figure A10.4. The rotated new co-ordinate system x-y from 1-2 at angle θ 231

Figure A10.5. Positive directions for stress resultants and couples in multilayer plate 233

Figure A10.6. All four edges simply-supported plate subjected to in-plane load 237

List of Tables

Table 2.1 Standard orthogonal arrays ... 51

Table 2.2 Orthogonal array for $L_{18}(2^1 \times 3^7)$ ... 52

Table 2.3 The Response Table of factor effects for an $L_{18}(2^1 \times 3^7)$ array ... 56

Table 2.4 The ANOVA table for an $L_{18}(2^1 \times 3^7)$ array ... 63

Table 2.5 Modified ANOVA table for an $L_{18}(2^1 \times 3^7)$ array by using Pooling techniques ... 63

Table 2.6 Decision Risks [79] ... 64

Table 3.1 Fabric types used in whole project ... 70

Table 3.2 Resin types used in whole project ... 71

Table 3.3 Mechanical properties of cured resins as obtained from datasheets of material supplier [86-89] ... 71

Table 3.4 Geometries of tensile specimens ... 83

Table 3.5 Elastic property of typical unidirectional GFRP lamina ... 84

Table 3.6 Densities of composite components for the calculation of fibre volume fractions ... 85

Table 4.1 Properties of intersecting square cells and their crushing results ... 87

Table 4.2 Properties of composite plates and their crushing results ... 93

Table 5.1 Laminate properties of S-cell ... 111

Table 5.2 Laminate properties of C-cell ... 112

Table 5.3 Laminate properties of H-cell ... 112

Table 5.4 Crushing results of S-cells ... 120

Table 5.5 Crushing results of C-cells ... 120

Table 5.6 Crushing results of H-cells ... 121

Table 6.1 Flexure testing Samples ... 134

Table 6.2 Flexure testing results ... 135

Table 7.1 DCB testing Samples ... 152

Table 7.2 DCB testing results ... 154

Table 7.3 ENF testing Samples ... 157

Table 7.4 ENF testing results ... 158

Table 7.5 Mode-I and Mode-II fracture mechanisms at the flat sides of geometric cells................. 169

Table 7.6 Mode-I and Mode-II fracture mechanisms at the core section of geometric cells............ 169

Table 7.7 Energy absorbed by Mode-I & II delaminations in crushing samples.............................. 170

Table 7.8 Normalized energy absorption capacity related to the Mode-I & II delaminations in crushing samples 171

Table 8.1 Schematic sketches of stitching gap combined with beam web length 185

Table 8.2 Control factors and their levels for the Robust Design... 187

Table 8.3 Parameters for each experiment in the Robust Design using the L_{18} (2^1 x3^7) orthogonal array 188

Table 8.4 Crushing results of Robust Design 189

Table 8.5 The Response Table of the crushing results: Mean 190

Table 8.6 The Response Table of the crushing results: S/N ratio... 191

Table 8.7 ANOVA table for pooled mean values.. 193

Table 8.8 ANOVA table for pooled S/N ratio... 193

Table 8.9 Predicted values and confidence intervals for factors 195

Table 8.10 Prediction and confirmation regarding to S/N ratio 195

Table 9.1 Crushing forms for all geometric cells 203

Table A10.1 $F_{\alpha, v1,v2}$ Values 241

Abbreviations and Acronyms

ANOVA	–	analysis of variance
BWL	–	beam web length
CoFRM	–	continuous filament random mat
DCB	–	double cantilever beam
DOE	–	design of experiment
DOF	–	degree of freedom
EMS	–	error mean square
ENF	–	end notch flexure
FEM/FEA	–	finite element method / finite element analysis
FRP	–	Fibre-reinforced plastic
NCF	–	non-crimp fabric
OA	–	orthogonal array
PEEK	–	polyetheretherketone
PW	–	plain-woven
SCRIMP	–	Seemann composites resin injection moulding process
SCS	–	sustained crushing stress
SEA	–	specific energy absorption
SSCS	–	specific sustained crushing stress
SSE	–	sum of squares due to error (or, sustained structural efficiency)
SSM	–	sum of squares due to mean
SST	–	total sum of squares
StiGap	–	stitching gap
UD	–	unidirectional
S-cell	–	square cell
C-cell	–	circular cell
H-cell	–	hexagonal cell
D/t ratio	–	width-to-thickness ratio
S/N ratio	–	signal-to-noise ratio
P/t ratio	–	thickness-to-perimeter ratio

Abstract

The challenge faced by structural designers is becoming increasingly difficult as the imposed design criteria of energy absorbing structures requires weight reduction of structures without compromising cost and crushing performance. The current research is thus aimed at investigating the energy absorption of fibre reinforced composites measured as a function of geometry and scale within weight-critical structures.

At the first stage, an innovative structure composed of four intersecting composite plates was tested. It was found that the structural stability played a crucial role in this intersecting structure. In order to avoid generating buckling failure before turning to a progressive crushing regime, Finite Element Method (FEM) was used on composite structures as a technical tool.

At the second stage, three geometric structures containing corrugated composite laminates and possessing better structural stability were designed and examined. To increase the interlaminar fracture toughness properties of composite materials, through-thickness stitching methods were introduced. Fracture toughness (Mode-I and Mode-II) and flexure tests were performed on composite materials for comparing the effectiveness of different crushing mechanisms. Fracture toughness results presented a significant improvement of using stitching methods on Mode-I properties, while slight reduction on Mode-II properties was also detected. They also indicated the flexural properties of structural composites can significantly affect their energy absorption capabilities.

At the final stage, six different factors including resin type, fibre architecture, crushing speed and stitching parameters were scaled in several levels in a modified geometric structure. An optimization approach based on Taguchi methods was utilised in order to statistically determine the relationship and assist in evaluating the contribution of each factor on crushing properties. It showed that by selecting the combinations of these factors with correct levels, the energy absorbed can be improved remarkably. It found that the crushing performance of this structural composite was mainly dominated by resin and fibre architecture, which contributed 71% capability of energy absorption. The other 29% capability was dominated by trigger, beam web length, edge stitching density and the crushing speed.

Chapter 1. Introduction

1.1. Background and motivation

Composite materials and structures have gained much attention over the last three decades. In addition to their excellent performance with high specific strength and specific stiffness, they possess good energy absorption capability [1]. Well-designed composites generally absorb more specific energy than conventional metals.

Unlike metals, which absorb energy by bending and folding mechanisms, the improvement in energy absorption for composite structures occurs through a series of processes involving central crack propagation, splitting of fronds, delaminations, fibre fracturing and tearing, and friction in the laminate and with the crushing platen as well as bending of fronds [2].

The energy absorbing process in composite structure is initiated through a trigger. If a composite structure crushes without a trigger or the trigger is not incorporated into the structure, failure can be catastrophic and brittle. A trigger is typically machined to a specific geometry, such as a chamfer, at one of the edges of the crush structure to provide a stress concentration that will initiate a localised failure area. Consequently, this failure guides the composite structure into a stable and high efficient crushing mode.

As one may anticipate, the energy absorption capability of composite materials and structural components is affected by a number of factors. These factors can be broadly classified into material properties, fabrication conditions, test conditions, also geometry and dimensions of the structures [1]. Fibre-reinforced plastic (FRP) composite materials are governed by the fibre, matrix, fibre/matrix interface, and fibre volume fraction. In terms of laminate structure, the fibre stacking sequence and fibre orientation are also important factors. Testing conditions involves the testing environment, boundary conditions of samples, and strain rate, depending on the strain sensitivity of materials. Geometry may include the triggering system, the cross-sectional shape and construction variance, such as sandwich configurations.

After more than three decades in development, although a complete set of energy absorbing systems based on composite materials has been built up, the vast majority of those investigations are restricted to specific structural forms. As a result, most energy absorbing composites for practical applications are either in tubular or conical forms.

Nowadays, the global trend in materials technologies is moving towards light-weight and yet high-performance, because this saves energy, fuel, and while contributing positively to the low carbon agenda, reduces costs and leads to higher performance. This trend has been an essential factor in aerospace and defence industries, and also has become a new challenge for other sectors such as automotive/vehicles and construction industries. Therefore, to satisfy an increasing demand for light-weight and high stiff/modulus protection structures, energy absorbing composite materials need to be organized in some kind of large and continuous forms, such as the sandwich panel.

Based on the crushing behaviour of sandwich panels composed of thin-walled steel tubes [3], it was determined that the energy absorption properties are dependent upon tube layout within the panel, number of tubes, tube geometry as well as the response of sandwich skins. The design of energy absorbing panels is therefore quite complex.

In comparison with metals, only a few energy absorbing composite materials so far have been developed into the sandwich panels, for example, Nomex^{TM}, egg-box panel [4, 5] and hollow three-dimensional (3-D) integrated core [6, 7]. But none of them was built on those progressive crushing mechanisms that were discussed in previously sections. It is mainly because, when a number of individual structures are placed together in a large panel, the interaction between those individuals as well as the joints between them will remarkably affect the energy absorption capability of entire structure. In contrast to the metals that fail in local buckling mode, the composite materials have to undergo a highly stable, sustained fracture to achieve an effective crush. Any unexpected cracking, bending, buckling or tearing of the laminate can dramatically reduce the energy absorption of composite materials. And those unexpected failures could easily occur around the junctions between individual elements of the panel.

1.2. Aim and objectives

The project therefore seeks to combine existing knowledge on simple plate crushing with geometric shapes that could be utilised to form the internal core of an advanced composite panel optimised for energy absorption units, for example, blast resistant constructions. The objective was to identify how local geometry influences basic crush behaviour and to seek a route of optimizing the specific energy absorption for such core material.

Therefore, a series of structural composites which represent the minimum repeat unit in a large panel are created. On the one hand, these structural composites consist of most well-understood individual structures that are flat plates and tubes. On the other hand these flat plates and tubes are reorganized into the transition geometries with the forms of circular, rectangular, hexangular, or combination of these forms with a certain proportion.

Due to the anisotropic properties of composite materials, it is also necessary to evaluate the influence from other factors which includes the types of fabric and resin, stacking sequence and fibre orientations. A range of experimental approaches are also required for optimizing the effectiveness of different crushing mechanisms within these transition geometries. Robust design is applied in this research as a cost-effective method to improve the performance of products by reducing its variability in energy absorbing performance [8].

Chapter 2. Literature Review

This chapter has two objectives, firstly to explain the principles of energy absorption in composites materials and structures and secondary to describe the optimization methodologies that have been used in this work. Both of these will be explained in terms of relevant literature.

2.1. Crushing mechanisms of composites

To evaluate the suitability of a composite structure for energy absorbing applications, the most widely used practice is to understand the crushing behaviour of composite structure subjected to axial compressive load. Axial compression can be carried out into two different ways: quasi-static crushing tests and dynamic impact tests. Most researchers tend to use the former as it is easy to conduct.

2.1.1. Structural instability and buckling

Composites can crush in a number of ways under the application of a compressive load. Their crushing mechanisms and energy absorption capability are primarily determined by structural stability and crushing failure modes. When in-plane loads are compressive, the composite laminates not only undergo in-plane displacements, but also may undergo lateral displacements. Thus, there does occur a coupling between in-plane loads and lateral displacements. This phenomenon is called *elastic instability* or *buckling* [9].

Global buckling on composite structure during crushing normally causes unexpected failure, and consequently terminates stable and efficient crushing. Therefore, in the design of the energy absorbing composite, structural stability must be considered as a crucial factor. Under most situations, the critical buckling load, $P_{cr,}$ is applied to analyse structural stability. It is defined as the smallest load at which the equilibrium of the structure fails to be stable as the load is slowly increased from zero [10].

The critical buckling load is significantly affected by boundary conditions and the structural geometry. In classical laminate theory (see Appendix 1), three basic boundary conditions are normally considered for buckling analysis, which are i) free edge, ii) simply-supported, and iii) clamped. Take example for a column, the result for the critical load of a clamped column at both ends is four times that of a simply-supported column at both ends [10]. In practice, the boundary conditions of structures are very complicated.

In Price and Hull's investigation [11], the failure mode was found to depend on specimen profile, wall thickness and sample height. They tested composite tubes made of random orientation E-glass mat and polyester resin. The range of geometries tested is illustrated in Figure 2.1 (left). Four tube profiles were tested, three square tubes with various corner radii, 10, 20, and 30mm, and round tubes. All round tubes failed by progressive crushing regardless of wall thickness or height, and square tubes with wall thickness (*t*) that greater than 2mm failed also by progressive crush. But the failure mode of square tubes with t = 2mm depended on corner radius (*R*) and specimen height (*h*) [11]. Increasing *R* resulted in progressive crush, while increasing *h* favoured catastrophic shell failure that caused by buckling. These trends are shown in Figure 2.1 (right).

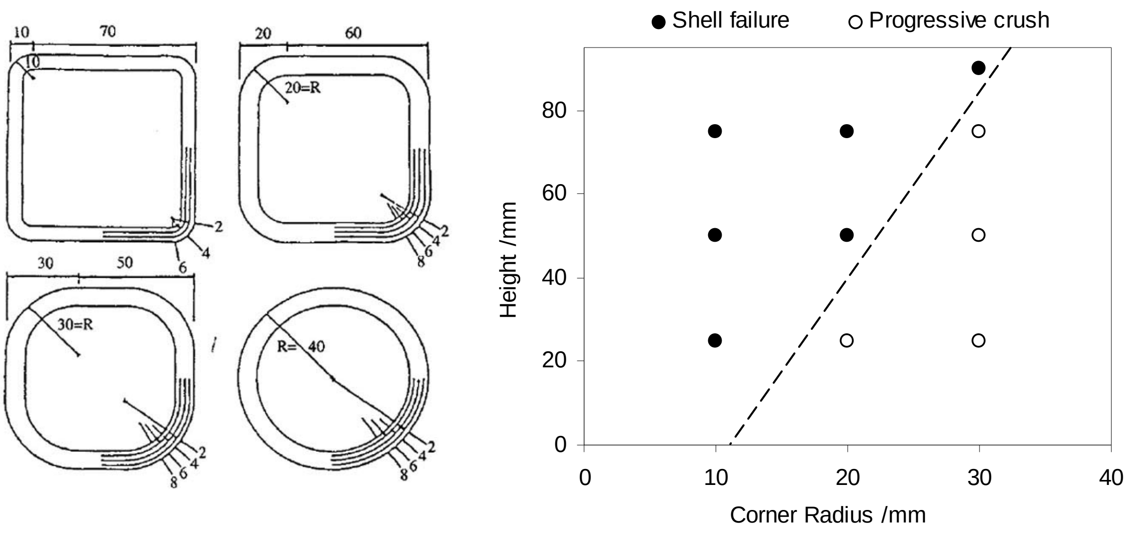

Figure 2.1 **Sketches of different cross-sectional profile of tubes (left) and variation of failure mode with height and corner radius (right) [11]**

Therefore, to avoid buckling in an ideal energy absorbing composite material, its critical buckling load should be larger than its crushing strength. Buckling analysis for anisotropic composite materials is much more complicated than isotropic materials. A solution for an all edges simply-supported crossply orthotropic plate can be found in

Appendix 1 or in Vinson and Chou's book [9]. More detailed analysis about boundary conditions, critical buckling stress, and geometry of composite structures will be discussed in Chapter 4.

2.1.2. Composite failure modes

Composites can fail in a number of ways, as mentioned before, these can be separated into two groups: catastrophic and progressive failure modes [12, 13]. Figure 2.2 illustrates the typical load-displacement curves for both catastrophic and progressive axial compressive failure of tubular composite structures.

Under axial compressive load, a composite crush structure without trigger is likely to fail either by compressive shear or axial splitting of composite structure [12]. Its load-displacement curve (Figure 2.2 left) shows that the load increases to a very high peak value followed by a low post failure load. Therefore, a composite structure that fails in a catastrophic failure mode is not suitable for absorbing energy due to its low energy absorbing level and sudden failure mechanism.

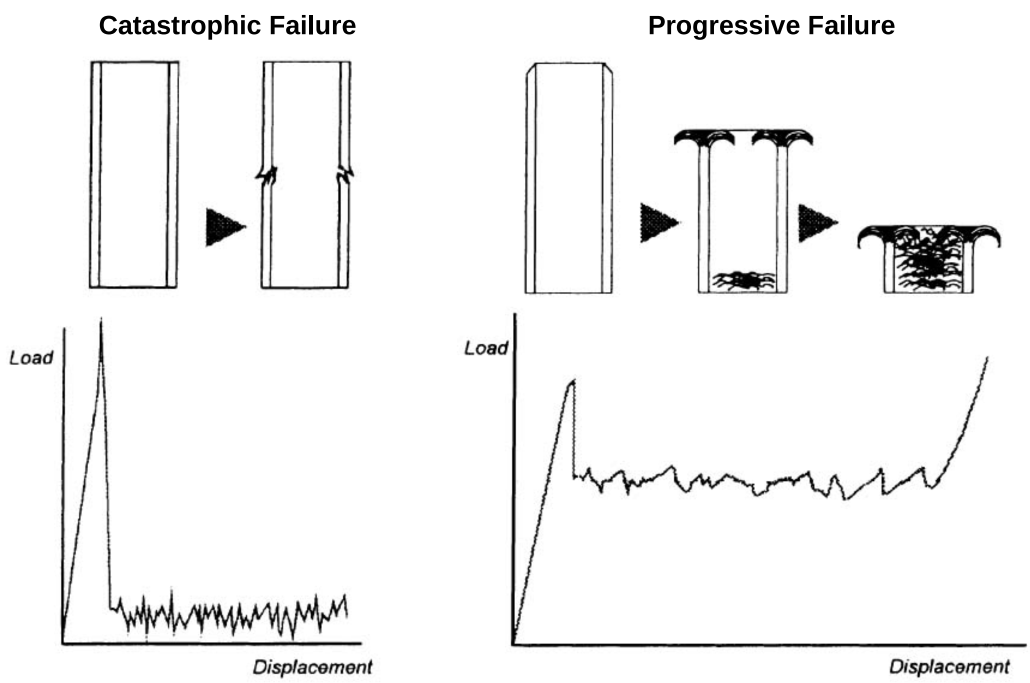

Figure 2.2 Energy absorption in two different crushing failure modes [13]

Depending on the sequence of microfracture events that lead to the formation of the progressive crush zone, the progressive crushing mode was grouped by Farley [14] into four failure modes (Figure 2.3):

1) Transverse shearing;

2) Lamina bending;

3) Brittle fracturing;

4) Local buckling.

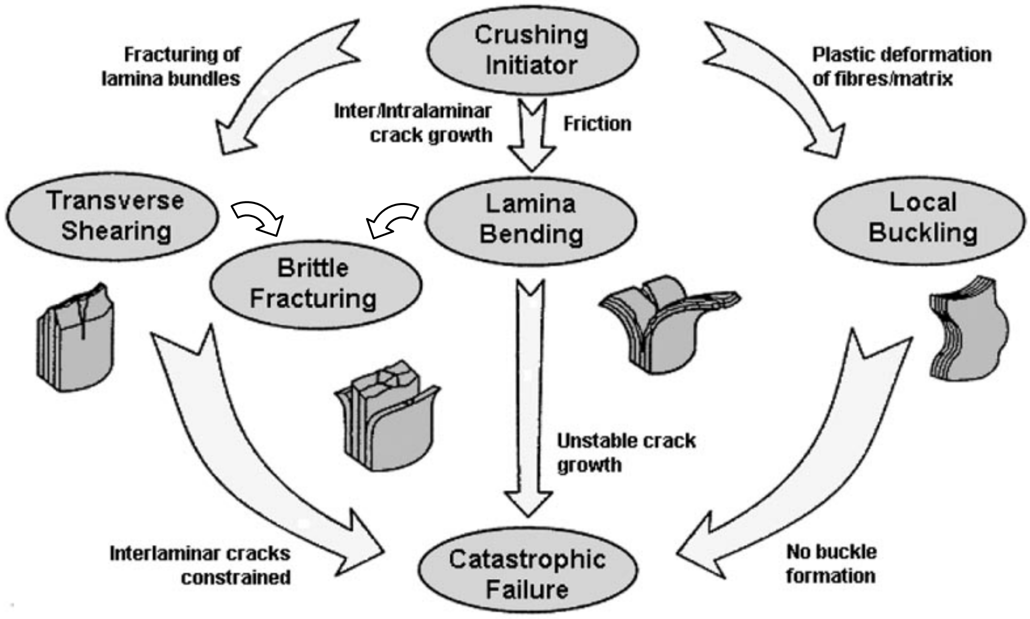

Figure 2.3 Crushing modes of continuous fibre-reinforced composite tubes [14]

2.1.2.1. Transverse shearing (fragmentation)

The transverse shearing crushing mode is characterized by a wedge-shaped laminate cross section with one or multiple short interlaminar and longitudinal cracks [14]. The characteristic of transverse shearing mode is that the length of the interlaminar and longitudinal cracks is less than the thickness of the laminate [14]. Interlaminar crack propagation and lamina bundle fracture control the energy absorption mechanism. Not only the mechanical properties of matrix and fibre as well as their interface, but also the fibre orientation in the laminate can affect the interlaminar crack propagation. The fracture strength of a lamina bundle is principally a function of the stiffness and failure strain of the fibre [14].

2.1.2.2. Lamina bending (splaying)

The lamina bending crushing mode is developed by long interlaminar, intralaminar and parallel-to-fibre cracks [14]. The lamina bundles exhibit significant bending deformation, but they do not fracture [14]. The principal energy absorption mechanism for this mode is the matrix crack growth [14]. Additionally, friction between adjacent lamina bundles and between composite and crushing surface also the increase energy absorbing level of composite materials [14].

2.1.2.3. Brittle fracturing

The brittle fracturing crushing mode is a combination of the transverse shearing and lamina bending modes [14]. Typically, the lengths of the interlaminar cracks are between 1 and 10 lamina thickness in this mode [14]. Lamina bundles in the brittle fracturing mode exhibit some bending and can fracture near the base of the lamina bundle [14]. When a lamina bundle fractures, the load is redistribute within the specimen, and the cyclic process of interlaminar crack propagation and lamina bundle bending and fracturing is repeated [14].

2.1.2.4. Local buckling (folding)

The local buckling crushing mode can occur in both brittle and ductile FRP composites. This crushing mode is similar to that exhibited by ductile metals [14]. The plastic deformation of the fibre and/or matrix controls the energy absorption mechanism [14]. Ductile-fibre-reinforced composite materials, such as Kevlar® and Dyneema®, deform along the compression side of the buckled fibres. In brittle-fibre-reinforced composite materials, the local buckling crushing mode only occur when i) the interlaminar stresses are small relative to the strength of the matrix, ii) the matrix has a higher failure strain than the fibre, and iii) the matrix exhibits plastic deformation under high stress [14]. Local buckling crushing mode is an inefficient crushing mode for composite structures.

The highest energy absorption of composite materials has been observed in brittle fracturing and lamina bending crushing modes [15, 16]. Hence, the crushing mechanism of composite structures investigated in present study is designed towards a balance between the brittle fracturing and lamina bending modes.

2.1.3. Trigger mechanisms

The design of trigger geometry can have a large effect on the sustained crushing load. The purpose of the trigger is to initiate sustained crushing in an efficient energy absorbing mode, rather than to have a catastrophic failure of the composite structure with little or without post failure energy absorption [17]. In most cases, trigger configurations consist of machining a special geometry in one of the edges of the composite structure [13].

Various trigger configurations have been developed for tubes [13, 18-20], I-beams [13, 21] and plates [17, 22]. Due to its ease of machining and suitability for the purposes of laboratory evaluation, mainly angle and steeple chamfers were preferred for most energy absorbing composites, previously.

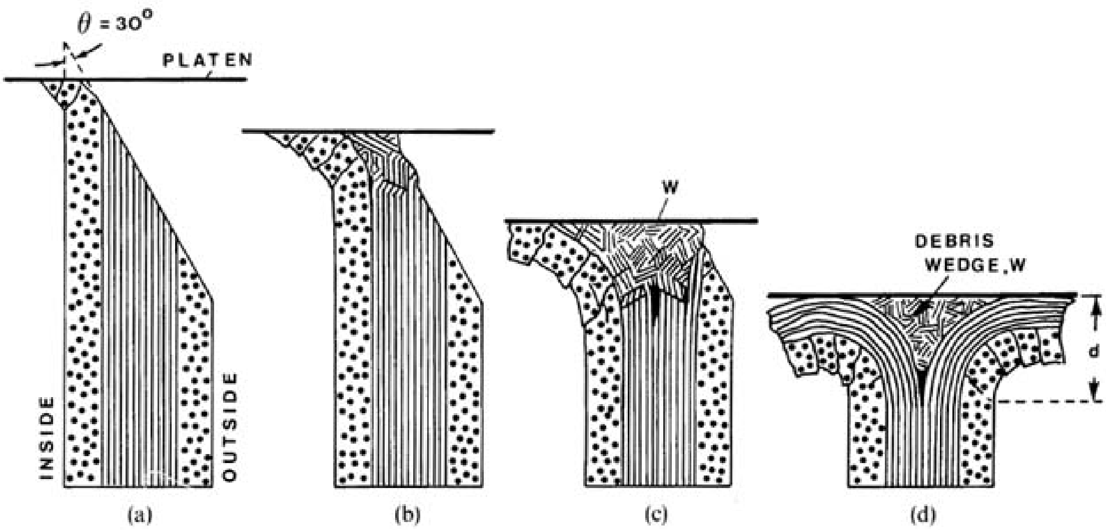

Figure 2.4 Schematic representation of formation of progressive failure mode (splaying mode) crush zone based on microscopic examination of polished sections [15]

The development of a stable crush zone in a chamfered tube wall is illustrated schematically in Figure 2.4. Progressive crushing initiates at the trigger that has been machined into the crush structure. At the trigger, the stresses are higher than those within the rest of the structure, hence microfracture initiates at that point (Figure 2.4a). The inside layers of the crushing tube eventually separate from the central layers as buckling progresses in both central and inside layers (Figure 2.4b). The fractured material henceforth spreads inwards thereby causing the inner layers to collapse. This results in the formation of a well defined zone of crushed material that acts as a wedge (*w* in Figure 2.4c). Eventually, the wedge causes the microfractures to grow into a central crack within the thickness, creating a stable crush zone which progresses along the structure at the speed of the loading (Figure 2.4d) [15]. Laminates with a steeple trigger exhibits a very similar crushing behaviour.

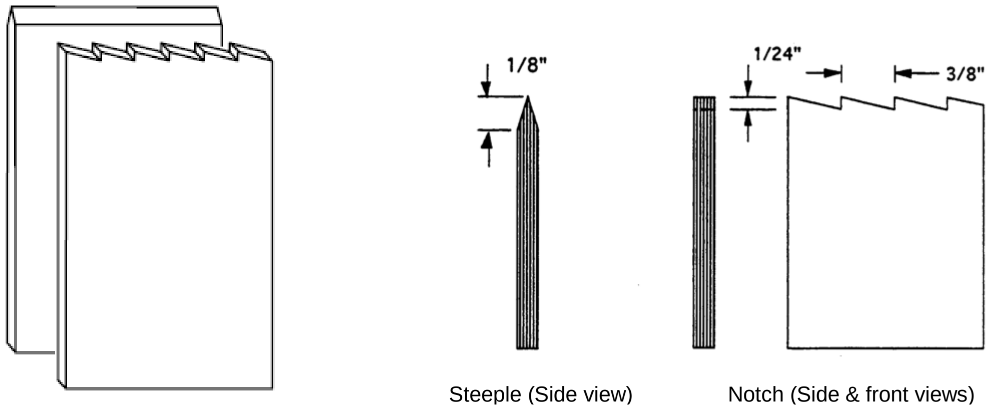

Figure 2.5 **Schematic sketch of typical crushing triggers: Steeple and notch [17, 22]**

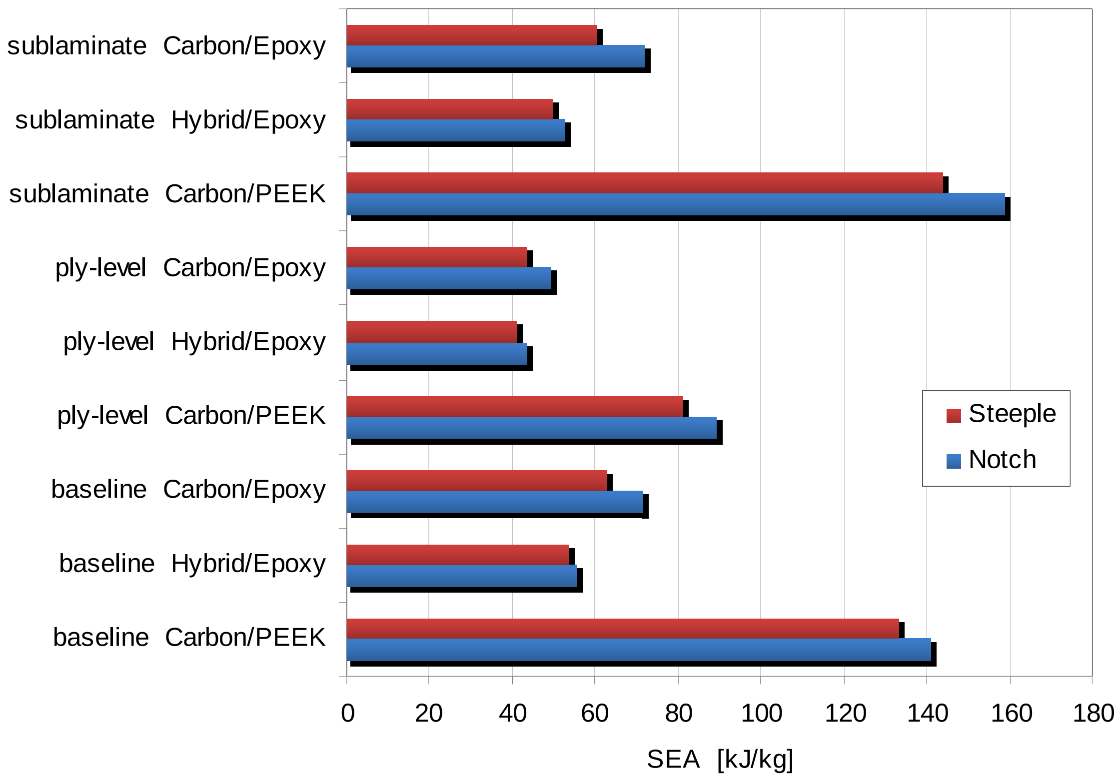

Figure 2.6 **Comparison of crushing results between notch and steeple triggers [17]**

Lavoie *et al*. [17, 22] compared notch trigger with steeple trigger on composite plates. Their geometric sketches are shown in Figure 2.5, and their crushing result can be found in Figure 2.6. Notch trigger achieved slightly higher sustained crushing load, while steeple trigger exhibited higher crushing efficiency than notch trigger. The crushing efficiency, η, can be defined as the average load, F_{av}, divided by the peak load, $F_{\max}$ [23]:

$$\eta = \frac{F_{av}}{F_{\max}} \tag{2.1}$$

If the peak load is too high compared with the sustained crushing force, the efficiency of the crush will be reduced thereby reducing the overall energy absorption capacity, as well as introducing high deceleration curves. Ideally, the crushing efficiency should equal to one.

Although triggers are typically machined into a structure, it would be ideal to incorporate the trigger as the component is made. For this purpose, Thuis and Metz [18] examined five different trigger configurations on tubes. These trigger configurations and their crushing results are shown in Figure 2.7.

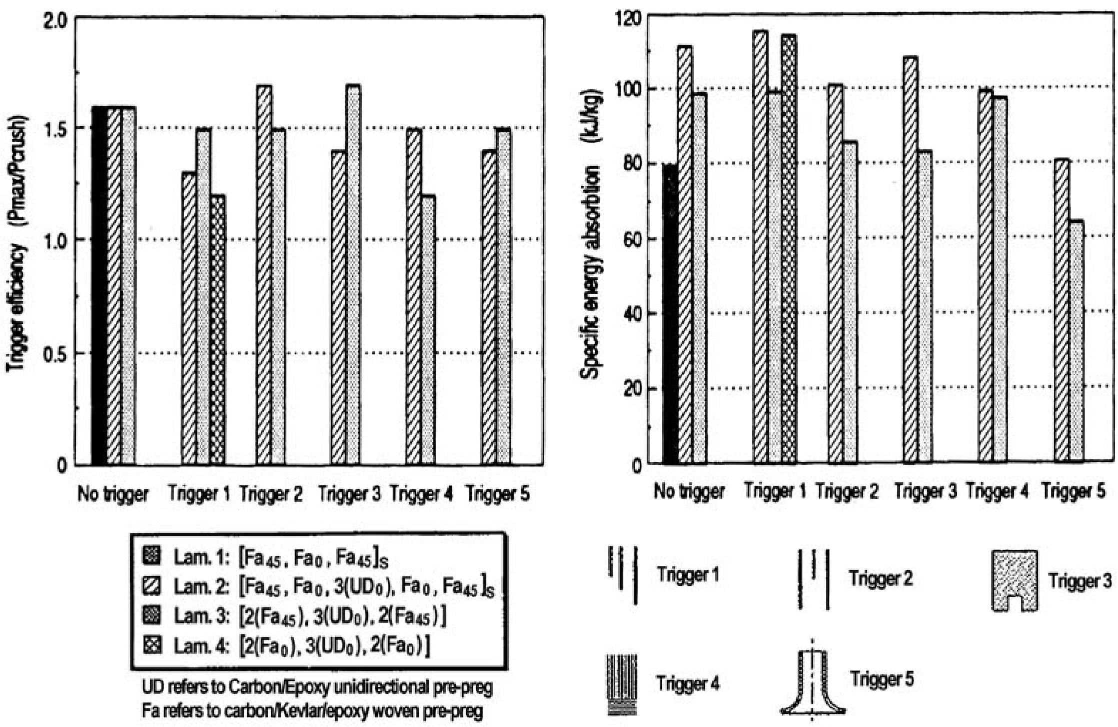

Figure 2.7 Effect of trigger configuration and laminate lay-up on the energy absorption capability and crushing efficiency [18]

Considering both crushing efficiency and specific energy absorption, the best triggers manufactured in this way include the shortening of the central unidirectional (UD) layers by ply drop-off in every 2mm (Trigger 1) and shortening of the central unidirectional layers by 10mm but filling the space with 90° lateral fibres (Trigger 4). In addition, an out-of-plane trigger by the addition of a flange to one end of the tube (Trigger 5), crushed in a very low energy absorption level, but it exhibited a good crushing efficiency [18].

Therefore, when selecting the trigger geometry for an energy absorption element, it is not only important to take into account an ability to exhibit a sustained load during crushing, but also the peak load level which is reached during this sustained crush [13].

2.1.4. Energy absorption in progressive crushing mode

2.1.4.1. Crushing process

The progressive crushing process of simply-supported plate with steeple trigger was divided into four distinct stages in Cauchi-Savona and Hogg's work [16]. A typical load vs. displacement curve is plotted in Figure 2.8.

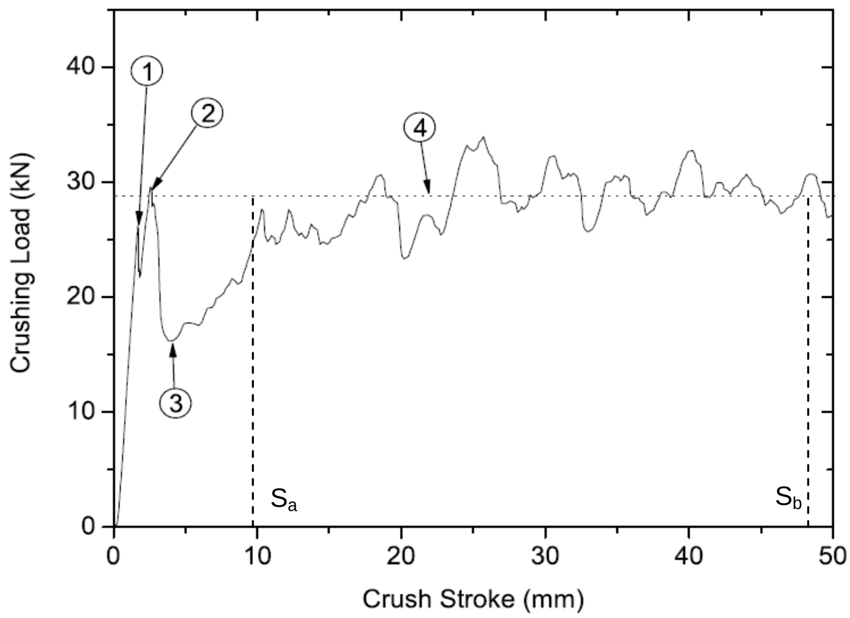

Figure 2.8 Typical plot of splaying crushing mode with steeple trigger: (1) first peak; (2) second peak; (3) drop after initial split; and (4) specific sustained crushing stress [16]

① a first peak resulting from the collapse of the triggering (steeple chamfer) tip;

② a second peak resulting from the split of the chamfer to produce two fronds for crushing;

③ a drop in stress, the magnitude of which is determined by the distance that the split extends into the laminate; and

④ a region of sustained crushing with the splayed fronds tearing along side-support rigs.

2.1.4.2. Evaluation of crushing energy

The energy absorbed or total work done during crushing, *U*, is represented as the area under the load-displacement curve. Thus, using the nomenclature in Figure 2.8 the total energy absorbed for this progressive crush is:

$$U = \int_0^{S_b} F dS = F_s \left(S_b - S_a\right) \tag{2.2}$$

where F_s is the sustained (steady or average) crush load, and $(S_b - S_a)$ is the region of sustained crush. In order to be able to compare data between different materials [12], the specific energy absorbed in crushing, or the absorbed energy per unit mass of material, is typically defined as the *specific energy absorption (SEA)*, which is given by:

$$SEA = \frac{U}{m} = \frac{F_s\left(S_b - S_a\right)}{V\rho} = \frac{F_s\left(S_b - S_a\right)}{AL\rho} \tag{2.3}$$

where *m* and ρ are the mass and density of the material, respectively. *V*, *A* and *L* are the volume, cross-sectional area and length of crushed portion of the crush structure, respectively. In some references the SEA is also described as *specific sustained crushing stress* (SSCS). If $S_b >> S_a$, then, $(S_b - S_a) \approx S_b$. And if the debris is dispersed during crushing, then ideally, $S_b = L$. Hence, the specific absorbed energy during crushing can be written as:

$$SEA = \frac{F_s}{A\rho} = \frac{\sigma_s}{\rho} \tag{2.4}$$

where σ_s is the average crushing stress. In some references, the σ_s is also described as *sustained crushing stress* (*SCS*).

2.1.4.3. Energy absorbing mechanisms

During progressive crushing, the composite laminate undergoes many forms of fracture. Depending on the observations from micrographs in previous research [15, 16], a schematic sketch of these energy absorbing mechanisms is presented in Figure 2.9, which illustrates the cross section area of a crushed composite laminate.

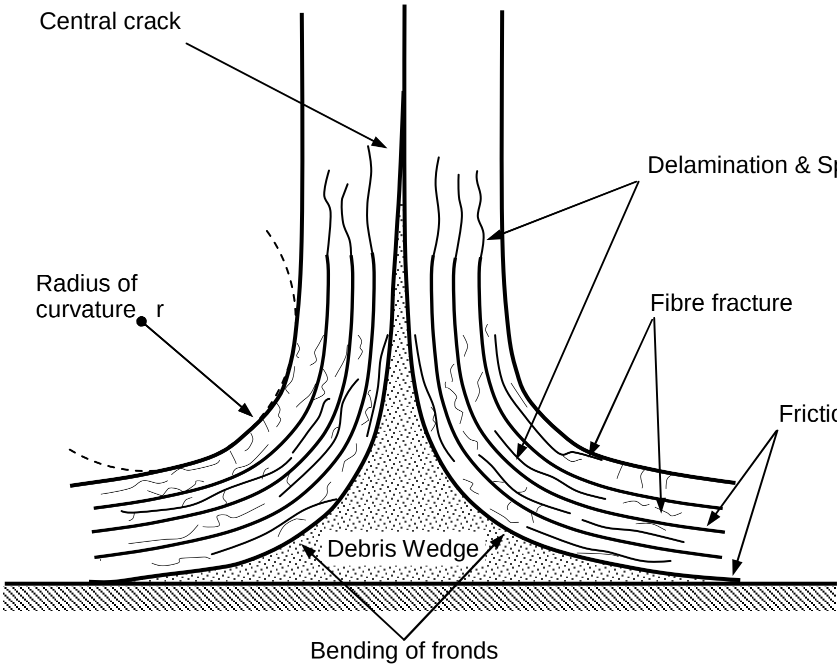

Figure 2.9 schematic sketch of cross-sectional area for the typical composite laminate during crushing and different energy absorption mechanisms [24]

In previous studies [24, 25], the total energy absorption (U) in progressive crushing, has been defined and categorized into seven parts. Initially, the composite splits along the central crack of laminate, and this is presumed to be related to the Mode-I properties (U_{IC}). And then, the torn splayed fronds split (U_{sp}) and delaminate (U_{de}) through Mode-II shearing deformation. Bending of the fronds (U_{σ}), fibre fracture (U_{ff}) as well as friction (U_{fr}) within crushed fronds and at the platen surface, absorb further energy during crushing. In addition, other forms (U_{other}) include Mode-III tearing effects also help to absorb energy. The schematic sketches of three mentioned interlaminar displacement modes, Mode-I, Mode-II and Mode-III, can be found in Figure 2.24. Therefore, the energy absorption amount, U, is expressed as:

$$U = U_{sp} + U_{de} + U_{IC} + U_{ff} + U_{fr} + U_{\sigma} + U_{others} \tag{2.5}$$

With increasing crushing displacement, the debris wedge forces the laminate to bend to either side of it, while the radius of curvature of the fronds forces them to delaminate and split into a number of thin beams. The magnitude of the bending stresses (σ) that the fronds experience on either side depends on the radius of curvature (r), the thickness (t_b) and elastic modulus (E) of the beams. This is expressed as:

$$\sigma = \frac{Et_b}{2r} \tag{2.6}$$

It is important to note that the smaller the radius of curvature, the higher bending stress, and consequently, the energy higher absorption that is achieved. Steady central crack growth linked to Mode-I properties tends to generate a small radius of curvature. Stitching to control central crack growth was thus used in the latter part of this study. Furthermore, in order to understand and evaluate the influence from different crushing mechanisms, Mode-I, Mode-II and flexure tests are performed on different composite materials in the present study.

2.2. Factors of controlling energy absorption capability of composites

2.2.1. Effect of material properties

The crushing characteristics of composite are dependent on various internal and external factors. The material properties can significantly affect the energy absorbing capability. These properties include type of fibres and matrices, interface, volume fraction, fibre orientation and stacking sequence [26].

2.2.1.1. Fibre types

Many researchers have investigated the composites involving fibres of carbon, glass or aramid (Kevlar®) in a thermosetting resin. In general, the carbon and glass fibre reinforced thermoset tubes progressively crush by lamina bending and brittle fracturing modes. The tubes manufactured with carbon fibres may also fail catastrophically [14], because the carbon fibres are so brittle that the interlaminar cracks before lamina bundles bend or fracture.

In general, the carbon fibre reinforced tube display higher specific energy than the glass fibre reinforced tube. This is attributed to the lower density of carbon fibres compared with glass fibres. In Ramakrishna's work [12], composite tubes reinforced with three different types of fibre, which are AS4 carbon fibre, IM7 carbon fibre and S2 glass fibre, were investigated. AS4 carbon fibre has higher tensile strain than IM7. The thermoplastic resin, polyetheretherketone (PEEK) was used as their matrix. In Figure 2.10, the results shows that glass reinforced tubes possess approximately 20% lower SEA than the carbon reinforced tubes. It was also found both AS4/PEEK and IM7/PEEK tubes displayed similar specific energy, despite AS4 being more ductile than IM7.

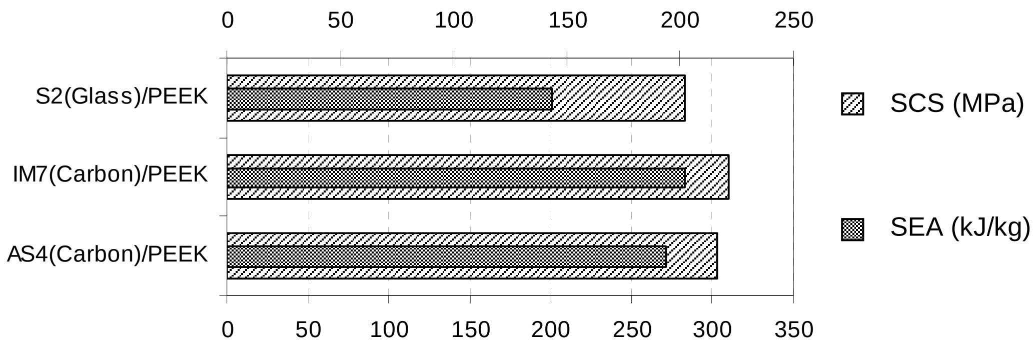

Figure 2.10 Specific energies and crushing stress comparisons of PEEK matrix composite tubes with different fibres [12]

However, within through-thickness stitched laminates [2], glass fibres seem to produce more consistent results in comparison to carbon fibres, and seem to be less sensitive to the distortions and misalignment caused by the stitches. Furthermore, the glass fibres are compatible with different resins which make them more suited for a lower-cost production process [2].

Compared with carbon and glass fibre, the aramid fibre reinforced composite tubes crush by a local buckling crushing mode. The aramid fibres fail at a rather higher strain which is approximately 8%, compared with the carbon and glass fibres which fail at approximately 1% and 5% strain, respectively [12]. The aramid fibres present lower SEA levels than carbon in general. The comparisons of energy absorbing capability between carbon fibres and aramid fibres can be found in Figure 2.11.

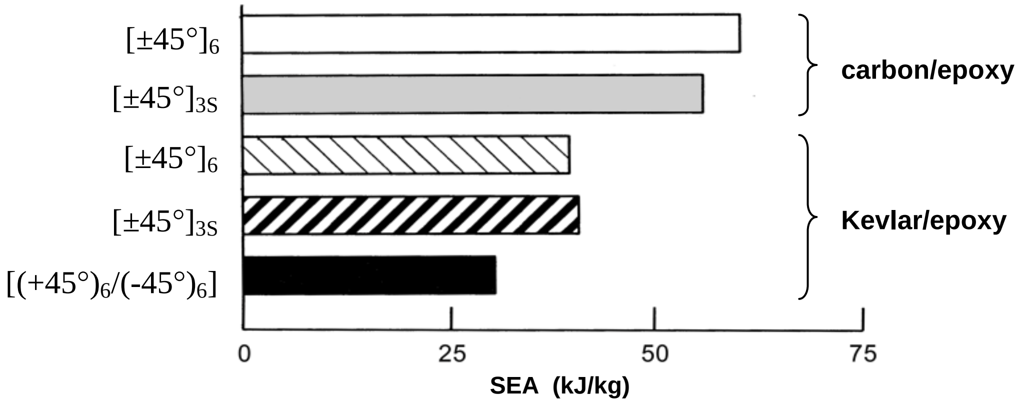

Figure 2.11 **Effect of stacking sequence on energy absorbing capability of [±45] tubes [14]**

Hybrid fibres have been developed in an attempt to combine the best energy absorption characteristics of different fibres into a single material. Hybrid braided tubes containing carbon, glass and Kevlar® fibres would crush in a stable manner.

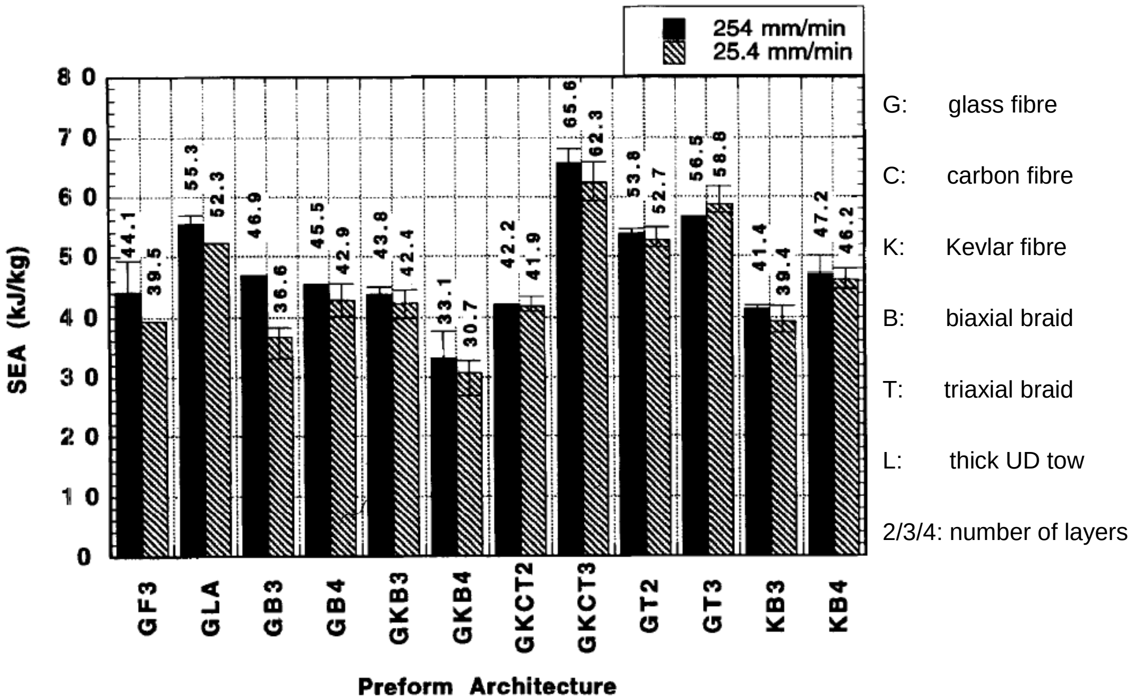

Figure 2.12 Comparison of SEA as a function of preform architecture [27]

Harbhari and Haller [27] investigated crush performance of braided and hybrid composite tubes under quasi-static speeds. It was found that the best performance was that of the hybrid glass-Kevlar®-carbon architecture with the carbon tows in the axial (or crushing) direction. This result is shown in Figure 2.12. In a triaxial architecture, the use of tailored hybridization can result in enhanced SEA levels with combination of nearly all types of progressive crushing modes that was mentioned previously. It also can be found in that the triaxial architectures (GT2, GT3) show better performance than the biaxial architectures (GB3, GB4). More discussion about the effects of fibre architecture can be found in Section 2.2.1.3.

2.2.1.2. Matrix systems

In general, thermoplastic composite materials display higher energy absorption than the thermoset based composite materials. This is attributed to the higher fracture toughness of thermoplastic matrix based composite materials [12]. Although the thermoplastic composites exhibit higher energy absorbing levels, thermosetting matrices were still more popular than thermoplastic in previous and current applications as thermosetting composites have relatively lower processing cost.

Polyester, epoxy and vinyl ester resins are the three most widely used thermosetting matrices. Polyester resins are widely used in transport applications. Their properties vary strongly with chemical formulation but generally they offer a high performance per cost ratio. Compared with polyester, most epoxy resins offer better moisture resistance, higher modulus, lower shrinkage and larger strain to failure, but costs are around five times that of polyester. Vinyl ester resins have gained popularity as they have more remarkable adhesion and fatigue properties than polyester while costing less than epoxy. Typically the costs of vinyl ester resins are around twice that of polyester.

Warrior *et al.* [28] investigated the effects of resin properties and resin processing parameters on the crush behaviour of thermoset composite tubes. At the first stage of their study, three thermosetting resins, polyester (Norpol® 420-100), vinyl ester (Dion® 9500), and epoxy (Crystic® D5316) were considered. Composite tubes were made from a continuous filament random mat (Unifilo® U751-375) with a fibre volume fraction of 23%. Their crush test results are shown in Figure 2.13. It reveals that epoxy absorbed slightly more energy than vinyl ester, and polyester exhibits poorest performance.

The processing conditions including cure temperature, post-cure duration and resin composition also change resin properties and consequently can affect energy absorbing capability of composites. Warrior *et al.* testified this result at their second stage of experiment (see Figure 2.14). Besides filament random mat (Unifilo U750-450), BTi 0/90° warp knitted fabric (Stitchmat) was also used at their second stage. It is interesting to note that the cure temperature does not change the energy absorbing properties, while the post-cure duration was shown to result in a large increase in composite mechanical properties [28].

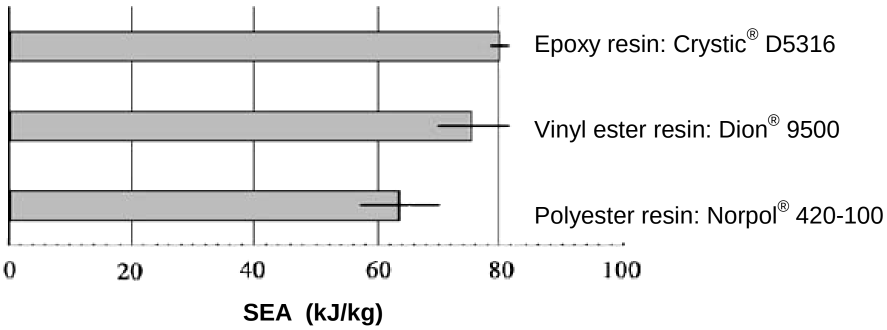

Figure 2.13 Energy absorption of composite tubes reinforced by random fibre mat in three different thermosetting resins [28]

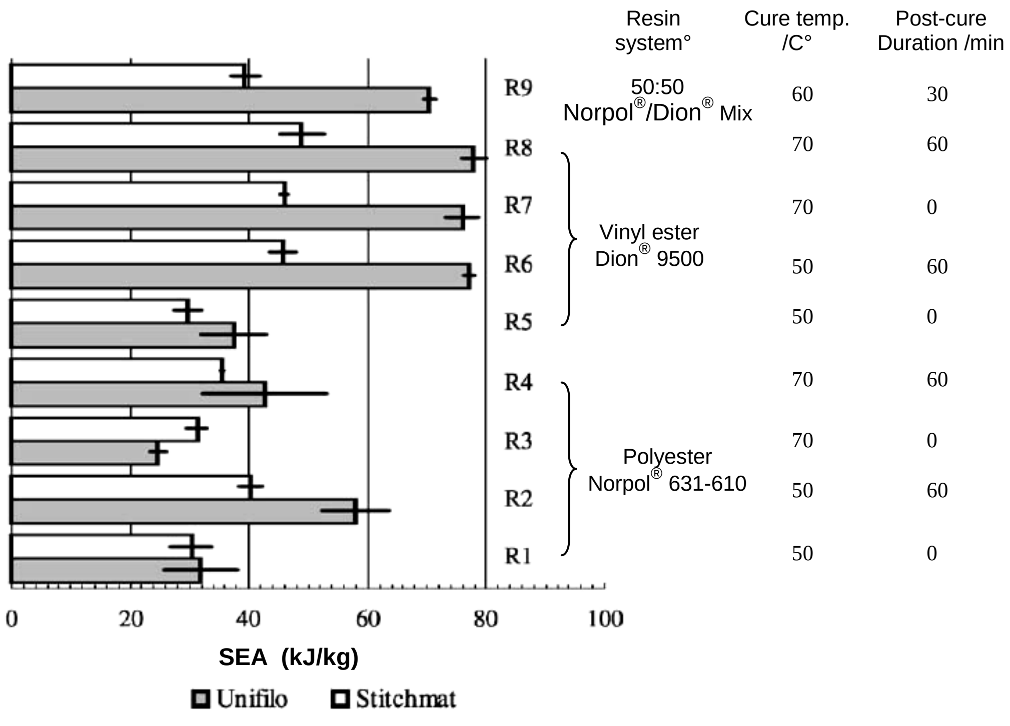

Figure 2.14 Effects of processing conditions on SEA of composite tubes [28]

However, different resins seem to have little influence on composite plates that were made of multiaxial Non-Crimp Fabrics (NCFs) [16]. The plates were tested at varying unsupported widths to identify the stability of the different orientations. Figure 2.15 shows that for the resins selected, there was apparently no performance gain when using epoxy resins over polyester resins. The reason for this could be that the different resins do not have significantly differing mechanical properties. It is also possible that the two different laminates underwent a change in their interlaminar fracture toughness properties when the matrix was altered [16].

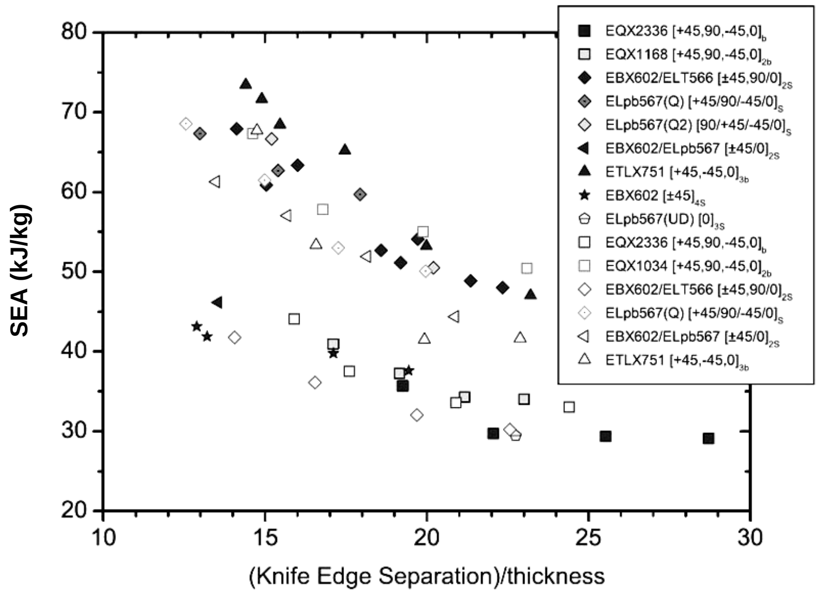

Figure 2.15 Energy absorption perform on different dimensions for composite plates with various fibre orientations: closed symbols represent polyester matrix laminates, while open symbols represent the equivalent laminate with an epoxy matrix [16]

For the comparison between thermoset and thermoplastic matrices, Ramakrishna in his previous study [12] investigated the energy absorption characteristics of carbon fibre reinforced epoxy (thermoset) and PEEK (thermoplastic) composite tubes. The carbon/PEEK tubes absorbed 180 kJ/kg specific crushing energy, while the carbon/epoxy tubes absorbed 53 kJ/kg specific crushing energy. This is attributed by Ramakrishna to the higher interlaminar fracture toughness of thermoplastic PEEK composite materials compared with that of epoxy composite materials. PEEK matrix offers a high resistance to crack growth between the fibres and prevents failure by this mode until the onset of stable progressive crushing. Some very similar results can be found in Lavoie *et al.*'s study [17] (see Figure 2.18) and Hamada *et al.*'s study [29].

Furthermore, during the same study, Ramakrishna investigated carbon fibre reinforced composite with different kinds of thermoplastic matrices: polyetherimide (PEI), polyimide (PI), and polyarylsulfone (PAS). It was found that the specific energy of thermoplastic tubes follows the order PAS < PI < PEI < PEEK. In Figure 2.16, plots of their specific energy levels are shown.

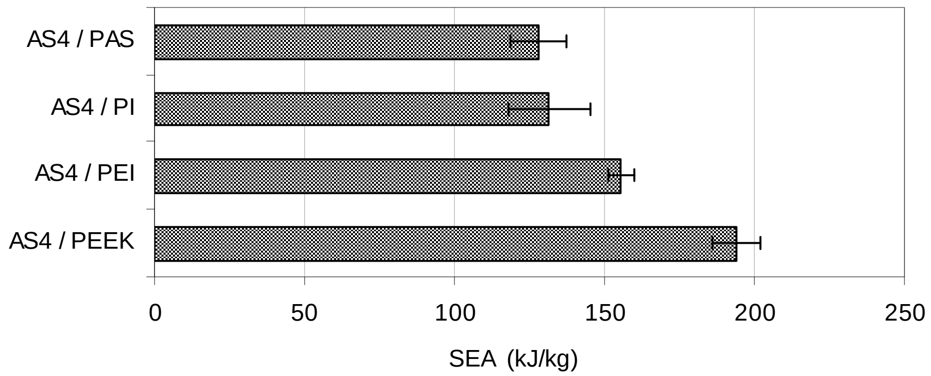

Figure 2.16 Specific energies of carbon fibre reinforced thermoplastic composite tubes [12]

2.2.1.3. Fibre architecture

The energy absorption characteristics of composite materials are sensitive to the fibre architecture. In this section, three main forms conducting on fibre architecture are discussed: stacking sequence, fibre orientation and through-thickness stitching. Most previous investigations concerning fibre architecture were studied on composite tubes and plates.

- ***Stacking sequence***

Laminate stacking sequence is used to tailor in-plane and bending stiffnesses and damage tolerance of a structure. In general, positioning 0° fibre plies on the exterior of the stacking sequence increases bending stiffness. 0° fibre plies would be positioned in the interior of the stacking sequence if the damage tolerance is more important [14].

Farley [14] in his first set of samples compared the energy absorption capability of the [±45] composite tubes which were fabricated using carbon/epoxy and Kevlar/epoxy. It was found that changes in stacking sequence result in variation in energy absorption between 5% and 25%. These results have already been stated previously in Figure 2.11.

The second set of tubes in his study consists of $[+45_F^H / 0_{10T}^{Gr} / -45_F^H]$ and $[0_{5T}^{Gr} / \pm 45_F^H / 0_{5T}^{Gr}]$, where *H*, *F*, *Gr*, and *T* refer to hybrid, fabric, carbon, and unidirectional tape, respectively. It was found that placing the 0° layers oriented along the crushing direction on the exterior of the tubular sample decreases the capability of energy absorption by 20% when compared with one that had the 0° plies on the interior. This is attributed to the interior 0° plies which crush in a transverse shearing mode. Transverse shearing mode exhibited as a more efficient crushing mode than the lamina bending mode when the 0° layers were on the exterior.

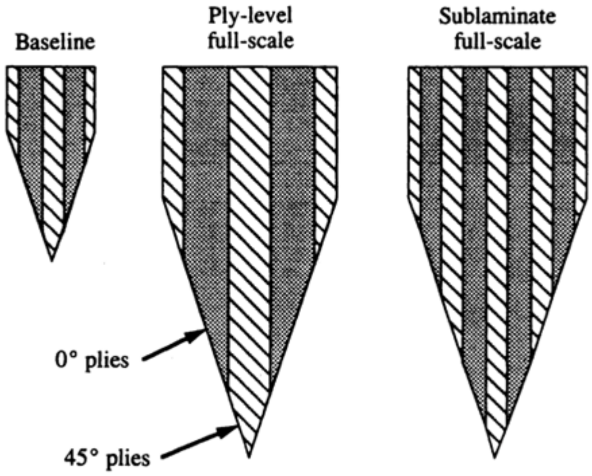

Figure 2.17 Schematic cross section of baseline, ply-level, and sublaminate-level scaled composite plates with steeple trigger [17]

Lavoie *et al.* investigated composite plates consist of symmetric ±45/0 plies within three different stacking sequences. They chose $[\pm45/0_4/\pm45]_S$ as the baseline lay-up. Then full-scale lay-ups were created by doubling the in-plane dimensions and thickness of the baseline plates. The chosen laminate stacking sequences were $[(\pm45)_2/0_8/(\pm45)_2]_S$ for ply-level, and $[\pm45/0_4/\pm45]_S$ for sublaminate-level. The cross section of baseline and full-scale samples were schematically shown in Figure 2.17.

They found the SEA levels for baseline and sublaminate-level scaled plates were close. However, energy absorption of ply-level scaled plates was much below that of baseline and sublaminate-level scaled plates. This can be seen in Figure 2.18. For this reason, laminates made of thinner fabric plies seems to possess better energy absorbing capability than one with thicker plies.

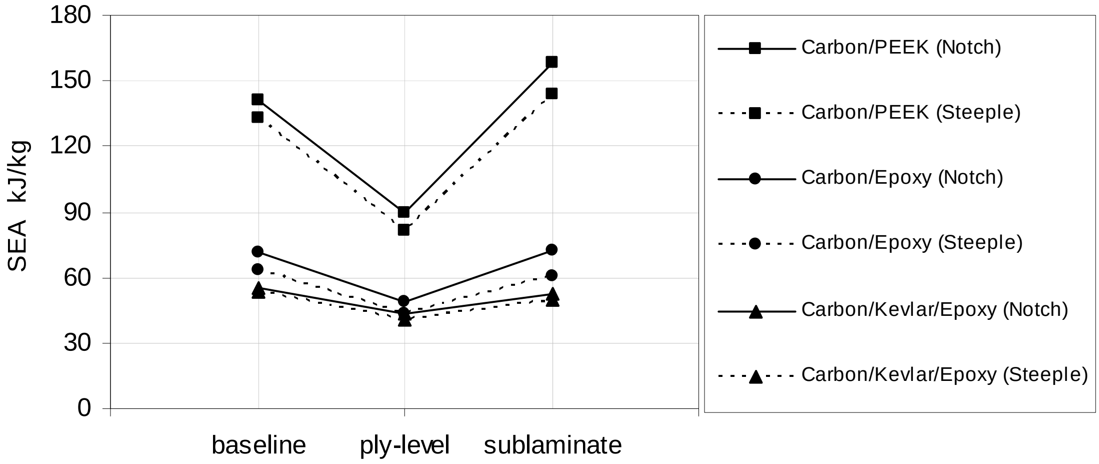

Figure 2.18 Comparison of specific sustained crushing stress for composite plates made of Carbon/PEEK, Carbon/Epoxy, and Carbon/Kevlar® Epoxy with different triggers [17]

- ***Fibre orientation***

It has been proved that the energy absorption capability varies with ply orientation. In particular, it is very sensitive to the proportion of 0° layers. Many researchers have investigated the influence of $\pm\theta°$ tows on energy absorption. Herein, the angle, θ, is the angle between the fibre direction and the longitudinal axis of the composite structure, which normally is the same as crushing direction.

Ramakrishna [12] obtained different results in carbon/PEEK tubes with θ in the range of 0°-30°. The specific energy initially increased with increasing θ up to ±15° and then decreased with further increase of θ. All tubes crushed progressively by lamina bending crushing mode except the tubes with θ = ±30°, which failed catastrophically by transverse shearing mode. Ramakrishna attributed this variation in specific energy to the changes in the microfracture processes in the crush zone.

Hull [15] investigated the energy absorption behaviour of filament wound glass/polyester circular tubes with θ in the range of ±35°-90° under quasi-static crush. Showing in Figure 2.19, the specific energy increased with increasing θ up to ±65°. Morphologically, tubes with θ in the range ±35° to ±55° crushed by lamina bending mode. Tubes with θ higher than ±65° crushed by fragmentation mode, thus, their specific energy are decreased. Very similar results were found in Song *et al.*'s study [30] in which circular glass/epoxy tubes were tested. As the winding angle θ increases from 15 to 90°, the macroscopic collapse mode of the tube changes from lamina bending to local buckling and then to transverse shearing. Both Hull and Song's crushing results on tubes are compared in Figure 2.19.

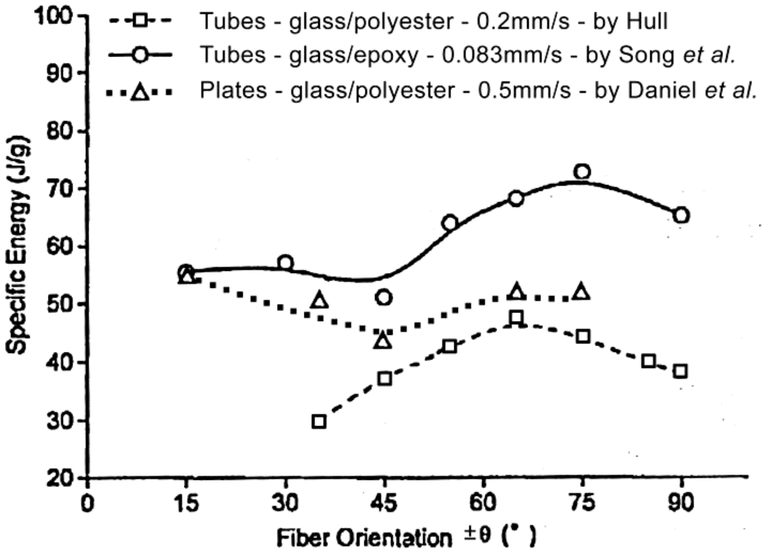

Figure 2.19 Effect of fibre orientations (±θ) on SEA for tubes and plates [15, 30, 31]

Daniel *et al.* [31] tested simply-supported plate samples which were fabricated using Uni-directional (UD) E-glass fibres and polyester resin with different orientations: ±15°, ±35°, ±45°, ±65°, and ±75°. Compared with Hull's circular tubes, there was no significant trend within the crush results of their plates. In Figure 2.19, the literature data presented by Daniel are also plotted. It is interesting to note, there are no transverse forces acting on the flat plate during crushing, hence it is unlikely that 90° or other near horizontal fibres within flat plates will offer benefit as same as the hoop-wound fibres do in tubular structures [24]. More discussions about plates will be presented in Section 2.2.4.4.

Farley [32] carried out quasi-static tests on [0/±θ] circular tubes made out of carbon/epoxy, glass/epoxy and aramid/epoxy. The energy absorbing capability of carbon/epoxy tubes was decreasing as θ increased for θ between 0° and 45°. However, little variation was observed in glass/epoxy and aramid/epoxy circular tubes for θ between 0° and 45°. The energy absorbing capability of either glass/epoxy or aramid/epoxy tubes was increasing with increasing θ for θ larger than 45°. More details can be seen in Figure 2.20.

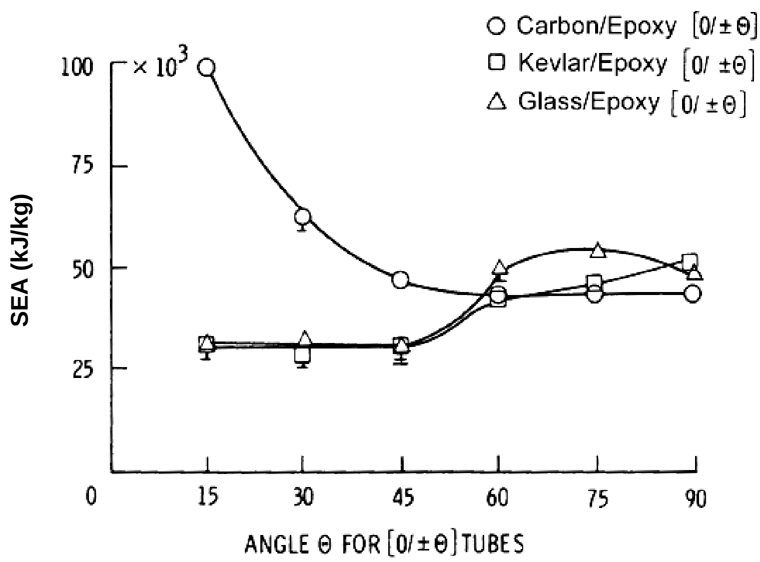

Figure 2.20 Effect of fibre orientation [0/±θ] on SEA for circular tubes [32]

Solaimurugan and Velmurugan [33] also studied carbon/epoxy, glass/epoxy and aramid/epoxy circular tubes with similar architecture [0_2/±θ], dynamic tests were carried out instead. In their report, specific energy absorption of specimens all generally increase with increasing θ.

Composite tubes with a large hoop constraint tend to fail in a fragmentation mode whereas tubes with less hoop constraint fail by lamina bending mode [12]. Hull [15] investigated woven glass/polyester tubes with full range of hoop-to-axial (H:A) ratios from 8.5:1 to 1:8.5. Under quasi-static crush, it was found that specific energy increased with increasing H:A ratio from 8.5:1 to 1:4. In other words, the specific energy increases with increasing the proportion of axial fibres. Higher proportion of axial fibres can improve compressive strength and succeeding crushing stress. The hoop constraints led to a sharp radius of curvature at the crush front and successive fracture of the axial fibres into short lengths. However, the tubes with H:A ratio of 1:7 and 1:8.5 showed a high initial strength, the specific energy then dropped to a very low value. It revealed that extra high amount of axial fibres may result in only axial splitting and delamination in the wall of tube, instead of generating fibre fractures and fibre shear cracks [15].

2.2.1.4. Fibre volume fraction

The fibre volume fraction is still an important parameter whose influence on mechanical response must be taken into account during composite structural design [14]. Studies on the effect of fibre volume fraction [12, 14, 26, 34] suggested an increase in fibre content would not always, as one would normally think, improve the energy absorption capability of a composite material.

Tao *et al*. [34] varied the fibre volume fraction between 10 and 60% in glass/epoxy composite material. They found that the specific energy improves with increasing fibre volume fraction and it reaches saturation at fibre content above 50%. As the fibre density is generally higher than resin density, the composite material density increases as the fibre content increases. When the increase in the crush load does not exceed the increase in the material density, the specific energy would be saturated or decreased (see equation 2.4).

Farley [14] tested composite tubes which were fabricated from carbon/epoxy. Specimens had fibre volume fractions between 40% and 55%, and three fibre orientations that were $[\pm45]_6$, $[0/\pm15]_4$ and $[0/\pm75]_4$. Shown in Figure 2.21, the crushing results of these specimens with $[\pm45]_6$ and $[0/\pm15]_4$ lay-ups exhibited a decrease in energy absorption capability with increasing fibre volume fraction. Herein, specimens with $[0/\pm15]_4$ lay-up failed predominately by a lamina bending mode during crushing, and specimens with $[\pm45]_6$ lay-up exhibit a combination of lamina bending and brittle fracturing. It has been found that crush in either the lamina bending or brittle fracturing mode is significantly influenced by the interlaminar strength of the material [14]. As the fibre volume fraction increases, the fibre spacing decreases. The close fibre spacing results in higher interlaminar stresses within the matrix. Therefore, the interlaminar strength is reduced [14].

The specimens with $[0/\pm75]_4$ lay-ups crushed in a brittle fracturing mode and displayed a slight increase in energy absorption capability with increasing fibre volume fraction [14]. One the one hand, tubes with $[0/\pm75]_4$ have more circumferential fibres which proved lateral support to stabilise the 0° fibres instead of the matrix and control interlaminar crack growth. Therefore, there is little influence from changes of fibre volume fraction. On the other hand, the approximate 4% decrease in the laminate density due to the increase in fibre volume fraction, resulted in a slight increase in energy absorption capability [14].

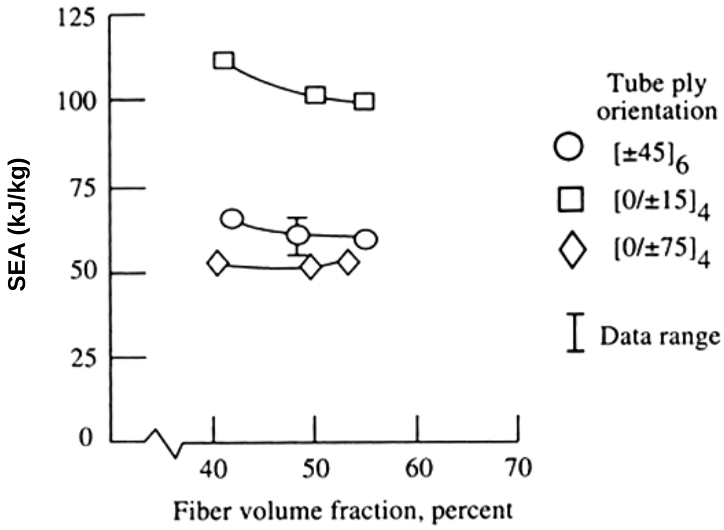

Figure 2.21 Influence of fibre volume fraction on energy absorption capability of carbon/epoxy composite tubes [14]

In the same way, Jacob *et al.* [26] tested composite plates manufactured from chopped carbon fibre and epoxy resin with two different fibre volume fractions: 40% and 50%. They found that an increase in fibre volume fraction caused a decrease in the specific energy absorption for chopped carbon fibre composite plates with fibre length of 2 inches. In contrast, for those plates with fibre length of 1 inch, the specific energy absorption displayed an increase with increasing fibre volume fraction. They concluded this difference was also caused by changing of interlaminar strength and composite density.

2.2.2. Effect of fracture toughness

Fracture toughness is a measure of a material's resistance to brittle fracture when a crack is present. It can be expressed by the critical stress intensity factor, K_C, or the critical strain energy release rate, G_C, both of which are based on fracture mechanisms. The most common approach is to assume that the materials behave in a linear elastic fashion so that linear elastic fracture mechanics (LEFM) can be employed.

2.2.2.1. Energy analysis

Elastic strain energy is stored in the body when it is deformed elastically. As the crack grows through the body, this energy is released. The released strain energy is used to create the new surfaces that are formed as the crack propagates.

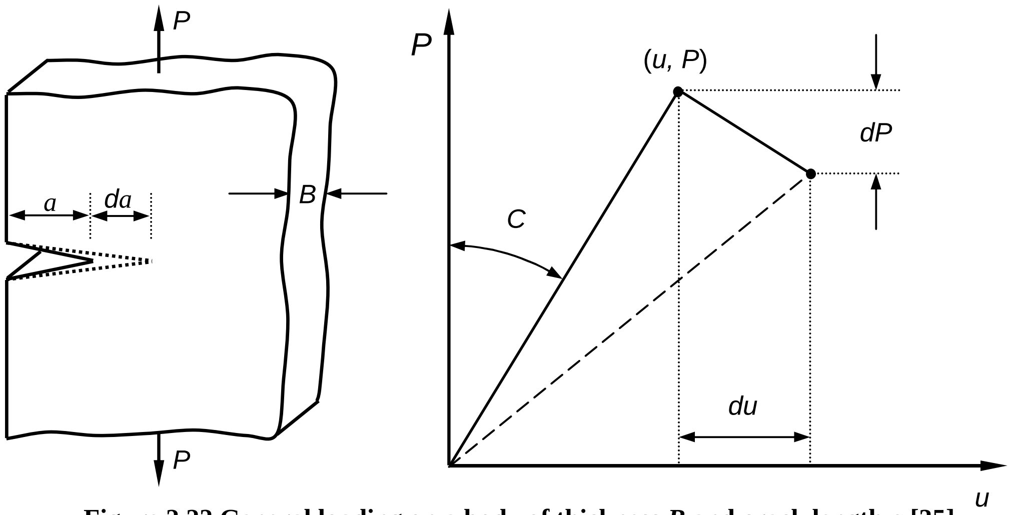

Figure 2.22 General loading on a body of thickness *B* and crack length *a* [35]

If a load *P* is applied to an elastic body having a thickness *B* and containing a crack of length, *a*, and the body deforms elastically, and then a linear load-deflection curve (Figure 2.22) is obtained. The compliance, *C*, which is also determined as the inverse of the stiffness, is defined as:

$$C = \frac{u}{P} \qquad (2.7)$$

where u is the deflection.

Consider the energy involved as the load changes by dP, and the deflection by du. The released energy, dU, can be defined as [35]:

$$dU = U1 + U2 - U3 = \frac{1}{2}Pu + \left(P + \frac{dP}{2}\right)du - \frac{1}{2}(P + dP)(u + du)$$

or, $$dU = \frac{1}{2}(Pdu - udP) \qquad (2.8)$$

where *U1* = Initial energy stored, i.e. the area under the solid line in Figure 2.22 (right) ;

U2 = External work done;

U3 = Final energy stored, i.e. the area under the dash line in Figure 2.22 (right).

If the crack grows an amount *da* then the crack area increase by *B da*. Thus, by neglecting the product of small quantities, the strain energy release rate, *G*, can be expressed as [35]: $$G = \frac{1}{B}\frac{dU}{da} = \frac{1}{2B}\left(P\frac{du}{da} - u\frac{dP}{da}\right) \qquad (2.9)$$

According to equation 2.7, the compliance, C, can be differentiated with respect of a [35]:

$$P^2 \frac{dC}{da} = P\frac{du}{da} - u\frac{dP}{da} \qquad (2.10)$$

Substituting equation 2.10 into equation2.9, G can be expressed in the terms of compliance as:

$$G = \frac{P^2}{2B}\frac{dC}{da} = \frac{u^2}{2BC^2}\frac{dC}{da} \qquad (2.11)$$

Furthermore, G equal to G_C at fracture; where G_C is known as the *critical strain energy release rate*. If both P and u are measured at fracture, then both dC/da and G_C can be thus determined.

2.2.2.2. Local stresses

For metals and polymers, the fracture toughness is often expressed in terms of the critical stress intensity factor, K_C, which can be computed by analysing the local stresses around the crack tip. The crack acts as a stress concentrator giving high stresses at the crack tip as shown in Figure 2.23.

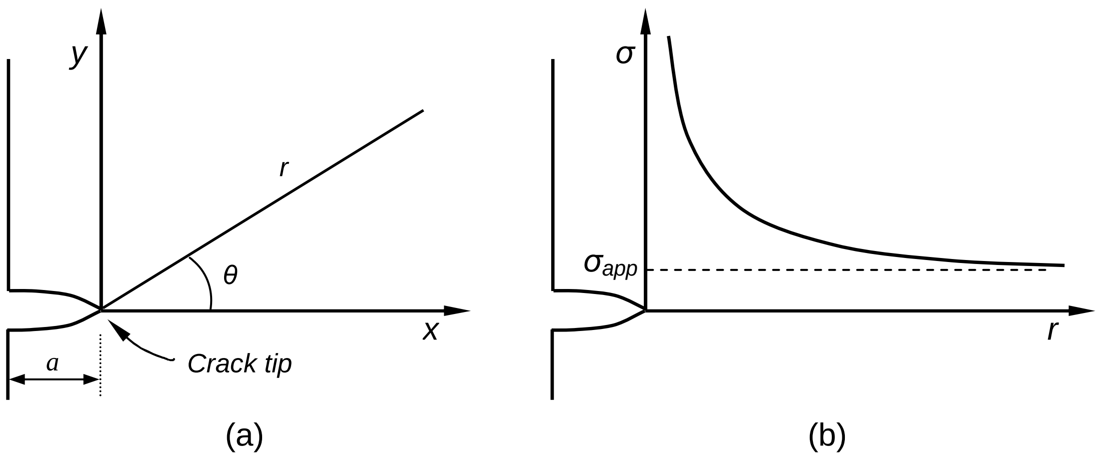

Figure 2.23 Schematic sketch of local stresses at the crack tip: (a) the coordinate system used; (b) the stress *σ* as a function of *r* at the crack tip [35]

According to elasticity theory, the stresses at any point (r, θ) in the vicinity of the crack tip can be expressed as [35]:

$$\sigma_{yy} = \frac{K}{(2\pi r)^{1/2}} \cos\frac{1}{2}\theta(1 + \sin\frac{1}{2}\theta \sin\frac{3}{2}\theta)$$

$$\sigma_{xx} = \frac{K}{(2\pi r)^{1/2}} \cos\frac{1}{2}\theta(1 - \sin\frac{1}{2}\theta \sin\frac{3}{2}\theta) \qquad (2.12)$$

$$\sigma_{xy} = \frac{K}{(2\pi r)^{1/2}} (\cos\frac{1}{2}\theta \sin\frac{1}{2}\theta \cos\frac{3}{2}\theta)$$

where K is the *stress intensity factor*. The crack propagates when K reaches K_C, which is termed the *critical stress intensity factor*. For linear elastic isotropic materials, the relationship of K_C and G_C can be shown as:

$$K_C = EG_C \quad \text{(for plane stress conditions)} \qquad (2.13)$$

$$K_C = \frac{EG_C}{(1-\nu^2)} \quad \text{(for plane strain conditions)} \qquad (2.14)$$

E is the modulus of elasticity. For an infinite plate containing a central crack of length $2a$ under a uniaxial load σ, we obtain:

$$K^2 = \pi\sigma^2 a \quad \text{and} \quad G = \frac{\pi\sigma^2 a}{E} \qquad (2.15)$$

At fracture, σ is the fracture stress σ_C and $G = G_C$ when the crack propagates. Additionally, for a completely brittle material, G_C can be shown to be equal to twice the surface energy per unit area, γ:

$$G_C = 2\gamma \qquad (2.16)$$

Hence, the above fracture stress can be rewritten as:

$$\sigma_C = \left(\frac{2\gamma\ E}{\pi\ a}\right)^{1/2} \qquad (2.17)$$

This is the well known Griffith equation. π is the calibration factor for the infinite plate. But often the crack is not small in comparison with the specimen, then a different calibration factor needs to be used:

$$K_C = Y\sigma_C \sqrt{\pi \cdot a} \qquad (2.18)$$

where Y is a calibration factor that depends on the crack length and specimen dimensions.

2.2.2.3. *Modes of crack surface displacement*

As shown in Figure 2.24, the interlaminar crack propagation can occur under opening (Mode-I), sliding (Mode-II) and tearing (Mode-III), or a combination thereof. In composite materials, delamination fracture toughness is normally characterized by the critical strain energy release rate, G_c.

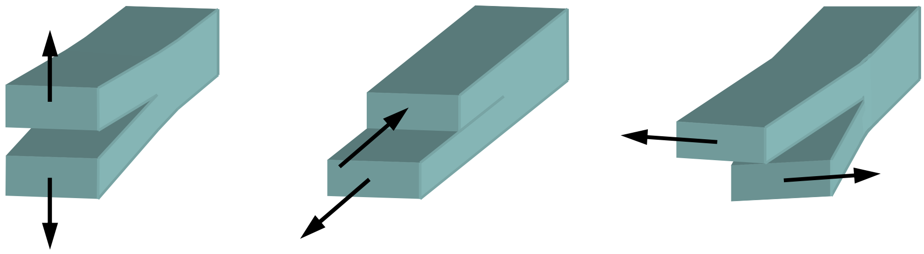

Figure 2.24 the three modes of crack surface displacement

As mentioned before, the ideal progressive crushing mechanism in composite is a combination of many fracture forms, including delamination, splitting and central crack of laminate. Thus, the interlaminar fracture toughness is an important property in crush of composite structures. Generally, the composite materials which have higher fractures toughness exhibit higher energy absorption capability.

Cauchi-Savona and Hogg [24] studied the relationship between energy absorption of glass fibre reinforced plastic (GFRP) composite plates with their Mode-I and Mode-II fracture toughness properties. According to their results that show in Figure 2.25, materials that possess low Mode-I and Mode-II values exhibited low crushing energies. Mode-I properties are required to be high to prevent the central crack from growing too fast once the crushing is initiated. Mode-II properties showed a very strong correlation with the absorbed energies, which indicated that the shear cracking is a very important factor during crushing.

Similar work has been done recently by Hadavinia and Ghasemnejad [36]. They investigated the effects of fibre orientation on Mode-I, Mode-II and SEA of carbon fibre reinforced plastic (CFRP) twill/weave composite box sections. Their results indicated that interlaminar crack propagation in Mode-I and Mode-II contributed significantly to the type of the progressive crushing mode and SEA. The interfaces of 0/45 and 0/0 have higher Mode-I and Mode-II interlaminar fracture toughness and as a result the crushed box with these lay-ups showed a higher energy absorption capability in comparison with crush box lay-up of 45/45.

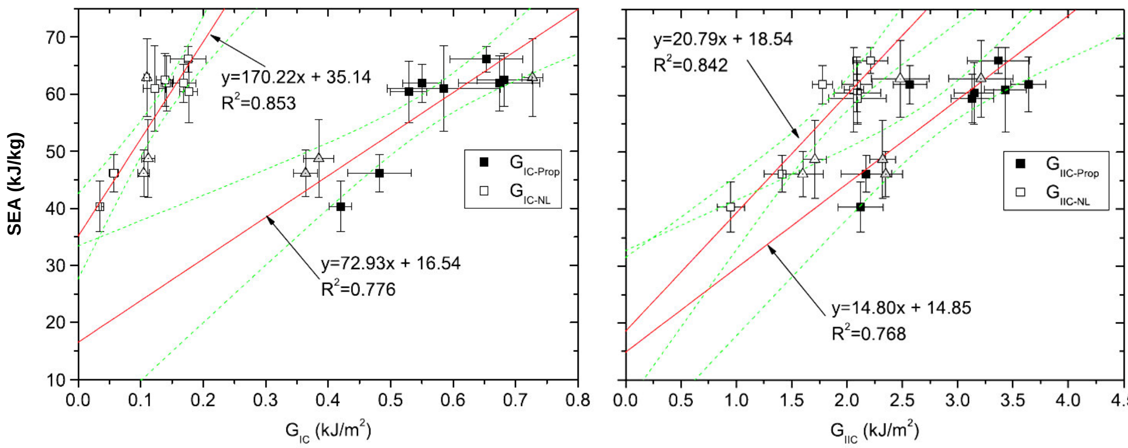

Figure 2.25 Effects of Mode-I (left) and Mode-II (right) fracture toughness properties on the SEA of composite plates. Square and triangle symbols refer to quadriaxial and triaxial laminates, respectively [24].

There are a few different ways to increase the interlaminar fracture toughness properties in composite material, but not all of them will contribute to its energy absorption capability. Warrior *et al.*[37] studied the influence of toughened resins, through-thickness stitching, thermoplastic resin additives and thermoplastic interleaving on the interlaminar fracture toughness (G_{IC}) and the SEA for continuous filament random mat (CoFRM) and 0/90 NCF E-glass reinforced polyester composite tubes. They reported that all above mentioned factors increase G_{IC}, but only toughened resin and through-thickness stitching can increase energy absorbing capability of composite materials.

2.2.2.4. Effect of stitching

Most traditional FRP laminates, which have a layered two-dimensional (2D) fibre architecture, have relatively poor through-thickness mechanical properties because the load applied in the translaminar direction is predominately carried by the resin matrix. During last two decades, a considerable amount of research has been devoted to improving the through-thickness mechanical properties of composite laminate by developing the 3-D fibre architecture [38].

The stitching process involves sewing a high tensile strength yarn through the laminate structure using an industrial sewing machine [39]. A lot stitching variables, such as thread material, stitching density, stitching type and thread tension, can affect the mechanical properties of a composite structure as well as the quality and proficiency of the stitching process [40].

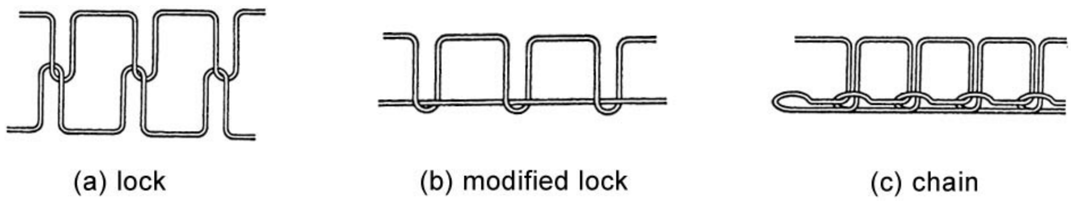

Figure 2.26 Illustrations of the various stitch types used to reinforce laminates [39]

There are three most common types of stitches used to reinforce composites, as illustrated in Figure 2.26: lock stitch, modified lock stitch and chain stitch [39]. Regarding to the fibre architectures of the textile reinforcement and the appearance of the stitch formation within the textile patterns after the sewing process, modified lock stitch offers the most suitable stitch type for different performing aspects. In modified lock stitch, the knots linking the needle and bobbin threads are formed at one surface of the laminate to minimise the in-plane fibre distortion (Figure 2.26 b) [39].

A problem with stitching is that localised damage occurs where the sewing needle and yarn penetrate the materials. This damage includes fibre breakage at the stitch hole, misalignment and spreading of the fibres around stitch, and formation of resin-rich region generated by fibre-free region at stitch hole [38]. Hence, many studies reported some degradation of strength and stiffness while other studies found that stitching does not affect or slightly improves the same properties [39].

The main aim for stitching is to improve the interlaminar fracture toughness of composites. The interlaminar delamination resistance of FRP laminates under Mode-I loading has the most significant improvement from stitching. Depending on stitching density and type, the interlaminar fracture toughness (G_{IC}) could be increased by a factor of 1.5 - 2.8 in GFRP [41, 42], and up to 15 times in CFRP [43]. Scanning electron micrographs (see Figure 2.27) were taken by Watt *et al.* [41] show the stitches bridge the crack for a short distance behind the crack front before breaking. In general, some of the threads are pulled from the surface, which additionally increasing the toughness [41, 43].

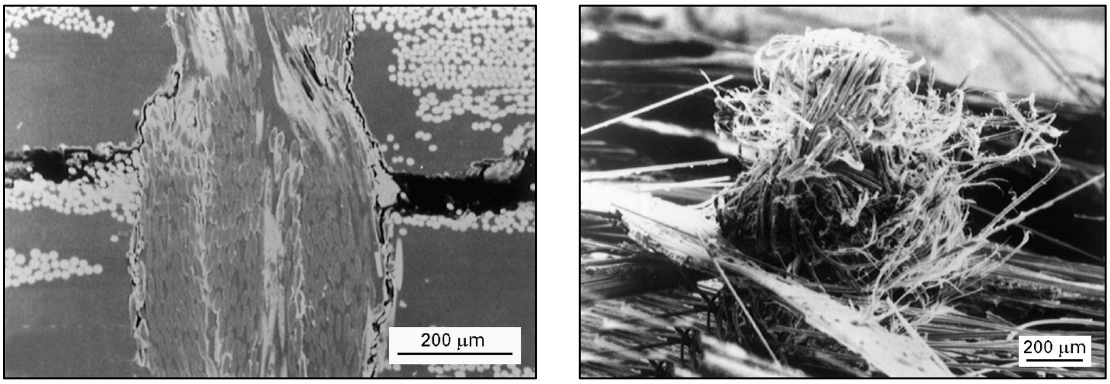

Figure 2.27 Scanning electron micrographs showing a stitch bridging an interlaminar crack (left) and a broken Kevlar® thread partially pulled from a Mode-I fracture surface [41]

The number of papers on the effects of stitching on the Mode-II fracture toughness of FRP composites is very few [44]. In general, the benefit from the addition of stitches has been stated very little in Mode-II fracture toughness [2, 44-46]. However, Jain *et al.* [45] and Sankar *et al.* [44] both found a significant improvement on the Mode-II fracture toughness of carbon/epoxy composites. Furthermore, they observed the crack propagation in stitched laminates was more steady and gradual, unlike in unstitched laminates where it was unstable and sudden [44, 45].

Cauchi-Savona [2] investigated stitched plates and revealed that stitching can improve the energy absorption capability of composite materials. The higher Mode-I fracture toughness of the stitched laminate was believed to contribute the stability and higher SEA, but there is a limit to how much an improvement in Mode-I can stabilize a crush. They found the main benefit of the stitching forced the splayed fronds into a tighter radius of curvature which was resisted by the flexural stiffness of the fronds and the energy dissipated in fracturing the fibres.

It is also interesting to note that the unstitched material has SEA values equal to most of the other stitched composites, though the crushing efficiency of the stitched laminate is better. This implied that varying the variables of stitching, such as stitching density, materials and types, can actually reduce the crushing performance of materials.

2.2.3. Effects of crushing strain rate

Since most energy absorbing systems are applied to dynamic loading, the influence of strain rate, and therefore crushing speed, must be understood on the crushing process.

Because of the complexity and diversity of composite materials and testing conditions, it is difficult to have a consistent conclusion on the effects of strain rate for composite materials, according to previous data [24, 27, 47-53]. Moreover, other parameters including geometry, failure mode, friction coefficient and the speed range, also can easily change strain rate sensitivities of composite materials. Therefore, this section mainly focuses on these arguments.

2.2.3.1. Higher strain rates increase energy absorption capability

The strength and stiffness of composite materials can be a function of strain rate. Some scientists believe that quasi-static testing is not sufficient to predict the energy absorption capabilities in most crash situations, unless the matrix could retain its properties at high speeds [24]. As mentioned previously in Figure 2.12, the crush results of braided tubes indicated that the SEA slightly increased in most cases with the strain rate increased from 25.4mm/min to 254mm/min [27].

Similarly, Thornton [50] tested pultruded glass fibre reinforced plastic tubes, which were made with either polyester or vinyl ester resin, at quasi-static and dynamic crush. The strain rate sensitivities of the specific energy for the polyester GFRP tubes was positive, with increases of up to 20% greater than the quasi-static values for crush rate of 12m/s. But those for some vinyl ester pultrusions were found negative, depending upon the crush modes dominated under dynamic crush. Thus, it is necessary to mention that the mechanical properties of some materials are strain rate insensitive.

Farley and Jones [48] crushed Kevlar/epoxy and carbon/epoxy tubes with different stacking sequences and fibre orientations at crushing speeds between 0.01m/s and 13m/s (see Figure 2.28 and Figure 2.29). All Kevlar® tubes exhibited the characteristic local buckling crushing mode [48]. The energy absorption capability of all $[0/\pm\theta]_2$ and $[\pm\theta]_3$ Kevlar® tubes evaluated was a function of crushing speed, in which the percentage change was most significant between speeds of 6m/s and 12m/s. The energy absorption capability increased most as a function of crushing speed for tubes have ply orientation θ = 15. The crushing speed effect on the energy absorption capability of Kevlar/epoxy tubes was attributed to the mechanical properties of Kevlar® fibre, which are strain rate sensitive. The Kevlar fiber is a polymer-based fiber. The mechanical properties of most polymers are strain rate sensitive [48].

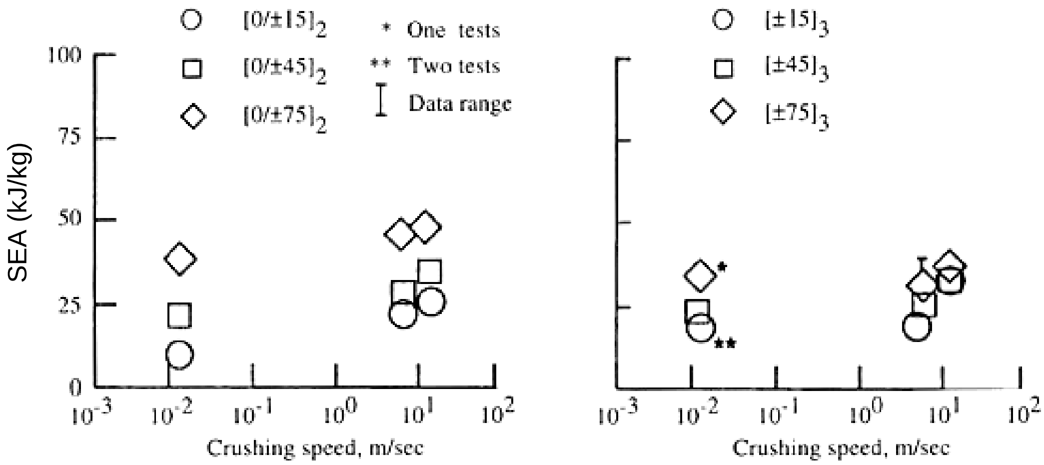

Figure 2.28 **Effects of crushing speed on Kevlar/epoxy tubes [48]**

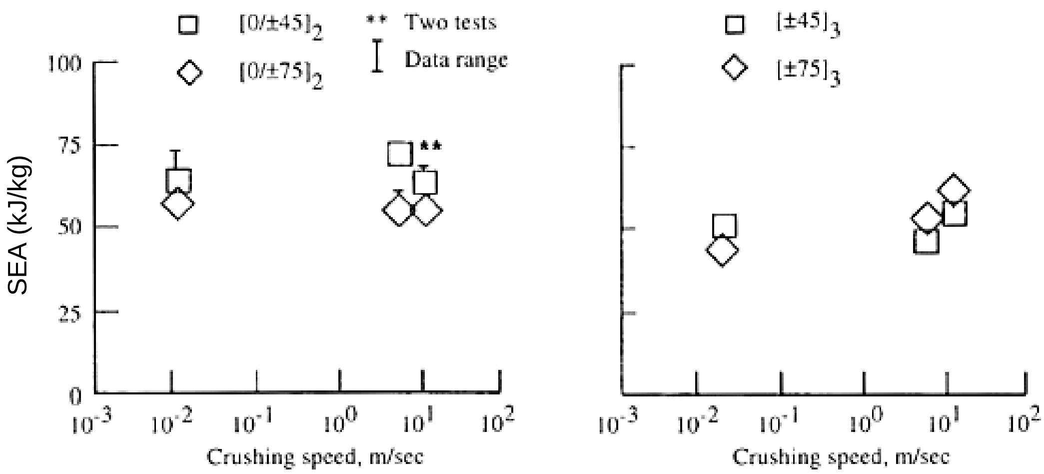

Figure 2.29 **Effects of crushing speed on carbon/epoxy tubes [48]**

However, the mechanical properties of the brittle fibres are generally insensitive to strain rate [49]. Though the energy absorption capability of both Kevlar/epoxy and carbon/epoxy $[\pm\theta]_3$ tubes was shown to be strain rate sensitive, it became strain rate insensitive if 0° fibres were included in ±θ tubes. Kevlar® fibre behaves more brittle at higher speed. As a result, Kevlar® tubes might not fail by local buckling crushing mode any more at higher crushing speed.

On the one hand, the mechanical properties of the fibres control the crushing process within $[0/\pm\theta]_2$ tubes. The 0° fibres undertake the axial crushing loading while the off-axis fibres provide foundation support for the lamina bundles and control the interlaminar crack growth. Since the 0° fibres are not strain rate sensitive, the energy absorption capability of $[0/\pm\theta]_2$ tubes were hardly affected by the crushing speed.

On the other hand, within $[\pm\theta]_3$ the mechanical properties of the matrix control the crushing process. The matrix provides significant contributions to the longitudinal stiffness of the lamina bundles and controls interlaminar crack growth, thus, the energy absorption capability of $[\pm\theta]_3$ tubes were affected by the crushing speed.

The evidence that absorbed energy increases with the increase of strain rate was also stated on 3-D braided composites by Gu and Chang [51]. These composite samples were constructed from E-glass and epoxy resin using resin transfer moulding (RTM) process, and tested on a split Hopkinson pressure bar (SHPB) apparatus.

2.2.3.2. Higher strain rates decrease energy absorption capability

In contrast, composite materials were also found losing energy absorption capability at high crushing strain rate in many other studies. Lavoie and Kellas [47] reported that the energy absorption capability of the laminated composite plates made of thermoplastic matrices might drop significantly in high speed crushing due to a transition to a less efficient crushing mode. They attributed this result to the reduced toughness of thermoplastic matrices at high strain rates. They tested carbon/PEEK and carbon/epoxy plates with orientations of $[\pm45/0_4/\pm45]_{2S}$, $[45_2/\text{-}45_2/0_8/45_2/\text{-}45_2]_S$ and $[\pm45/0_4/\pm45]_{2S}$, which were referred to as baseline, ply-level and sublaminate scaling, respectively; and two types of trigger geometries, notch and steeple (see Figure 2.5 and Figure 2.17).

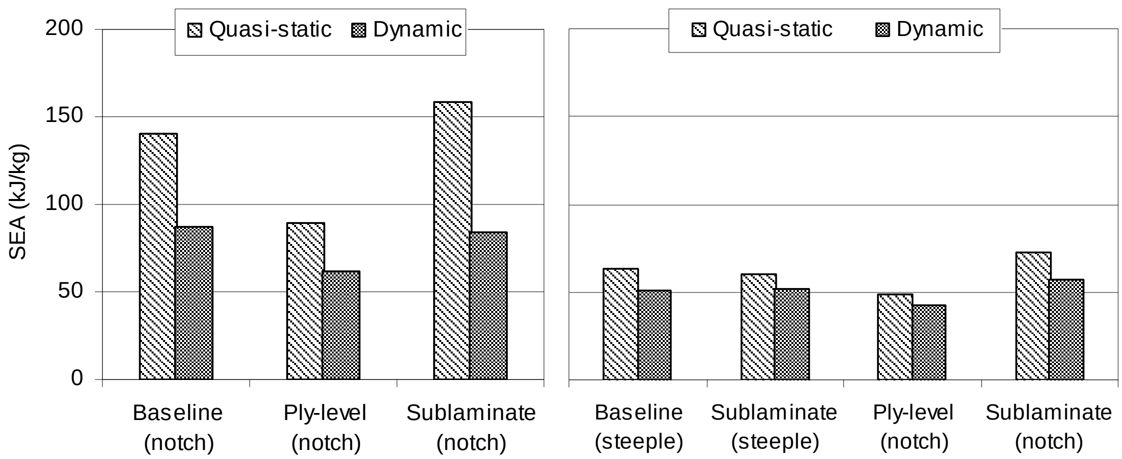

Figure 2.30 Comparison of specific energies of quasi-static and dynamic tested plates: carbon/PEEK (left) and carbon/epoxy (right), with different triggers [47]

All plates tested lost some energy absorption capability at high crush rates (5m/s to 7m/s), but in particular, carbon/PEEK plates exhibited a dramatic reduction in the energy absorption capability. These results can be found in Figure 2.30. The important difference for carbon/PEEK was that, at the quasi-static rate, the crushing proceeded by efficient energy absorption mode of brittle fracturing and fragmentation, while it transited to an lamina bending mode at the dynamic rate [47].

Although the carbon/epoxy plates also showed a slight reduction of energy absorption at the dynamic crush rate, the change was much less than that of carbon/PEEK plates. This was because the lamina bending crushing mode was dominant at both crush rates for carbon/epoxy plates [47].

Similar observations were reported by Schmueser and Wickliffe [52], and Mamalis *et al*. [53]. Schmueser and Wickliffe investigated $[0_2/\pm45]_S$ circular tubes made of epoxy resin and carbon, glass and Kevlar® fibres, respectively. They indicated that the energy absorbed under quasi-static crushing was higher than the energy absorbed under dynamic crushing for all materials. Mamalis *et al*. reported that the absorbed energy was reduced during dynamic crushing for the glass/polyester circular tubes and frusta, due to different energy absorbing mechanisms.

2.2.4. Effects of structural geometries

As important as material properties, the structural geometries significantly influence crushing behaviour and energy absorbing performance of composite materials. This section is aimed at evaluating the crushing responses of different structural geometries. As a trend on composite structural design, sandwiches subjected to energy absorption are also presented in the end of this section.

2.2.4.1. Cones

The nose cone of the formula one racing car was not only chosen for aerodynamic purpose, but also was designed as an effective energy absorber. A cone is a compromised solution to increase the collapse stability without significant penalties on the absorbed energy per unit mass [54]. The angle that the narrow end of the cone makes with the normal is called the *cone vertex angle* and it can have a significant effect on the crushing characteristics.

Mamalis *et al*. [55] investigated the failure mechanisms of thick-walled circular conical shells, which were made of chopped strand glass mat of random fibre orientation pre-impregnated with a polyester resin. A conical shell under compressive loading may fail by different deformation modes, which depends on its wall thickness and the cone vertex angle. They reported all conical shells with a cone vertex angle less than 25° crushed in a progressive mode, but cones with greater angles exhibited catastrophic splitting after a short distance of progressive crushing.

Alkateb *et al.* [56] in their research confirmed Mamalis *et al.*'s conclusion. They crushed composite cones made of [90/0] woven roving glass fibre with a range of cone vertex angle between 0° and 24°. Similarly, the crushing behaviour of the cones is very sensitive to the change in the vertex angle. They found the average crushing load increases as the vertex angle increases, while the crushing peak load decreases.

2.2.4.2. Tubes

Composite tubes have been intensively investigated in the energy absorbing research field, because tubular specimens provide ideal results since they have no free edges, and can be tested easily under laboratory conditions. Typically, tubes crushed between two flat platens instead of a complicated rig. The energy absorption capability of composite tubes is significantly affected by their cross-sectional dimensions [11, 57-59].

Farley tested circular tubes [57] manufactured from $[\pm 45]_n$ carbon/epoxy and Kevlar/epoxy, with a range of tube inside diameter to wall thickness (D/t) ratios. It was indicated that the energy absorption capability falls nonlinearly as D/t ratio increases (see Figure 2.31). He concluded that the increase in energy absorption as D/t ratio decreases is related to a reduction in interlaminar cracking. The nonlinear response suggests that care must be taken in selecting specimen geometry for energy absorption characterization studies. In Farley's other paper [58] the same results were obtained for square tubes, which were made out of same materials. As the tube inside width to wall thickness (w/t) ratio increases, the energy absorption capability falls (see Figure 2.32).

In addition, it was interesting to note that the energy absorption capability of $[\pm 45]_n$ Kevlar/epoxy tubes was geometrically scalable but energy absorption of carbon/epoxy was not geometrically scalable. In other words, the geometrically scalable specimens (Kevlar/epoxy) exhibited similar energy absorption capacities for the same D/t and w/t ratio, although different diameters and wall thickness. It is important to know that carbon/epoxy specimens crushed via a brittle fracturing mode mixed with lamina bending, while the Kevlar/epoxy specimens exhibited a ductile buckling and folding crushing manner [57, 58].

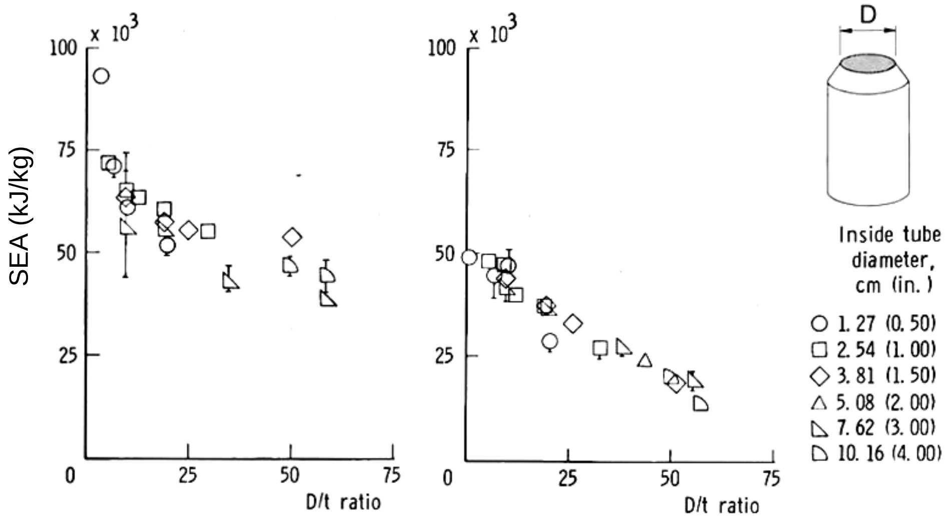

Figure 2.31 Effects of D/t (inner diameter/wall thickness) ratio on the energy absorption of $[\pm45]_n$ carbon/epoxy (left) and Kevlar/epoxy (right) circular tubes [57]

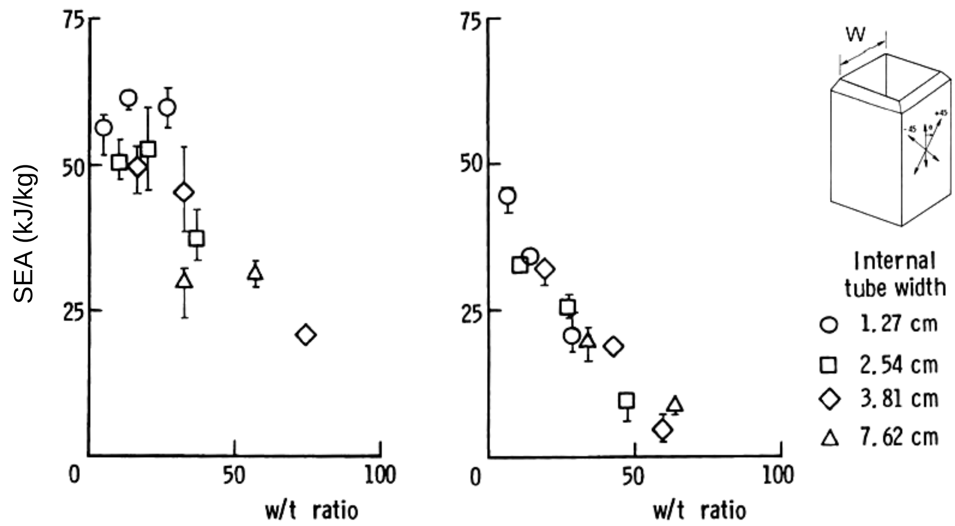

Figure 2.32 Effects of w/t (tube width/wall thickness) ratio on the energy absorption of $[\pm45]_n$ carbon/epoxy (left) and Kevlar/epoxy (right) square tubes [84].

According to the crushing results of circular tubes to square tubes shown in Figure 2.31 and Figure 2.32, it also can be seen that circular tubes had greater crushing capability over square tubes. Price and Hull [11] compared the effects of corner radius of composite tubes, and got the same conclusion. These tubes have been described previously in Section 2.1.1 and Figure 2.1.

It shows that increasing the corner radius increases the energy absorption capability of the tubes (see Figure 2.33). In these tubes with sharp corners, the flat sections failed in a local plate strip buckling mode, thereby decreasing the overall energy absorption capability of the section. It was concluded [11] that the overall crushing capacity of a 'complex rounded corner section' is the sum of the capacities of the individual segments.

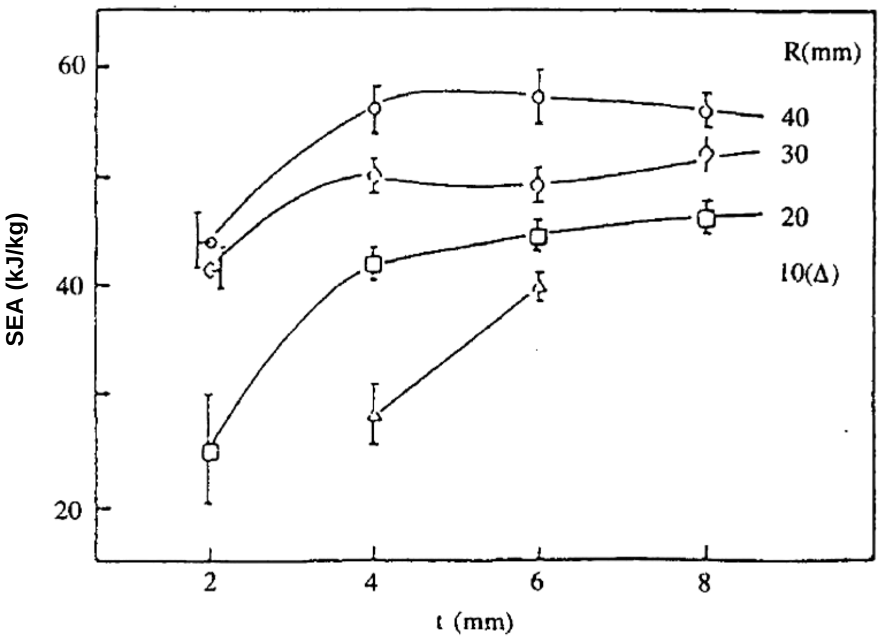

Figure 2.33 **Effects of corner radius of composite tubes on energy absorption [85].**

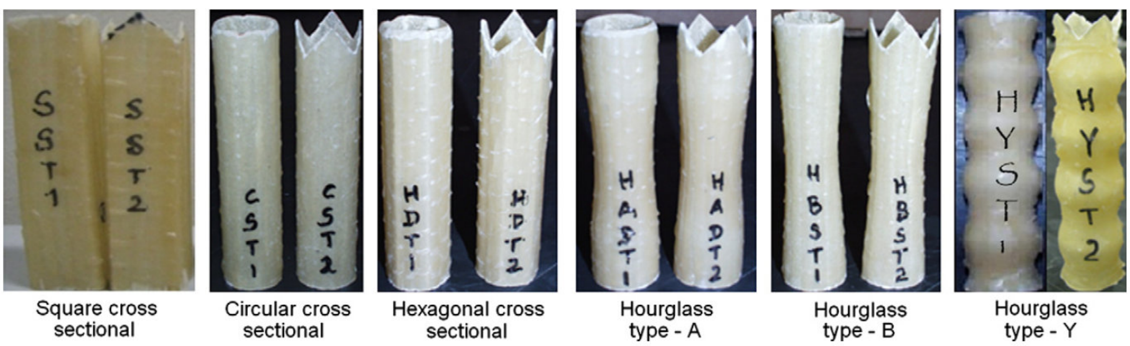

Figure 2.34 **Pictures of finished composite tube specimens with triggering [60]**

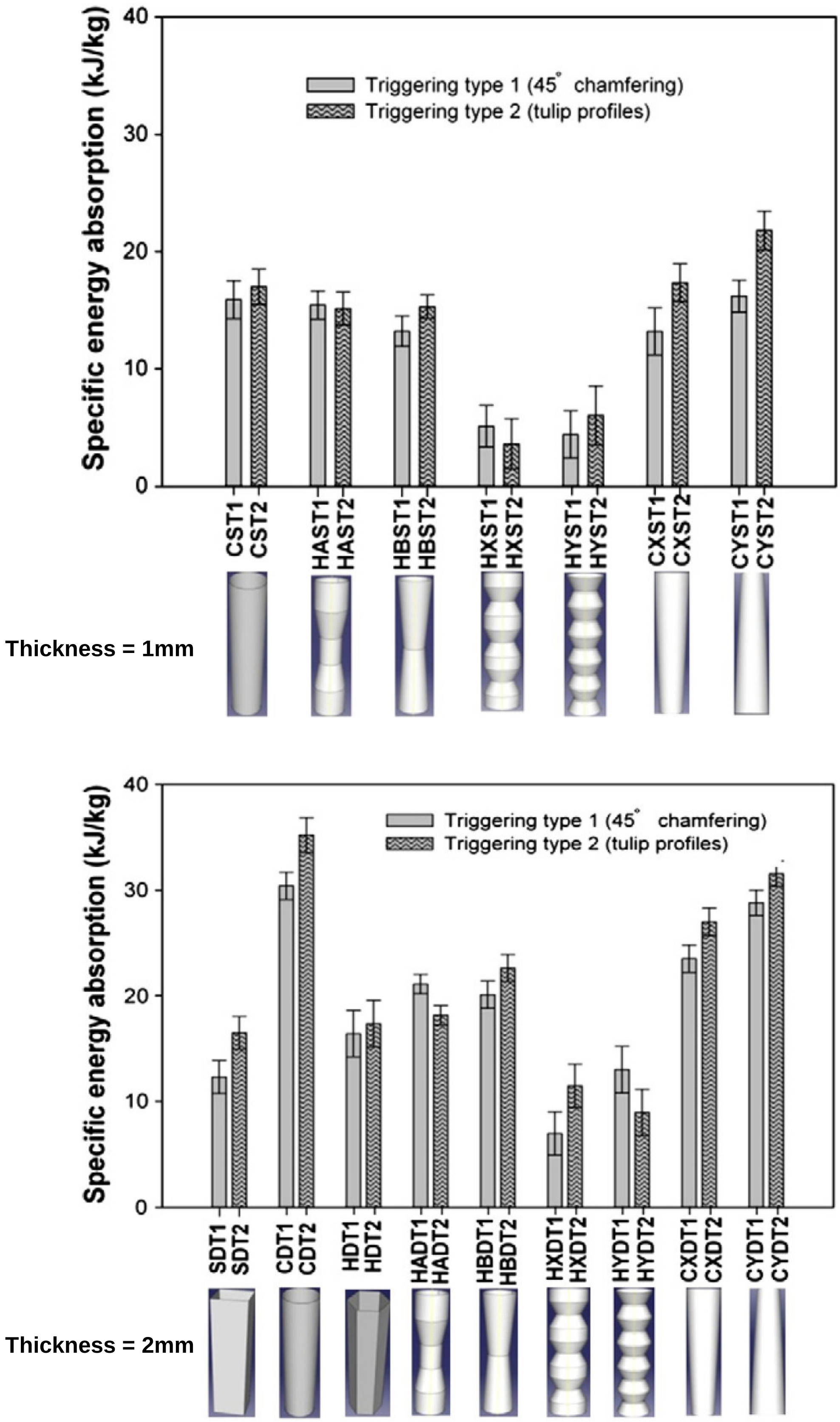

Figure 2.35 **Specific energy absorption of composite tubes with different geometrical shapes: top) thickness of tubes = 1mm; bottom) thickness of tubes = 2mm [60]**

Recently, Palanivelu *et al*. [60] investigated the crushing performance of nine different geometrical shapes of small scale composite tubes. The pictures of these tubes and their specific energy absorption are shown in Figure 2.34 and Figure 2.35, respectively. From this research, it was found that the crushing characteristics and the corresponding energy absorption of the special geometrical shapes are better than the standard tubes with square and hexagonal cross sections. Furthermore, the tulip triggering attributed to a lower peak crush load followed by a steady mean crush load compared with the 45° chamfering triggering profile which resulted into a higher energy absorption in most of the geometrical shapes of the composite tubes.

2.2.4.3. Beams

While tubes can be tested under well controlled conditions, under axial compression tubes are yet an abstraction and may not always represent realistic energy absorbing structures [61]. Thus, a few types of composite beams have been developed as they are closer to practical structures.

As a representative crashworthy structure using in the subfloor of helicopter fuselage, sine wave beams were initially designed to dissipate the kinetic energy in a helicopter crash without compromising the integrity of the fuselage. Hanagud *et al.* [61] discussed the effects of various geometric parameters of the sine wave beam specimens. It was found that only a small variation in energy absorption performance with reduction in the included angle of the sine web from 180° to 90°. However, because of local buckling, the energy absorption performance dropped dramatically in the specimens which had included angle smaller than 90°. Furthermore, the role of width (wave count) in sine wave beams was shown to be only a secondary influence for the specimen geometries.

At almost the same time, Farley [62] tested sine wave beam and found that the sine wave beams composed of included angle of 180° exhibited the same energy absorption as circular tube. Furthermore, he investigated circular tube stiffened beams and rectangular stiffened beams, which consist of tube elements and web elements. As a result, it was found the energy absorption performance of entire beam structures could be accurately predicted by summing up the energy absorption performance of all characteristic elements that compose the structures, which can be expressed as following:

$$SEA^{S.E.} = \sum_{i=1}^{N} \left(\frac{A_{ith}^{C.E.}}{A^{S.E.}} \cdot SEA_{ith}^{C.E.} \right) \tag{2.19}$$

The terms $A_{ith}^{C.E.}$ and $A^{S.E.}$ are the cross-sectional areas of the *i*th characteristic element (*C.E.*) and the structural element (*S.E.*) respectively. The corresponding meaning also applies to the terms $SEA_{ith}^{C.E.}$ and $SEA^{S.E.}$. This procedure can thus minimize the complicity of designing a large range of energy absorbing structures, only if the crushing modes of the beam characteristic elements are similar to the modes exhibited by the tube specimens [62].

2.2.4.4. Plates

The composite plate crush testing was pursued during last two decades because it is less expensive and easier to fabricate than tubes or sine wave beams [22, 63]. However, due to the free edges, the plates would fail under local buckling rather than required progressive crushing mode. Thus some special test fixtures, such as knife-edge rig [16], were designed to stabilise the plate specimen during crushing process and promote crushing. Stability is very important for the energy absorption capability of flat plate specimens, and it is determined by the geometries of plate [63].

Cauchi-Savona and Hogg [16] identified the energy absorbing capabilities of composite plates which have been mentioned previously in Section 2.2.1.2. Their results (see Figure 2.15) revealed that the quadriaxial laminates had better crushing efficiencies and more consistent than that for the triaxial orientations. They concluded that it was more likely because of the lower amount of 0° fibres in quadriaxial laminates. In the triaxial laminates, due to higher ratio of 0° fibres, the crushing stress requires a long stroke to stabilize due to the longer central crack formed after the peak stress. A long central crack can possibly destabilise the laminate if the Mode-I propagation properties are not large enough to arrest the crack propagation [16]. For optimizing the Mode-I, therefore, stitching mechanisms were applied into their latter work [2].

2.2.4.5. Energy absorption in sandwich panels

In many industrial applications, there is a fast moving trend towards lightweight materials and structures for military vehicles, motorcar, railway, aircraft, building and construction. The challenge faced by structural designers is thus becoming increasingly difficult as the imposed design criteria require to reduce the weight of products without compromising performance and increasing cost.

Compared with the monolithic constructions, sandwiches can significantly reduce the weight of entire structures but meanwhile keep relatively high flexural rigidity. The flexural rigidity of sandwich beam (D_{flex}) is expressed as [64]:

$$D_{flex} = \frac{E_f bt^3}{6} + \frac{E_f btd^2}{2} + \frac{E_c bc^3}{12} \tag{2.20}$$

where, E_f , E_c= moduli of elasticity of faces (index f) and core (index c), respectively;

b = width of sandwich beam;

d = thickness of sandwich beam;

t = thickness of faces

c = thickness of core

Dimensions mentioned above are showing in Figure 2.36. If d >> t and E_c is low [65], equation 2.20 can be expression as:

$$D_{flex} = \frac{E_f btd^2}{2} \tag{2.21}$$

Figure 2.36 Dimensions of a typical sandwich beam

Additionally, a number of new core topologies for sandwiches that have emerged, showing structural advantages over monolithic constructions. The capability of energy absorption or dissipation of sandwich panels is actually depending on the configuration of cores. Thus, according to different core topologies, the energy absorbing sandwich systems can be classified into four categories: foam, corrugated, honeycomb and truss (see Figure 2.37)

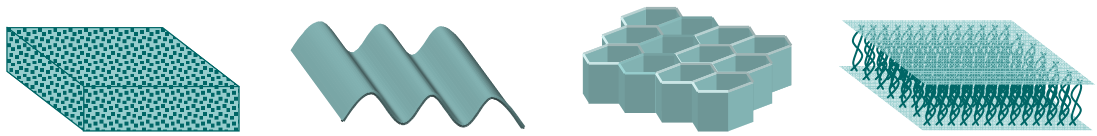

Figure 2.37 Core types in sandwich sacrificial panels

Foam cores which include polymers and metallic foams are usually homogenous materials. Balsa wood can be also grouped into this category, but balsa wood is an anisotropic material. In general, they are the least expensive and offer some advantages in machineability and sandwich manufacturing. Metallic foams are usually very outstanding energy absorbing systems, not only because of their lightweight, but also their homogenous properties, less moisture-dependent and potential use at high temperatures.

Corrugated core materials include a large variety of geometries, often providing highly directional core stiffness for certain applications. In general, clamped plates are representative of the structures used in the design of commercial and military vehicles [66]. The advantage of using corrugated core in blast resistant sandwich panel is that they provide high longitudinal shear and stretching strengths.

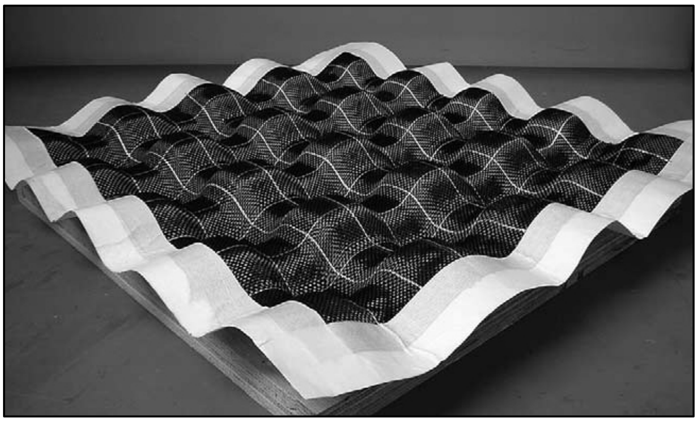

Figure 2.38 The perspective view of a typical egg-box [4]

Recently, researchers [4, 5, 67] have investigated the crushing and energy absorbing performance of a novel corrugated core structure, which is often called "egg-box". The perspective view of this core structure is shown in Figure 2.38. However, it has been found that this egg-box core achieves much lower energy absorbing performance than composite plates and tubular structures, which is between 1 and 7 kJ/kg [67].

Honeycomb core sandwich structures are widely used in the aerospace industry. Unlike corrugated cores, which have cell openings in the in-plane direction, honeycomb cores have only openings in the thickness direction and provide a bi-directional support for the skins. Honeycomb cores also possess relatively higher stiffness to weight ratio due to its large space in cells. Though the hexagonal cells are the most commonly used core in composite structures, in the honeycomb terminology it also includes other types of core, for example, triangular honeycomb [68], square honeycomb [69-71], sinusoidal honeycomb [72], Ox-Core®, Flex-Core® and Double-Flex®. The latter three special honeycomb cores are produced by Hexcel Corporation [73]. Wu and Jiang [74] measured the crushing performance of aluminium honeycombs with different dimensions. Those honeycombs achieved SEA values between 22 and 39kJ/kg.

Having a fully open structure is the main characteristic of truss cores. Although they have negligible longitudinal strength, truss cores normally have a relatively high specific crushing strength and energy absorption capacity. Truss cores also have additional potential by virtue of their opening structure for multi-functional applications. For example, sandwich panels with solid skins and truss cores can serve as heat transfer elements simultaneously carrying loads. The cavity between the skins could be used for storage of a liquid or pressurized gas in other applications [75].

It the previous studies, it has been revealed that metallic sandwich panels have structural advantages over monolithic plates of equal mass in blast resistant structural applications [76, 77]. However, it is important to note that most existing sandwich structures subjected to energy absorption are made out of metals and foams.

In the literature discussed above, it is also important to note that these energy absorbing systems made of sandwiches or panel type structures possess lower SEA levels than those individual systems, such as cones and tubes. The main reason is that the existing sandwich cores crush by relatively low efficient crushing mechanisms. If the sandwich cores crush by lamina bending mode, then the energy absorption of whole sandwich panel could be increased significantly.

2.3. Robust design experiments

In order to evaluate the energy absorbing capacity of different structural composites, many factors need to be measured. At the latter stage of this study, an optimization process, called Robust Design, was used. Robust design is an engineering methodology for improving productivity during research and development so that high-quality products can be produced quickly and at low cost [78]. Robust design is also known as Taguchi method because it is the result of a research effort of a team led by Dr. Genichi Taguchi.

Robust engineering methods are from traditional quality control procedures and industrial experimentation in various respects. This method uses small, statistically planned experiments to vary the settings of key control parameters. For each combination of control parameter settings in the experiment, product or process performance characteristics are measured to reflect the effects of manufacturing variation.

2.3.1. Classification of factors

A number of parameters (*parameter* is equivalent to the word *factor* in Robust Design) can influence the quality characteristic or response of the product. Mainly, these parameters can be divided into three classes:

1. **Control factors (Z)**: These design or process parameters can be directly controlled by designer. They normally possess the 'best' level which designer concerns. The major parameters in an experiment such as temperature, pressure and time are all control factors.

2. **Signal factors (M)**: These factors influence the average values of the quality characteristic but not the variability of the quality characteristic. They are normally set by the designer to express the intended value for response of the experimental results. They are so-called 'target-control' factors.

3. **Noise (error) factors (X)**: These factors have uncontrollable and unpredictable influences over the quality characteristic. Only the statistical characteristics, such as the mean and variance, of noise factors can be known but actual values in specific situations cannot be known. The optimal control factors should make the quality characteristic insensitive to noise.

A parameter diagram (P-diagram) which is drawn in Figure 2.39 illustrates the various factors that affect the quality characteristic or the response variable (*Y*). It shows the latter is a function of noise factors (*X*), signal factors (*M*), and control factors (*Z*). A robust product or a robust process is one whose response is least sensitive to all noise factors [78].

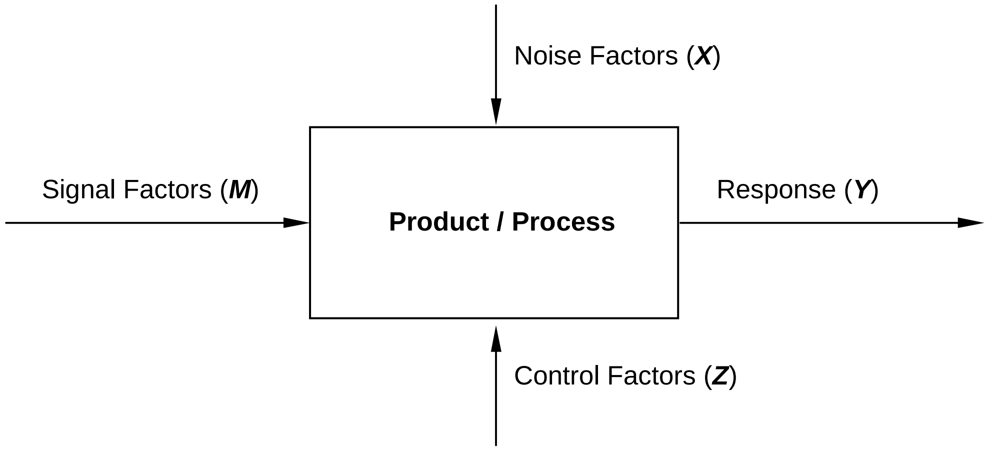

Figure 2.39 Block diagram of a product / process: P Diagram

2.3.2. The design of experiments process

The *design of an experiment* (DOE) is a series of steps which follow a certain sequence for the experiment to yield an improved understanding of product or process performance [79]. The DOE process is divided into three main phases which encompass all experimentation approaches. Moreover, the three phases can be extended into eight steps [78]. The structure of phases and steps is shown in Figure 2.40.

The planning phase is the most important phase for the experiment to provide the expected information. Generally, an experimental operator obtains either positive or negative information from experiment. Positive information is an indication of which factors and which levels lead to improved product or process performance. Negative information is an indication of which factors do not lead to improvement, no indication of which factors do. The experiment will tend to yield positive information, if the experiment includes the real, influential factors and appropriate levels, and vice versa.

The second most important phase is the conducting phase during which the test results are actually collected. If experiments are well planned and conducted, the analysis will become much easier and more likely to yield positive information about factors and levels.

The analysis phase is least important in terms of whether the experiment will successfully yield positive results. However, this phase is the most statistical in nature of the three phases of the DOE approach.

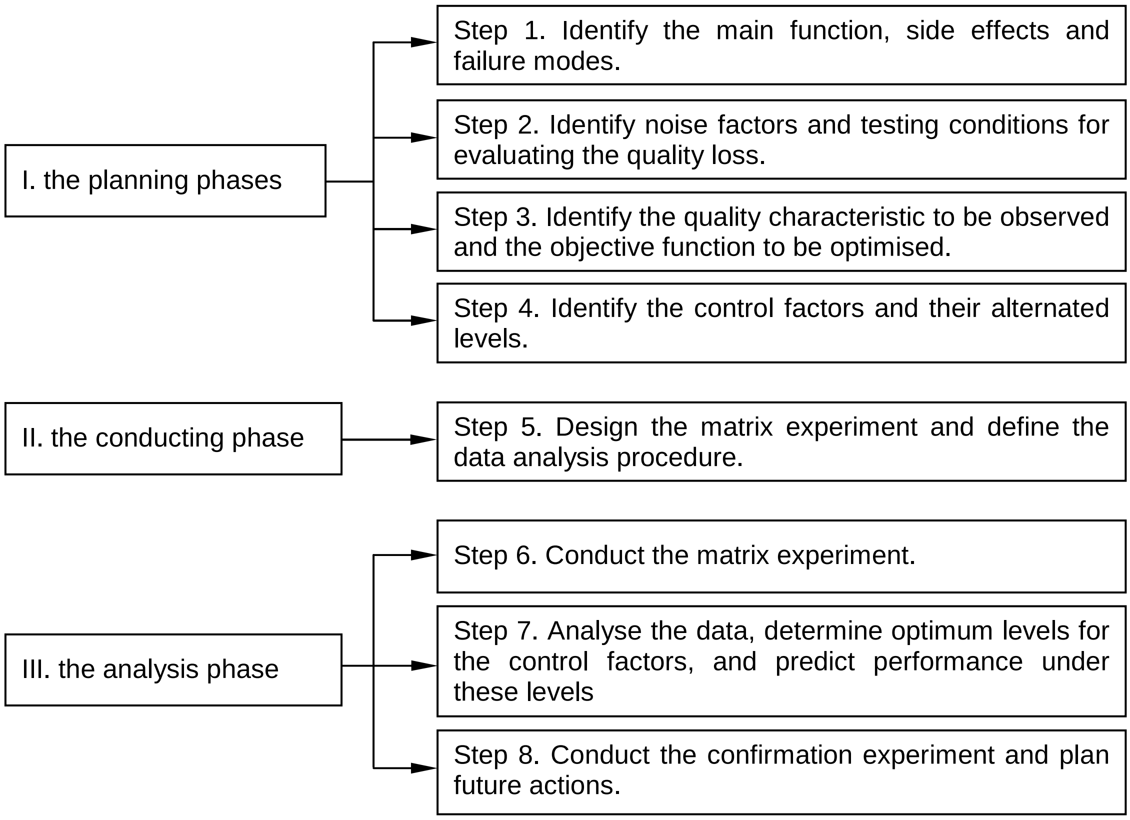

Figure 2.40 Phases and steps in Robust design

2.3.3. Orthogonal array, loss function and signal-to-noise ratio

By analysing and minimizing these effects, Robust engineering methods can remarkably reduce variation by reducing the influence of sources of variation instead of by controlling variations.

Therefore, Taguchi robust design methods are a cost-effective technique for improving product or process performance. Three major tools used in Taguchi methods are: orthogonal arrays, quality loss functions, and signal-to-noise ratios. These basic aspects of robust design methods will be discussed in the following sections.

2.3.3.1. *Orthogonal arrays*

Robust engineering methods are based on a matrix of experiments called *orthogonal arrays* (OA). These are a set of experiments where the factors and levels used as the setting of various parameters are changed according to the matrix. Orthogonal arrays are matrices containing numbers arranged in columns and rows, where the columns represent a specific factor that can be changed from experiment to experiment, while the rows represent the state of the factors per experiment [80]. They are called orthogonal because the levels of the various factors are balanced and can be separated from the effects of the other factors within the experiment allowing key effects to be identified.

Table 2.1 Standard orthogonal arrays

2 levels	3 levels	4 levels	5 levels	Mixed Levels
$L_4(2^3)$	$L_9(3^4)$	$L_{16}(4^5)$	$L_{25}(5^6)$	$L_{18}(2^1 \times 3^7)$
$L_8(2^7)$	$L_{27}(3^{13})$	$L_{64}(4^{21})$	/	$L_{32}(2^1 \times 4^9)$
$L_{12}(2^{11})$	$L_{81}(3^{40})$	/	/	$L_{36}(2^{11} \times 3^{12})$
$L_{16}(2^{15})$	/	/	/	$L_{36}(2^3 \times 3^{13})$
$L_{32}(2^{31})$	/	/	/	$L_{54}(2^1 \times 3^{25})$
$L_{64}(2^{63})$	/	/	/	$L_{50}(2^1 \times 5^{11})$

Taguchi has tabulated eighteen orthogonal arrays that are called *standard orthogonal arrays* [81]. These arrays can be used most of the time; however it is possible to modify these arrays to increase the amount of factor levels that can be studied per array. These eighteen arrays are shown in Table 2.1.

In the mixed level $L_{18}(2^1 \times 3^7)$ experimental array, there are eight columns labelled A to H represent the eight factors that can be assigned to this array. Each of these columns has numbers that represent the levels of the factors that are assigned to the column. Therefore, experiment number 1 would have all factors at level 1, i.e. experiment 1 is studied with the factor levels at *A1*, *B1*, *C1*, *D1*, *E1*, *F1*, *G1* and *H1*.

The arrays are designed such that interactions can be studied between factors, at a cost of the amount of factors that can be studied in the array. An interaction occurs when the effect of one factor depends on the level of another factor. If an interaction effect is significant, the prediction of the effect of a selected factor becomes more difficult. Therefore, it is desirable to select factors that would not have interaction effects. If a column that can be used to study interactions is used to study another factor, then the results of the factor could be confounded with the interaction of the other factors.

Table 2.2 **Orthogonal array for $L_{18}(2^1 \times 3^7)$**

	Factors							
Expt. No.	**A**	**B**	**C**	**D**	**E**	**F**	**G**	**H**
1	1	1	1	1	1	1	1	1
2	1	1	2	2	2	2	2	2
3	1	1	3	3	3	3	3	3
4	1	2	1	1	2	2	3	3
5	1	2	2	2	3	3	1	1
6	1	2	3	3	1	1	2	2
7	1	3	1	2	1	3	2	3
8	1	3	2	3	2	1	3	1
9	1	3	3	1	3	2	1	2
10	2	1	1	3	3	2	2	1
11	2	1	2	1	1	3	3	2
12	2	1	3	2	2	1	1	3
13	2	2	1	2	3	1	3	2
14	2	2	2	3	1	2	1	3
15	2	2	3	1	2	3	2	1
16	2	3	1	3	2	3	1	2
17	2	3	2	1	3	1	2	3
18	2	3	3	2	1	2	3	1

2.3.3.2. Quality loss functions

Taguchi emphasizes the quality variation is the main enemy of quality engineering. The best quality is achieved when the deviation from a target is reduced to the minimum value [80]. Accordingly, he introduces the loss function. If the quality characteristic of a product is *y*, and the target value for *y* is *m*, the (quadratic) quality loss *L(y)* can be expressed as:

$$L(y) = k(y - m)^2 \tag{2.22}$$

where *k* is a constant called quality loss coefficient, which can be determined when L(y) is known for a particular value of *y*. The three most common characteristics of the (quadratic) loss function are:

- Nominal-is-best: the nominal value is best because it is the one that satisfies the user-defined target value. The characteristic value away on either side of the target value is undesirable. The values may be positive or negative, such as the stitching density or vacuum pressure.

- Smaller-the-better: a smaller value is better and higher values are undesirable, such as surface defects or leakage of vacuum bag.
- Larger-the-better: a larger value is better and smaller values are undesirable, such as bond strength of adhesive or absorbed energy during impact.

Take the nominal-is-best type for example, let $m \pm \Delta_0$ represent the deviation at which functional failure of the product (or process) occurs, and let the loss at $m \pm \Delta_0$ be A_0. Then by substitution in equation 2.22, we have:

$$k = \frac{A_0}{\Delta_0^2} \tag{2.23}$$

Thus the loss function for the nominal-is-best type can be written as [78]:

$$k_N = \frac{A_0}{\Delta_0^2}(y - m)^2 \tag{2.24}$$

$$k_S = \frac{A_0}{\Delta_0^2} y^2 \tag{2.25}$$

$$k_L = A_0 \Delta_0^2 \frac{1}{y^2} \tag{2.26}$$

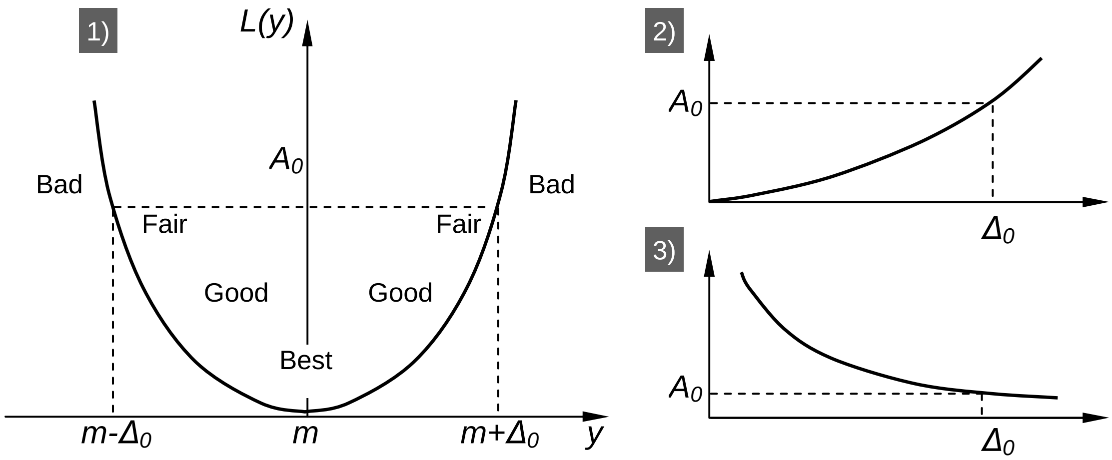

Figure 2.41 Quadratic loss functions: 1) nominal-is-best; 2) smaller-the-better; 3) larger-the-better

According to above expression, the nominal-is-best loss function is plotted in Figure 2.41 (1). It shows the loss L(y) decreases slowly when the quality y goes close to m, but as it goes further from m the loss L(y) increases more rapidly. Equation 2.25 and equation 2.26 present the smaller-the-better and the larger-the-better loss functions, respectively. They are also plotted in Figure 2.41 (2&3) [78]

2.3.3.3. Signal-to-noise (S/N) ratio

The signal-to-noise ratio is an index of robustness as it measures the quality of energy transformation that occurs within a design. The quality of its energy transformation is expressed as the ratio of the level of performance of the desired function to the variability of the desired function [82]. In Robust Design, the *signal-to-noise* (S/N) ratio, η, is defined as:

$$\eta = \frac{power \quad of \quad signal}{power \quad of \quad noise} = \frac{\mu^2}{\sigma^2} \tag{2.27}$$

The S/N ratio is used as the objective function to be maximized, i.e. the higher the S/N ratio, the higher the quality. For improved activity of the control factor effects, it is common practice to take logarithmic transform of (μ^2/σ^2) and express the S/N ratio in decibel (dB) scale:

$$\eta = 10\log_{10}\frac{\mu^2}{\sigma^2} \tag{2.28}$$

Suppose we have a set of characteristics y_1, y_2, y_3, ..., y_n, the S/N ratios for each of three types of quality characteristic can be defined as [78, 80]:

- Nominal-is-best:

$$\left.\begin{aligned} \eta &= 10\log_{10}\frac{\mu^2}{\sigma^2}, \\ \mu &= \frac{1}{n}\sum_{i=1}^{n} y_i \\ \sigma^2 &= \frac{1}{n-1}\sum_{i=1}^{n}\left(y_i - \mu\right)^2 \end{aligned}\right\} \tag{2.29}$$

- Smaller-the-better:

$$\eta_S = -10\log_{10}\left[\frac{1}{n}\sum_{i=1}^{n} y_i^{\ 2}\right] \tag{2.30}$$

- Larger-the-better:

$$\eta_L = -10\log_{10}\left[\frac{1}{n}\sum_{i=1}^{n} \frac{1}{y_i^{\ 2}}\right] \tag{2.31}$$

The optimization strategy consists of the following four steps [78]:

1) Evaluate the effects of control factors under consideration on η, and on the mean function.
2) For factors that have a significant effect on η, select levels that maximize η.
3) Select any factor that has no effect on η but a significant effect on the mean function as an adjustment factor. Use it to bring the mean function on target. This is a main quality control procedure in Robust Design. It is more important to find the right adjustment factor than to find the actual level of the adjustment factor.
4) For factors that have no effect on η as well as the mean function, e.g. the cost, then any level that is convenient from other considerations can be selected.

2.4. Analysis methods used in Robust Design

There are two methods for calculating the results produced through an orthogonal array; these are the analysis of the means method and the analysis of the S/N ratio method. The former is simply calculated from the mean value of the experiments, while the analysis of the S/N ratio method relies on the experimenter calculating the S/N ratio (see 2.3.3.3). In this study, the main purpose of using Robust Design is to maximize the SEA level of structural composites. Therefore, only the "Larger-the-better" of quality characteristics type is applied onto analysis.

The analysis of the means method only requires one value from each experiment to be successfully calculated, while the analysis of S/N Ratio method requires a series of experiments. In addition, each method can be calculated in two ways, either simply by a response table, or by the more complicated analysis of variance method.

2.4.1. The Response Table

After the experimental results are obtained, the mean value ($\bar{y}_i$) and the S/N ratios can thus be calculated. In addition, the effects of levels of each factor also can be compared by taking the average of each result in those experiments. Take the factor A in $L_{18}(2^1\times3^7)$ orthogonal array (see Table 2.2) for example, the mean effects (or S/N ratios) of its level 1 and level 2 can be expressed as:

$\bar{y}_{A1}$ = mean effect (or S/N ratio) of experiments 1 to 9

$\bar{y}_{A2}$ = mean effect (or S/N ratio) of experiments 10 to 18

Similarly, for three levels (or S/N ratio) of factor B:

$\bar{y}_{B1}$ = mean effect (or S/N ratio) of experiments 1, 2, 3, 10, 11 and 12

$\bar{y}_{B2}$ = mean effect (or S/N ratio) of experiments 4, 5, 6, 13, 14 and 15

$\bar{y}_{B3}$ = mean effect (or S/N ratio) of experiments 7, 8, 9, 16, 17 and 18

Table 2.3 The Response Table of factor effects for an $L_{18}(2^1\times3^7)$ array

	Factors							
	A	B	C	D	E	F	G	H
Level 1	$\bar{y}_{A1}$	$\bar{y}_{B1}$	$\bar{y}_{C1}$	$\bar{y}_{D1}$	$\bar{y}_{E1}$	$\bar{y}_{F1}$	$\bar{y}_{G1}$	$\bar{y}_{H1}$
Level 2	$\bar{y}_{A2}$	$\bar{y}_{B2}$	$\bar{y}_{C2}$	$\bar{y}_{D2}$	$\bar{y}_{E2}$	$\bar{y}_{F2}$	$\bar{y}_{G2}$	$\bar{y}_{H2}$
Level 3	-	$\bar{y}_{B3}$	$\bar{y}_{C3}$	$\bar{y}_{D3}$	$\bar{y}_{E3}$	$\bar{y}_{F3}$	$\bar{y}_{G3}$	$\bar{y}_{H3}$
Difference	-	-	-	-	-	-	-	-
Rank	-	-	-	-	-	-	-	-
Optimum	-	-	-	-	-	-	-	-

Table 2.3 shows a typical response table for the $L_{18}(2^1\times3^7)$ array. The difference is obtained from the subtraction of the highest and lowest values for each factor. According to the required quality characteristic, e.g. larger-the-better or smaller-the-better, then the optimum factors can be selected from the response table. Depending on the chosen criterion, the largest or smallest values can then be picked and the optimum condition created according to the ranking order. It should be noted that while the ranking gives the order of importance of a factor, it does not indicate the relative magnitude of that importance.

2.4.2. Analysis of Variance (ANOVA)

Different factors affect the quality of product or process to a different degree. The relative magnitude of the factor effects can be evaluated from Table 2.3. Another better approach for the relative effect of the different factors can also be obtained by the decomposition of variance. Or commonly, this alternative approach is called *Analysis of Variance* (ANOVA).

2.4.2.1. Equations for calculating ANOVA

An important purpose of ANOVA is to determine the relative importance of the various factors. ANOVA is also required to estimate the error variance for the factor effects and variance of the prediction error [78]. The following equations are the basic equations for calculating ANOVA:

- The overall mean (average), $\bar{y}$

$$\bar{y} = \frac{\sum_{i=1}^{n} y_i}{n} \tag{2.32}$$

where y_i is a particular number in a set of n numbers

- The square of the sum of y_i in a set of n numbers, SS

$$SS = \left[\sum_{i=1}^{n} y_i\right]^2 = \left(y_1 + y_2 + y_3 + \cdots + y_n\right)^2 \tag{2.33}$$

- The grand total sum of squares of y_i in a set of n numbers, SST_{grand}

$$SST_{grand} = \sum_{i=1}^{n} y_i^2 = y_1^2 + y_2^2 + y_3^2 + \cdots + y_n^2 \tag{2.34}$$

The grand total sum of squares can be decomposed into two parts: sum of squares due to mean and total sum of squares [78].

- The sum of squares due to mean, SSM. It is often called the *Correction Factor*.

$$SSM = n\bar{y}^2 = n \times \frac{\left(\sum_{i=1}^{n} y_i\right)^2}{n^2} = \frac{\left(\sum_{i=1}^{n} y_i\right)^2}{n} \tag{2.35}$$

- The total sum of squares of y_i in a set of n numbers, *SST*

$$SST = \sum_{i=1}^{n} \left(y_i - \bar{y}\right)^2 \tag{2.36}$$

which by combining equation 2.32 becomes:

$$\begin{aligned} SST &= \sum_{i=1}^{n} \left(y_i^2 + \bar{y}^2 - 2y_i\bar{y}\right) = \sum_{i=1}^{n} y_i^2 + n\bar{y}^2 - 2n\bar{y}\cdot\bar{y} \\ &= \sum_{i=1}^{n} y_i^2 - n\bar{y}^2 \end{aligned} \tag{2.37}$$

Therefore, equation 2.37 can be also expressed as:

$$SST = SST_{grand} - SSM \tag{2.38}$$

- The sum of squares for factor A, S_A, following equation 2.37:

$$S_A = \frac{\left(n_{A1}\times\bar{y}_{A1}\right)^2}{n_{A1}} + \frac{\left(n_{A2}\times\bar{y}_{A2}\right)^2}{n_{A2}} + \cdots + \frac{\left(n_{Am}\times\bar{y}_{Am}\right)^2}{n_{An}} - SSM$$

Ref: [83] (2.39)

Or alternatively, following equation 2.36 S_A can also be expressed as:

$$S_A = n_{A1}\left(\bar{y}_{A1} - \bar{y}\right)^2 + n_{A2}\left(\bar{y}_{A2} - \bar{y}\right)^2 + \cdots + n_{Am}\left(\bar{y}_{Am} - \bar{y}\right)^2$$

Ref: [78] (2.40)

where *m* represent the number of levels for factor A. Accordingly, n_{Am} is the number of observations for a particular level (namely level *m*) for factor A.

- The sum of squares due to error, SSE

The sum of squares due to error is also known as the *residual sum of squares*. The orthogonality of the matrix experiment implies the following relationship among the various sums of squares [78]:

(Total sum of squares) = (sum of the sums of squares due to various factors)

+ (sum of squares due to error) (2.41)

Alternatively, for the $L_{18}(2^1\times3^7)$ array, the *SSE* can be written as:

$$SSE = SST - \left(S_A + S_B + S_C + \cdots + S_H\right) \tag{2.42}$$

- The degrees of freedom, *D*

The number of independent parameters associated with an entity like a matrix experiment, or a factor, or a sum of squares is called its *degrees of freedom*

[78]. The overall mean always has one degree of freedom ($D\bar{y}$ = 1) and so does the sum of squares due to mean (D_{SSM} = 1).

The total degrees of freedom equals to the total number of observations in the data set for the method of ANOVA [79]. The total degrees of freedom equals to the total number of observations in the data set for the ANOVA [79]. Thus if a full $L_{18}(2^1 \times 3^7)$ array with eighteen rows experiments and each experiment has five observations, then the total degrees of freedom equals has 18 × 5 = 90 degrees of freedom and so does the grand total sum of squares ($D_{SSTgrand}$ = 90).

Similar to equation 2.38, the degrees of freedom of the total sum of squares (D_{SST}) is equal to the degrees of freedom of the grand total sum of squares ($D_{SSTgrand}$) minus the degrees of freedom of the sum of squares to the mean (D_{SSM}). Thus in above example, the degrees of freedom associated with the total sum of squares are:

$$D_{SST} = D_{SSTgrand} - D_{SSM} = 90 - 1 = 89 \tag{2.43}$$

In general, one starts with n degrees of freedom and loses one degree of freedom for every sample mean calculated. The remaining degrees of freedom are used to make the independent fair comparisons. Accordingly, the degrees of freedom associated with a factor are also one less than the number of levels. For example, in the $L_{18}(2^1 \times 3^7)$ array, the factor A has two levels. Hence factor A has only one independent parameters, and one degree of freedom. Similarly, the rest factors B to H have two degrees of freedom each.

Furthermore, following the equation 2.41, we can obtain the relationship among the various degrees of freedom:

(Degrees of freedom for the total sum of squares, D_{SST})

= (sum of the degrees of freedom for the various factors, $D_A + D_B + \ldots + D_H$)

+ (degrees of freedom for error, D_e) (2.44)

- The error mean square, *EMS (or* error variance, V_e*)*

The error mean square, which is equal to the error variance, V_e, can be estimated as follows:

EMS = V_e = (sum of squares due to error) / (degrees of freedom for error)

$$= \frac{SSE}{D_e} \tag{2.45}$$

- The variance for factor A, V_A

  The variance is also known as the *mean square* [78, 80]. The variance, V_A, for factor A is defined as the sum of squares of observations for factor A divided by the degrees of freedom of factor A; in this example,

$$V_A = \frac{S_A}{D_A} \tag{2.46}$$

2.4.2.2. F-ratio and F-test

Statistically, there is a method by calculating *F-ratio*, which provides a decision at some confidence level as to whether the two sample variances are significantly different. This method is called *F-test*, named after Sir Ronald Fisher, a British statistician who invented the ANOVA method [84]. In this study, the *F-ratio* is used to calculate the ratio of a variance for a particular factor to the error variance, V_e. The F-ratio for factor A, F_A, is thus expressed as:

$$F_A = \frac{V_A}{V_e} \tag{2.47}$$

If the variance about the sample mean square values is not significantly different from the individual variance, then the F-ratio becomes approximately equal to one. But if this ratio (F_A in this case) becomes large enough, then the two sample variances are accepted as being unequal at some *confidence level*. In order to determine whether an F-ratio of sample variances is large enough, three points need to be considered:

1) confidence level, CL, can be expressed as:

$$CL = 1 - \alpha \tag{2.48}$$

   where α is the risk. It is often expressed as a percentage. Typically, α = 5%.

2) degrees of freedom associated with the sample variance in the numerator, D_1;

3) degrees of freedom associated with the sample variance in the denominator, $D_{2.}$

In the case of this study, D_2 is the degrees of freedom for error, D_e. Each combination of risk, numerator degrees of freedom and denominator degrees of freedom has an F-ratio associated with it. The format for representing this explicit value is expressed as

$F_{\alpha,D1,D2}$. Tables which list the required F-ratios to achieve some confidence level are provided in Appendix 2. Alternatively, the $F_{\alpha,D1,D2}$ also can be calculated by using embedded function, *FINV()*, of Microsoft Office Excel programme.

2.4.2.3. Percent contribution, P%

The portion of the total variation observed in an experiment attributed to each significant factor is reflected in the percent contribution, *P%*. The percent contribution indicates the relative power of a factor to reduce variation [79].

- The percent contribution for factors A, $\kappa_A\%$

  The contribution of factor A to the total sum of square is defined as [83]:

  $$P_A = \text{(sum of squares for factor A)} - \text{(degree of freedom for factor A)} \times \text{(error mean square)}$$

  $$= S_A - D_A \times EMS \tag{2.49}$$

  Hence, the percent contribution for factor A is written as [83]:

  $$P_A\% = \frac{P_A}{SST} \times 100 = \frac{S_A - D_A \times EMS}{SST} \times 100 \tag{2.50}$$

  The percents of contribution for other factors (e.g. factors B to H in L_{18} array) are determined similarly.

- The percent contribution due to error, $P_e\%$

  The contribution of error to the total sum of square is defined as [83]:

  $$P_e = \text{(sum of squares due to error)} + \text{(sum of the degrees of freedom for the various factors)} \times \text{(error mean square)}$$

  $$= SSE + (D_A + D_B + ... + D_H) \times EMS \tag{2.51}$$

  Hence, the percent contribution due to error is written as [83]:

  $$P_e\% = \frac{P_e}{SST} \times 100 = \frac{SSE + (D_A + D_B + ... + D_H) \times EMS}{SST} \times 100 \tag{2.52}$$

  Since the total percentage contribution must add up to 100 percent, percentage contribution due to error can alternatively calculated by subtracting all the accountable sources from 100 percent.

  The percentage contribution due to error provides an estimate of the adequacy of the experiment. If the percentage contribution due to error is lower than 15%, then it is assumed that no important factors were omitted form the experiment. If it higher than 50%, then some important factors were definitely omitted, conditions were not precisely controlled, or measurement error was excessive [79]. However, if the percentage contribution due to error is high, it also can be a good opportunity for further improvement and more experimentation may prove beneficial.

2.4.2.4. The ANOVA summary table and pooling techniques

The results of ANOVA calculations are normally presented in a typical ANOVA summary table, which is shown in Table 2.5. In this table, *SSq* denotes the sum of squares and *D.o.F* denotes the degrees of freedom.

In the ANOVA of S/N ratio, the combining of column effects to better estimate error variance is referred to as '*pooling'* [79]. The purpose of pooling is that any effect that is not statistically significant can be eliminated. There are two pooling strategies: pooling-up and pooling-down.

The pooling-up strategy entails F-test the smallest column effect against the next larger one to see if significance exists. If no significant F-ratio exists, these two effects are pooled together to test the next larger column effect until some significant F-ratio exists [79]. In most cases, around half the number of factors are pooled. This is because the more factors that are pooled, the more degrees of freedom of pooled error, $D_{Pooled\text{-}e}$, would have; and thus the estimate of the error sum of squares would be better.

The pooling-down strategy entails pooling all but the largest column effect and F-test the largest against the remainder pooled together. If that column effect is significant, then the next largest is removed from the pool and those two column effects are F-tested against all others pooled until some insignificant F-ratio is obtained [79].

The Table 2.5 is thus modified such that an extra column '*Pool'*, and an extra row '*Pooled Error*' are added. If a particular factor is pooled into the error, then the symbol 'Y' is assigned into the corresponding '*Pool'* column. The sum of squares for pooled error (SSE_{Pooled}) is calculated by adding the *SSE* to the sum of squares of the pooled factors. This is similarly done to calculate the degrees of freedom of the pooled error, $D_{Pooled\text{-}e}$. The *F'-ratios* and $F'_{\alpha,D1,D2}$ of non-pooled factors are then re-calculated using the variances these non-pooled factor divided by the pooled error.

Table 2.4 **The ANOVA table for an $L_{18}(2^1 \times 3^7)$ array**

Source	*SSq*	*D.o.F*	*Variance*	*F-ratio*	$F_{\alpha,D1,D2}$ (α=5%)	*Contribution %*
Factor A	S_A	D_A	V_A	F_A	$F_{\alpha,D1,D2}$	P_A
Factor B*	S_B	D_B	V_B	F_B	$F_{\alpha,D1,D2}$	P_B
...	...	...	...	...	...	...
Factor H	S_H	D_C	V_H	F_H	$F_{\alpha,D1,D2}$	P_H
Error	*SSE*	D_e	V_e	*1.00*	...	P_e
Mean	*SSM*	*1*	-	-	-	-
Total	*SST*	*n-1*	-	-	-	*100%*

Table 2.5 **Modified ANOVA table for an $L_{18}(2^1 \times 3^7)$ array by using Pooling techniques**

Source	*Pool*	*SSq*	*D.o.F*	*Variance*	*F'-ratio (non-pooled)*	$F'_{\alpha,D1,D2}$ (α=5%)	*Contribution %*
Factor A	-	S_A	D_A	V_A	$F'_{A\text{-}pooled}$	$F'_{\alpha,D1,D2}$	P_A
Factor B*	*Y*	S_B	D_B	V_B	-	-	P_B
...	...	...	...	...	...	...	...
Factor H	-	S_H	D_C	V_H	$F'_{A\text{-}pooled}$	$F'_{\alpha,D1,D2}$	P_H
Error	-	*SSE*	D_e	V_e	-	...	P_e
Pooled Error	-	SSE_{Pooled}	$D_{Pooled\text{-}e}$	$V_{Pooled\text{-}e}$	1.00	-	$P_{Pooled\text{-}e}$
Mean	-	*SSM*	*1*	-	-	-	-
Total	-	*SST*	*n-1*	-	-	-	*100%*

* assume Factor B is pooled

2.4.2.5. Alpha and beta mistakes

When making the decision of whether to use a new design based on test data, there are four possible outcomes, as shown in Table 2.6. When using the pooling-up strategy and judging many columns to be significant, the decision will be to use these factors for further experimentation and perhaps product or process design. The tendency will be to make the alpha mistake more often, thinking that some factor will cause an improvement, when, in truth, that factor will not help.

When using the pooling-down strategy and judging few columns to be significant, the decision will be to ignore many factors and use only a few for future experimentation and perhaps product or process design. The tendency will be to make the beta mistake more often, thinking that some factor makes no improvement, when, in truth, that factor will help.

Once a factor has been judged to be insignificant, that factor will probably not be included in further rounds of experimentation and the beta mistake will never be exposed. However, if an alpha mistake is made, that factor will be included in further experimentation and the alpha mistake will potentially be exposed. Since it is impossible to make both the alpha and beta mistakes simultaneously, the pooling-up strategy should be used, which will tend to prevent the beta mistake of ignoring helpful factors.

Table 2.6 Decision Risks [79]

<table>
<tr><td colspan="2" rowspan="2"></td><td colspan="2">The truth about the product</td></tr>
<tr><td>There is no improvement</td><td>There is some improvement</td></tr>
<tr><td rowspan="2">Decision based on test data</td><td>Do not use new design</td><td>OK</td><td>Beta mistake</td></tr>
<tr><td>Do use new design</td><td>Alpha mistake</td><td>OK</td></tr>
</table>

2.4.3. Estimated mean and confidence intervals in confirmation experiment

A confirmation experiment is usually carried out at the final step of the Robust Design process. A confirmation experiment is performed by conducting a test using a specific combination of the factors and levels previously evaluated. The purpose of the confirmation experiment is to validate the conclusion drawn during the analysis phase. The steps in conducting a confirmation experiments are [79]:

(a) Determine the preferred combination of the levels of the factors and interactions indicated to be significant (and insignificant) by the analysis;

(b) Calculate the estimated mean (and estimated average S/N ratio) for the preferred combination of significant factors and interactions;

(c) Calculate the confidence interval value;

(d) Calculate the confidence interval for the true mean around the estimated mean;

(e) Determine the sample size for the confirmation experiment;

(f) Conduct tests under specified conditions;

(g) Compare the confirmation test average result with the confidence interval for the true mean;

(h) Determine the next course of action if it is necessary.

In the step (b), the estimated mean, $\hat{y}$, can be calculated by (assuming L_{18} array is applied):

$$\hat{y} = \bar{y} + \left(\bar{y}_A^{'} - \bar{y}\right) + \left(\bar{y}_B^{'} - \bar{y}\right) + \cdots + \left(\bar{y}_H^{'} - \bar{y}\right) \quad (2.53)$$

or,
$$\hat{y} = \left(\bar{y}_A^{'} + \bar{y}_B^{'} + \cdots + \bar{y}_H^{'}\right) + \left(n' - 1\right) \times \bar{y} \quad (2.54)$$

where, $\bar{y}$ is the mean of entire experimental results, $\bar{y}_A^{'}$ is the mean of preferred level of factor A. By using pooled techniques, the pooled factors should not be included in above equations. Thus the number of quality means, *n'*, is equal to the number of non-pooled factors.

The estimate of the mean $\hat{y}$ is only a point estimate based on the averages of results obtained from the experiment. The experimenter would tend to have a range of values within which the true average would be expected to fall with some confidence [79]. Confidence, in the statistical sense, means there is some chance of a mistake. In the robust design process, the confidence intervals (CIs) are used for different average values, including $\hat{y}$. The confidence interval is the maximum and minimum value between which the true average should fall at some percentage of confidence.

There are three different types of confidence intervals (CIs) described by Taguchi, depending on the purpose of the estimate [79]:

1. Around the average for a particular treatment condition in the existing experiment, which can be written as:

$$CI_1 = \sqrt{\frac{F_{\alpha,D1,D2} V_e}{n_c}} \quad (2.55)$$

The *F* ratio is determined from the same F tables (see Appendix 2). The *D1* is always equal to 1 as it represents the degree of freedom for the numerator associated with the mean. The degree of the freedom for the denominator, *D2,* is the degree of freedom D_e associated with the pooled error variance V_e of the experiment [79]. The n_c is the number of tests under the specific condition.

2. Around the estimated average of a treatment condition predicted from the experiment, which can be written as:

$$CI_2 = \sqrt{\frac{F_{\alpha,D1,D2}V_e}{n_{eff}}} \tag{2.56}$$

where $$n_{eff} = \frac{N}{1 + D_{pooled}} \tag{2.57}$$

The N is the number of entire experiment runs, e.g. in an L_{18} array, N = 18. The D_{pooled} is the total degree of freedom associated with items used in $\hat{y}$, i.e. the total degree of freedom of pooled factors.

3. Around the estimated average of a treatment condition used in a confirmation experiment to verify predictions, which can be written as:

$$CI_3 = \sqrt{F_{\alpha,D1,D2}V_e\left[\frac{1}{n_{eff}} + \frac{1}{r}\right]} \tag{2.58}$$

The r is the sample size for the confirmation experiment.

Chapter 3. Experimental Techniques

All specimens tested in this study were manufactured by using quick and relatively low-cost resin infusion processes called SCRIMP^{TM}, which is the shortened form of "Seemann Composites Resin Infusion Moulding Process" [85]. To identify and evaluate the key parameters that could affect the crushing performance of the structural composites, a large number of experiments are generally needed. Glass fibres were thus chosen as the reinforcement, which is to keep material costs low.

As the primary method, a crushing test is introduced in this chapter, but the variable parameters of each structural composite sample will be described in the latter chapters. Mode-I, Mode-II and flexure tests were performed on composite materials in order to understand the effects of different crushing mechanisms. For predicting the critical buckling load, tensile tests were also carried out to evaluate the elastic properties of the composite materials.

3.1. Experimental stages

This work is divided into three stages. In an attempt to transfer previous crushing results based on composite plates to a practical application, an intersecting square cell was adopted in the initial stage. An experimental programme compared the critical buckling predictions using finite element methods to measure structural stability and observed failure.

At the second stage, three modified composite structures with different shapes of cross section were developed. A number of fibre orientations were also compared. In a departure from the first stage, through-thickness stitching technique was used to improve the interlaminar properties. Fracture toughness and flexural properties were investigated to evaluate the link between crushing mechanisms and stitching-enhanced toughening mechanisms in structural composites.

Based on the conclusions of the previous stages, the third stage concentrated on investigating a modified structural cell with a number of factors including stitching, resin types, geometric sizes, and fibre orientations. The Robust Design was applied at the last stage for the design of experiments aiming to optimise the energy absorption capability. The outline of these three stages is illustrated in Figure 3.1.

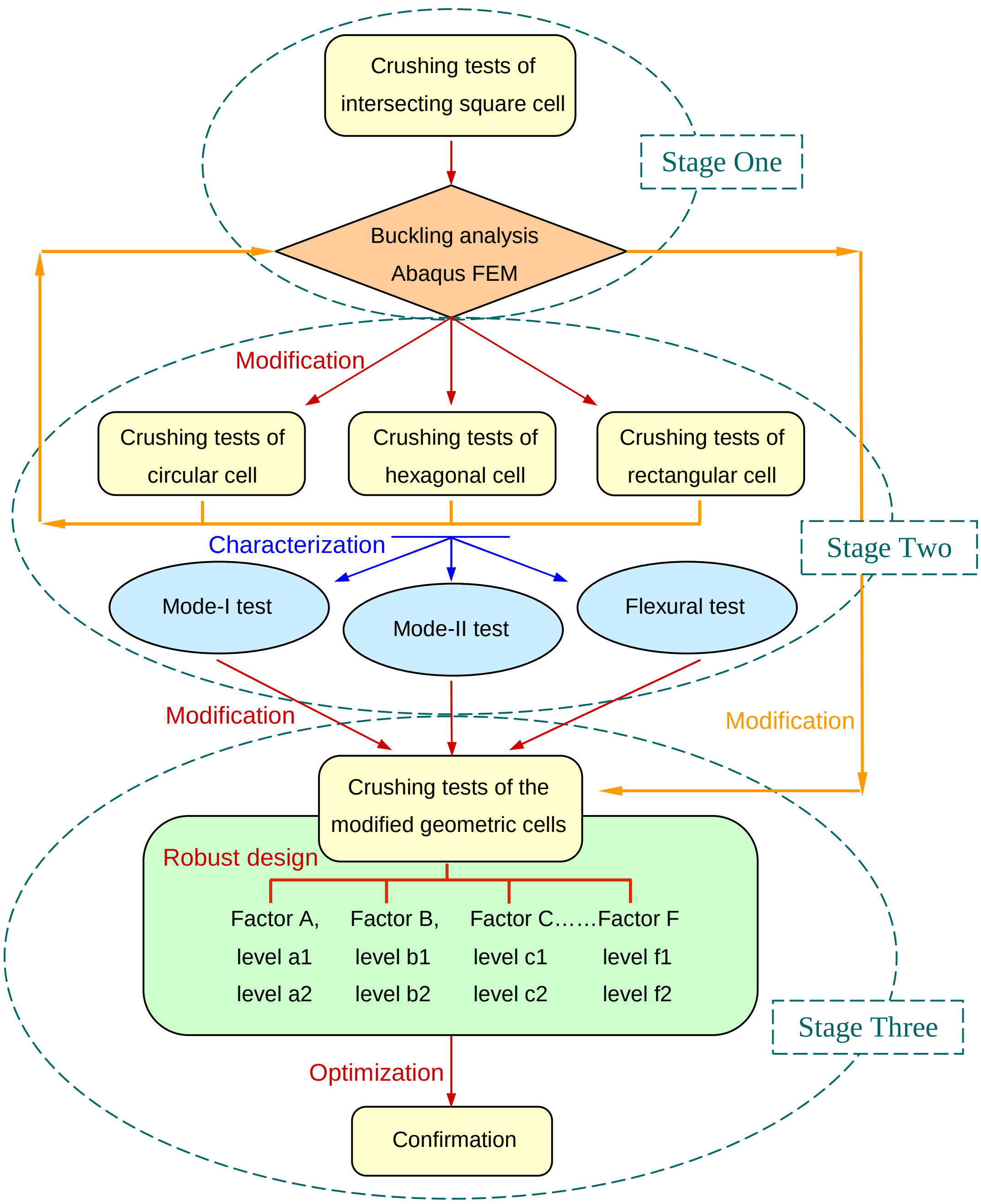

Figure 3.1 Outline of experimental work of present research

3.2. Materials

Due to the size of experiments required for this investigation, E-glass fibres were chosen to be the fibre types in order to reduce material costs and allow identification of key parameters. The range of fabrics used includes uniweave, biaxial and plain woven fabrics. Three thermosetting resins were used, which were polyester, vinyl ester and epoxy.

3.2.1. Fabrics

All types of fabrics used are shown in Table 3.1. The variety of fabrics was chosen to allow an assessment of the role of fabric constructions used in the laminates on the crushing behaviour.

During the first stage, the fabrics used were plain woven glass fabrics (GWR400P and GWR600P) produced by Carr Reinforcements Ltd, and unidirectional, biaxial NCFs produced by Saint-Gobain BTI. The unidirectional NCFs, ELPb-567, are in reality 90% UD fibres held together with 10% UD fibres at a transverse orientation.

During the second and third stage, the UD fabrics DV060, supplied by Sigmatex (UK) Ltd., were used instead of fabrics ELPb-567. These UD fabrics DV060 consist of 100% glass fibres at longitudinal orientation and fusible binder in the transverse direction. The ±45° biaxial fabrics of first stage, EBX-602, were also replaced by another very similar ±45° fabrics, FGE104 ST, which were produced by Formax (UK) Ltd. Moreover, only the plain woven fabrics GWR400P were used for the last two stages, which place 600tex fibres in both warp and weft yarns. The substitution of fabrics in stage two and three was prompted by supply problem and not by a desire to change the materials for performance reasons.

3.2.2. Resins

The resins used to make the laminates are listed in Table 3.2. Concentrating on isolating a few parameters, only polyester resin (Crystic® 489PA) was used at the first two stages. This Crystic® 489PA is an unsaturated isophthalic polyester resin and supplied by Scott Bader Co. Ltd. It was generally cured with 1.5% Butanox® M50 under room temperature for 24 hours followed by 3 hours at 80°C post-curing.

At the third stage, vinyl ester (Dion® 9102-500) supplied by Reichhold (UK) Ltd., and epoxy resin (Araldite® LY564) supplied by Huntsman Corporation., were used for evaluating the influence of resins on the crushing behaviour. Dion® 9102-500 is a preaccelerated and low-viscosity epoxy based vinyl ester resin. It has slightly higher mechanical properties than the epoxy resin, which is shown in Table 3.3.

In this study, it was mixed with 2% catalyst M.E.K.P (supplied by Jacobson Chemicals Ltd.) followed by the same curing schedule as polyester resin. Compared with the other two resins, the warm-curing epoxy system which is based on Araldite® LY564 and Hardener XB 3487 possesses a very long pot life, which can potentially facilitate the production of very large composite structures. They were cured and post-cured at 80°C for 8 hours after a resin infusion process.

The Hysol EA9460 is also listed in Table 3.2 and Table 3.3. It acts as an adhesive to bond two parts of the structural cell into one unit. More details will be presented in the latter chapter.

Table 3.1 **Fabric types used in whole project**

Fabric Description	Supplier	Dry thickness (mm)	Weights in each axis or Areal density (g/m²)			
		Stage One				
Non-crimp Fabrics			***0°***	***-45°***	***90***	***+45***
ELPb-567 (unidirectional)	Saint-Gobain BTI	0.50	567		50	
ELT-566 (biaxial 0,90)	Saint-Gobain BTI	0.50	283		283	
EBX-602 (biaxial ±45)	Saint-Gobain BTI	0.45		301		301
Woven Fabrics						
GWR400P (plain weave)	Carr Reinforcements	0.25	400			
GWR600P (plain weave)	Carr Reinforcements	0.40	600			
		Stage Two & Stage Three				
Non-crimp Fabrics			***0°***	***-45°***	***90***	***+45***
DV060 (unidirectional)	Sigmatex	0.40*	480			
FGE104 ST (biaxial ±45)	Formax	0.40*		300		300
Woven Fabrics						
GWR400P (plain weave)	Carr Reinforcements	0.25	400			

* value is not available on datasheet, but measured with vernier

Table 3.2 **Resin types used in whole project**

Resin Description (Part A)	Curing agent (Part B)	Mix ratio of A:B (by weight)	Supplier
	Stage One & Stage Two		
Crystic® 489PA (polyester)	Catalyst M	1 : 1.5%	Scott Bader
EA9460, white (adhesive)	EA9460, black	1 : 1	Hysol
	Stage Three		
Crystic®489PA (polyester)	Catalyst M	1 : 1.5%	Scott Bader
Dion® 9102-500 (vinyl ester)	M.E.K.P	1 : 2%	Reichhold
Araldite® LY564 (epoxy)	Hardener XB 3487	100 : 34	Huntsman

Table 3.3 **Mechanical properties of cured resins as obtained from datasheets of material supplier [86-89]**

Resin	Strength (MPa)	Modulus (GPa)	Strain to failure (%)
Crystic®489PA (polyester)	75	3.20	3.5
Dion® 9102-500 (vinyl ester)	79	3.40	4.5
Araldite® LY564 (epoxy)	72-76	2.94 – 3.10	8.0 - 8.5
EA9460 (adhesive)	30	2.76	3.5

3.2.3. Description of laminate orientations

The orientation of the laminates is written in a manner to distinguish between laminates made from separate layers and one complete fabric. When an NCF consists of layers with different orientations, a comma ‘,’ is used to separate the different orientations of each layer, while when separate layers or plies are listed, a forward slash ‘/’ is used. The subscript, ‘*s*’, implies that a laminate is of a symmetric orientation, while a subscripted number signifies the number of times that orientation is repeated in each half of the laminate. In addition, plain woven fabric and biaxial fabric in orientation of +45° and -45° are abbreviated ‘PW’ and ‘±45’, respectively.

As an example, laminates $[(\pm45)/(90,0)]_{2S}$, implies the use of a ±45° biaxial NCF together with another 90°, 0° biaxial NCF which the combination included twice per symmetry plane. And $[PW400/0_2]_S$ represents a laminate of symmetric orientation that consists of two outer layers of plain woven fabrics and four inner layers of UD fabrics.

3.3. Manufacture of composite panels

Low-cost manufacturing processes have evolved that can be used to manufacture structural composites at fractions of the cost of autoclave moulding, while resulting at the same time in high quality lamination. Seemann composites resin injection moulding process (SCRIMP) is one such process. In SCRIMP, a flow medium is inserted between the vacuum bag and the fabrics. This lifts the bag slightly away from the fabrics allowing resin to rapidly travel across the surface of the part. Impregnation then involves permeation through the thickness of the part. This process is much quicker than conventional vacuum infusion in which the resin has to permeate through the thickness of the reinforcement stack and then proceed towards the end of the part. In this investigation, all specimens are manufactured using this SCRIMP technique.

For flat panels, the SCRIMP is performed over a polished steel mould with dimension of 550mm×550mm, around which a dam had been created with tacky tape. The area inside of the dam is coated with three layers of Frekote® release agent. The required amount of pre-cut sheets of fabric are weighed on scales and laid up according to the orientation desired.

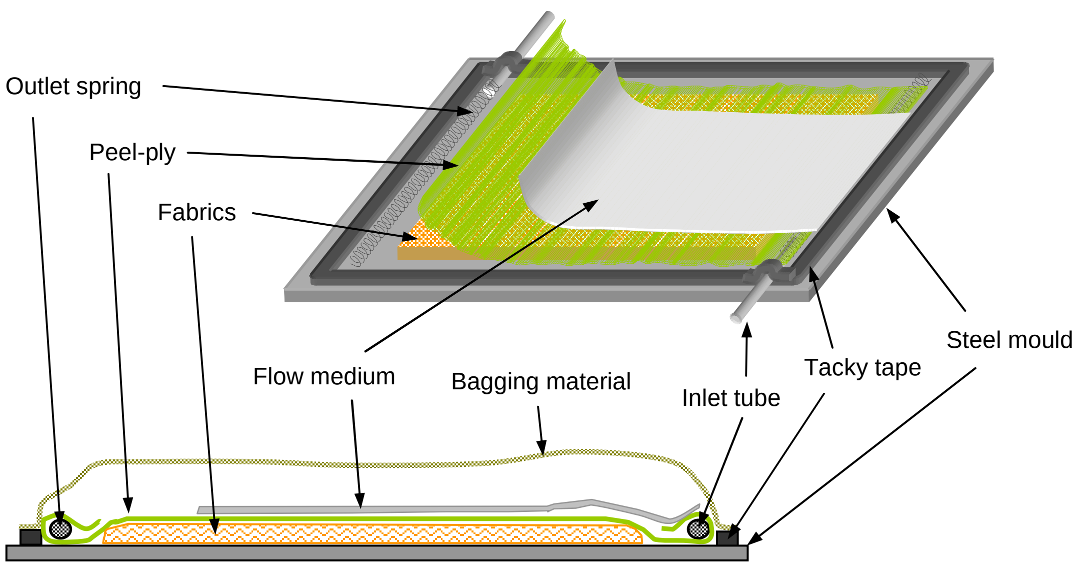

Figure 3.2 Schematic sketch of SCRIMP setup

Then, a sheet of peel-ply which facilitates the removal of the cured laminate is draped over the top after placing the fabric onto the plate. A spring is connected to a tube that acts as the resin reservoir during infusion process. They are laid over one end of the mould and wrapped up with one layer of peel-ply. Under the vacuum condition, the resin inlet reservoir would suck the resin and allow the resin rapidly to travel to the opposite end of the inlet. In the same way, the outlet made of a spring and a tube is laid over the other end. After this, a flow media which is used to distribute the resin is placed over the top of the inlet spring and over the peel-ply. A sheet of bagging material is finally laid over the tacky tape to seal the mould. The whole setup of resin infusion process can be seen from Figure 3.2.

Before infusing resin, the whole set up system must to be tested if it is properly sealed and vacuum. The resin is infused through inlet tube followed by transferring to the flow medium and starts to saturate the fabric layers underneath with resin. At the end, fabric layers are fully wet out by resin and resin flows through the outlet tube into the resin trap. After the whole infusion procedure finishes, the composite laminate should not be demoulded until it has been completely cured and post-cured. For those corrugated structural composites which were developed in this study, their manufacturing processes and mould geometries will be introduced in the Chapter 5 and Chapter 8.

3.4. Experimental methods and their specimens

A range of test methods was conducted in this study. Details of these test methods are summarized in the sections below. Five specimens per configuration were tested for all experimental methods mentioned in the following sections. All samples which were investigated in this study were tested under room temperature. Humidity was not controlled for the mechanical tests, but relative humidity in the mechanical testing room was usually about 50±5%. Most samples were exposed under a very similar environment condition before the tests.

3.4.1. Crushing test

3.4.1.1. Crushing test for plates

The crushing test for composite plates was carried out in a fixture designed by QinetiQ Group (see Figure 3.3) and was previously used in Cauchi-Savona's work [2]. This fixture consists of four movable knife-edges that offer the simply-supported boundary condition on plate samples. The top parts of the knife-edges clamp the plate and prevent the plate sample from opening as the test progresses. Loading is achieved through a rod attached to the load cell. The loading block is present to ensure that the load is spread over the whole top of the specimen [2]. A similar fixture was also developed by Jackson *et al.* [22]. The crushing test was performed at 20mm/min in an Instron universal testing machine (5584).

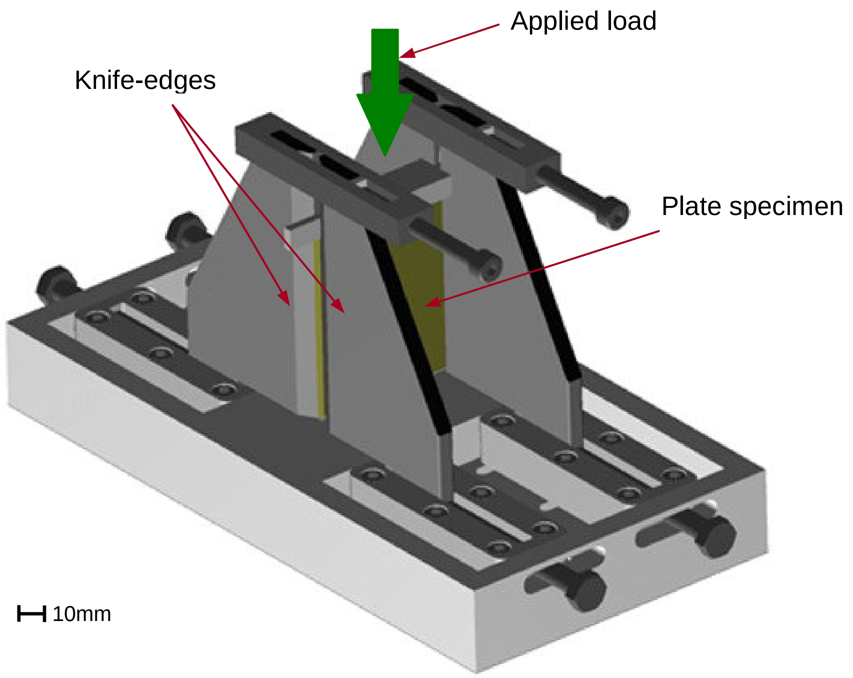

Figure 3.3 Illustration of the crushing test for simply-supported plates [2]

3.4.1.2. Crushing test for composite structures

There was no crushing standard method available for those particular composite structures designed in this research. The Instron universal testing machine (5584) with 150kN load cell was also used to carry out quasi-static crushing test on structural composite cells. The crush rig consists of two parallel steel platens, which is illustrated in Figure 3.4. Whereas a 1000kN servo hydraulic test machine were also used for the samples that excesses the loading capacity of 150kN. In this study, crushing tests were performed at speed of 20mm/min at the first and second stages, while this was changed to a range from 1mm/min to 400mm/min to evaluating the effect of test speed at the third stage. Specimen preparations of each composite structure will be detailed later on in Chapter 4, Chapter 5 and Chapter 8, respectively.

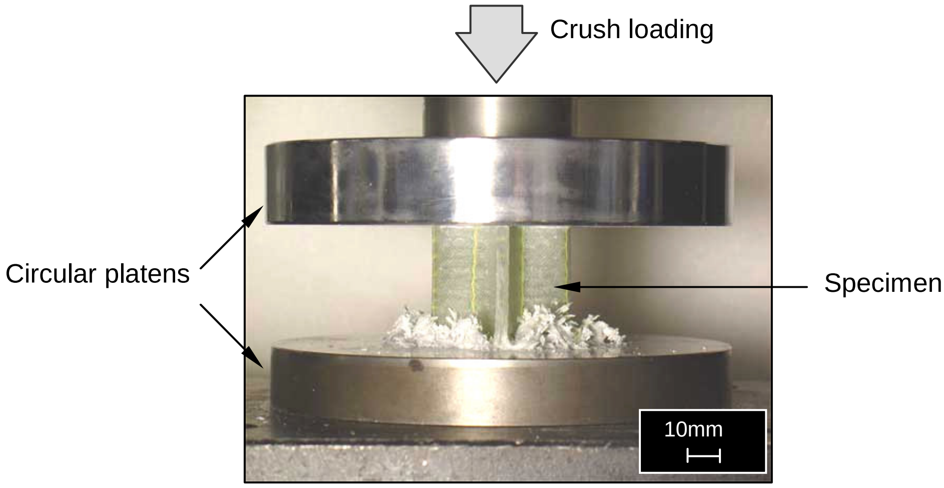

Figure 3.4 Image of the crush rig as used in this research

3.4.2. Fracture toughness test

Laminated fibre-reinforced composites made of high strength fibres in a relatively weak matrix material are susceptible to delamination [90]. And delamination is an important mechanism in the sustained crushing of composites. This section describes methods for measuring the interlaminar fracture toughness in Mode-I and Mode-II testing. Mode-I and Mode-II testing were by the double-cantilever beam method (DCB) and 4-point end notch flexure method (4-ENF), respectively.

3.4.2.1. Mode-I testing – Double cantilever beam (DCB)

For the Mode-I interlaminar fracture toughness tests, the ASTM D5528-01 standard [91] was followed. An insert of a 12μm thick releases film (Aerovac A6000) was inserted at the midplane of laminate during lay-up to form an initiation site for the delamination. This was selected as its opaque blue colour allowed easy identification in the cured glass fibre composite

Specimens were cut from flat composite panels into section of 142mm long and 20mm wide. According to the standard, the length of the insect film was approximately 63mm. This distance corresponds to an initial delamination length (a_0) of approximately 50mm, plus the extra length required for the piano hinge tabs.

The sides of the specimens were then coated with a thin layer of white spray paint, and thin ticks were marked by pencil on the white layer, starting from the insert edge. The lines were drawn every 1mm and totally marked length of 40mm. After this, piano hinge tabs were bonded to the both faces of specimen. The dimensions and configuration of a DCB specimen is show in Figure 3.5.

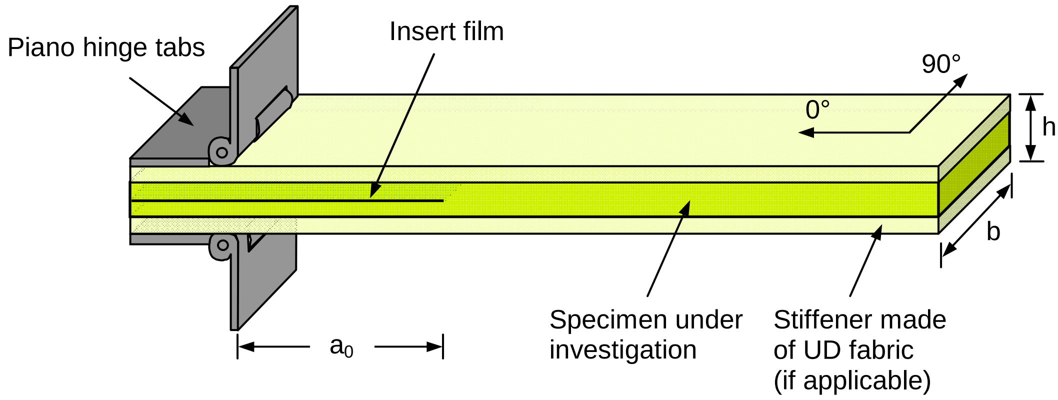

Figure 3.5 Dimensions and configuration of the DCB specimen

The use of thin DCB specimens was not only to reduce the specimen cost; it also allowed for the study of thin laminates under test conditions similar to practical cases [92]. In order to keep the fibre architecture of DCB specimens as close as that used in crushing specimens, thicknesses of DCB specimens in this study were thus between 2.2mm and 3.6mm. At the latter part of this study, a few DCB specimens stiffened by UD materials were also tested as a comparison to these thin DCB specimens.

A Hounsfield H25KS screw-driven universal testing machine equipped with a 100N load cell was used to perform DCB tests. Each specimen was pre-cracked at 1mm/min for the first 5mm of crack extension and, provided the crack grew in a stable manner, and then the same loading rate was applied for the remaining length. The specimen was unloaded at 10mm/min. Each time the crack propagated, the load and displacement were captured by pressing a PC hot-key linked to a custom written programme to record this particular crack length. Meanwhile, the crack length was detected by using a live web-camera and recorded continuously.

The ASTM standard gives three methods for calculating the Mode-I strain energy release rate, G_{IC}. These methods are: a compliance calibration (CC), a modified compliance calibration (MCC) and a modified beam theory (MBT). The G_{IC} values determined by the different methods differed by only 3%, however, the ASTM standard points out that the MBT method yielded the most conservative values of G_{IC} for 80% of the specimens tested and recommends the use of this method [91]. The expression of MBT method for G_{IC} is as follows:

$$G_{IC} = \frac{3P\delta}{2b\left(a + |\Delta|\right)} \tag{3.1}$$

where P = load,

δ = displacement,

b = specimen width,

a = delamination length,

$|\Delta|$ = correction factor for delamination length

The delamination length is the sum of the initial delamination length plus the increment of growth determined from the tick marks. In order to correct for the rotation that may occur at the delamination front, Δ is introduced to treat the DCB as if it contained a slightly longer delamination, $(a + |\Delta|)$ [91]. Δ can be determined experimentally by generating a least-squares plot of the cube root of compliance, $C^{1/3}$, as a function of delamination length (see Figure 3.6 left). The compliance, C, is the ration of the displacement to the applied load, δ/P.

Due to the stitching applied to most DCB specimens, the ratio of the opening displacement at the delamination onset, δ, to the delamination length, a, was greater than 0.4. Therefore, large displacement corrections were applied to the calculated values of Mode-I strain energy release rate, $G_{IC,}$ especially for the thin specimens. This procedure can be found in the standard [91].

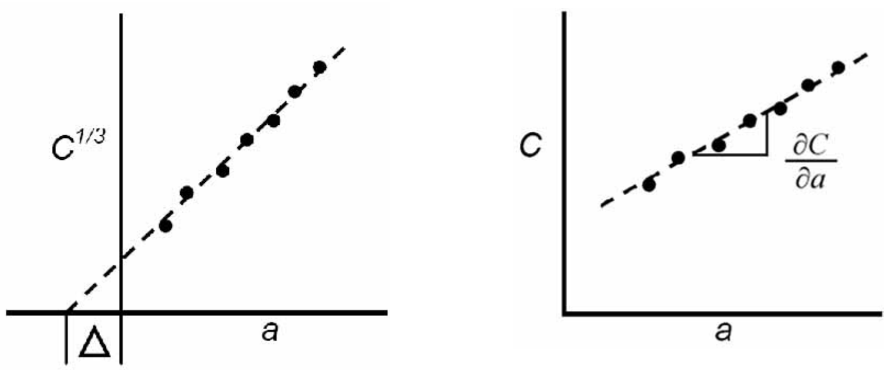

Figure 3.6 Determination of Δ (left) for DCB test, and ∂C/∂a (right) for ENF test

3.4.2.2. Methods of identifying delamination initiation

It is important to mention here that the precise identification of delamination initiation by visual inspection is usually difficult and highly operator dependent. In order to obtain some degree of repeatability, the ASTM standard proposes three approaches of relating points on the load-displacement curve for identifying delamination initiation.

i. Visual observation (VIS)

A visually observed initiation value for G_{IC} should be recorded corresponding to the load and displacement for the first point at which the delamination is seen to grow from the insert on either edge of the specimen.

ii. Deviation from linearity (NL)

The initiation value for G_{IC} can be typically calculated from the load and displacement at the point of deviation from linearity, or onset of nonlinearity (NL). This calculation assumes that the delamination starts to grow from the insert in the interior of the specimen at this point [91]. The NL value represents a lower bound value for G_{IC}. For brittle matrix composites, the NL value is generally the same point as the VIS value (see Figure 3.7 a). However, for tough matrix composites, a non-linear region may precede the visual observation of the initiation of delamination at the specimen edges (see Figure 3.7 b).

iii. 5% offset/maximum load (5%/Max)

According to the ASTM standard, the value of G_{IC} also can be calculated from the intersection of the load-deflection curve with a line drawn from the origin and offset by a 5% increase in compliance from the original linear region of the load-displacement curve. If the intersection occurs after the maximum load point, then the maximum load should be used to calculate the initiation value for G_{IC}.

3.4.2.3. Mode-II testing – 4-point bend end-notched flexure (4-ENF)

For the Mode-II fracture toughness testing, the three-point bend end-notched flexure (3-ENF) test is perhaps the most commonly used test for determining the Mode-II strain energy release rate, G_{IIC}, of laminate composites [93]. However, as a result of the three-point bend configuration, a vertical shear force acting within the delaminated a)

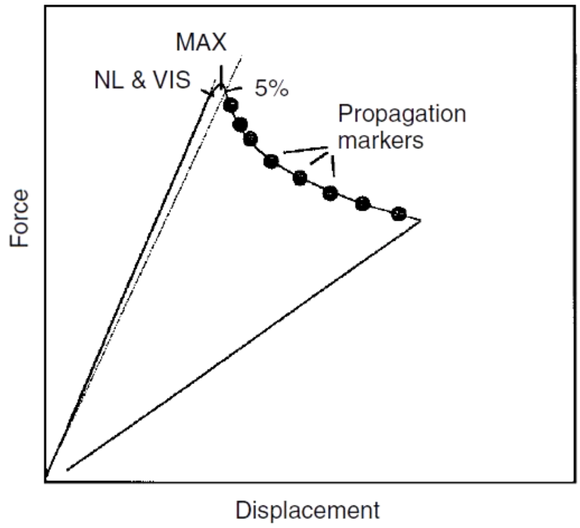

b)

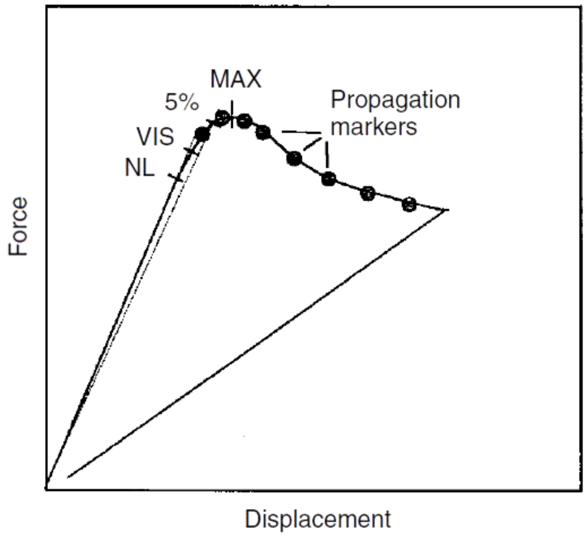

c)

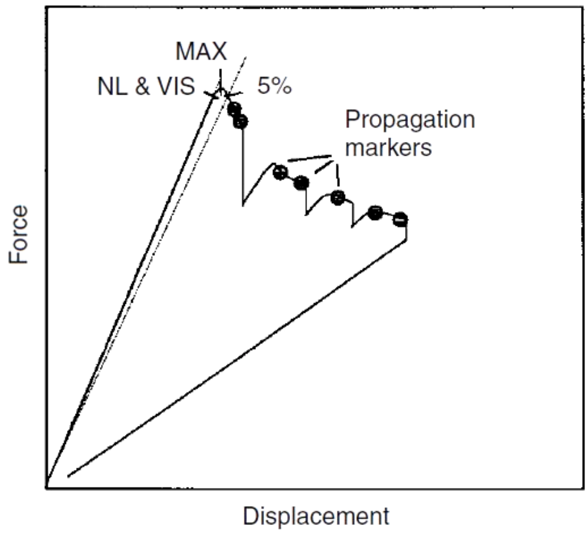

Figure 3.7 The load-displacement trace from DCB tests can follow three typical patterns: a) brittle matrix, b) tough matrix, and c) unstable crack growth [90]

regions and at the delamination tip causes friction. This friction may result in an unstable delamination growth [94].

The four-point bend end-notched flexure (4-ENF) test has been proposed as an alternative method for Mode-II testing. Unlike the 3-ENF, in the 4-ENF test, crack growth is stable under displacement control. In this study, the same 4-ENF testing procedure detailed in previous studies [2, 93-95] was followed.

The dimensions and configuration of a 4-ENF specimen is show in Figure 3.8. Specimens were cut from composite panels, 140mm long and 20mm wide, leaving an insert film length of 50mm. The spans for the loading rollers and the supporting rollers were 60mm and 100mm, respectively, which presented an effective initial delamination length (a_0) of 30mm. The sides of the specimens were prepared as for DCB specimens. The lines were drawn also every 1mm with a total marked length of 40mm.

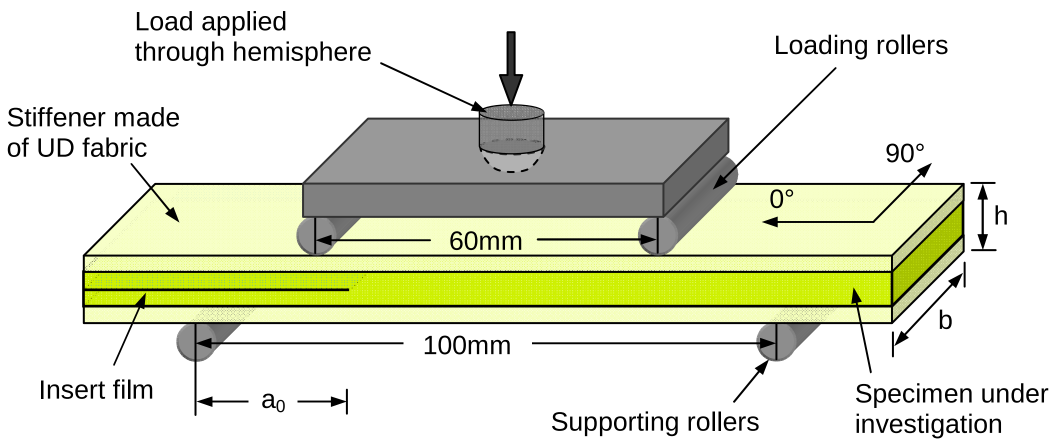

Figure 3.8 Dimensions and configuration of the 4-ENF specimen

In a like manner as the DCB specimens, 4-ENF specimens were produced using the same lay-up as crushing specimens. Since this resulted in laminates that are not thick and stiff enough to be tested without excessive bending, laminates were equipped with six layers of UD glass fabric bonded on each side to increase the bending stiffness of the 4-ENF specimens.

The 4-ENF tests were performed in Hounsfield testing machine with a 5kN load cell. The loading rate for the pre-crack of approximately 5mm and remaining length was 0.5mm/min. The crosshead also returned at 10mm/min when the delamination length was around 40mm. The strain energy release rate, G_{IIC}, was calculated by the following equation:

$$G_{IIC} = \frac{P^2}{2b}\frac{\partial C}{\partial a} \tag{3.2}$$

where P = load,

b = specimen width,

C = compliance

a = delamination length,

$\partial C/\partial a$ = slope of the compliance to the delamination length in the Compliance Calibration (CC) chart (see Figure 3.6 right).

3.4.3. Flexure test

Flexure tests were performed in three-point bending according to the ASTM D790-02 standard [96]. Instron machine (5584) with 1kN load cell was used. Figure 3.9 shows a schematic sketch of this test. As recommended by the standard, the span-to-thickness ratio was set at 40:1 for all flexure specimens in this study. The specimen width was fixed to 20mm. The length was kept up to approximately two times of support span, so that the specimen had long enough extent outside the supporting rollers during bending test.

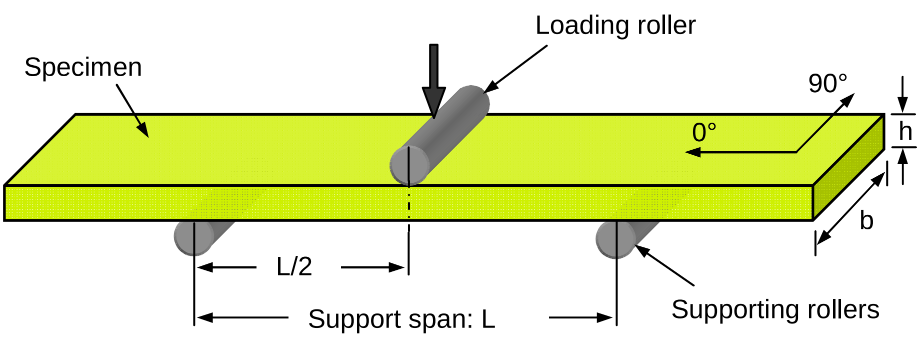

Figure 3.9 Schematic sketch of the flexure test

The test was terminated when the maximum strain (r) in the outer surface of the specimen reached 0.05. The rate of crosshead motion was calculated by following equation:

$$R = \frac{ZL^2}{6h} \tag{3.3}$$

where R = rate of crosshead motion,

L = support span,

h = thickness of specimen,

Z = rate of straining of the outer surface (0.01/min in this study).

The results of the flexural strength and bending modulus, as well as the area that is below stress-strain curve and before yielding are reported. Flexural stress and bending modulus were calculated by following equations:

$$\sigma_f = \frac{3PL}{2bh^2}\left[1+\left(\frac{rL}{h}\right)^2 - \frac{2r}{3}\right] \tag{3.4}$$

$$E_B = \frac{L^3 m}{4bh^3} \tag{3.5}$$

where P, b, L and h have already been mentioned previously in equation 3.1 and 3.3.,

σ_f = stress in the outer fibres at midpoint,

r = maximum strain, (0.05 in this study),

E_B = modulus of elasticity in bending (flexural modulus),

m = slope of the linear portion of the load-deflection curve.

3.4.4. Tensile specimen

Tensile tests were carried out in order to obtain the elastic properties of the UD lamina that consist of fabric DV060 and polyester resin Crystic® 489PA. The results including tensile modulus and Poisson's ratio are considered as a reference in the analysis and prediction of buckling stress, though the precision of the values of those elastic properties is not crucial compared with structural geometry and boundary conditions. The geometries of the tensile specimens are listed in Table 3.4.

Instron machine (5584) with 30kN load cell was used, and the ASTM standard D3039/D3039M-00 [97] was followed for tensile tests. To increase the gripping force, 1.5mm thick tabs with bevel angle of 90° were bonded on both ends of tensile specimen. During the test, strain was measured by a 2-element cross strain gauge FCA-5-11-1L produced by Tokyo Sokki Kenkyujo Co., Ltd. Tensile specimens were pulled at a constant crosshead speed of 2mm/min. Figure 3.10 schematically shows the positions of tabs and strain gauge on the specimen.

Table 3.4 Geometries of tensile specimens

Fibre Orientation	Width (mm)	Thickness (mm)	Overall Length (mm)	Tab length (mm)
Unidirectional $[0]_3$	20.45 ± 0.04	1.162 ± 0.055	250	56
Unidirectional $[90]_6$	25.45 ± 0.02	2.204 ± 0.020	175	25

values behind the ± are standard deviations

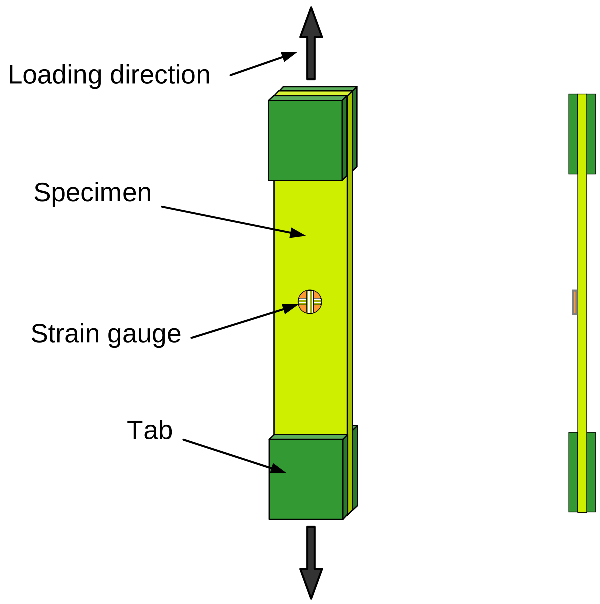

Figure 3.10 Schematic sketch of the tensile test

3.4.5. Finite element method (FEM)

In order to compare the critical buckling stress within different composite structures, analysis of numerical models were required. In this study, the finite element method was used as a technical tool rather than a precise simulation for the real structure. The finite element models were created and analysed by the commercial software ABAQUS/Standard version 6.6.

The simulation processes described in reference [98] and Abaqus Example Problems Manual [99] are followed. The critical buckling loads N_{cr} of the laminate structures are calculated by the eigenvalue buckling analysis implemented in the ABAQUS programme. In finite element analysis, the laminate structures are modelled by four-node general-purpose shell elements (S4). The formulation of this shell element allows transverse shear deformation and it is suitable for both thin and thick composite shells [100].

In this study, only the elastic behaviour of materials was taken into account, lamination or other section failures were not considered. The linear elastic properties of the UD GFRP lamina were the basis of the classical theory analysis, and it is also necessary for materials property to be input in FEMs. The linear elastic properties used in this study are listed in Table 3.5.

Table 3.5 Elastic property of typical unidirectional GFRP lamina

Type of Lamina	E_{11} (GPa)	E_{22} (GPa)	ν_{12}	ν_{21}	G_{12} (GPa)	G_{13} (GPa)	G_{23} (GPa)	Cured Thickness (mm)	VF%
UD GFRP	36.70	13.10	0.30	0.11	16.90	16.90	8.45	0.38	53.8%

The 1-direction is along the fibres, the 2-direction is transverse to the fibres in the surface of the lamina, and the 3-direction is normal to the lamina. VF% is the fibre volume fraction.

E_{11} and E_{22} represent the elastic modulus of single layer UD lamina in the longitudinal and the transverse direction, respectively. ν_{12} is the major Poisson's ratio. The definitions of the suffix of moduli are shown in Appendix 1. Most data in the list were obtained from the tensile test of $[0]_3$ and $[90]_6$ (see Table 3.4). The shear modulus G_{12} and G_{13} were deduced via classic laminate theory (see Appendix 1). The out-of-plane shear modulus, G_{23}, was not measured in experiment. For UD GFRP and CFRP, it was found that the G_{23} is normally smaller than G_{12} (or G_{13}) [101, 102]. However, in the prediction of critical buckling stress because the effect of G_{23} is very small (predicted critical buckling stress increases by 2% if G_{23} was assumed as 16.90 GPa)， G_{23} was assumed as the half of the G_{12} (or G_{13}).

3.4.6. Density measurement

In order to obtain SEA values out of crushing results, the densities of materials crushing specimens must be measured. This measurement was preformed by Archimedes' principle using a Density Determination Kit made by Ohaus Corporation. In addition, the densities of cured resins (see Table 3.6) were also measure for calculating the fibre volume fractions.

Table 3.6 Densities of composite components for the calculation of fibre volume fractions

Component	Density [g/cm^3]
Resin	
Crystic®489PA (polyester)	1.20
Dion® 9102-500 (vinyl ester)	1.15
Araldite® LY564 (epoxy)	1.14
Fibre	
E-glass fibre	2.56 [a]
Kevlar® yarn	2.56 [b]

a: obtained from reference [103]

b: The density of Kevlar® was assumed as same as glass fibre due to the quantity of Kevlar® yarns is neglectable

Chapter 4. Intersecting Square Cell and Buckling

This chapter is concerned with the investigation of an intersecting structural composite made of flat FRP laminates, as well as the improvement of structural stability basing on critical buckling analysis.

4.1. Intersecting square cell

The first stage of transferring previous results that were obtained from plate crushing [2, 16] into an realistic energy absorbing structure, involved the investigation of an transition geometry consisting of intersecting plates. Polyester resin was selected as the only resin system. In total six types of fabric (see Table 3.1) were used at this stage. A steeple chamfer was chosen as the trigger type since it is easily machined on flat plate.

4.1.1. Specimen preparation

FRP laminates were manufactured by following the process introduced in the previous chapter. The flat panels were then weighed and cut into smaller plates to the required dimensions by a water-cooled diamond saw. Two slots were also cut on each plate by a milling machine.

Slotted plate specimens were then clamped again in the milling machine equipped with 45° angle-cutting bit and a steeple chamfer was machined. Square cell specimens were scaled in a range of dimensions, as well as different laminate thicknesses by varying lay-ups.

To simplify the scaling process, the length (*L*) to width (*D*) ratio was restricted to the range 1.5-1.7. And the distance from slot to the end of plate was fixed to half of the separation width between two slots. Table 4.1 lists the dimensions and fibre orientations for the intersecting square cells test. The schematic sketch of machined plate and the photograph of the intersecting square cell are shown in Figure 4.1.

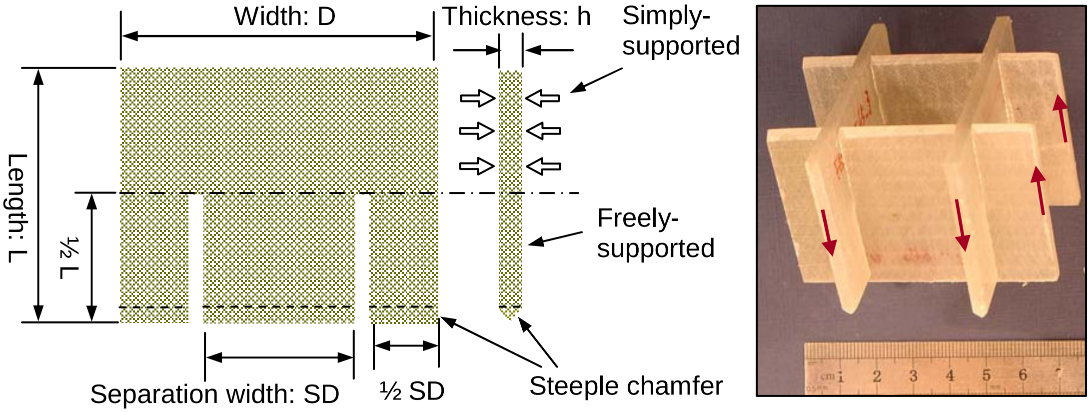

Figure 4.1 Schematic sketch of machined plate and intersecting square cell

Table 4.1 Properties of intersecting square cells and their crushing results

Reference	Orientation	h (mm)	L (mm)	SD/h ratio	D/h ratio	VF%	Crushing result	
							SEA (kJ/kg)	CV %
F1536_ISC	$[PW400]_8$	2.47±0.059	44.35	12.14	26.6	49.0	34.31±2.66	7.76
F1537_ISC	$[PW400]_{10}$	3.03±0.081	44.52	9.90	21.7	47.9	43.79±1.58	3.60
F1538_ISC	$[PW400]_{12}$	3.62±0.068	44.41	7.99	18.1	49.2	35.86±4.24	11.83
F1540a_ISC	$[PW600]_6$	2.60±0.081	39.26	9.62	21.2	53.9	34.45±0.65	1.88
F1540b_ISC	$[PW600]_6$	2.62±0.048	51.25	12.99	28.3	53.9	29.58±1.47	4.95
F1541a_ISC	$[PW600]_8$	3.65±0.125	45.31	7.93	17.9	50.6	37.07±1.11	3.00
F1541b_ISC	$[PW600]_8$	3.67±0.181	60.45	9.79	21.9	50.6	35.97±1.78	4.94
F1534_ISC	$[\pm45/(90,0)]_{2S}$	3.94±0.089	44.35	7.10	16.3	46.3	44.47±1.07	2.40
F1535_ISC	$[\pm45/(90,0)]_{2S}$	3.99±0.126	64.57	10.80	23.6	46.4	32.12±1.55	4.84
F1564_ISC	$[\pm45/0_3]_{2S}$	3.55±0.107	45.22	8.35	18.9	56.8	32.29±3.99	12.34
F1567_ISC	$[\pm45/PW600]_{2S}$	3.51±0.089	46.10	8.49	19.1	54.8	36.05±2.26	6.26

SD: Separation width; D: Real width; L: Length; h: Thickness

VF: Fibre volume fraction

CV: Coefficient of variation = (standard deviation / SEA average value) x 100.

values behind the ± are standard deviations

It is important to note that red arrows on right of the photo in Figure 4.1, indicate the sliding directions of plates during crushing. Under crushing load, stresses were concentrated on the triggered front and at the bottom of the slots. The crushing stoke would not be able to progress further, unless the intersecting plates tore each other at the bottom of slots. Because of this intersecting assembly, the tearing mechanism reduced the integrity of specimen and indirectly destabilized the structure during crushing as a result of laminate cracking.

4.1.2. Comparison between single-cell and multi-cell specimens

One single unit geometric cell was chosen as the sample to be investigated. The crushing stress – displacement curves of a multi-cell specimen and its constituent single cell structure, a single-cell $[PW400]_{10}$ are plotted in Figure 4.2. It can be seen that the difference between the multi-cell and the single-cell samples is almost negligible. In other words, the single-cell samples can be considered as a representative of a final assembly that contains multiple cells made of intersecting laminates. Therefore, to minimize the material cost and labour cost, this study will be only focused on the single-cell structure.

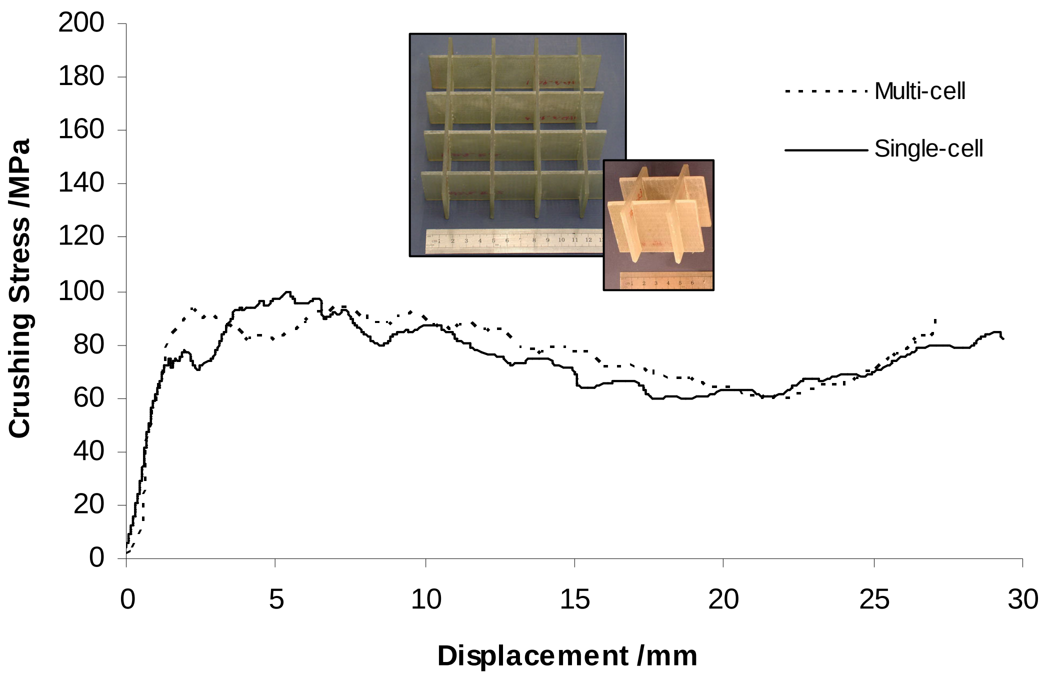

Figure 4.2 Comparison of crushing stress vs. displacement curve between single-cell tube and multi-cell specimens

4.1.3. Crushing response of intersecting square cells

Figure 4.3 illustrates that a typical crushing process of ISC sample can be divided into 4 stages:

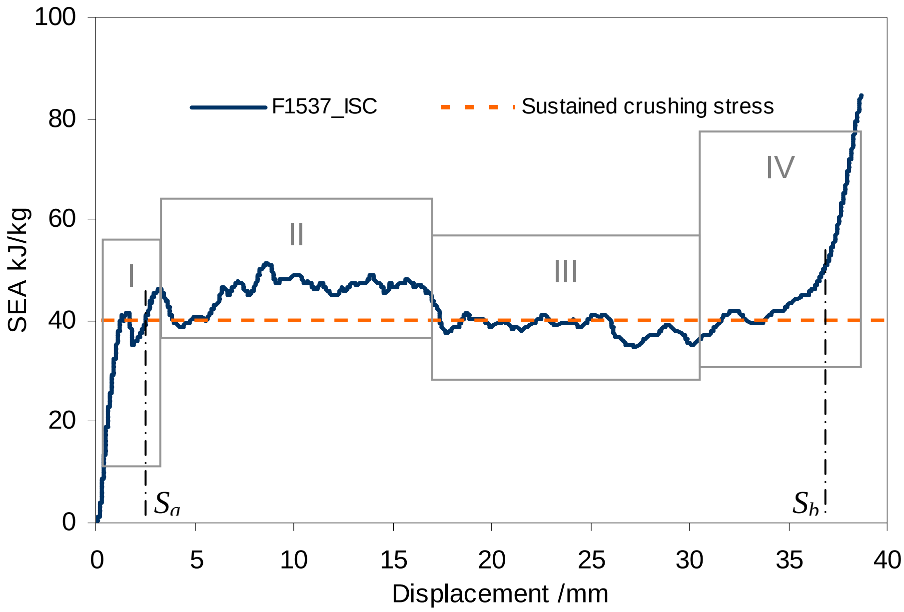

Figure 4.3 Typical stages in the crushing process of intersecting square cell

Stage I) Initiation of crushing (Figure 4.4a): when a compressive load is applied to the chamfered end of the composite structure, the stresses concentrated at the tip of the trigger are much higher than stresses imparted in the body of the structure. As a result, the chamfered tip rapidly generates microfractures and forms a debris wedge [15]. Eventually a stable crush zone is created after S_a which is shown in Figure 4.3.

Stage II) Progressive crushing (Figure 4.4b): after crushing of the composite structure is triggered, the load reaches a steady equilibrium. Each laminate plate is split into two splaying fronds by the debris wedge. The load gradually increases and saturates at a mean crushing load that has small fluctuations characteristic of stable crushing.

Stage III) Reduction of crushing load (Figure 4.4c): laminates bend and crack at freely-supported boundaries in some parts of intersected laminates. The load starts dropping after the sample reaches about 17mm in Figure 4.3.

Stage IV) Compaction of debris (Figure 4.4d): The fragments of the laminate formed at the crushing fronds gradually accumulate inside of the tubular cell. When the quantity of the fragments reaches a certain level, and can not be compacted any further, then the crushing load increases rapidly after S_b shown in Figure 4.3. More discussion will be carried out in Chapter 9.

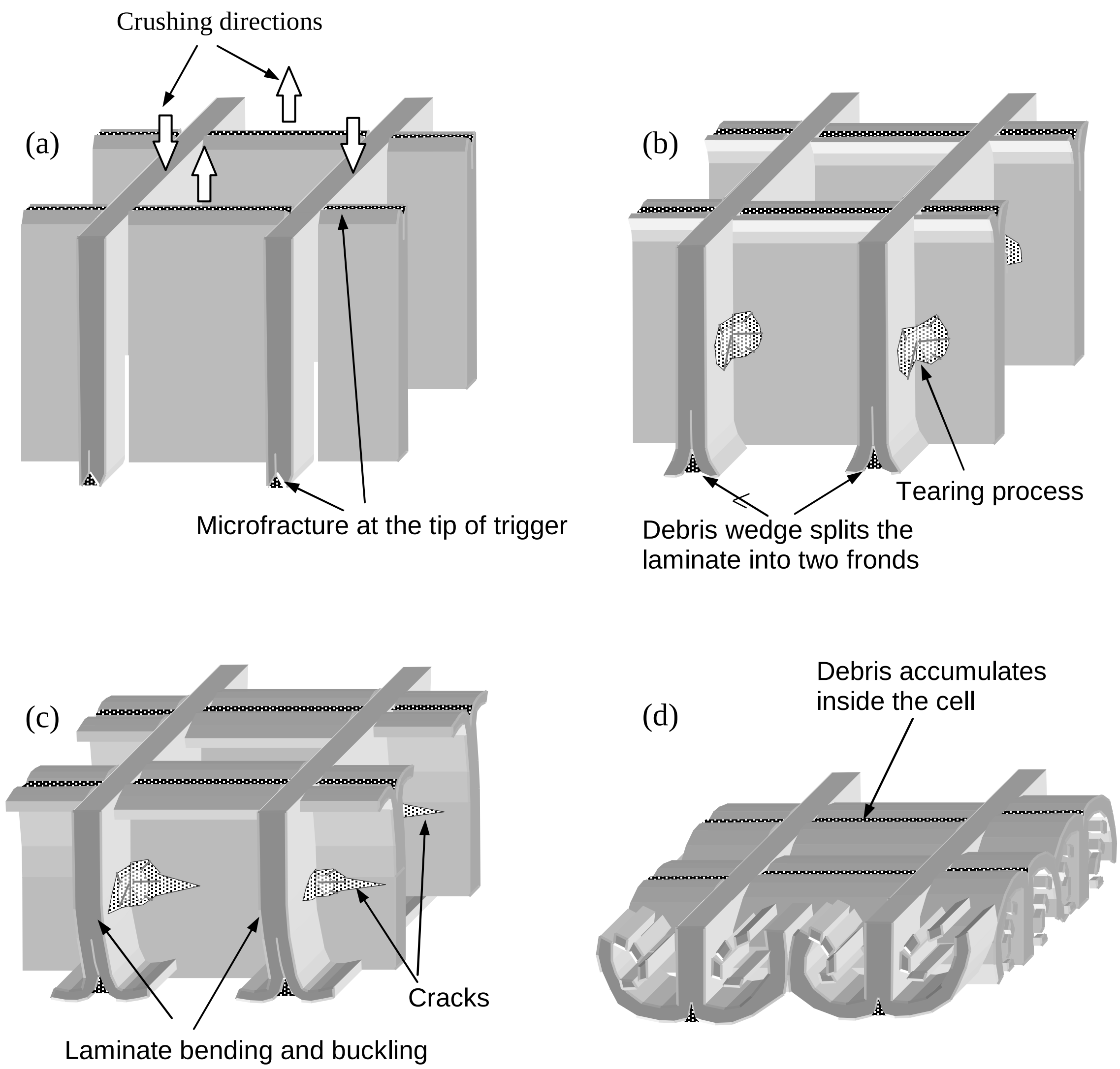

Figure 4.4 Schematic sketches of typical crushing process of intersecting square cell

4.1.4. Comparisons between intersecting square cells and plates

Because of cracks, large-scale delamination, bending and local buckling, the crushing of the intersecting square cell results in a very low SEA level. A comparison of photos between the crushed intersecting square cell (F1534_ISC) and the crushed plate specimen (F528, Ref [16]) can be found in Figure 4.5. Both specimens were made of polyester resin (Crystic®272 for F528) and the same fabrics with the same lay-up, $[\pm 45/(90,0)]_{2S}$.

It shows that the plate crushed more effectively than the intersecting specimens. This crushing mode involved a small radius of bending curvature and dense delaminations, accompanied by lots of fibre fractures and frictional loading in the fronds of plates. On the contrary, the intersecting specimen underwent unsymmetrical splaying without a clear central crack, also transverse cracks on the structure occurred after buckling.

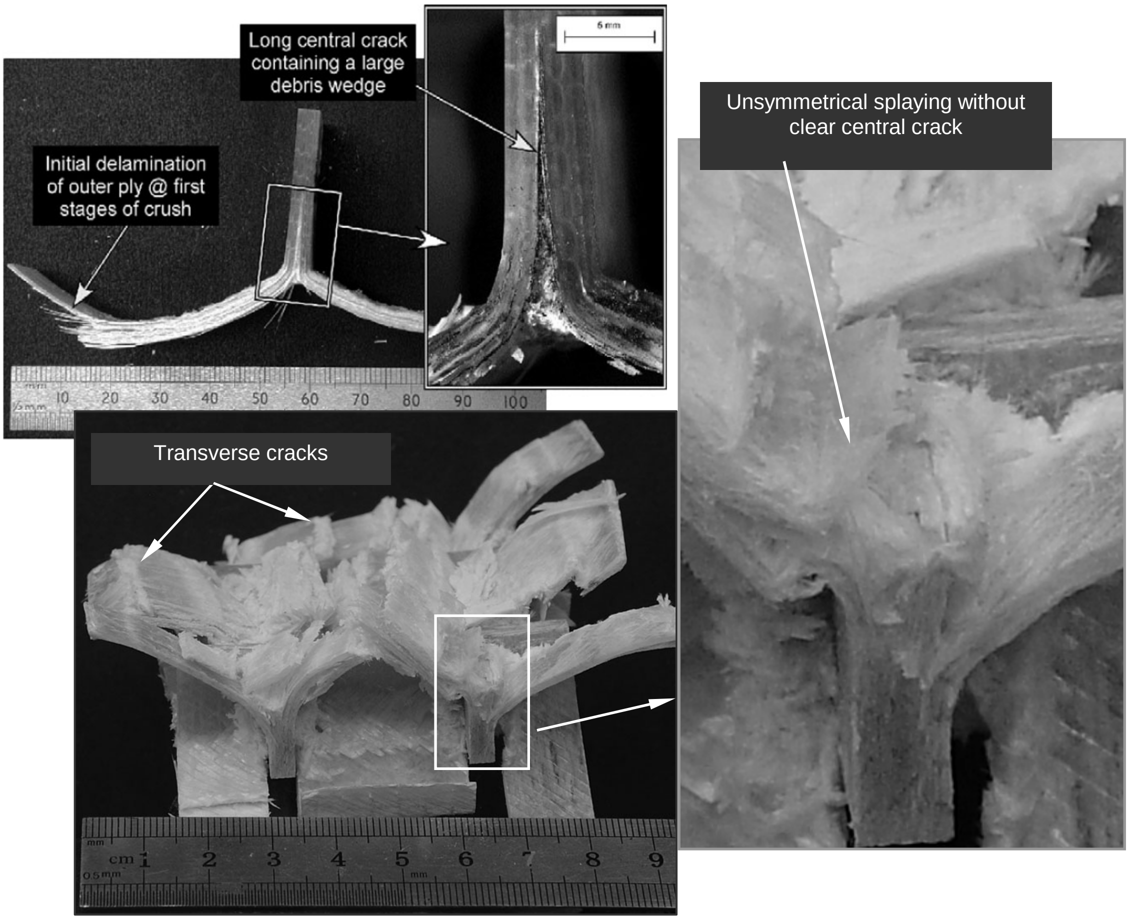

Figure 4.5 **Photographs of the sections of crushed [±45/(90,0)]$_{2S}$ laminates for plate (top-left, [16]) and intersecting square cell (bottom & right)**

These phenomena described above did not only occur in [±45/(90,0)]$_{2S}$ laminates, but also in all the other intersecting square cells and plates. Figure 4.6 clearly shows the difference of energy absorbing capabilities between intersecting square cells of this study and all tested data of plates obtained from reference [16]. Further comparison of this difference is presented in Figure 4.7, where the intersecting square cells are grouped according to the lay-up. The properties of composites plates which were used in following discussion and their crushing results are listed in Table 4.2.

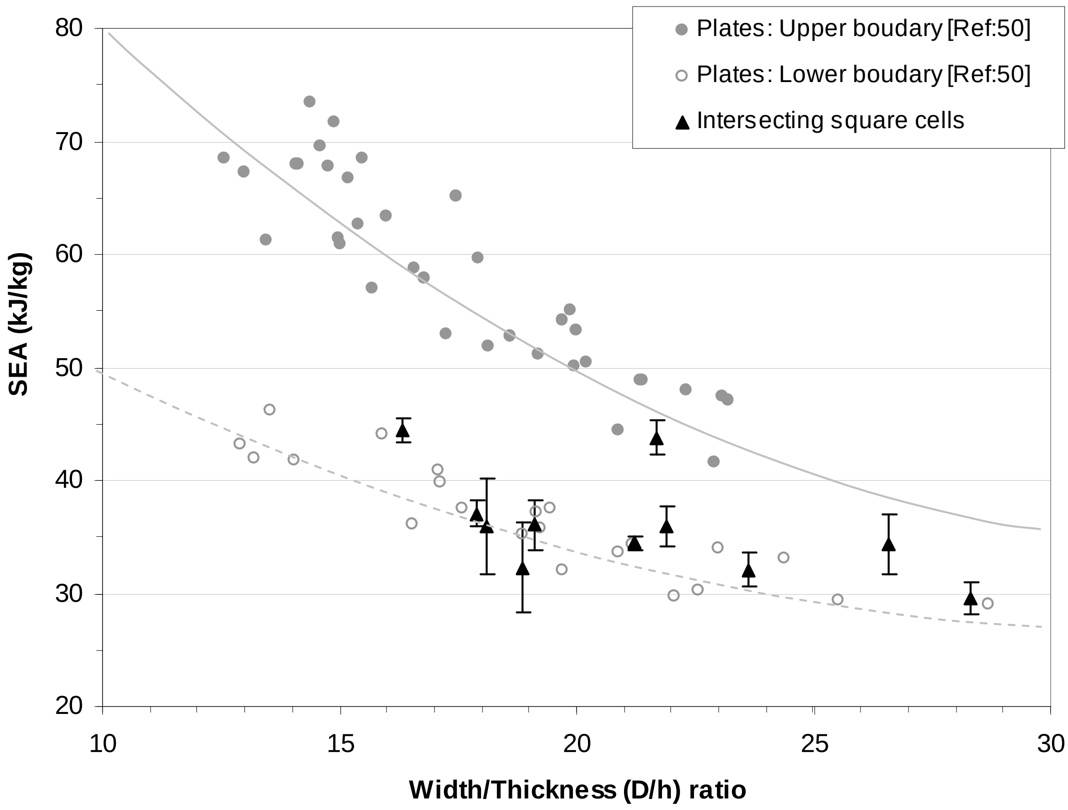

Figure 4.6 Comparison of intersecting square cells and simply-supported plates (For plates, D/h ratio = KES/h ratio, see Table 4.2.)

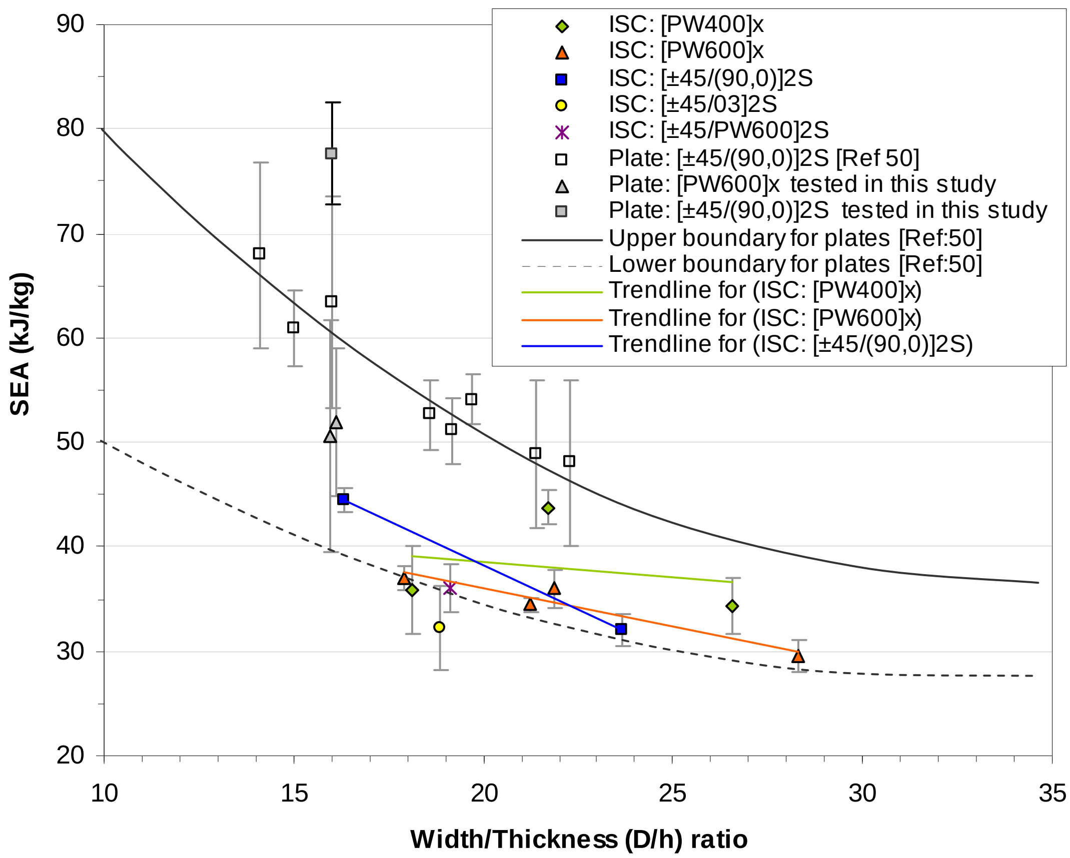

Figure 4.7 Comparison of intersecting square cells and simply-supported plates in further details (For plates, D/h ratio = KES/h ratio, see Table 4.2.)

Table 4.2 Properties of composite plates and their crushing results

Reference	Orientation	h (mm)	L (mm)	KES/h ratio	VF%	Crushing result	
						SEA (kJ/kg)	CV %
Data obtained from Ref [2, 16]							
F528_plate_a	$[\pm45/(90,0)]_{2S}$	4.09	80.0	16.01	45.4	63.35±10.16	16.03
F528_plate_b	$[\pm45/(90,0)]_{2S}$	4.08	80.0	18.59	45.4	52.68±3.34	6.35
F528_plate_c	$[\pm45/(90,0)]_{2S}$	4.06	80.0	21.35	45.4	48.85±7.11	14.56
F528_plate_d	$[\pm45/(90,0)]_{2S}$	4.22	80.0	22.34	45.4	48.03±7.89	16.42
F549_plate_a	$[\pm45/(90,0)]_{2S}$	4.55	80.0	14.12	45.0	67.93±8.90	13.11
F549_plate_b	$[\pm45/(90,0)]_{2S}$	4.46	80.0	19.19	45.0	51.14±3.63	7.10
F549_plate_c	$[\pm45/(90,0)]_{2S}$	4.28	80.0	15.04	45.0	60.87±3.16	5.19
F549_plate_d	$[\pm45/(90,0)]_{2S}$	4.33	80.0	19.71	45.0	54.10±2.36	4.37
Data obtained from this study							
F1533_plate	$[\pm45/(90,0)]_{2S}$	4.06	77.8	16.0	48.5	77.65±4.92	6.33
F1540_plate	$[PW600]_6$	2.61	79.1	16.1	53.9	51.93±7.05	13.58
F1541_plate	$[PW600]_8$	3.66	46.7	16.0	50.6	50.55±11.14	22.03

KES: Knife-edge separation. The crushing fixture for composite plates have the knife-edges that contact the specimen and offer simply-supported boundary condition;

L: Length. Sample F528 and F549 were cut into 80mm long, but their length was not measured;

h: Thickness; VF: Fibre volume fraction.

CV: Coefficient of variation = (standard deviation / SEA average value) x 100.

values behind the ± are standard deviations.

Figure 4.6 and Figure 4.7 show that the SEA levels of intersecting square cells are located in the lower boundary curve of the plates crushing results. In the same way as the composite plate, the SEA value of the intersecting square cell increases if the D/h ratio decreases. However, for the same material, the composite plate possesses approximately 40% higher SEA than the intersecting square cell.

Figure 4.8 presents the difference between intersecting square cell and composite plate on the curves of specific energy absorption against displacement. Compared with the flat plate, the intersecting square cells seem unable to reach the full energy absorbing potential. According to the above discussion, the possible explanation for the energy loss on intersecting square cell is that the large radius of bending curvature and buckling issue at fronds directly lower its crushing performance.

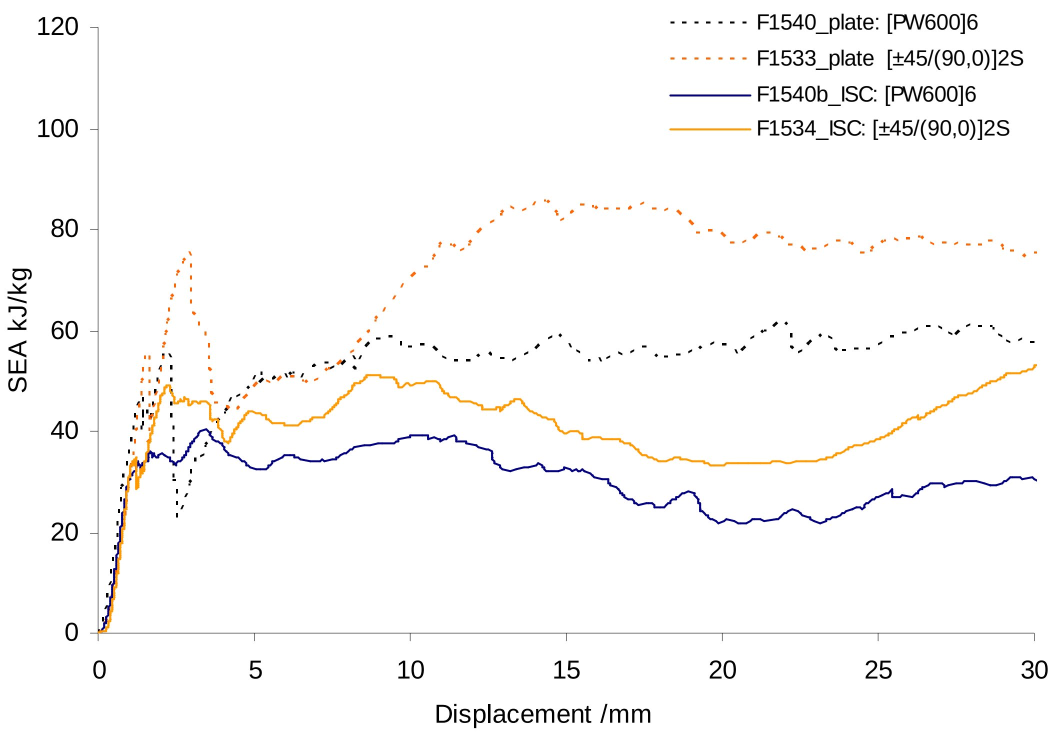

Figure 4.8 **Comparison of specific energy absorption vs. displacement curve between intersecting square cells and simply-supported plate for $[PW600]_6$ laminate**

The effect of radius of bending curvature at fronds is mainly dependent on the Mode-I interlaminar fracture toughness at the middle layers of laminate. Splaying fronds with large radius of bending curvature are normally caused by the rapid central crack inside the laminate. The effect of the Mode-I interlaminar fracture toughness has been investigated previously on composite plates in Cauchi-Savona and Hogg's work [24].

They found that that the SEA values of composite plates located on the upper boundary (see Figure 4.6) would normally generate small radius of bending curvature at fronds. And those located on the lower boundary would normally generate large radius of bending curvature at fronds. These bent fronds with small radius would maximise crushing performance of laminate through a number of failure mechanisms, which include delamination, fibre fracture, laminar splitting, as well as interlaminar friction. In order to improve the Mode-I interlaminar fracture toughness and reduce the propagation speed of the central crack, Cauchi-Savona and Hogg introduced through-thickness stitches in the composite plates.

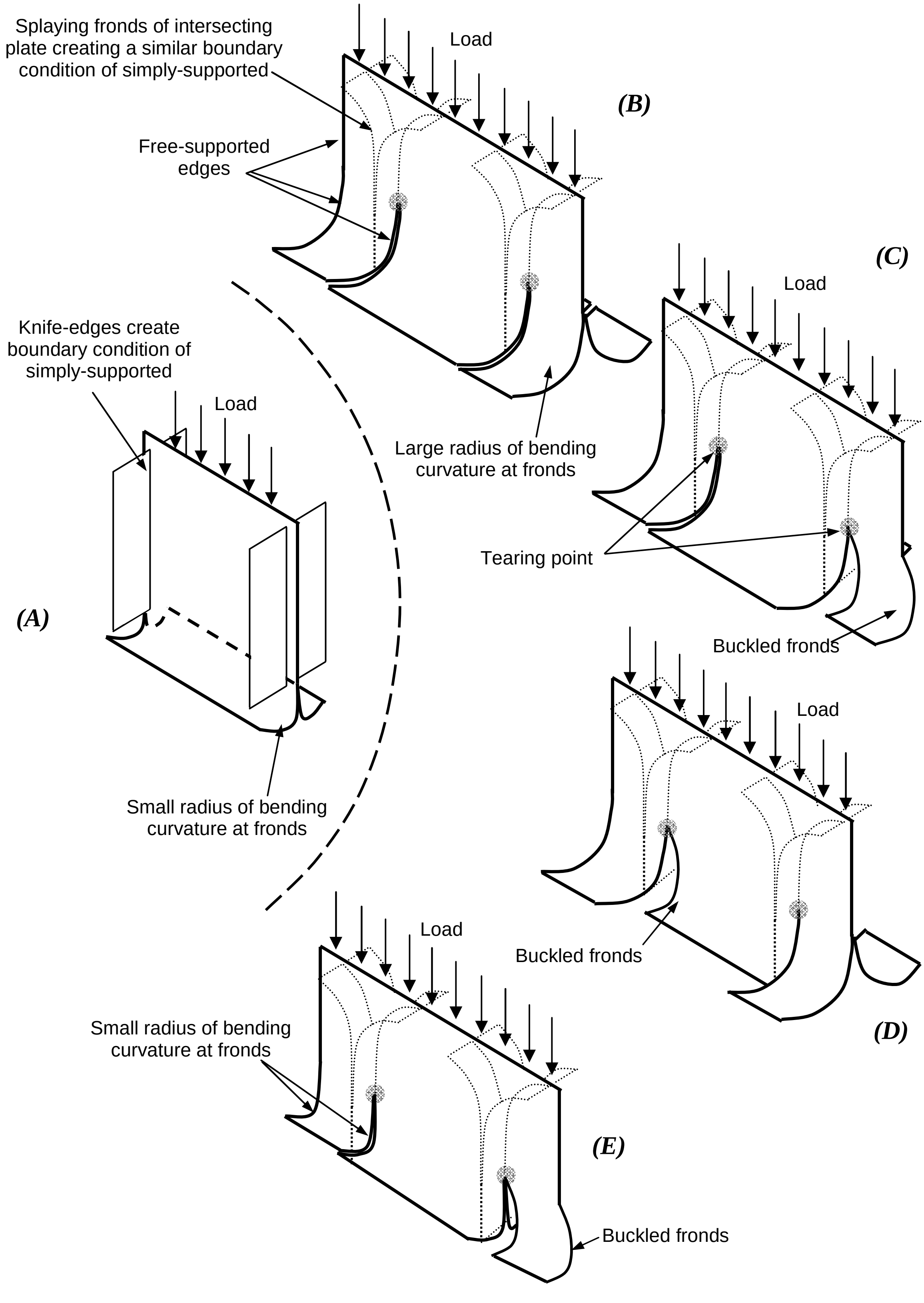

Figure 4.9 Schematic sketches of sample failure modes illustrating the difference between simply-supported composite plate and intersecting square cell.

However, even without the stitches, the Cauchi-Savona and Hogg's data presented in Figure 4.6 show that more than half of composites plates still crushed with small radius of bending curvature at the splaying fronds. This is attributed to the simply-supported boundary condition along the knife-edges (see Figure 4.9 A). The simply-supported boundary condition certainly constrains the fronds' opening.

In the intersecting cell, this constraint does not exist around the slotted areas. Instead, the boundary condition turns to freely-supported around these areas (Figure 4.9 B). If the plate is freely-supported, the laminate tends to crush with a large radius of bending curvature at the fronds. As a consequence, the effectiveness of all those failure mechanisms at splaying fronds can be significantly reduced. In many other cases, the intersecting square cells also experienced buckling and bending under compressive loads (Figure 4.9 C and D). It reveals that the energy absorption capability of composite structures is significantly related to the stability of structures.

Furthermore, it is also important to note that, in some intersecting square cells, the laminates also crushed with small radius of bending curvature at fronds (Figure 4.9 E). Sample $[PW400]_{10}$ (F1537_ISC) is a very typical example which exhibits an outstanding crushing performance which is about 43.8kJ/kg on SEA. This result is very close to the upper boundary of plate crushing data in Figure 4.7.

Because of the buckling issue however, the crushing results of some samples which crushed with a small radius of bending curvature, would still fall into the lower boundary in Figure 4.7. According to the experimental observation, the $[\pm45/PW600]_{2S}$ samples are more likely to fail by transverse cracks than $[PW400]_{10}$ samples.

Also the sample, the $[PW400]_{12}$ (F1538_ISC), behaved very unusually in this study. On average, it only achieved about 35.9kJ/kg on SEA with the D/h ratio of 18.1. Although $[PW400]_{12}$ only has extra two layers of woven fabric than $[PW400]_{10}$, according to the experimental observation, premature buckling was also the main cause for a reduction in crushing performance of the $[PW400]_{12}$ samples.

The photographs of crushed sample, $[PW400]_{10}$, $[\pm45/PW600]_{2S}$ and $[PW400]_{12}$ are shown in Figure 4.10. In order to improve the structural stability and avoid the buckling on crushing structures, it is necessary to evaluate the critical buckling load on each structure.

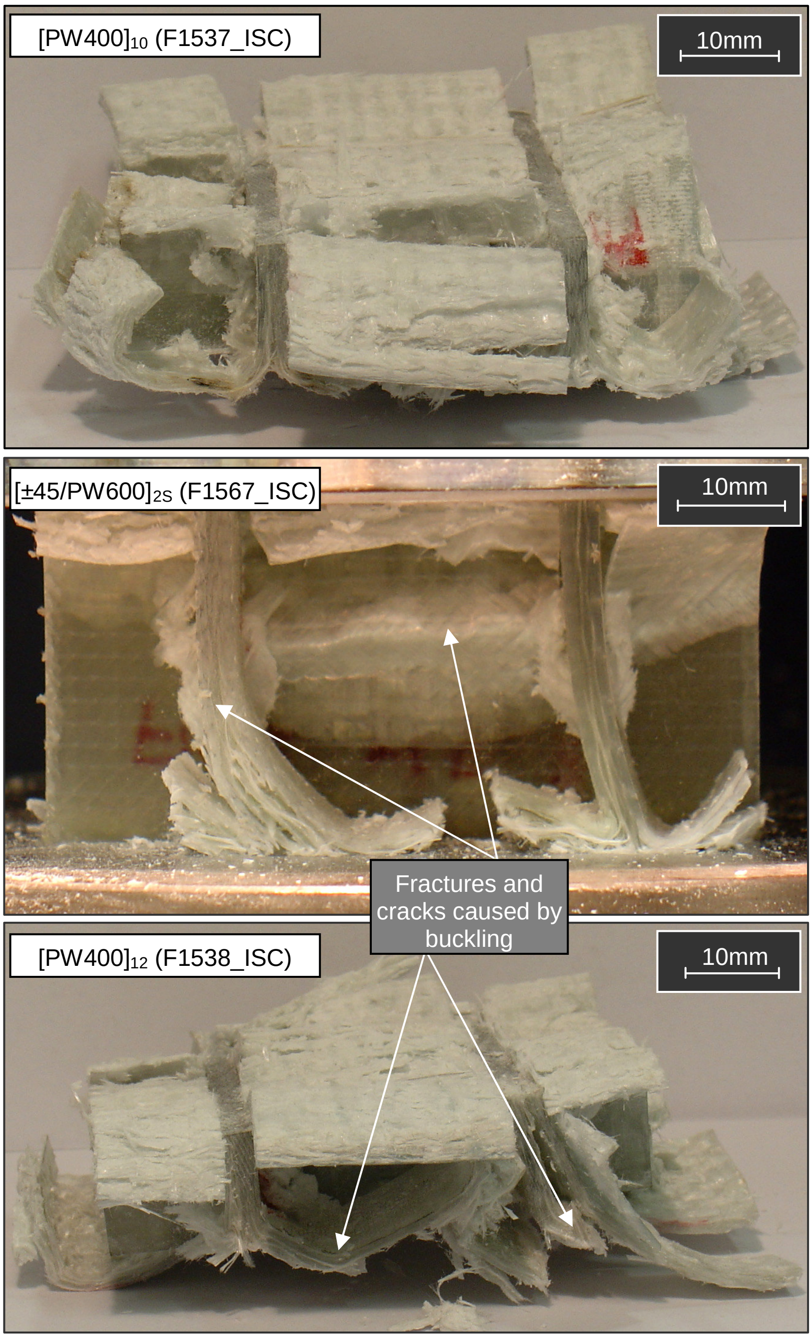

Figure 4.10 Photographs of crushed samples: [±45/PW600]$_{2S}$ (top) and [PW400]$_{12}$ (bottom)

4.2. Critical buckling analysis

It has been discussed in the literature that structural instability and buckling issues would divert the crushing into an unexpected failure mode, and consequently reduce the energy absorption capability of the structure. The main reason that causes the structural instability and buckling on intersecting square cells is the freely-supported boundary condition within this structure. To avoid freely-supported boundaries, the assembly mode of the geometric cell needs to be improved.

4.2.1. Buckling of isotropic plate

The actual stability of the structures can be typically determined by buckling theory performed either manually or via a finite element technique [22]. Therefore, this section introduces the analysis of critical buckling stress basing on classical equations. The finite element modelling will be performed in the next section for composite laminates with different geometries.

The prediction of critical buckling load (or stress) for isotropic materials has been systematically investigated in many references [10, 104, 105]. The buckling properties of isotropic plates that are simply-supported at four edges can be expressed as [104]:

$$\sigma_{cr} = k_c \frac{\pi^2 E}{12(1-\nu^2)}\left(\frac{h}{b}\right)^2 \tag{4.1}$$

where σ_{cr} = critical buckling stress,

E = compressive modulus of the isotropic material,

h = thickness of plate,

b = width of plate,

ν = Poisson's ratio

k_c is the compressive buckling coefficient that is a function of edge boundary conditions. Theoretically, k_c is determined by the number of half-waves (m) in the buckling mode and the ratio of length of plate (a) to width of plate (b), which is expressed as:

$$k_c = \left[\left(\frac{a}{mb}\right) + \left(\frac{mb}{a}\right)\right]^2 \tag{4.2}$$

As mentioned before, the critical buckling load is heavily affected by boundary conditions and structural geometry. Figure 4.11 shows the relationship between k_c, boundary condition and length/width ratio in the buckling plate. Taking simply-supported plate, C, as an example, the k_c value increases dramatically when the a/b ratio decreases from 1 to 0.

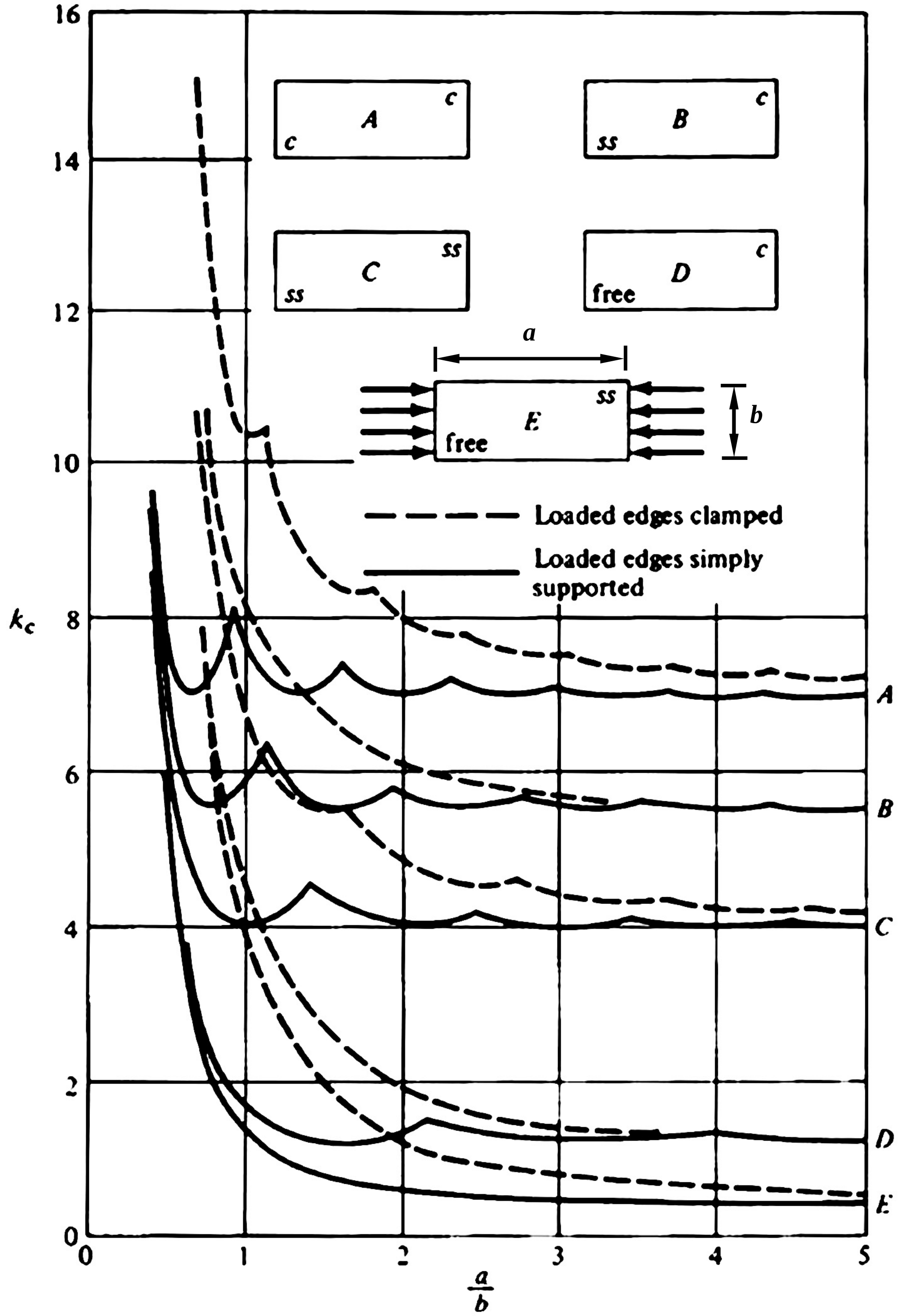

Figure 4.11 Influence of boundary conditions and a/b ratio on the buckling coefficients of isotropic plates subjected to in-plane compressive loading [10]

4.2.2. Buckling of anisotropic plate: Theory and Abaqus FEMs

Buckling analysis for anisotropic composite materials is much more complicated. However, Vince and Chou [9] developed a set of equations for the predicting the critical buckling load of orthotropic (crossply) plate under different boundary conditions. These equations are basing on classical laminate theory and the theorem of minimum potential energy (see Appendix 1). Except the Abaqus 6.6, a commercial software, EASComp version 2.1, was also applied as an assistant tool to analyse the elastic property of composites

The results of critical buckling analysis using classical theory were plotted in Figure 4.12 where it shows the relationship between critical buckling load and a/b ratio for crossply laminates with simply-supported boundary conditions. The critical buckling load per unit width calculated via ABAQUS FEMs is also compared in this figure. An embedded buckling analysis procedure in Abaqus (eigenvalue buckling analysis) was used.

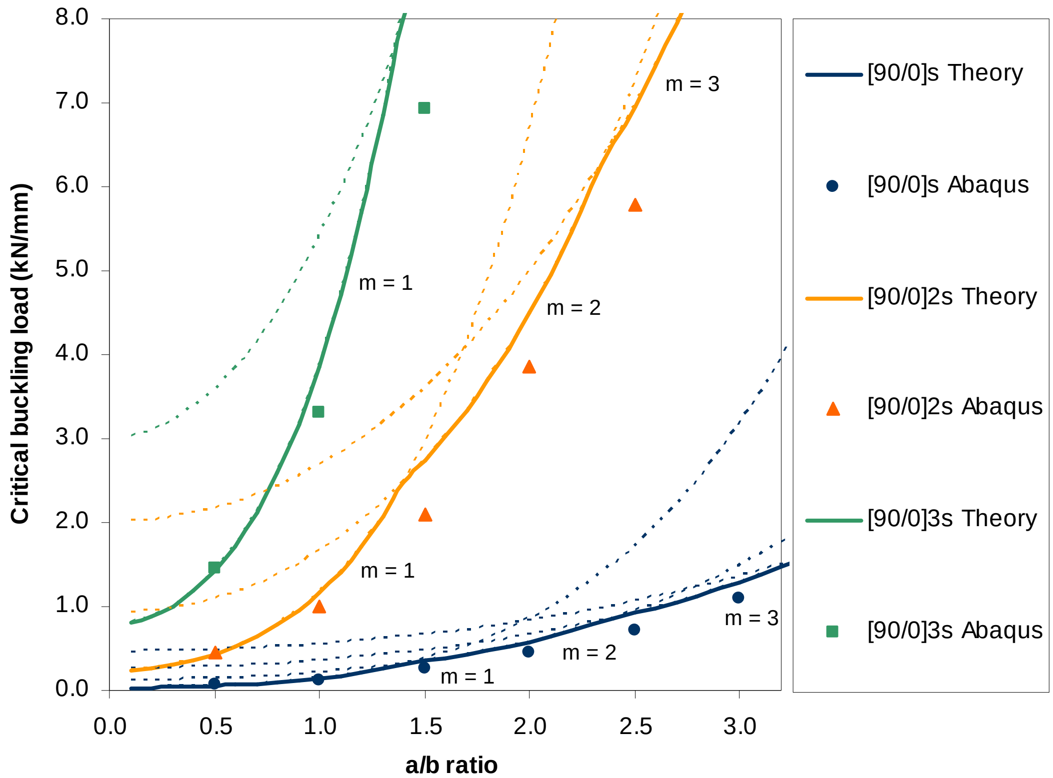

Figure 4.12 Classical theory and ABAQUS simulations for simply-supported plate with lay-ups of $[90/0]_{3S}$, $[90/0]_{2S}$, and $[90/0]_{S}$, where m is the number of half-waves.

In Abaqus, the critical buckling load is obtained by performing an eigenvalue buckling analysis. The buckling load estimate is obtained as a multiplier of the pattern of perturbation loads, which are added to a set of reference (or base state) loads.

The eigenvalue buckling analysis is a linear perturbation procedure, and is generally used to estimate the critical (or bifurcation) load of a stiff structure [100]. In the finite-element analysis, a system of nonlinear algebraic equations results in the incremental form:

$$[C_{tg}]\ d\{u\} = d\{p\} \tag{4.3}$$

where $[C_{tg}]$ = the tangent stiffness matrix,

$d\{u\}$ = the incremental nodal displacement vector,

$d\{p\}$ = the incremental nodal force vector.

When the structural is small and only behaviour within the elastic range, the nonlinear theory leads to the same critical load as the linear theory. Accordingly, if only the buckling load is to be determined, the calculation can be greatly simplified by assuming the deformation to be small. The nonlinear terms which are functions of nodal displacements in the tangent stiffness matrix can also be neglected. The linearized formulation then gives rise to a tangent stiffness matrix in the following expression [98]:

$$[C_{tg}] = [C_L] + [C_\sigma] \tag{4.4}$$

where $[C_L]$ = the linear stiffness matrix, and $[C_\sigma]$ = the stress stiffness matrix.

Assume $[C_\sigma]_{\mathrm{ref}}$ is the stiffness matrix corresponding to a reference load $\{p\}_{ref}$, the load level $\{p\}$ at current state can be obtain by applying a load multiplier, λ:

$$\{p\} = \lambda\{p\}_{ref} \tag{4.5}$$

Also we get, $$[C_\sigma] = \lambda[C_\sigma]_{ref} \tag{4.6}$$

If buckling occurs while the external loads are constant, i.e., $d\{p\}$=0, then the bifurcation solution for the linearized buckling problem can be determined from the following eigenvalue equation [100]:

$$([C_L] + \lambda_{cr}[C_\sigma]_{ref})\ d\{u\} = 0 \tag{4.7}$$

where λ_{cr} is the eigenvalue, and $d\{u\}$ is the eigenvector.

The eigenvector that defines the buckling mode shapes. Eventually, the critical load $\{p\}_{cr}$ can be obtained from equation:

$$\{p\}_{cr} = \lambda_{cr}\{p\}_{ref}. \tag{4.8}$$

In Figure 4.12, it shows results from ABAQUS FEMs are 15%-20% lower than the results calculated by classical theory. It is also important to note in the figure above that the critical buckling load is influenced by thickness of laminate.

4.2.3. Comparison of critical buckling of plates with tubes and ISCs

To understand the influence of buckling mechanisms on energy absorption capability, it is necessary to evaluate and compare the critical buckling stress between intersecting plate and simply-supported plate. Thus, ABAQUS FEMs were used as a technological tool for this purpose.

Three different geometries were modelled, they are: i) simply-supported plate that represents the plates tested by Cauchi-Savona and Hogg [16]; ii) intersecting plate (one plate out of four-plate intersecting square cell) that is investigated in this study; and iii) square tube that has same width as simply-supported plate. Three-dimensional ½ symmetry shell models were applied to former two geometries, respectively. Three-dimensional ¼ symmetry shell models were applied to the square tube (Figure 4.13).

Both top and bottom edges of all geometries were either simply-supported or freely-supported. However axial motion on the bottom edge that was constrained (degree of freedom 3 = 0). Herein, the degrees of freedom which are described by numbers, 1, 2 and 3, refer to the axial motion along the direction of x, y and z (see Figure 4.13), respectively. And the degrees of freedom which are described by numbers, 4, 5 and 6, refer to the rotational motion around the axes of x, y and z, respectively.

Boundary conditions for vertical edges of above models are varied: i) for the simply-supported plate, the left vertical edge is simply-supported (degree of freedom 1,2,4,5 = 0), while the right vertical edge is modelled as symmetry plane (degree of freedom 1,5,6 = 0); ii) for the intersecting plate, the right vertical edge is also modelled as symmetry plane. Moreover, the out-of-plane motion of the area (accurately a line) between the slot end and top edge was constrained (degree of freedom 2,4 = 0); iii) for the tube, both two vertical edges are modelled as symmetry plane (degree of freedom 1,5,6 = 0 and 2,4,6=0, respectively). These boundary conditions also can be found in Figure 4.13.

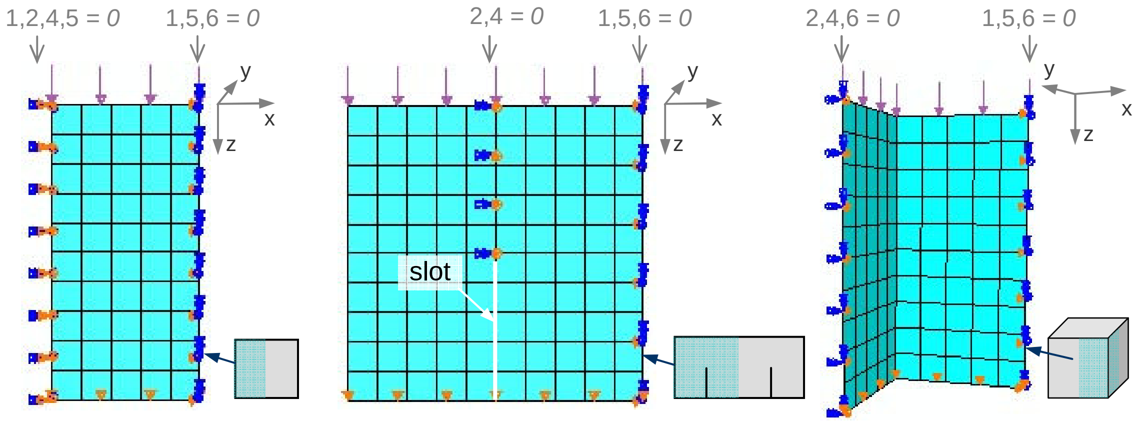

Figure 4.13 Boundary conditions (vertical edges) and loading conditions on different Geometric FEMs

The buckling characteristics of composites are dominated by the structural boundary conditions and geometric shapes as well as the dimensions. In order to simplify the simulation process and only concentrate on comparing the influences from geometry themselves, the length (a) for all structures was fixed to 50mm, and the lay-up was focused only on $[90/0]_{2S}$ that fixed their thicknesses to 3.04mm.

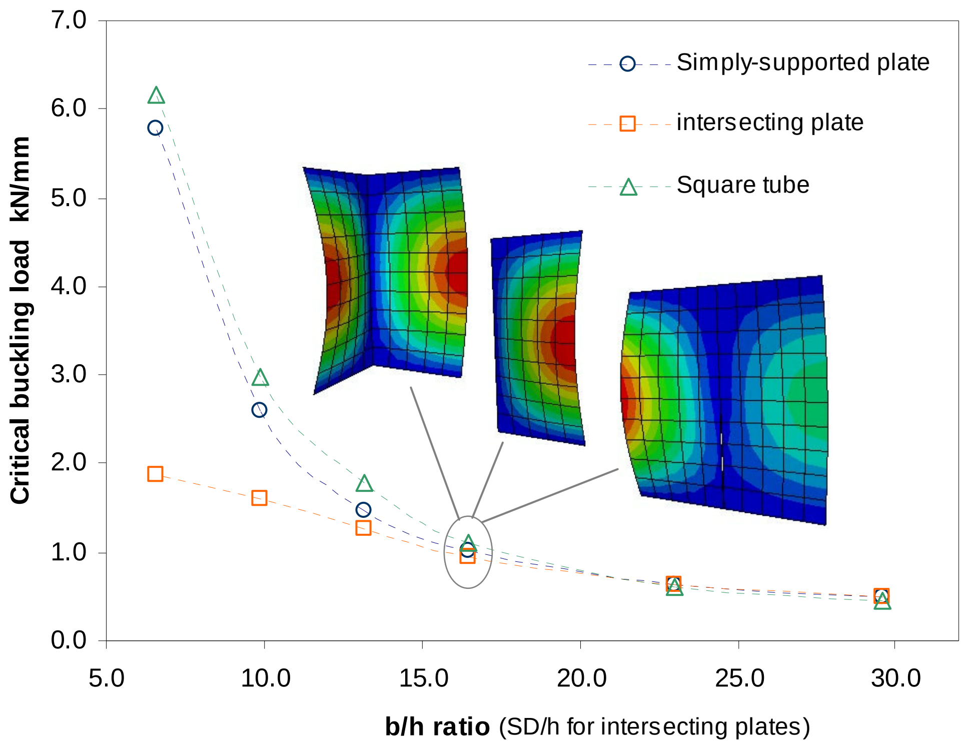

Figure 4.14 Buckling analysis of intersecting plate, simply-supported plate, and square tube: top and bottom boundaries are simply-supported

The width of plate was varied to control the width/thickness (*b/h*) ratio. During this step, the separation width (*SD*) was considered as the practical supporting width for intersecting plates. The modelling results of the critical buckling load per unit width are shown in Figure 4.14. It is important to note that FE models mentioned were simply-supported along the top and bottom edges.

It also reveals that the simply-supported plates behave more stably than the intersecting square cells under compression. And the difference of stability between these two structures is enlarged significantly along with decreases in the *b/h* (or *SD/h*) ratio. It is interesting to note that the square tube and the simply-supported plate, which have the same width, possessed a very similar value of critical buckling load per unit width. In other words, the walls of square tube can be approximately considered as simply-supported plates. Therefore, the transition geometries need to be modified by avoiding freely-supported edges. The corrugating structure could be a good option.

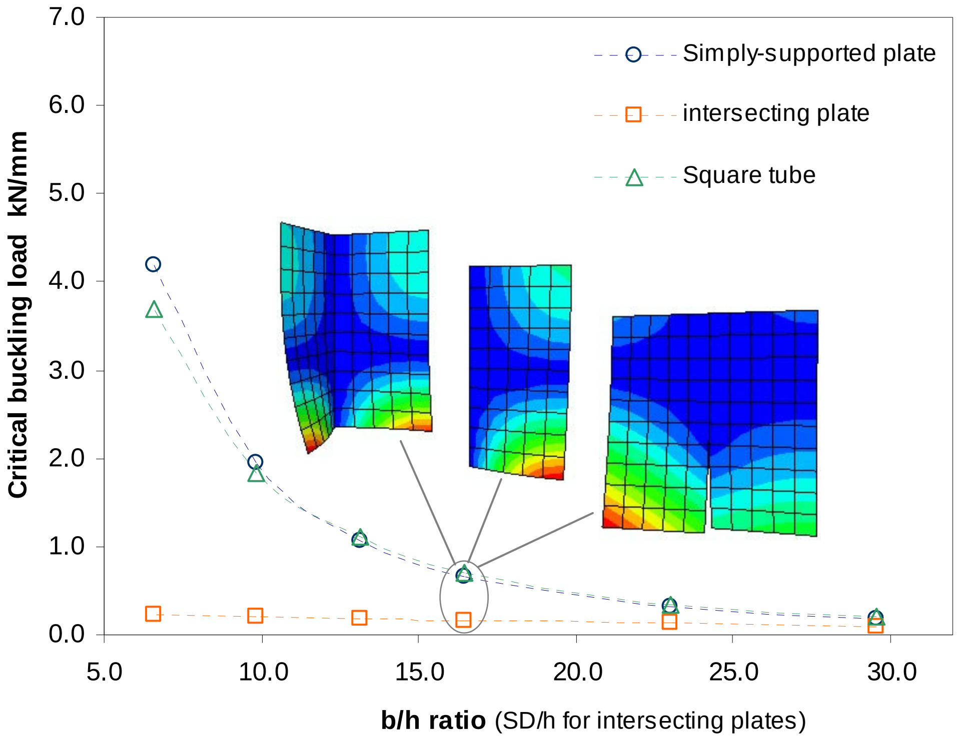

Figure 4.15 Buckling analysis of intersecting plate, simply-supported plate, and square tube: top and bottom boundaries are freely-supported

The von Mises stress distribution presented in Figure 4.14 shows the centre of those structures is most likely place to start buckling. However, according to the observation of crushing tests, the intersecting square cells tend to buckle at the bottom edge. If the freely-supported boundary conditions were applied along the top and bottom edges, the Mises stress distribution shown in Figure 4.15 for the buckled structures is more closed to the real situation. In this situation, the critical buckling load of intersecting square cells was significantly reduced. Compared with Figure 4.14, Figure 4.15 exhibits that the difference of critical buckling load between intersecting square cell and simply-supported plate is more sensitive to the *b/h* (or *SD/h*) ratio.

4.3. Effects of critical buckling stress on crushing performance

It is also interesting to note that, the critical buckling stresses of the intersecting square cells are generally lower than sustained crushing stresses (SCS or σ_s in equation 2.4) and initial peak crushing stresses (see Figure 4.16). Herein, the initial peak crushing stress is defined as the maximum stress that the crushing sample achieved before the sample entered the sustained crushing stage. In Figure 4.16, only $[90/0]_{2S}$ laminates were used for calculation. The thickness of laminates was fixed to 3.04mm, while the width of these structures was varied to control the *d/h* ratio.

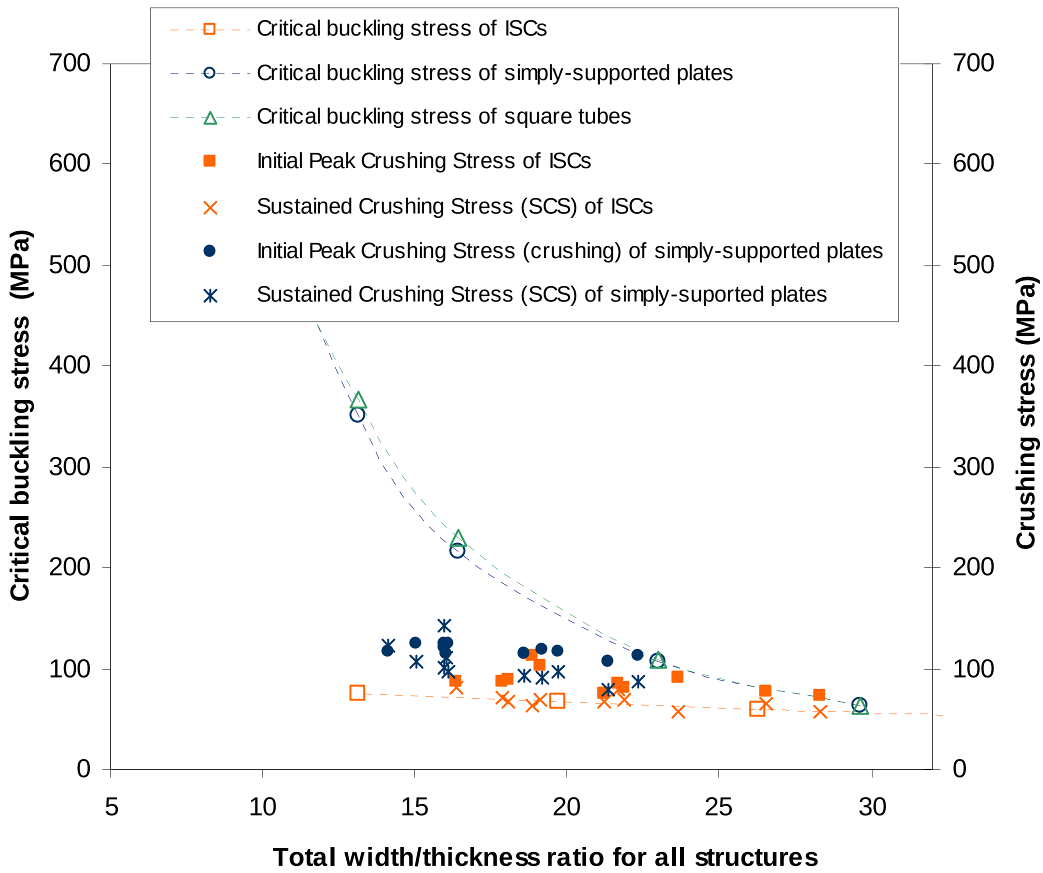

Figure 4.16 Relationship between critical buckling stress and crushing stress.

As a contrast, the critical buckling stresses of simply-supported plates and square tubes are generally higher than their sustained crushing stresses and initial peak crushing stresses. This result reveals that the intersecting square cells buckle more easily than plates or square tubes during crushing.

4.3.1. Buckling issues in composite plates during crushing

For the composite plates, two situations could happen during crushing. One is that after being triggered, the accumulated debris wedge splits the laminate into two fronds. Then the splaying fronds enlarge the supporting area on the platen. Consequently, the critical buckling stress of the plate is increased and plate will continue crushing instead of buckling. The other situation is that after being triggered, the critical stress of splitting the laminate is too high to be overcome by the debris wedge. Then the critical buckling stress is achieved before the plate could be promoted to a more stable crushing stage with laminar bending. Furthermore, because of the constraints generated by knife-edges, the composite plate starts to break and buckle as well as squash (see examples of composite plates shown in Figure 4.17, Ref [2]).

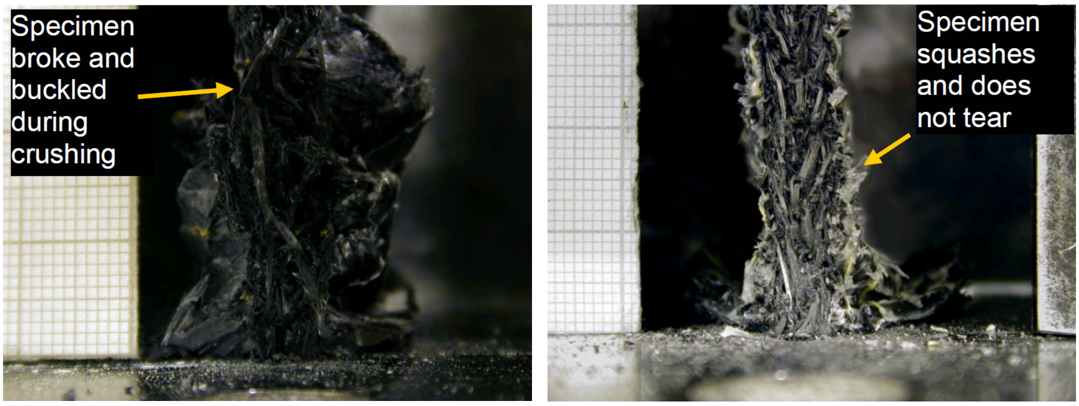

Figure 4.17 Photographs of crushed composites plates having a $[\pm45/0]_{2S}$ orientation and stitched by Kevlar® yarns in a transverse orientation [2]

4.3.2. Buckling issues in intersecting square cells during crushing

Different from the simply-supported plate, after being triggered the plates in an intersecting square cell easily reach their critical buckling stress at a relatively low crushing stress level. However, the intersecting plates do not tend to buckle straightway because the intersecting plates need to tear up each other at the contacting point (or tearing point, see Figure 4.9). Meanwhile, the triggered plate is also constrained by the opposite plates (drawn as the dashed lines in Figure 4.9) which offer a simply-supported boundary condition on the non-slotted areas. Within this particular constrained area, because the width/thickness ratio is approximately equal to 1, the critical buckling stress becomes extremely high. Therefore, the initial peak crushing stresses of the intersecting square cells are generally higher than the predicted critical buckling stress.

Once torn up some of the intersecting plates start to buckle and fold under the compressive load. Photos of the typical buckled fronds are shown in Figure 4.18. Therefore, the sustained crushing stress of the intersecting square cell closes to the critical buckling stress in general, but it is lower than the initial peak crushing stress.

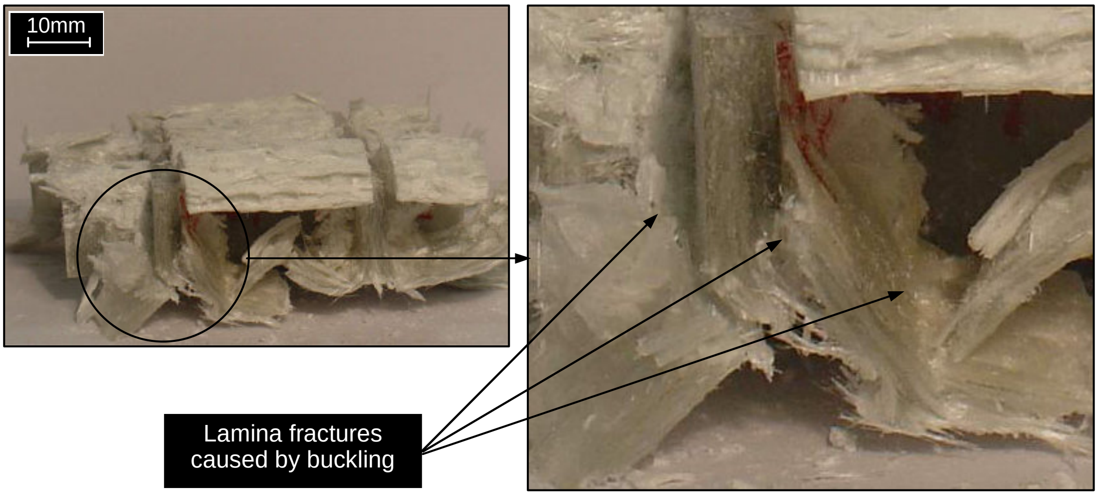

Figure 4.18 Photographs of crushed [PW600]$_8$ sample (F1541a_ISC)

4.4. Summary

Work done at this stage has shown that the energy absorption capability of intersecting square cell is dominated by its freely-supported boundary condition. The results from crushing tests show that intersecting square cells exhibited a lower SEA level compared with simply-supported plates. This reduction is witnessed by the photos of crushed samples. The deformation process generates large radius of bending curvature on fronds and an inconspicuous central crack accompanied by global buckling. In particular, the unstable global buckling can produce a negligible amount of energy absorption.

The analysis of the results of critical buckling loads revealed the structural stability was controlled by geometries and boundary conditions. The intersecting square cells exhibited lower stability than simply-supported plates or square tubes. This difference in stability between intersecting square cell and simply-supported plate increased along with the decrease of their width/thickness ratio. On the other hand, both intersecting square cell and simply-supported plate possess similar energy absorbing levels when their width/thickness ratios exceed 25.

To avoid freely-supported boundaries in structure, a good idea is to introduce the tubular cells or simply-supported plates directly into the structure, because both tube and plate have been intensively investigated and fully understood in the energy absorbing research field. Corrugated geometries for example, sine wave, also can be good options that increase the stability of structures. Although a similar attempt of combining tubes and plates in a continuous composite structure has been performed on crash-energy absorbing helicopter subfloor beams by Farley [48], the transition of different geometries, effect of fibre architecture, and dimensional relationship had not yet been investigated in depth before this work.

Chapter 5. Geometric Cells

The intersecting square cell would demonstrate the energy absorption capacity of a panel arrangement if they could crush without fracture buckling. In order to increase the stability of transition structures during crushing, three composite structures with different shapes but similar perimeters were created. They consist of plate and tubular cell elements and represent a unit cell of the composite core within the presumed large composite panel. This chapter is focused on the crushing response of these modified cells.

5.1. Specimens

Each specimen consists of two symmetrical parts, glued together on flat sides by using a Hysol adhesive that was mentioned in Table 3.2. Very small amounts of glass beads, diameter of 0.25mm, were added in to the Hysol adhesive in order to control the thickness of the adhesive layer. Each symmetrical half consists of a central corrugated part and two flat plates on both sides. The structural density can hence be controlled by the dimensional ratio of corrugated part to flat plate.

5.1.1. Geometric characteristics

The cross-sectional areas of these geometric cells are sketched in Figure 5.1. According to the conclusion of last chapter, it seems that the square tube may represent simply-supported plates in a structure. Hence, the first transition geometry was designed as a square cell with rounded corner of 5mm in radius which connects to the plate part (Figure 5.1a). The purpose of using round corner was to disperse stress under compressive loading, because the stress can be easily concentrated onto sharp corners that would potentially trigger an unstable crushing. This structure is named ‘S-cell’ for short in the rest of this thesis.

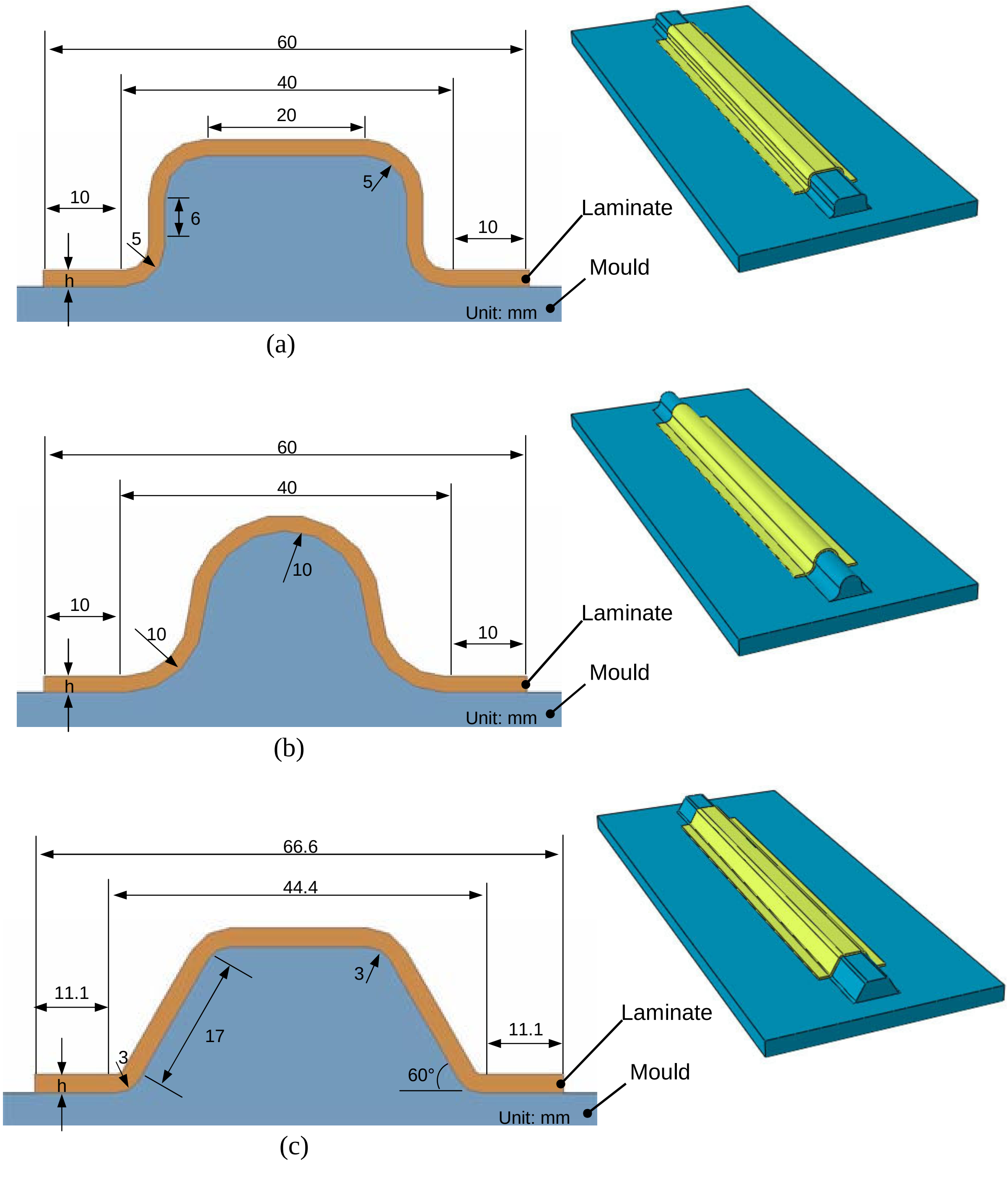

Geometry of core part	a) S-cell	b) C-cell	c) H-cell
Perimeter excluding flat sides	62.8mm	62.4mm	63.6mm

Figure 5.1 Geometric dimensions of the cross-sectional area (half) for three transition geometries: a) rectangular; b) circular; C) hexagonal

According to the observations that composite tubes possessing larger corner radii exhibit greater crushing capability [11], the second transition geometry was designed as a combination of sine wave and circular tube (Figure 5.1b). Its 10mm radius is set to produce a perimeter close in size to the S-cell. Hexagonal honeycombs are the most commonly used cores in composite sandwiches due to their geometric efficiency. Under flat-wise compressive loading honeycomb cores normally crush by local buckling. Thus the third transition geometry is designed to provide a hexagonal shape (Figure 5.1c). These two structures are named ‘C-cell’ and ‘H-cell’ for short, respectively.

5.1.2. Materials and laminate properties

Polyester resin was selected for the transition shape samples, the same matrix system as the intersecting square cells. Two NCFs (UD DV060 and ±45 FGE104 ST) and woven fabric (plain-woven GWR400P) with areal density of 400g/m^2 (see Table 3.1) were used at this stage. Many types of fibre architectures of tubes and plates have already been studied to assess the energy absorption under crushing conditions. This section is focused on the crushing response of transition geometries which combine a number of elements, and the effects of differences in fibre architectures in these geometries are also considered.

Table 5.1 Laminate properties of S-cell

Reference	Orientation	Cured Thickness h (mm)	Width D (mm)	Perimeter P (mm)	VF%
F1640_S	[90/0/90]	1.21±0.021	60.18±0.18	83.60±0.18	47.3
F1643_S	[0/90/0]	1.18±0.050	59.92±0.11	83.33±0.11	47.8
F1646_S	$[90/0]_S$	1.54±0.070	60.04±0.09	83.45±0.09	50.6
F1617_S	$[90/0_2]_S$	2.21±0.018	60.04±0.15	83.45±0.13	49.3
F1649_S	$[90/0]_{2S}$	2.90±0.041	59.95±0.14	83.36±0.14	51.1
F1653_S	[±45/0/±45]	1.28±0.033	59.73±0.13	83.15±0.13	50.5
F1656_S	$[\pm45/0]_S$	1.56±0.009	59.85±0.11	83.27±0.11	52.1
F1620_S	$[\pm45/0_2]_S$	2.33±0.014	60.26±0.13	83.67±0.13	50.3
F1659_S	$[\pm45/0_3]_S$	2.87±0.025	60.06±0.44	83.48±0.44	53.6
F1623_S	$[90/\pm45/0]_S$	2.40±0.019	60.23±0.08	83.64±0.08	49.5
F1662_S	$[90/\pm45/0_2]_S$	3.18±0.130	59.67±0.20	83.08±0.20	48.2
F1665_S	$[PW400/0]_S$	1.29±0.036	59.88±0.06	83.30±0.06	50.3

values behind the ± are standard deviations; VF: Fibre volume fraction

Table 5.2 Laminate properties of C-cell

Reference	Orientation	Cured Thickness h (mm)	Width D (mm)	Perimeter P (mm)	VF%
F1639_C	[90/0/90]	1.22±0.023	60.16±0.08	82.99±0.08	47.3
F1642_C	[0/90/0]	1.25±0.027	60.08±0.10	82.91±0.10	46.2
F1645_C	$[90/0]_S$	1.58±0.047	60.09±0.22	82.92±0.22	48.8
F1616_C	$[90/0_2]_S$	2.30±0.047	60.09±0.19	82.92±0.19	51.4
F1648_C	$[90/0]_{2S}$	2.98±0.078	59.98±0.11	82.81±0.11	51.1
F1652_C	[±45/0/±45]	1.28±0.033	59.92±0.04	82.76±0.04	51.6
F1655_C	$[\pm45/0]_S$	1.60±0.021	59.86±0.09	82.69±0.09	53.0
F1619_C	$[\pm45/0_2]_S$	2.36±0.028	60.07±0.07	82.90±0.07	52.8
F1658_C	$[\pm45/0_3]_S$	2.98±0.037	59.57±0.19	82.40±0.19	54.4
F1622_C	$[90/\pm45/0]_S$	2.44±0.032	60.20±0.16	83.04±0.16	50.6
F1661_C	$[90/\pm45/0_2]_S$	3.23±0.222	59.84±0.14	82.67±0.14	48.6
F1664_C	$[PW400/0]_S$	1.32±0.051	59.74±0.22	82.57±0.22	47.9

values behind the ± are standard deviations; VF: Fibre volume fraction

Table 5.3 Laminate properties of H-cell

Reference	Orientation	Cured Thickness h (mm)	Width D (mm)	Perimeter P (mm)	VF%
F1641_H	[90/0/90]	1.29±0.028	65.72±0.47	84.90±0.47	45.2
F1644_H	[0/90/0]	1.22±0.057	66.14±0.11	85.31±0.11	47.3
F1647_H	$[90/0]_S$	1.63±0.100	66.01±0.28	85.19±0.28	47.1
F1618_H	$[90/0_2]_S$	2.27±0.024	66.11±0.03	85.29±0.03	49.9
F1650_H	$[90/0]_{2S}$	2.97±0.063	65.85±0.47	85.03±0.47	50.4
F1654_H	[±45/0/±45]	1.29±0.014	65.72±0.20	84.90±0.20	49.4
F1657_H	$[\pm45/0]_S$	1.59±0.009	65.80±0.19	84.97±0.19	53.6
F1621_H	$[\pm45/0_2]_S$	2.42±0.009	66.36±0.45	85.53±0.45	50.9
F1660_H	$[\pm45/0_3]_S$	2.99±0.050	65.82±0.14	85.00±0.14	53.1
F1624_H	$[90/\pm45/0]_S$	2.44±0.011	66.08±0.20	85.26±0.20	49.8
F1663_H	$[90/\pm45/0_2]_S$	3.22±0.106	65.66±0.13	84.84±0.13	48.0
F1666_H	$[PW400/0]_S$	1.31±0.010	65.80±0.12	84.98±0.12	50.3

values behind the ± are standard deviations; VF: Fibre volume fraction

Twelve different types of lay-ups including biaxial, triaxial and quadriaxial orientations, were generated for different transition geometries by varying the ply number of fabrics and fibre orientations. Those laminate properties of different cells are shown in Table 5.1 - Table 5.3, respectively.

For the nomenclature of specimens, _S, _C, and _H represent square, circular and hexagonal cross-sectional geometries, respectively. The perimeter (P) presented in tables above is the total length of cross section of a half geometric cell including the flat side.

At this stage, an embedded trigger consisting of 90° UD fibres was chosen as the trigger type. It is manufactured from shortening of the central unidirectional layers by 5mm and filling the space with 90° lateral fibres. This trigger does not need the post-machining after infusion, which reduces the processing time. Flat trigger fronts also potentially offer an ideal connection area between core and skin when the form of final structure is a sandwich composite. Each specimen was cut to 50mm long and then crushed by 35mm (0.7 in crushing strain). Finished specimens are shown below.

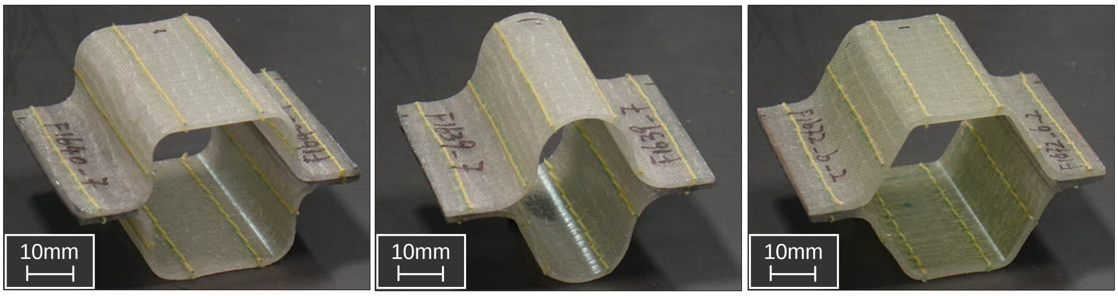

Figure 5.2 photographs of modified samples with three different transition geometries

5.1.3. Stitching parameters

In order to balance the effectiveness between central crack (or Mode-I properties) and fronds bending during laminate crushing, specimens were stitched at this stage. A Juki LU-563 industrial sewing machine equipped with DP/17 size 160 Groz-Beckert San-5 needles was used to perform the stitching process. The modified lock stitch (with the lock at the top) was chosen since it has been proven as the most effective stitching type for plate crushing [2]. The 120tex Kevlar® 29 thread with tenacity of 185~200 cN/Tex from Atlantic Thread and Supply was chosen, also because it is the best option stated in the previous literature [2].

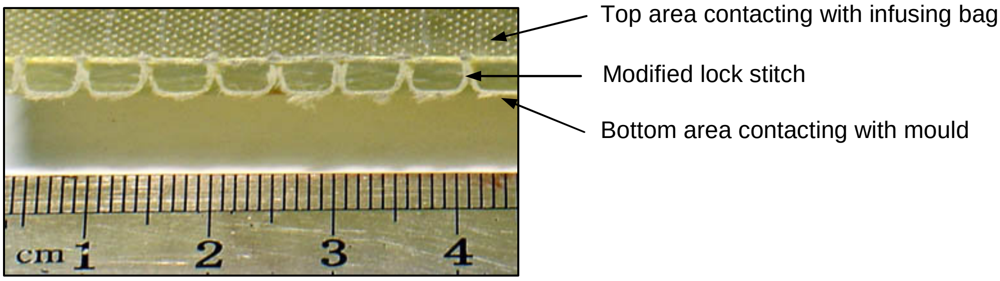

Figure 5.3 **Cross-sectional area of modified lock stitched laminate**

For these three transition geometries, their dry performs were stitched in parallel lines with 15mm separation between lines, and six lines for each half part. The distance between stitches in the same line was kept constant around 5mm (see Figure 5.3) since this was the maximum allowed by the sewing machine. Therefore, this gave a stitch density of 1.3stitches/cm^2.

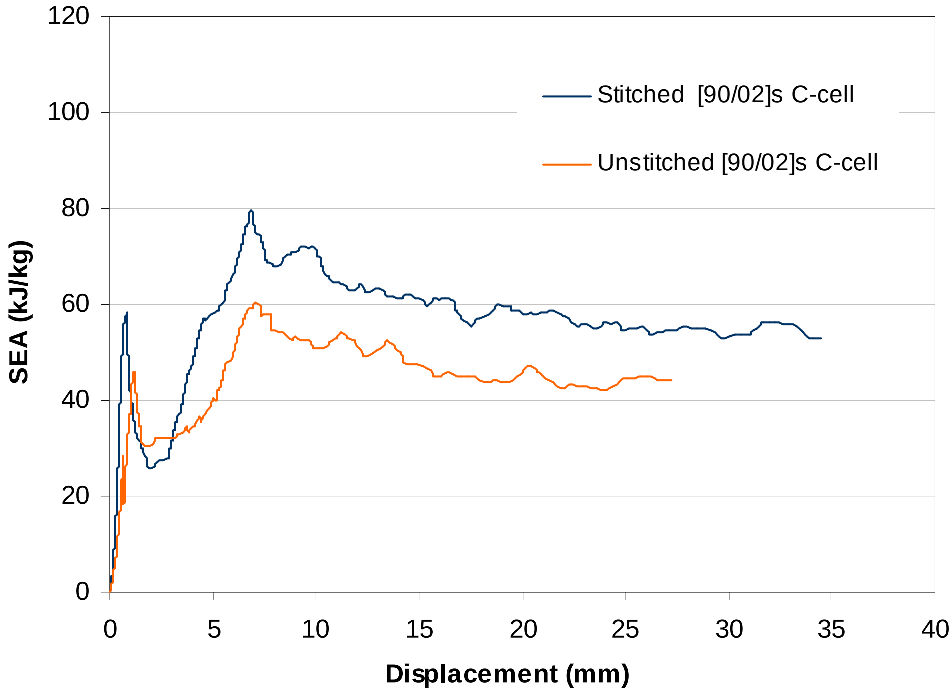

Figure 5.4 **Effects of stitching on the SEA of triaxial $[90/0_2]_S$ laminate of C-cells**

In the crushing performed on simply-supported plates, stitching benefits energy absorption through increasing the interlaminar shear strength (ILSS) [106] and stabilises the crushing process through improving the fracture toughness properties [24]. A comparison (Figure 5.4) between stitched and unstitched $[90/0_2]_S$ C-cells shows that proper stitching should also improve the energy absorption capability of these modified transition geometries.

5.2. Crushing stages and periods

A typical SCS/displacement curve obtained from $[90/\pm45/0]_S$ which is plotted in Figure 5.5 is representative of most crushing results. The crushing process of these transition geometries can be divided into three stages.

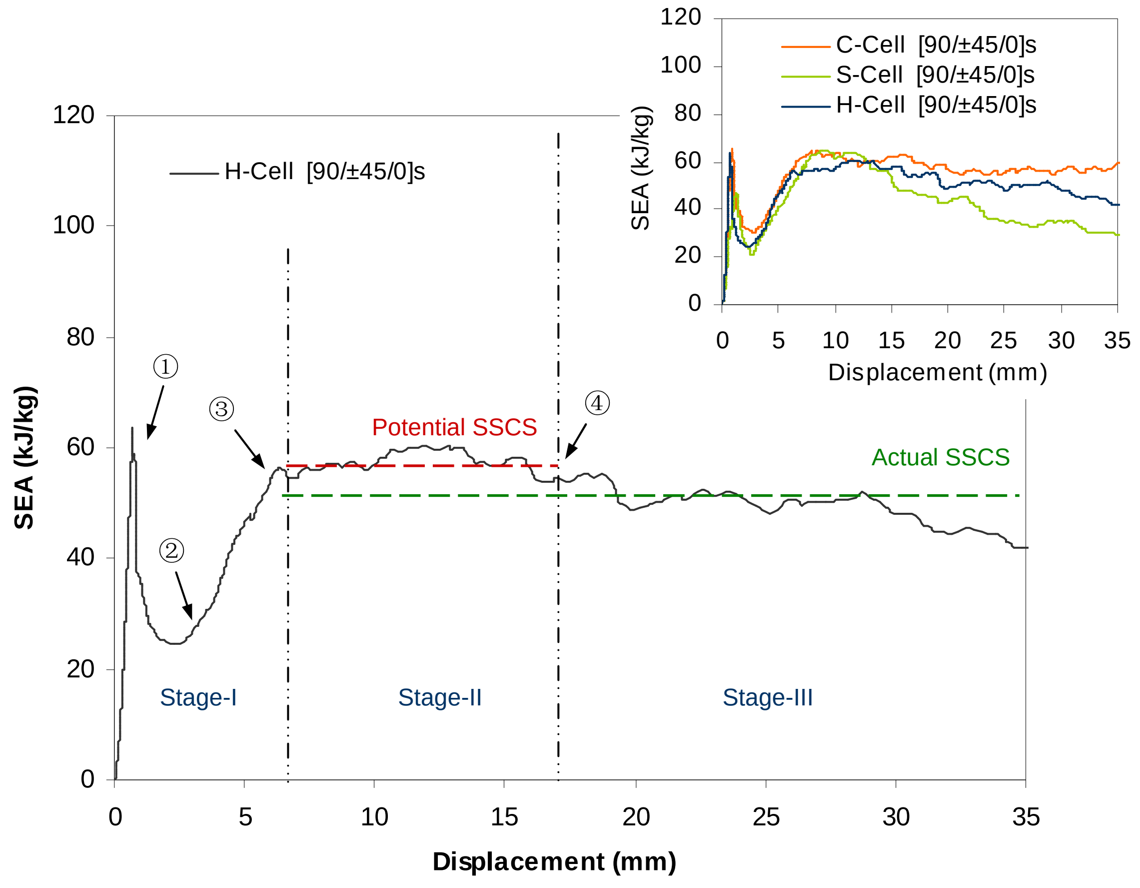

Figure 5.5 A typical SCS/displacement curve with three distinct stages

Stage-I: Unlike the chamfered trigger (see Figure 2.4), the trigger made of 90° lateral fibres has to overcome the interlaminar shear strength and forms a sharp steeple (or chamfered) tip under compressive loading. This process is illustrated in Figure 5.6 ①. Hence, the collapse of the triggering tip generates the first peak on the crushing curve shown in Figure 5.5. Following this, the chamfered tip behaves very similarly in triggering crushing as the chamfered trigger. Fibres on the tip were ground into debris (Figure 5.6 ②). Soon the debris forms into a wedge that generates a central crack (Figure 5.6 ③). Compared with the chamfering trigger, the trigger made of 90° lateral fibres potentially helps to retain the structural integrity before the crushing strength was achieved by external loads.

Stage-II: The laminate is then splayed by the accumulated debris wedge into two halves and crushed in a lamina bending mode. The region (③ - ④) of Stage-II varies from 5mm up to 25mm on stoke length, depending on crushing behaviour of different specimens.

Stage-III: Due to the interfacial weakness, the adhesive bonds between two half geometric samples might fail under the crushing load. The central crack generated by debris wedge also aggravates the debonding between two half parts. As a result, unexpected debonding might cause catastrophic collapse if the two half parts are completely separated during crushing. In addition, two longitudinal freely-supported edges might initiate buckles, especially for thin laminates. Therefore, those unexpected destabilizing effects, which are illustrated in Figure 5.7, result in the crushing load decreasing gradually during this stage. It is important to note that most destabilizing effects happen at both flat sides, but not at the core part of the cells.

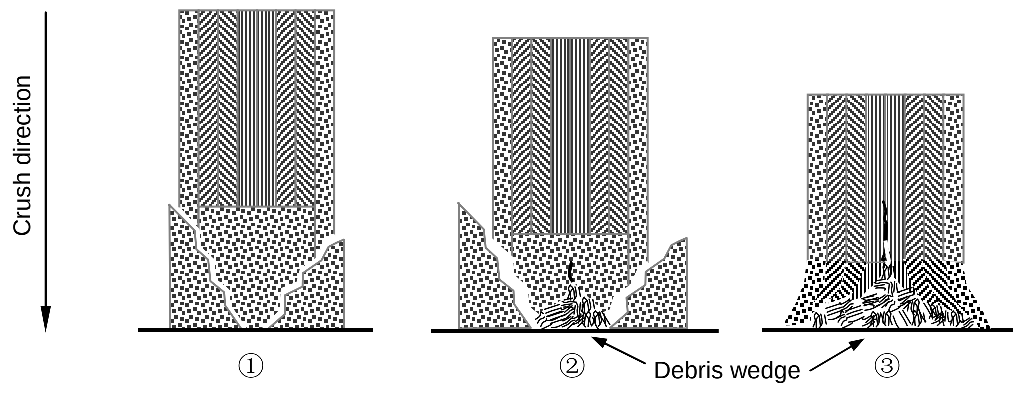

Figure 5.6 **Schematic representation of the trigger of 90-degree-fibre initiated at stage I**

However, the progressive lamina bending mode still was achieved by many specimens through out the whole crushing process. As a comparison, Figure 5.7 shows a stably crushed specimen. In a few cases, if the specimens were not separated during crush, the debris blocked inside the cell would normally increase the crush load a bit at the end of test.

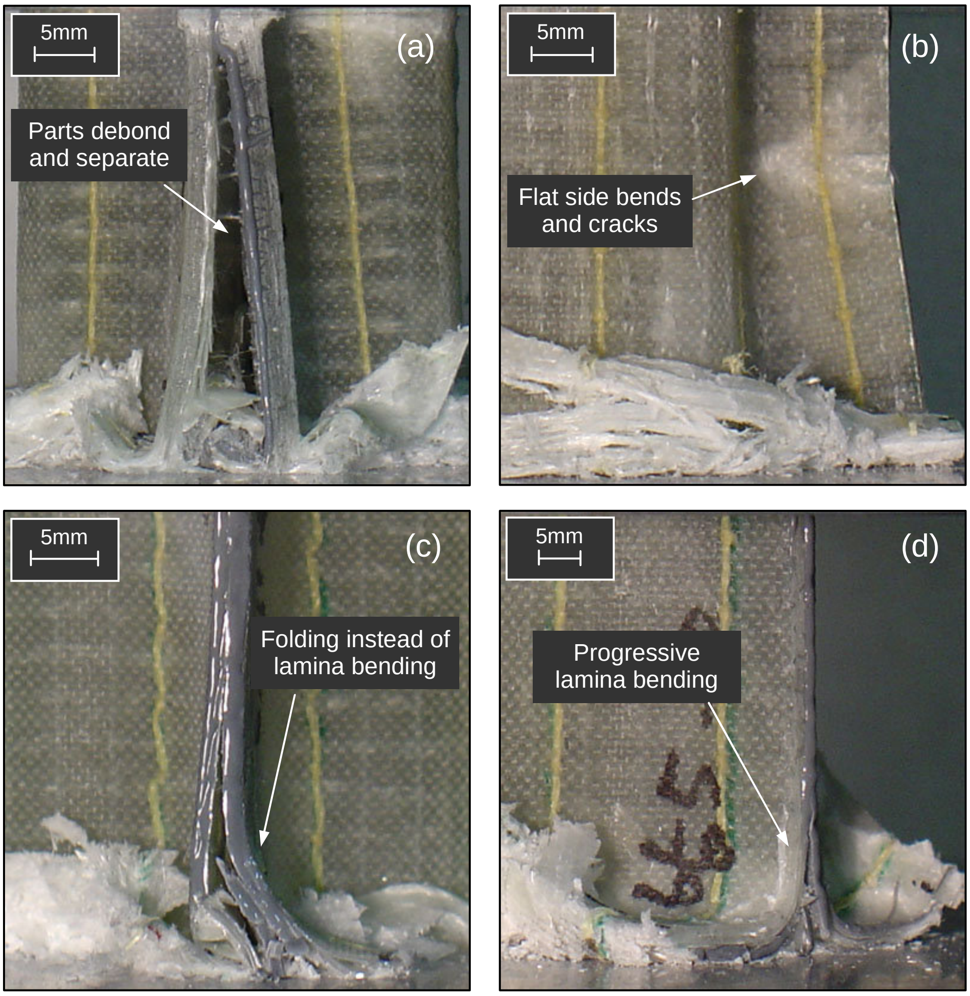

Figure 5.7 Photographs of modified geometric cells under unstable crushing: (a), (b) and (c); and stable crushing: (d)

Figure 5.5 suggests that the quadriaxial H-cell seems to absorb less energy than C-cell, but more than the S-cell during static crushing. In order to compare the behaviour of different geometric cells, the sustained crushing stress curve of each specimen was divided into three crushing periods:

1) Stage 1: Initiation of stable crushing, crushing period of first 10mm stroke started from the point ③ in Figure 5.5;

2) Stage 2: Stable crushing, crushing period of second 10mm stroke which is about between the displacement of 17mm to 27mm for that $[90/\pm45/0]_S$ H-cell shown in Figure 5.5;

3) Stage 3: Crushing becomes unstable, last crushing period which is from 27mm until

the end.

The SEA values of all geometric cells consisting of NCFs (i.e. excluding the $[PW400/0]_S$ cells), within different crushing stages are plotted against the perimeter/geometric thickness (P/t) ratio in Figure 5.8. The geometric thickness is the summation of two laminate halves ($t=2h$) listed in Table 5.1 - Table 5.3. It clearly reveals that the SEA levels of cells decrease as the P/t ratio increases in stage 1, the first 10mm stroke. In the second and last periods, the SEA levels of most cells decrease with increasing P/t.

In Figure 5.8, the geometric cells with larger thicknesses exhibit higher stability during early crushing, but lower sustainability afterwards. This phenomenon is also reflected in the dispersion of SEA data. Furthermore, as shown in both Figure 5.5 and Figure 5.8, C-cells seem to be more stable and sustainable than S- and H-cells during the whole crushing process. This result is seen more clearly on the normalized data which is shown in Figure 5.9.

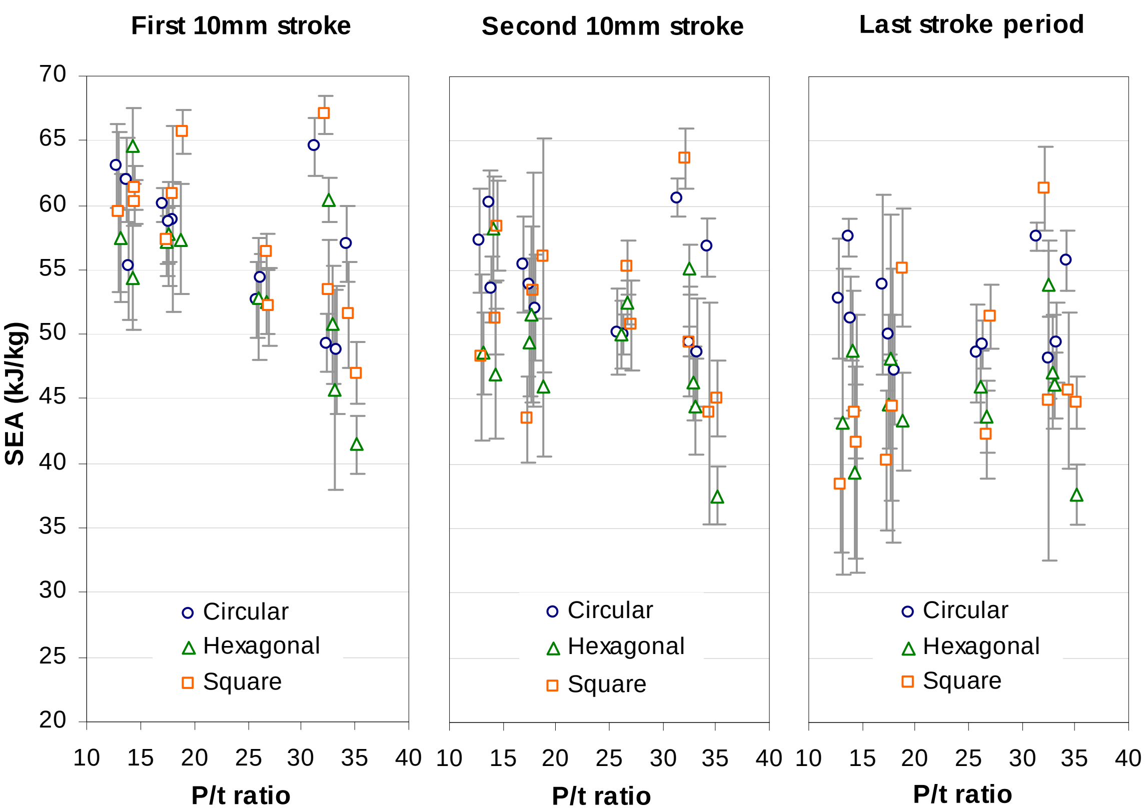

Figure 5.8 SEA values of all modified geometric cells in every crushing period of 10mm

But meanwhile, some specimens that have similar thicknesses still may exhibit different SEA level. In other words, in addition to the structural geometries, the fabric lay-ups also play a very important role in the energy absorption of geometric cells. In order to systemically and efficiently evaluate the crushing results of different geometric cells and lay-ups, it is necessary to isolate the influence from catastrophic structural failure caused by weak interfacial bonding between half samples. The concept of sustained structural efficiency (*SSE*) is thus introduced, which is discussed in section 5.4.

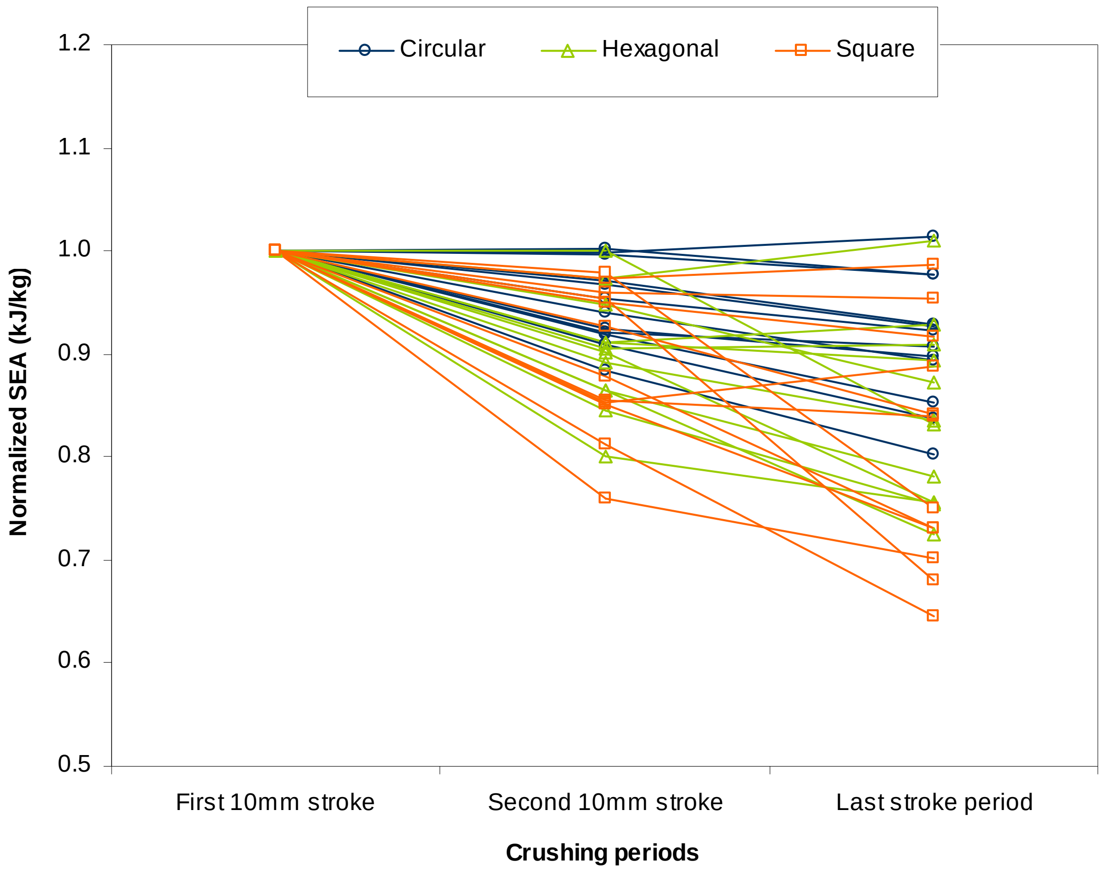

Figure 5.9 **Normalized SEA of all modified geometric cells in every crushing period of 10mm**

5.3. Crushing results

The crushing results of all modified geometric cells are presented in this section. Crushing data for each of the three geometric cells are listed in the Table 5.4, Table 5.5 and Table 5.6, respectively.

Table 5.4 Crushing results of S-cells

Reference	Orientation	P/t ratio	Potential SEA (kg/kJ)		Actual SEA (kg/kJ)		Sustained structural efficiency
			Average	CV%	Average	CV%	
F1640_S	[90/0/90]	34.5	54.15	4.57	47.62	11.16	87.8%
F1643_S	[0/90/0]	35.2	46.32	5.28	45.70	3.20	98.7%
F1646_S	$[90/0]_S$	27.0	53.29	5.45	51.50	4.78	96.7%
F1617_S	$[90/0_2]_S$	18.9	67.38	2.47	60.46	6.55	89.7%
F1649_S	$[90/0]_{2S}$	14.4	61.04	5.36	53.27	1.79	87.5%
F1653_S	[±45/0/±45]	32.5	54.86	4.99	49.27	11.73	89.8%
F1656_S	$[\pm45/0]_S$	26.7	60.19	3.95	51.97	2.37	86.5%
F1620_S	$[\pm45/0_2]_S$	17.9	64.83	2.47	55.74	6.82	86.0%
F1659_S	$[\pm45/0_3]_S$	14.6	66.33	4.24	56.17	4.29	84.9%
F1623_S	$[90/\pm45/0]_S$	17.4	63.04	5.77	50.22	5.29	79.8%
F1662_S	$[90/\pm45/0_2]_S$	13.1	63.03	12.34	51.78	11.65	82.3%
F1665_S	$[PW400/0]_S$	32.2	66.37	2.60	64.46	2.73	97.1%

values behind the ± are standard deviations; VF: Fibre volume fraction; CV: Coefficient of variation

Table 5.5 Crushing results of C-cells

Reference	Orientation	P/t ratio	Potential SEA (kg/kJ)		Actual SEA (kg/kJ)		Sustained structural efficiency
			Average	CV%	Average	CV%	
F1639_C	[90/0/90]	34.1	58.44	4.04	56.60	3.35	96.9%
F1642_C	[0/90/0]	33.2	49.78	6.71	48.92	7.91	98.2%
F1645_C	$[90/0]_S$	26.2	53.59	5.32	51.59	3.02	96.4%
F1616_C	$[90/0_2]_S$	18.0	60.02	11.48	54.51	10.35	91.1%
F1648_C	$[90/0]_{2S}$	13.9	56.70	6.85	53.76	5.91	94.9%
F1652_C	[±45/0/±45]	32.4	50.78	2.96	49.01	3.67	96.5%
F1655_C	$[\pm45/0]_S$	25.8	52.23	5.37	50.71	5.88	97.1%
F1619_C	$[\pm45/0_2]_S$	17.6	59.01	6.15	55.06	3.57	93.4%
F1658_C	$[\pm45/0_3]_S$	13.8	62.51	3.60	60.21	3.15	96.3%
F1622_C	$[90/\pm45/0]_S$	17.0	59.96	3.25	56.99	5.60	95.1%
F1661_C	$[90/\pm45/0_2]_S$	12.8	62.25	5.17	58.86	5.99	94.6%
F1664_C	$[PW400/0]_S$	31.3	64.47	3.07	61.27	2.27	95.1%

Table 5.6 **Crushing results of H-cells**

Reference	Orientation	P/t ratio	Potential SEA (kg/kJ)		Actual SEA (kg/kJ)		Sustained structural efficiency
			Average	CV%	Average	CV%	
F1641_H	[90/0/90]	33.0	50.90	5.67	45.65	7.65	89.7%
F1644_H	[0/90/0]	35.1	39.57	4.97	38.79	4.81	98.1%
F1647_H	$[90/0]_S$	26.1	53.57	6.25	50.23	5.69	93.8%
F1618_H	$[90/0_2]_S$	18.8	59.44	6.56	51.06	5.88	86.0%
F1650_H	$[90/0]_{2S}$	14.3	55.94	8.53	48.49	8.93	86.7%
F1654_H	[±45/0/±45]	32.8	52.18	4.35	48.36	3.85	92.7%
F1657_H	$[\pm45/0]_S$	26.8	55.92	5.19	49.76	2.84	89.1%
F1621_H	$[\pm45/0_2]_S$	17.7	59.65	7.61	53.93	10.59	90.2%
F1660_H	$[\pm45/0_3]_S$	14.2	68.06	5.02	58.84	5.64	86.4%
F1624_H	$[90/\pm45/0]_S$	17.5	59.68	5.72	51.51	3.48	86.4%
F1663_H	$[90/\pm45/0_2]_S$	13.2	59.91	8.28	51.95	12.65	86.7%
F1666_H	$[PW400/0]_S$	32.5	59.43	3.06	56.82	2.88	95.6%

In these tables, the SEA which is observed in stage-II in Figure 5.5 is the potential energy absorption capacity of geometric cells, while the actual SEA concerns the region of stage-II and stage-III is the practical energy absorption capacity of geometric cells during crushing tests. The sustained structural efficiency is the proportion of these two SEA values. More details will be discussed in Section 5.4.

These crushing data was also classified into three different groups by fibre orientations, which are biaxial, triaxial, and quadriaxial. For each orientation set, SEA values were plotted against the three crushing periods that were discussed in the previous section. These curves can be seen in the following Figure 5.10, Figure 5.11 and Figure 5.12.

It has been found that energy absorbing capabilities of all samples are determined by their crushing modes and bending forms. Over all samples, $[PW400/0]_S$ cells presented the most remarkable energy absorption capability. The thinner laminate exhibited the poorer energy absorbing capabilities, as most cells possessing small thickness were suffered by buckling and large radius-of-curvature bending. Although the cells with a thicker laminate experienced severe load drops during crushing, they still achieved rather high SEA levels during the first 10mm stroke.

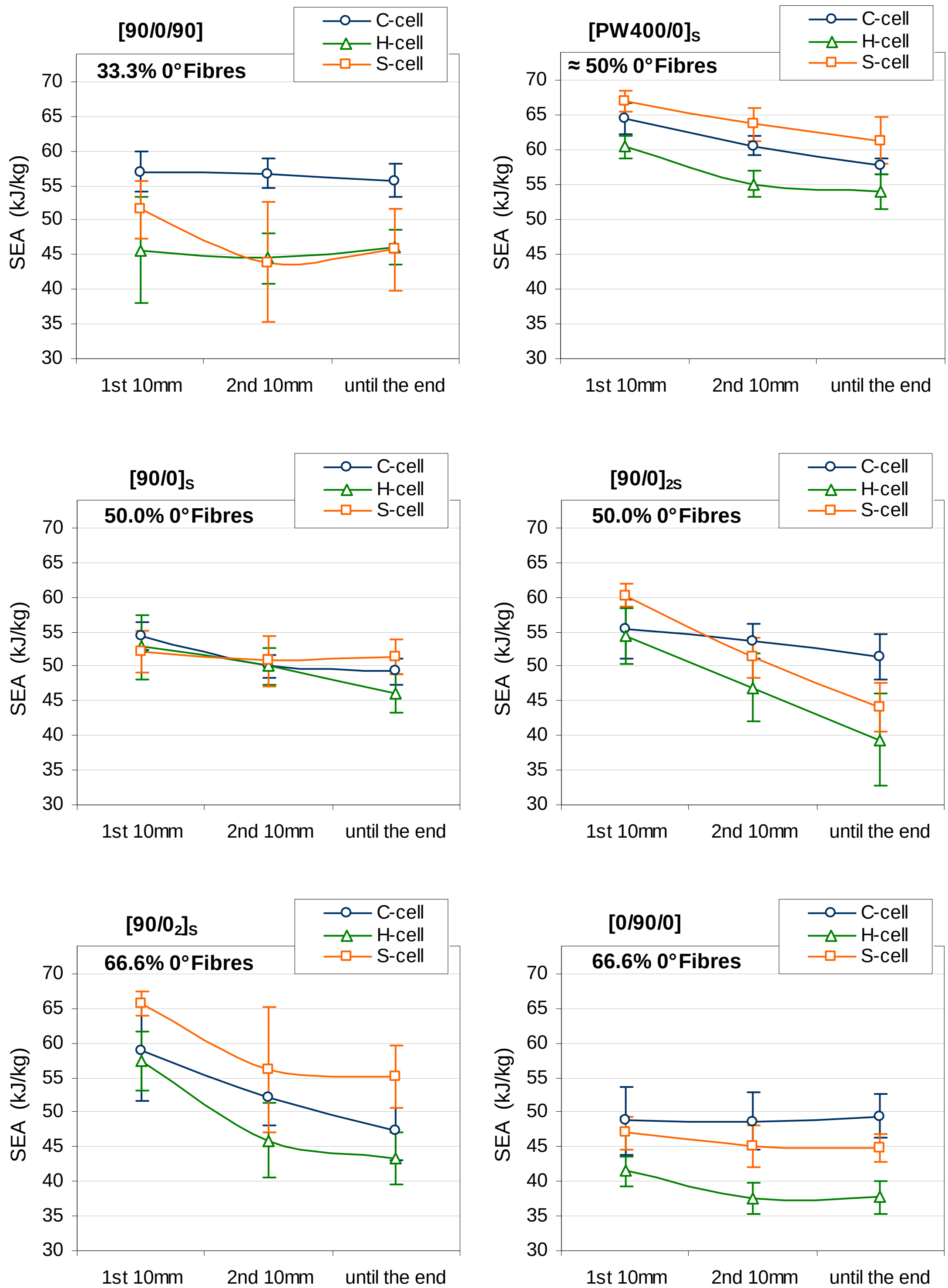

Figure 5.10 **Crushing responses of geometric cells made of biaxial fabrics during three different crushing periods**

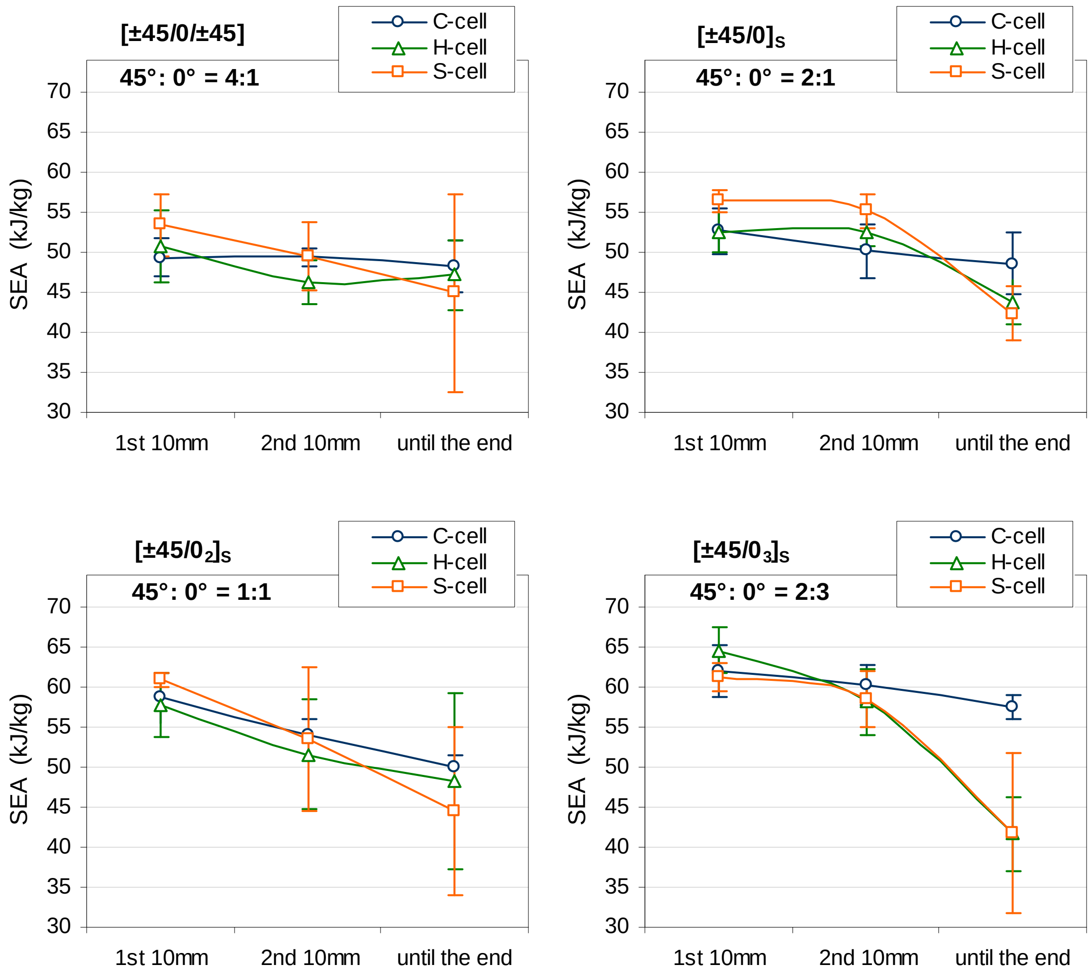

Figure 5.11 Crushing responses of the geometric cells that are composed of triaxial fabrics during three crushing periods

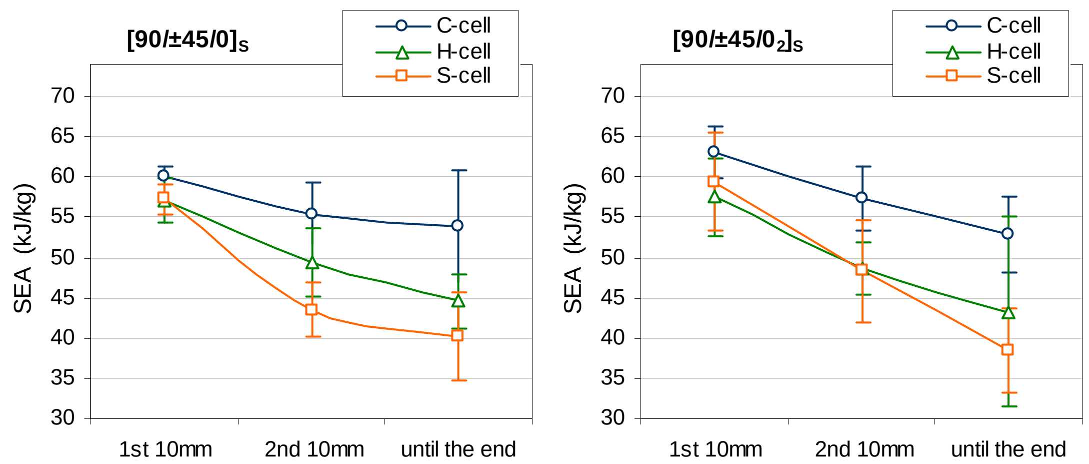

Figure 5.12 Crushing responses of geometric cells that are composed of quadriaxial fabrics during three different crushing periods

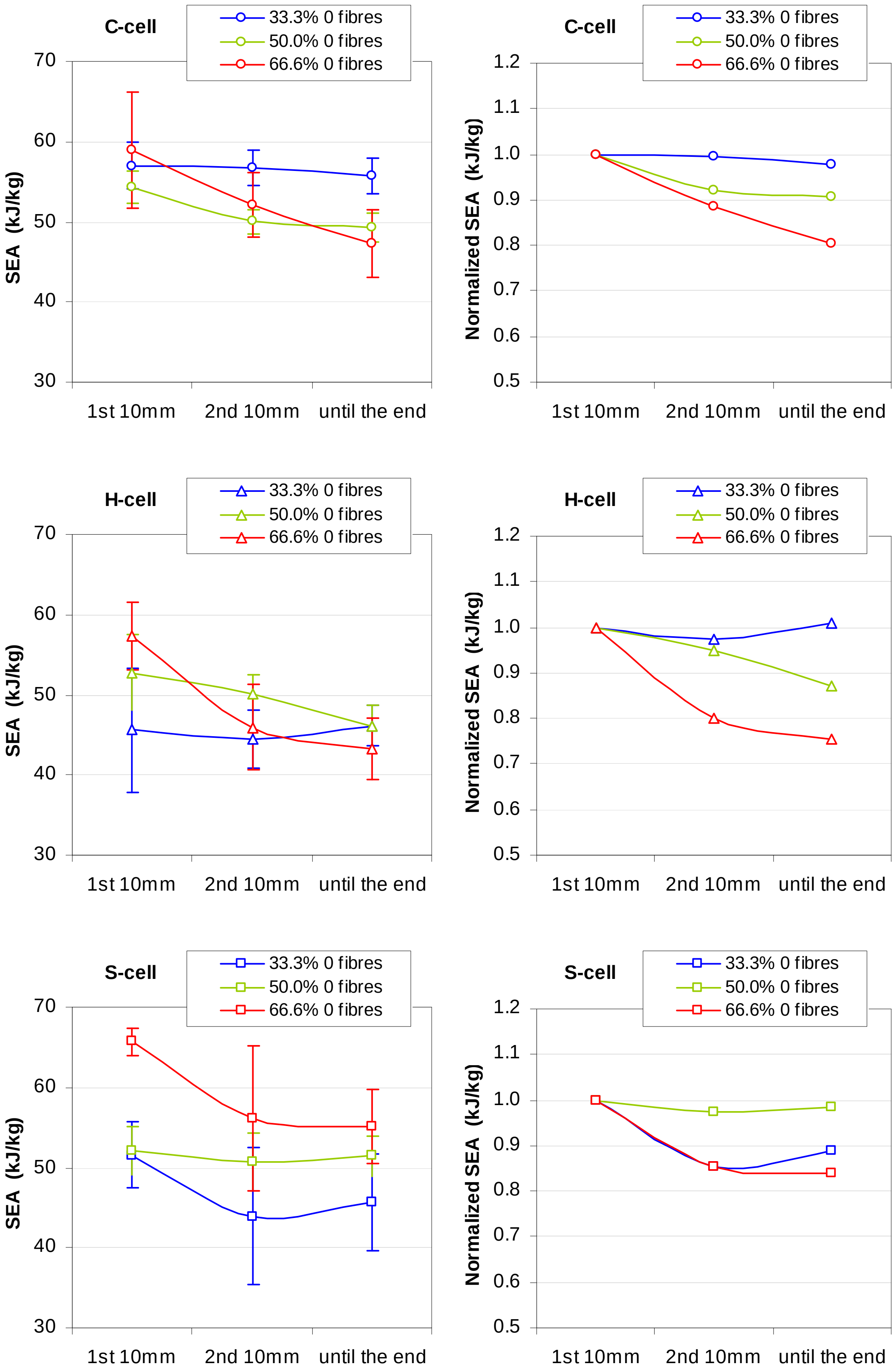

Figure 5.13 Crushing responses of biaxial cells during three different crushing periods

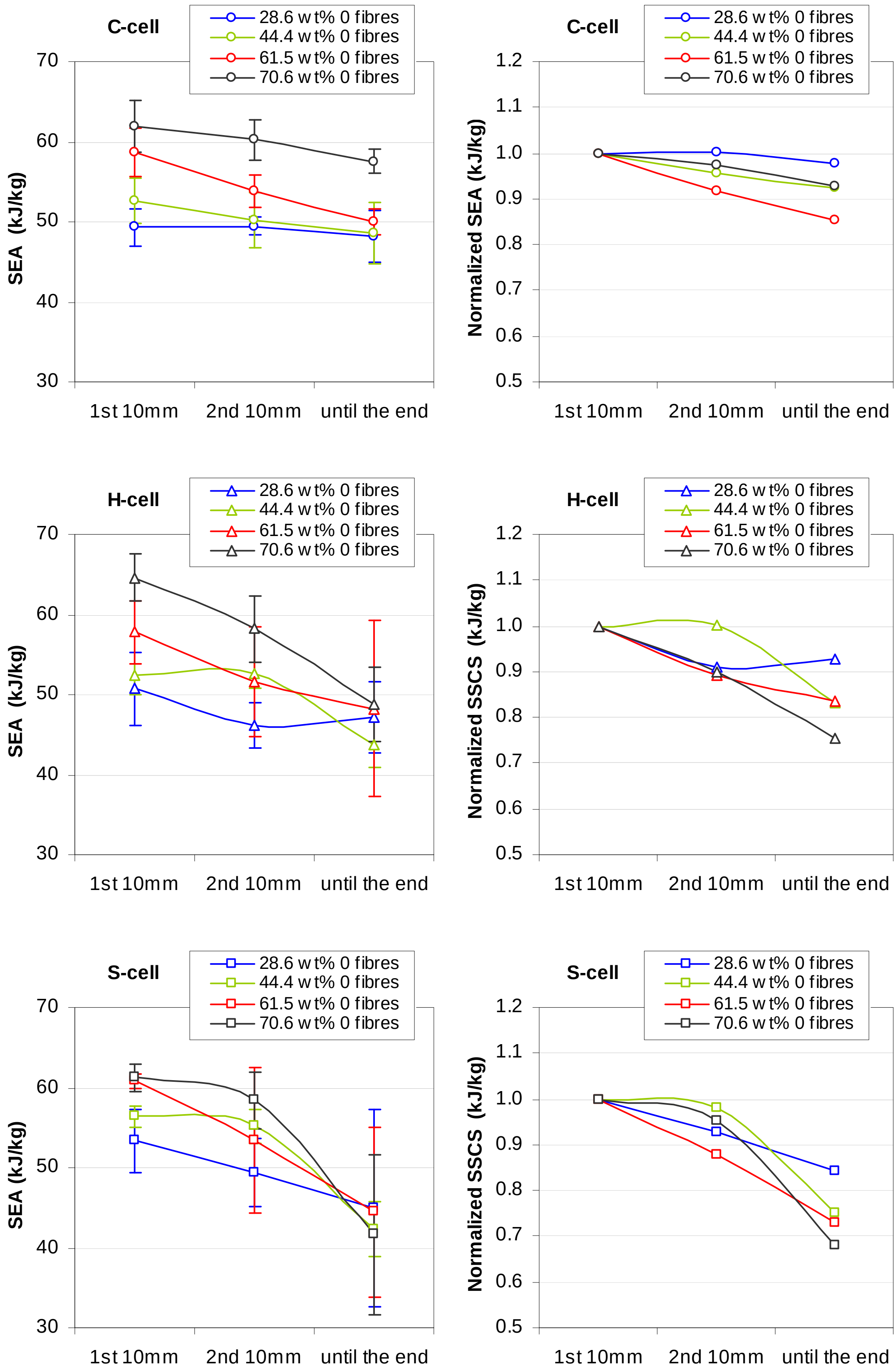

Figure 5.14 **Crushing responses of triaxial cells during three different crushing periods**

Furthermore, the SEA values as well as normalized SEA values were plotted against different crushing periods for samples grouped according to the weight fraction of 0° fibres in Figure 5.13 (biaxial cells) and Figure 5.14 (triaxial). Only the laminates in which the 0° fibres were placed in the middle layers are taken into consideration in these figures. The weight fraction of 0° fibres were estimated according to the manufacturing data that were shown in Table 3.1. For both biaxial C-cells and H-cells, it seems that the structures become less stable when the content of 0° fibres increases. But triaxial cells did not show the same results.

5.4. Sustained structural efficiency (SSE)

The observations of the crushing results suggest that the bonding effectiveness might be a very important factor. Once the adhesive failed during crushing, the instantaneously generated splitting and debonding between two sample halves are able to turn the crush into a low energy absorption level.

Conversely, if two sample halves were bonded perfectly by using other existing technologies, this low energy absorption level should not be considered as the potential energy absorption capacity level that those geometric transition cells were able to achieve. Therefore, both actual and potential energy absorbing capacities of those geometric transition cells need to be discussed at the same time.

Herein, the actual absorption capacity of a composite structure is defined as the raw crushing performance that is obtained from the experimental test. In contrast, the potential absorption capacity of a composite structure is defined as the estimated "best" crushing performance that the structure is able to achieve. The actual energy absorption capacity covers the region of stage-II and stage-III in Figure 5.5; while the potential energy absorption capacity covers the region of sustained crush, which is the stage-II only. The sustained structural efficiency (SSE) is the proportion of these two values, which is defined as:

$$SSE = \frac{U_{Actual}}{U_{Potential}} \times 100\% \tag{5.1}$$

where U_{Actual} = actual energy absorption capacity of structure;

$U_{Potential}$ = potential energy absorption capacity of structure.

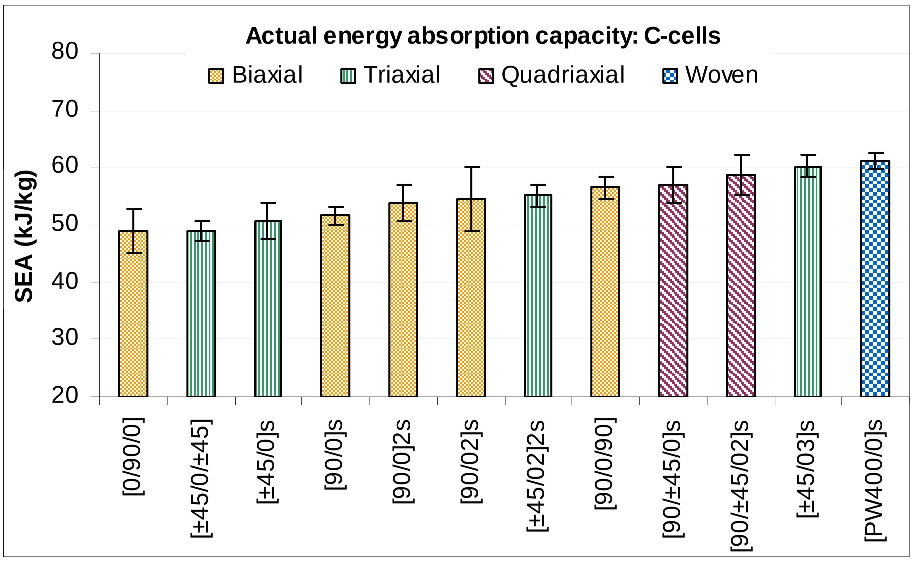

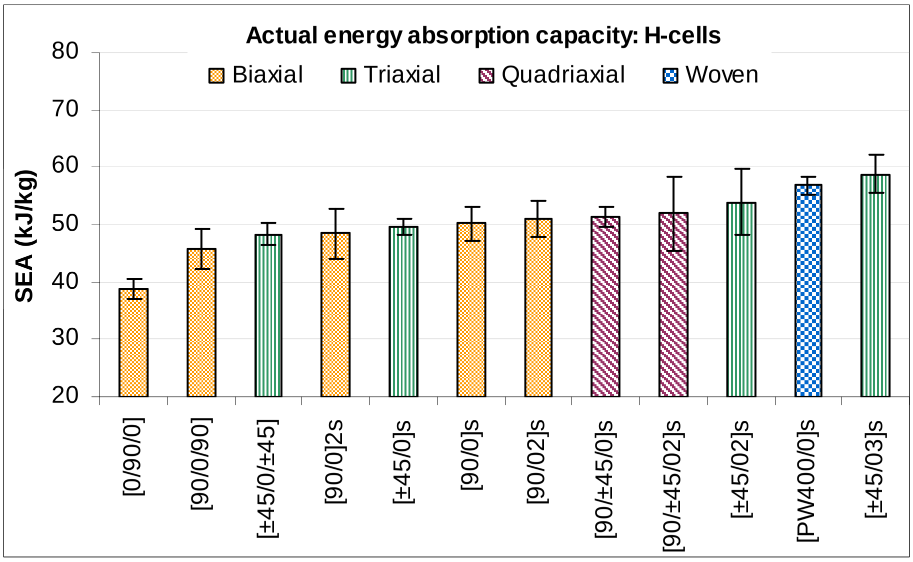

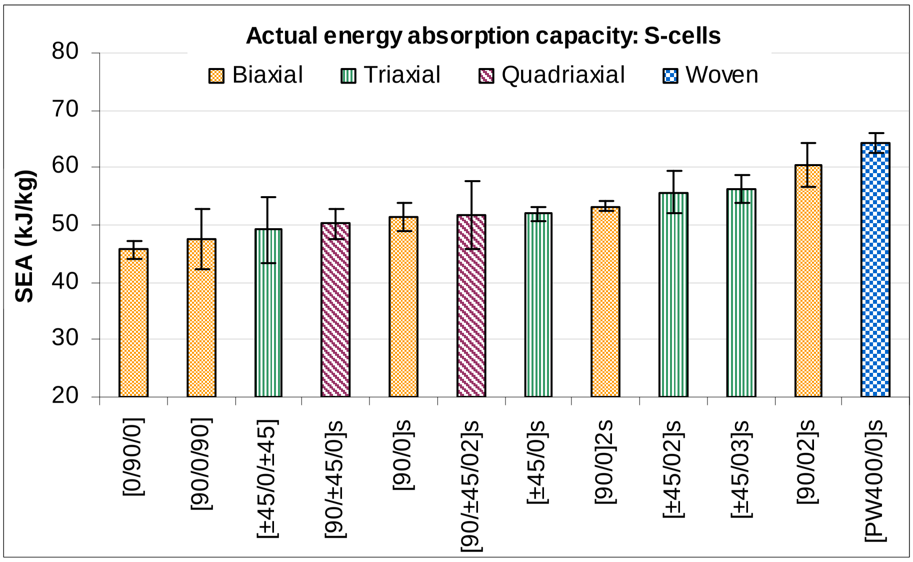

Figure 5.15 **Actual energy absorption capacity of all geometric transition cells**

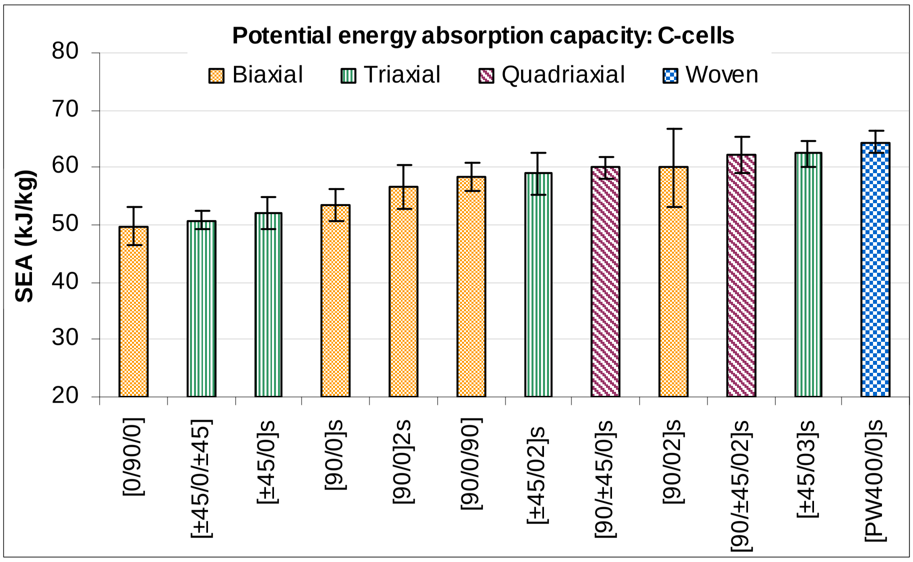

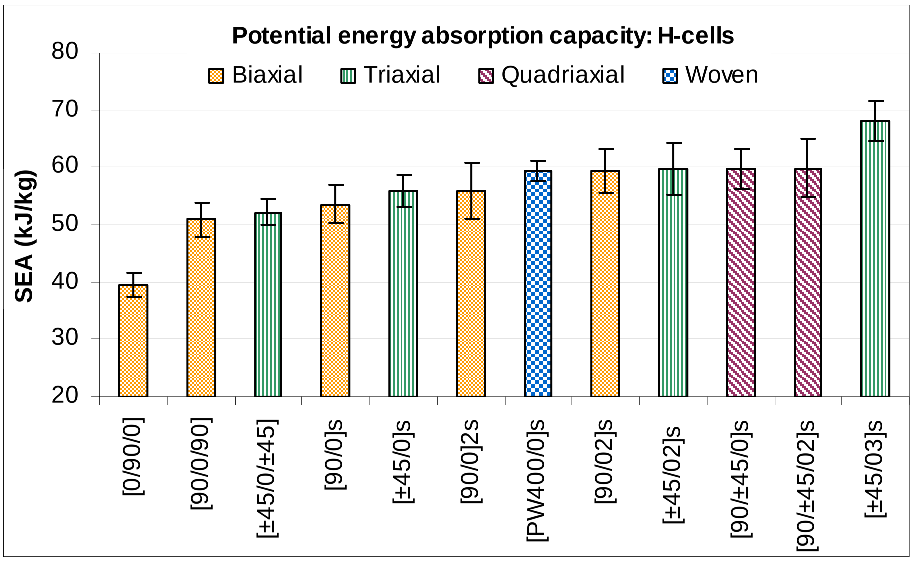

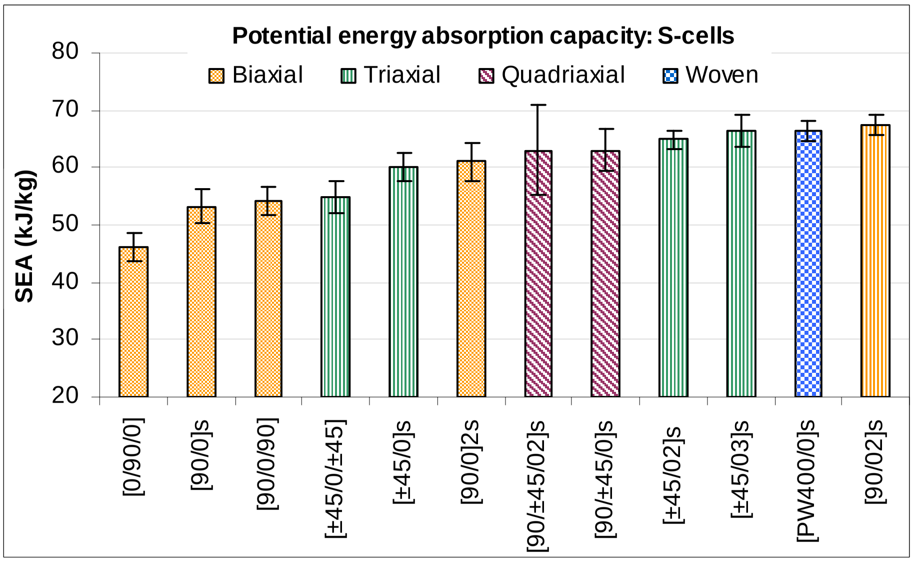

Figure 5.16 **Potential energy absorption capacity of all geometric transition cells**

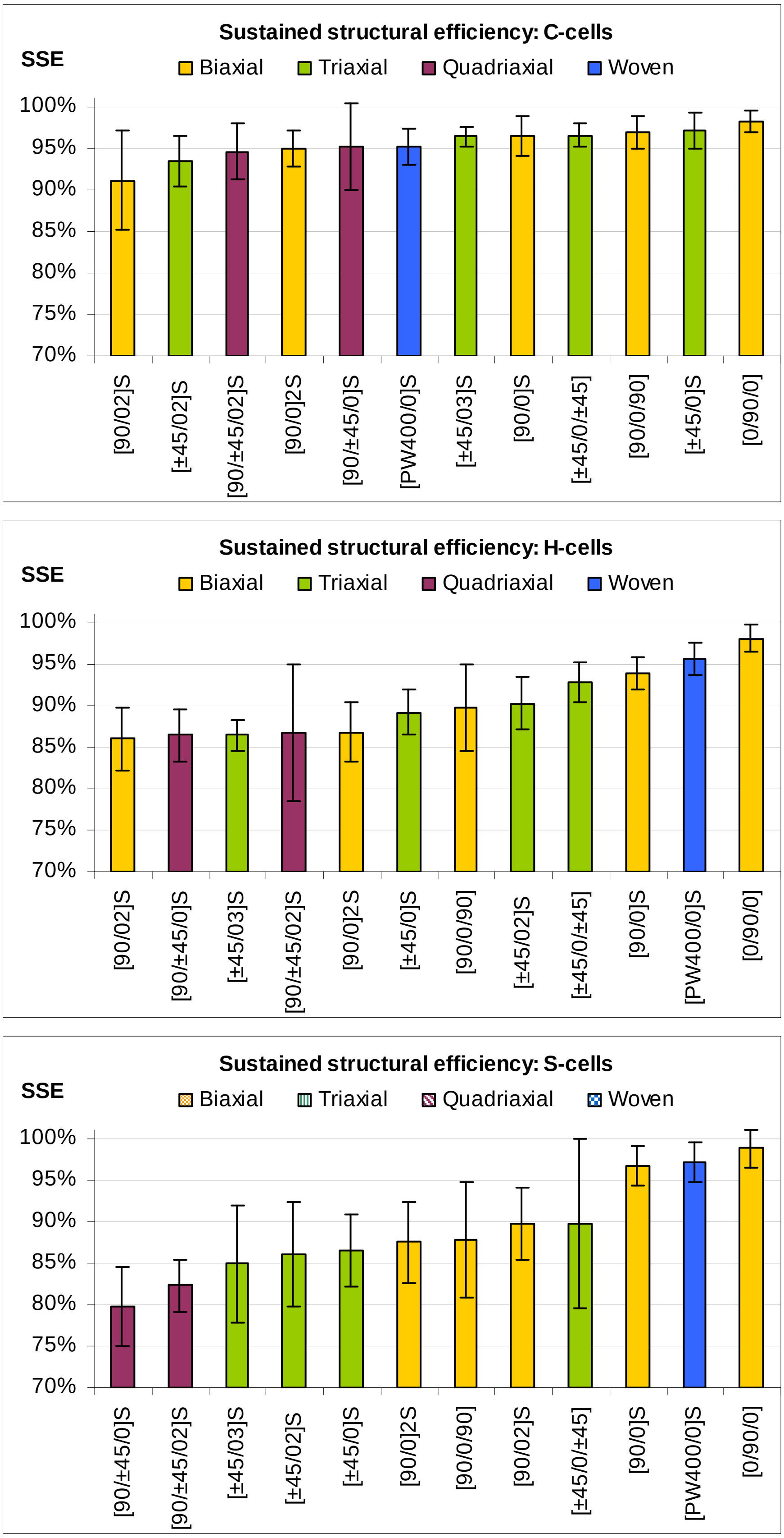

Figure 5.17 **Sustained structural efficiency of all geometric transition cells**

Both actual and potential energy absorption capacities of tested three geometric cells are shown in Figure 5.15 and Figure 5.16, respectively. And their SSE is shown in Figure 5.17. More obviously in these three figures, thicker laminates present superior energy absorbing capabilities compared with thinner laminates. For the NCF laminates, there is not a clear boundary or difference amongst bi-, tri- and quadric-axial fabrics. While it is interesting to note that the semi-woven $[PW/0]_S$ cells present more outstanding crushing performance than NCF cells.

According to above figures, it can be found that the sustained structural efficiency, or the difference between actual-potential SEA values, is affected by geometric shape of the core section. As mentioned previously, C-cells appeared to have highest sustained structural efficiency, while S-cell appeared lowest sustained structural efficiency but more than half specimens showing highest potential energy absorption capacity are S-cells.

For the S-cells, in both actual and potential figures, semi-woven $[PW400/0]_S$, biaxial $[90/0_2]_S$, triaxial $[\pm45/0_3]_S$, and $[\pm45/0_2]_S$ achieved the best SEA values. It is important to mention here that on average, the specific energy absorption of $[90/0_2]_S$, $[\pm45/0_3]_S$, and $[\pm45/0_2]_S$ S-cells at Stage-II, decreased approximately 10kJ/kg after stable crushing of Stage-I. These results can also be found in Figure 5.10 and Figure 5.11. Although quadriaxial $[90/\pm45/0]_S$ and $[90/\pm45/0_2]_S$ S-cells achieved more than 60kJ/kg of the potential SEA values, Figure 5.17 shows that the SSE of quadriaxial S-cells is only around 80%.

Unlike the S-cells, $[90/\pm45/0]_S$ and $[90/\pm45/0_2]_S$ C-cells possess much higher SSE. In terms of either SEA value or SEA order, very little difference can be found between potential and actual energy absorption capacity of C-cells. Potentially, the $[PW400/0]_S$, $[\pm45/0_3]_S$, $[90/\pm45/0_2]_S$, and $[90/0_2]_S$ samples possess the better SEA values. The crushing response of C-cells seems not to be very sensitive to their fabric orientations. Instead, C-cells with thicker laminate walls seem to possess higher SEA than those with thinner laminate walls. And this phenomenon presents also on both S-cells and H-cells.

Amongst H-cells, the triaxial $[\pm45/0_3]_S$ samples achieved the highest SEA level. In terms of actual energy absorption capacity, the semi-woven $[PW400/0]_S$ samples achieved slightly lower SEA level following after the $[\pm45/0_3]_S$ samples. Whereas in the potential energy absorption figure of H-cells, biaxial $[90/0_2]_S$, triaxial $[\pm45/0_3]_S$, quadriaxial $[90/\pm45/0]_S$ and $[90/\pm45/0_2]_S$ also have very similar SEA levels as $[PW400/0]_S$. In Figure 5.17, the SSEs of all H-cells are moderate, which are averagely lower than that of C-cells but higher than that of S-cells.

5.5. Summary

In order to compare the S-, C- and H-cells with previously investigated simply-supported plates [16] and intersecting square cells in parallel, their SEA data are plotted against width/thickness ratios in Figure 5.18. Again, it is necessary to state herein that the width/thickness ratio means the Knife-Edge-Separation/thickness [16] (K.E/t) ratio for simply-supported plates; the Separation width/thickness (SD/t) ratio for intersecting square cells; and the Perimeter/thickness (P/t, t=2h) ratio for three geometric cells.

It shows that these three geometric cells developed in this chapter have achieved greater energy absorbing levels than those intersecting square cells that investigated in last chapter. The section of corrugated core certainly prevents the structural composites from buckling during crushing, and consequently improved their energy absorption capabilities. However, the adhesive applied on flat sides did not work as effectively as it was expected.

Accumulated fibre debris between the flat sides and inside the cell would endeavour to push the two-part-glued cell back to two separated parts. Subsequently, each debonded half cell hardly crushed perpendicularly, and eventually failed in lower SEA levels. Especially for the square cells, debris from parallel edges at section of corrugated cell would normally generate more oppositely interacting force. Therefore square cell is more likely to be separated during crushing. As a contrast, circular corrugating composite structure is believed as the most stable geometric shape during crushing as the larger round corner can disperse the acting force from debris into different directions

Overall, for above discussed corrugated geometries, the square cell can achieve higher potential energy absorption capacity than other geometries. This could be attributed to it higher critical buckling or crushing strength. But with the progress of crushing, all geometric cells became unstable due to sides debonding. The relationship between strain energy release rate (i.e. fracture toughness) and flexural rigidity acting on energy absorption capability of these geometric cells still has not yet been evaluated. More discussion will be carried out during the following chapters.

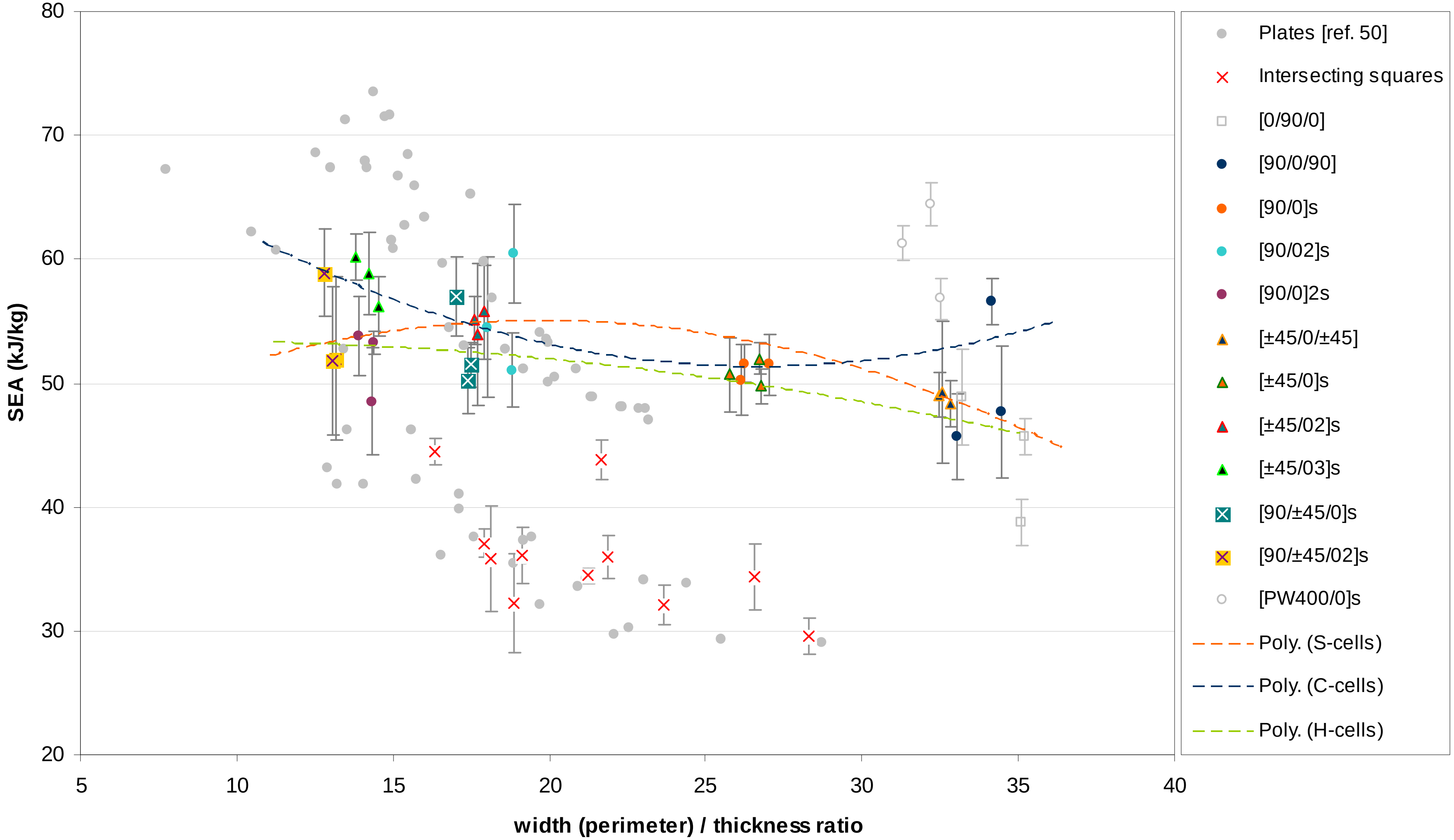

Figure 5.18 **Comparisons between geometric cells (actual crushing data), and intersecting square cells as well as simply-supported plates**

Chapter 6. Flexural Properties

According to the crushing results discussed during the last chapter, flexural properties seem to be important factors that dominate the crushing forms of structural composites. The flexural properties of a structure are highly related to structural dimensions and geometrical shape.

For the purpose of comparing testing results in parallel, flexural samples were made from the same materials as each of the corresponding crushing samples mentioned in the last chapter. To keep the same stitching configuration as the crushing samples, modified lock stitching was used for all flexure testing samples (as well as the DCB and 4-ENF referred to in the next chapter).

6.1. *Flexure testing samples*

Each sample was cut 20mm wide with one Kevlar® stitching line in the middle. This is considered as a compromise that represents the 15mm stitching gap in crushing samples but meanwhile satisfies all testing standards with one uniform setup. More details about the stitching configurations can be found in Figure 5.3. A typical flexural specimen is shown in Figure 6.1.

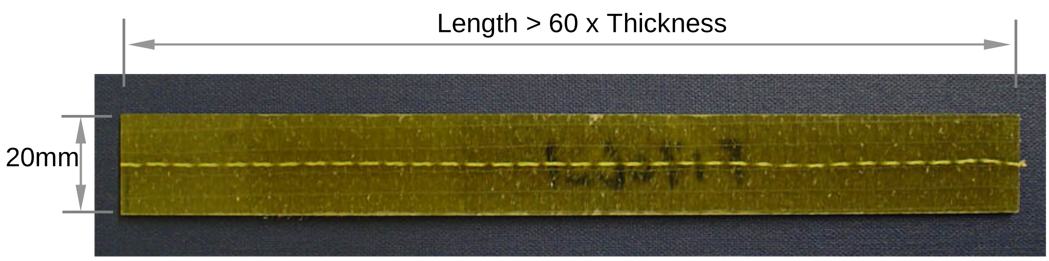

Figure 6.1 Picture of a typical flexural testing sample with a stitching line in the middle

The majority of samples were prepared using a polyester resin. Two other tougher resins, vinyl ester and epoxy, were also used for $[90/0_2]_S$ laminates at latter stages of this project. All the other samples details including fibre lay-up orientations and dimensions are listed in Table 6.1. Only stitched laminated were used for the flexure tests in this study, though stitching may degrade the flexural properties due to fibre damage [107].

Table 6.1 Flexure testing Samples

Reference	Orientation	Matrix	Thickness h (mm)	Width D (mm)	Crosshead speed R (mm/min)	VF%
F1689_Flex	[90/0/90]	Crystic® 489PA (polyester)	1.18±0.028	19.88±0.45	3.2	51.5
F1690_Flex	[0/90/0]	Crystic® 489PA (polyester)	1.17±0.014	20.11±0.05	3.1	51.5
F1691_Flex	[±45/0/±45]	Crystic® 489PA (polyester)	1.31±0.019	20.16±0.02	3.5	51.5
F1692_Flex	$[90/0]_S$	Crystic® 489PA (polyester)	1.54±0.009	20.16±0.02	4.1	51.9
F1693_Flex	$[\pm45/0]_S$	Crystic® 489PA (polyester)	1.62±0.013	20.05±0.04	4.3	51.9
F1694_Flex	$[PW400/0]_S$	Crystic® 489PA (polyester)	1.30±0.035	20.17±0.02	3.5	51.9
F1695_Flex	$[90/0_2]_S$	Crystic® 489PA (polyester)	2.22±0.044	20.16±0.03	5.9	53.5
F1696_Flex	$[\pm45/0_2]_S$	Crystic® 489PA (polyester)	2.27±0.061	20.13±0.10	6.0	53.5
F1697_Flex	$[90/\pm45/0]_S$	Crystic® 489PA (polyester)	2.31±0.032	20.15±0.05	6.2	53.5
F1698_Flex	$[90/0]_{2S}$	Crystic® 489PA (polyester)	2.90±0.016	20.15±0.05	7.7	53.6
F1699_Flex	$[\pm45/0_3]_S$	Crystic® 489PA (polyester)	2.99±0.053	20.06±0.08	8.0	53.6
F1700_Flex	$[90/\pm45/0_2]_S$	Crystic® 489PA (polyester)	3.11±0.024	20.21±0.03	8.3	53.6
F1707_Flex	$[90/0_2]_S$	Dion® 9102-500 (vinyl ester)	2.54±0.029	20.16±0.01	6.8	47.9
F1710_Flex	$[90/0_2]_S$	Araldite® LY564 (epoxy)	2.73±0.034	19.96±0.16	7.3	43.2

values behind the ± are standard deviations; VF: Fibre volume fraction;

6.2. *Flexure testing results*

All flexure testing results can be found in Table 6.2. The area under the stress-strain curve (see Figure 6.3) is the strain energy density (u_f) which is also mentioned as the strain energy per unit volume (J/m^3) in some literature. The strain energy density during flexural test is thus defined as:

$$u_f = \int \sigma \cdot d\varepsilon \tag{6.1}$$

where σ = flexural stress; ε = flexural strain.

Table 6.2 Flexure testing results

Reference	Orientation	Flexural strength (MPa)		Flexural modulus (GPa)		Strain energy density (GJ/m^3)	
		Average	Standard Deviation	Average	Standard Deviation	Average	Standard Deviation
F1689_Flex	[90/0/90] /PE	259.3	6.9	7.5	0.7	637.4	50.7
F1690_Flex	[0/90/0] /PE	1634.2	46.0	36.1	0.9	3451.3	264.4
F1691_Flex	[±45/0/±45] /PE	512.1	28.4	15.8	1.1	1129.0	135.9
F1692_Flex	$[90/0]_S$ /PE	392.7	7.8	13.0	0.5	967.2	58.2
F1693_Flex	$[\pm45/0]_S$ /PE	651.6	19.4	18.6	0.5	1459.1	101.2
F1694_Flex	$[PW400/0]_S$ /PE	907.7	58.0	27.5	1.9	2239.0	223.0
F1695_Flex	$[90/0_2]_S$ /PE	607.4	12.9	17.5	0.6	1457.3	104.9
F1696_Flex	$[\pm45/0_2]_S$ /PE	775.5	20.0	21.6	1.3	1786.8	124.9
F1697_Flex	$[90/\pm45/0]_S$ /PE	341.1	7.7	13.5	0.5	823.0	30.3
F1698_Flex	$[90/0]_{2S}$ /PE	644.5	17.1	18.5	0.3	1676.1	154.5
F1699_Flex	$[\pm45/0_3]_S$ /PE	869.9	26.7	23.7	1.1	2086.8	49.8
F1700_Flex	$[90/\pm45/0_2]_S$ /PE	428.6	9.5	14.0	0.4	1097.3	74.4
F1707_Flex	$[90/0_2]_S$ /VE	510.5	15.4	15.3	0.6	1330.6	36.3
F1710_Flex	$[90/0_2]_S$ /EP	987.9	22.4	13.7	0.9	2334.3	174.8

PE = Polyester; VE = Vinyl ester; EP = Epoxy

The data of flexural strength and flexural modulus (modulus of elasticity) are plotted in Figure 6.2. The strain energy density at flexural strength is calculated for each flexure testing sample. These results are also plotted in Figure 6.4. The flexural modulus of highly anisotropic laminates depends on the ply stacking sequence and is also dependent on the in-plane Young's modulus of laminate, but does not necessarily have the same result [108].

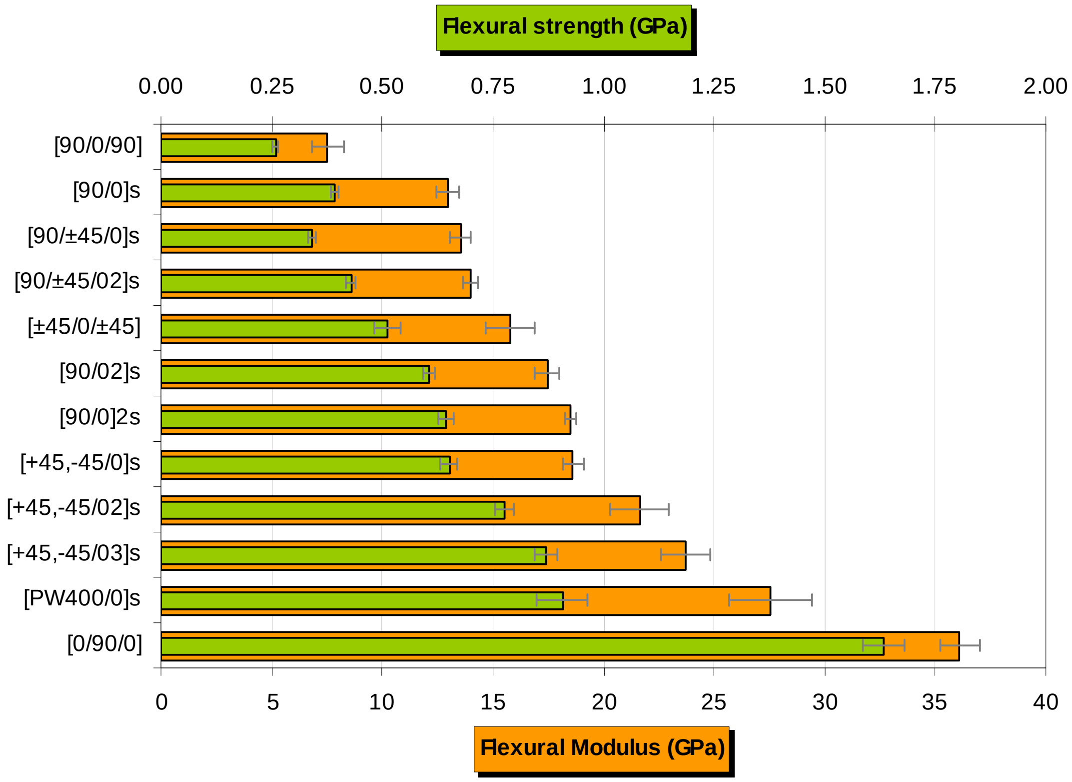

Figure 6.2 Comparisons of flexural strength and bending modulus

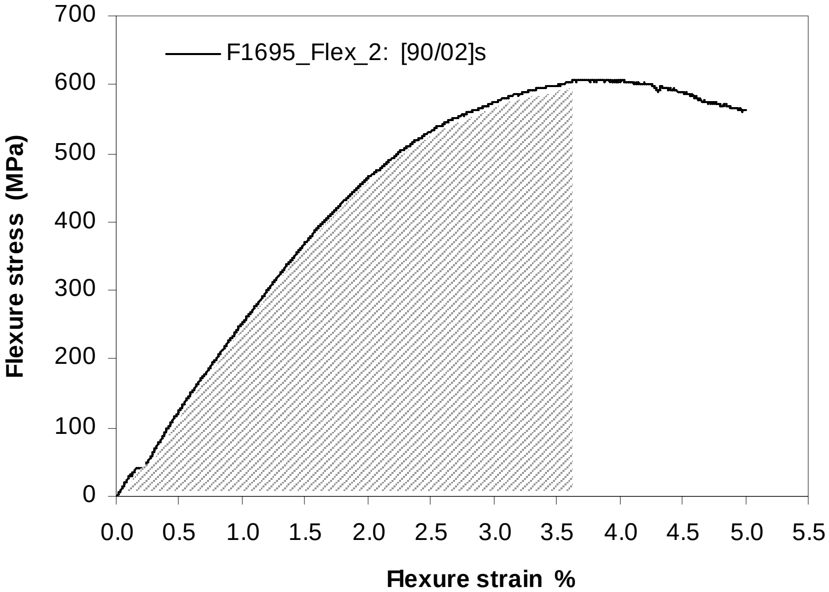

Figure 6.3 Schematic sketch of determination of strain energy density at flexural strength

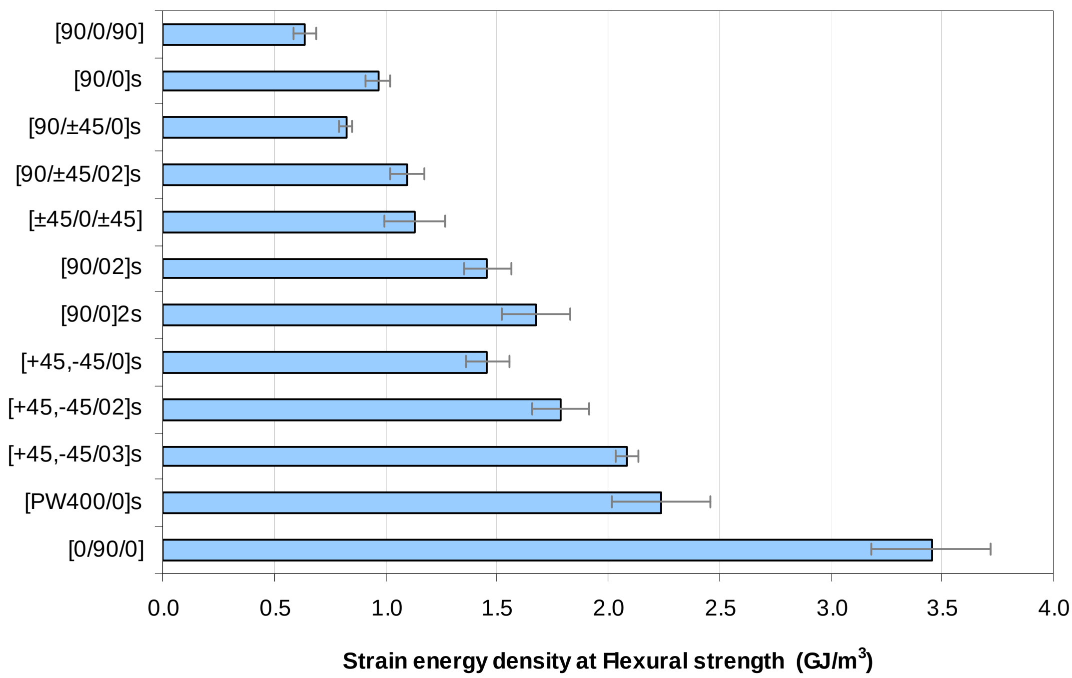

Figure 6.4 **Results of strain energy density at flexural strength**

In Figure 6.2 and Figure 6.4, the flexural strength, bending modulus and strain energy density show a very similar trend within these tested materials. The flexural performance of these materials increases with increasing percentage of the 0° fibres. It can be found that [0/90/0] sample achieves the highest flexural strength, modulus and strain energy density, and their flexural results exhibit values about five times larger than [90/0/90] samples. The triaxial samples generally possess better flexural properties than biaxial, because ±45° fibres undertake some stress under bending loads while 90° fibres hardly do.

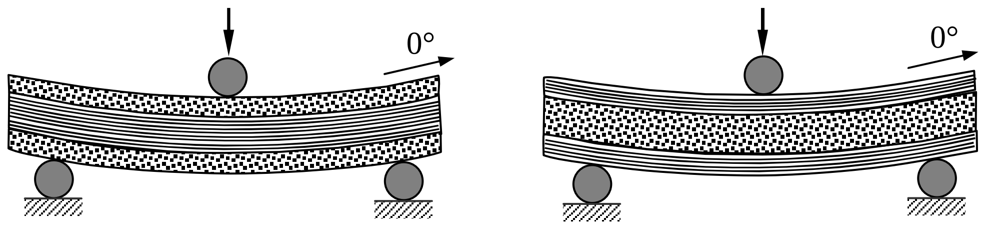

Figure 6.5 **Comparison of 0° fibres locations in three-point bending: 0° in inner layers (left) and 0° in outer layers (right)**

It is interesting to note that both F1695_Flex ($[90/0_2]_S$) and F1690_Flex ([0/90/0]) have the same proportion of 0° fibres, but F1690_Flex possesses approximately double the flexural properties of F1695_Flex. The reason for this is due to the position of 0° fibres. The laminated beam can be considered as a small-scale sandwich beam. According to previously mentioned equation 2.20 and equation 2.21, the flexural rigidity of a sandwich beam is mainly controlled by the flexural modulus of outer layer materials (see Figure 6.5). Therefore, [0/90/0] samples exhibit a greater stiffness than $[90/0_2]_S$ samples.

More interesting to note that the order of the above results plotted in Figure 6.2 and Figure 6.4, is very close to the results order of SEA values that were obtained from crushing test on same materials (see Figure 5.16). It seems that the energy absorption capacity of composite materials is linked to their flexural properties.

6.3. Discussion

For all geometric cells investigated in Chapter 5, the stitching lines were always along the direction of 0° fibres in these cells. Because of this configuration, the stitching yarn has much less chance to hook the external fabric layers when the external fabric layers are 0°. As a result, the interlaminar fracture toughness properties of these laminate can be significantly reduced if the stitches are only constrained by matrix.

Because the [0/90/0] geometric cell failed in a relatively low effective crushing mode with an early central crack, it is not included in this discussion. Apart from the [0/90/0] composite sample, all the other specimens failed via a stable lamina bending mode in the core section. Moreover, all crushing data which are presented in this section are the "potential energy absorption capacity" of composite structures. The term of the potential energy absorption capacity has been defined previously in Section 5.4.

6.3.1. Comparisons between flexural modulus and SEA data

As the flexural modulus of composite laminate increases with an increase in the proportion of 0° fibres, the energy absorption capability of structural composites were found to be closely linked to flexural modulus. The comparison between SEA data and flexural modulus for biaxial and triaxial samples plotted against the weight fraction of 0° fibres in Figure 6.6 and Figure 6.7, respectively.

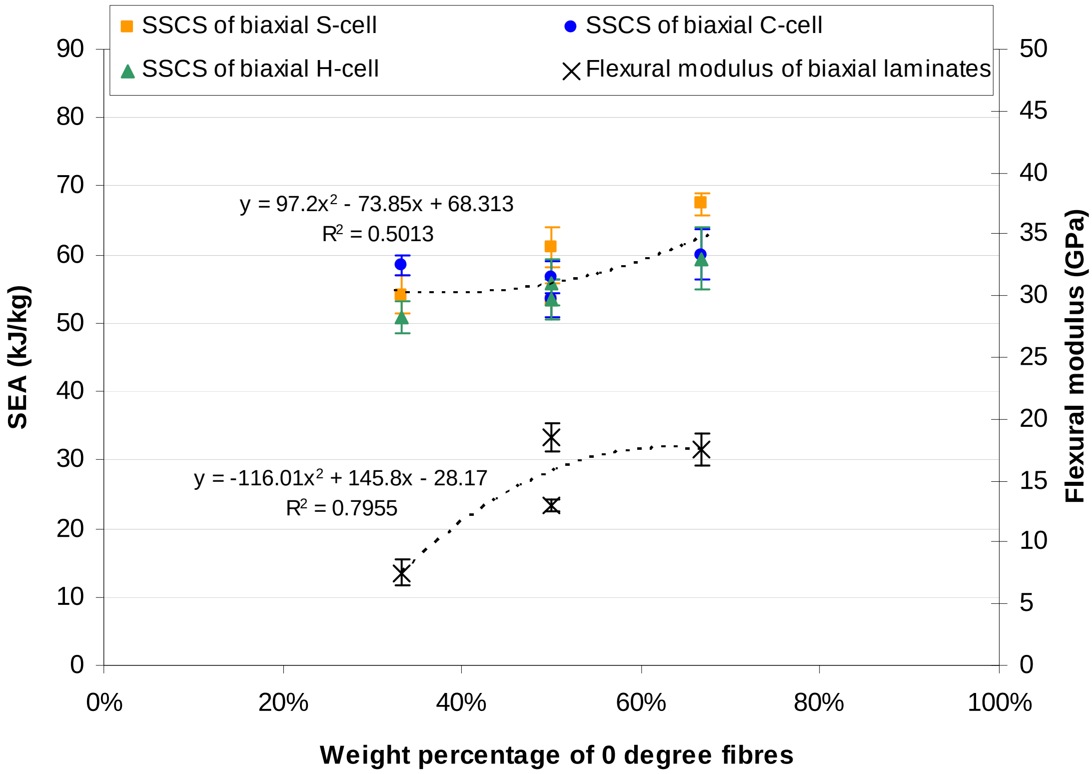

Figure 6.6 The relationships between potential energy absorption capability, flexural modulus and weight fraction of 0° fibres for biaxial laminates

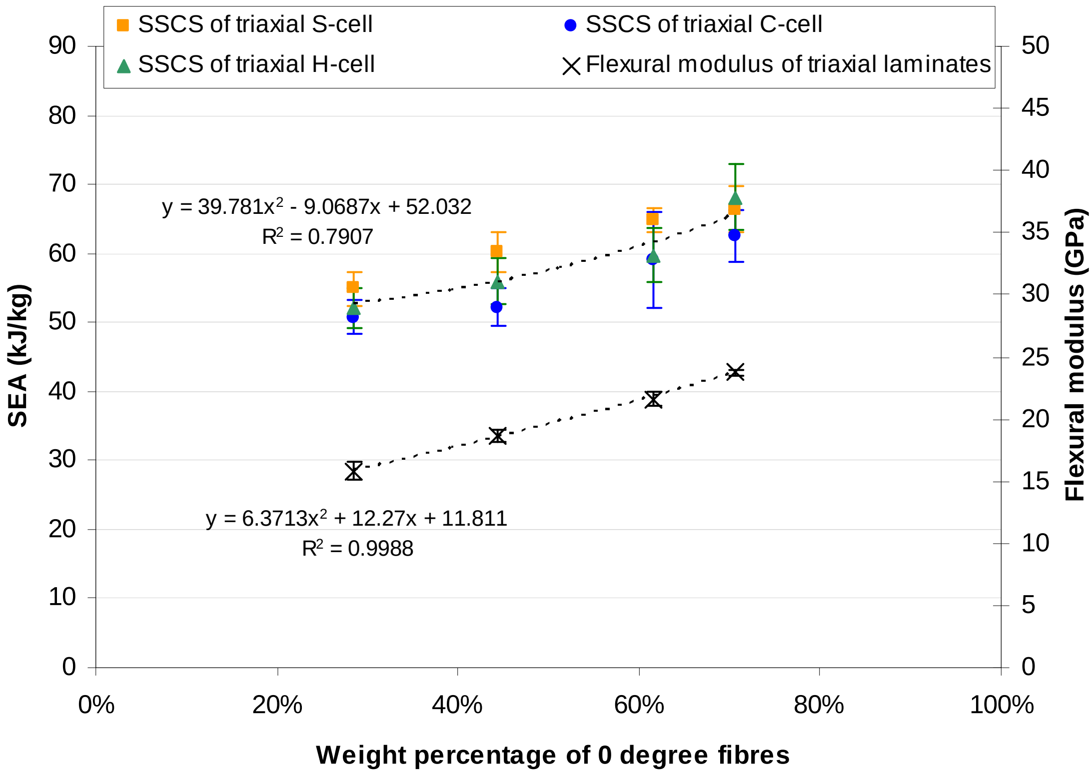

Figure 6.7 The relationships between potential energy absorption capability, flexural modulus and weight fraction of 0° fibres for triaxial laminates

Both Figure 6.6 and Figure 6.7 indicate that the SEA levels and flexural modulus of most crush test samples tend to increase with an increase in the weight fraction of 0° fibres, especially for triaxial samples. Combining biaxial data and triaxial data as well as the quadriaxial data, the relationships between potential SEA values and flexural moduli are compared in Figure 6.8. It shows that the SEA level of composite material increases when the flexural modulus increases.

Although triaxial laminates possess higher flexural moduli than biaxial laminates, thin triaxial C-cells, especially the [±45/0/±45] and [±45/0]S C-cells, exhibit lower energy absorption capacity than biaxial C-cells. Quadriaxial cells have moderate modulus and also achieved moderate energy absorption values. It seems that the energy absorption capability of structural composites is not only dependent on longitudinal fibres, in some cases lateral fibres also can absorb considerable amount of crushing energy.

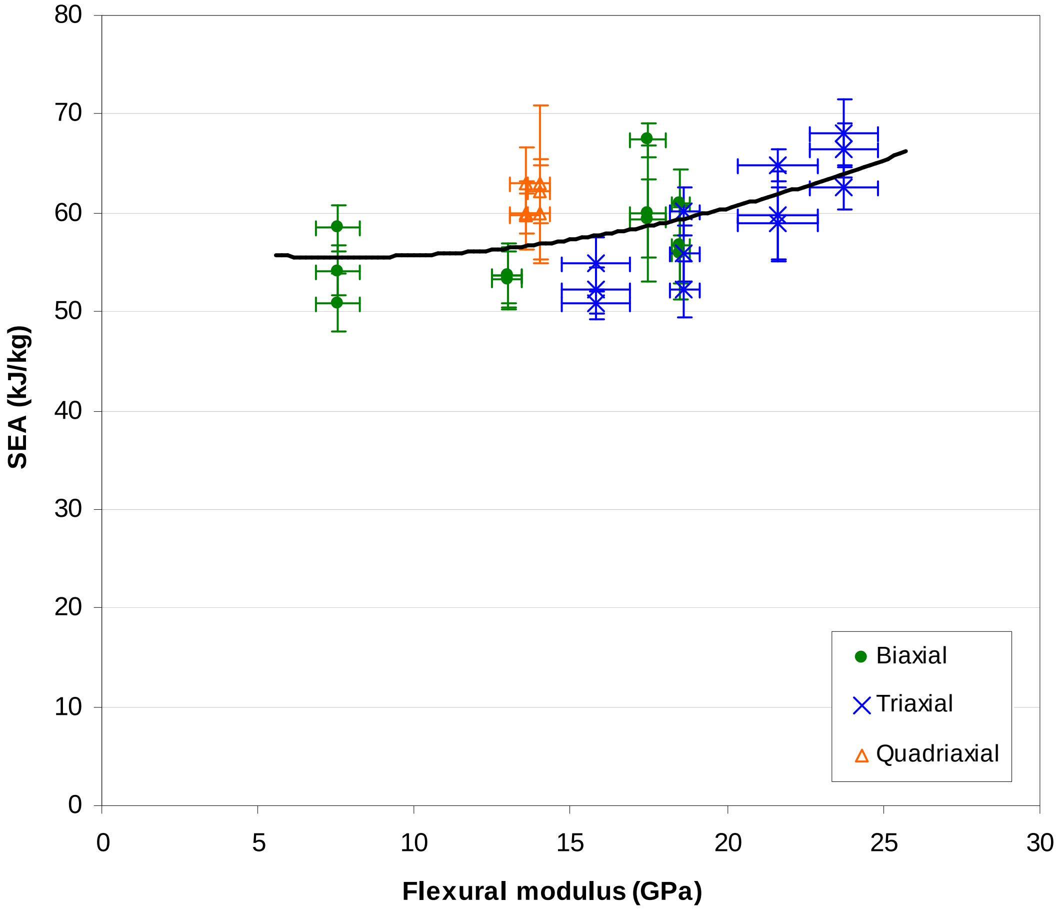

Figure 6.8 Potential energy absorption capability vs. flexural modulus for all laminates grouped according to lay-ups

Figure 6.8 also reveals that, at the same level of flexural modulus, the laminates containing 90° fibres achieved higher SEA values than the triaxial laminates that only contain ±45° and 0° fibres. The reason is that the 90° fibres provide a constraint to deformation, much the same as the hoop-wound fibres do in tubular structures during crushing process [15].

From the data presented in Figure 6.8, the cells which have the same shape are now considered as one group, and the data and trendlines are plotted in Figure 6.9. Thus, the relationship between SEA and flexural modulus can be seen regarding to different geometries of composite sample, irrespective of fibre lay-up. The R-squared values shown in Figure 6.9 indicate how good those second-polynomial equations are statistically predicting the trend of data. These R-squared are very low.

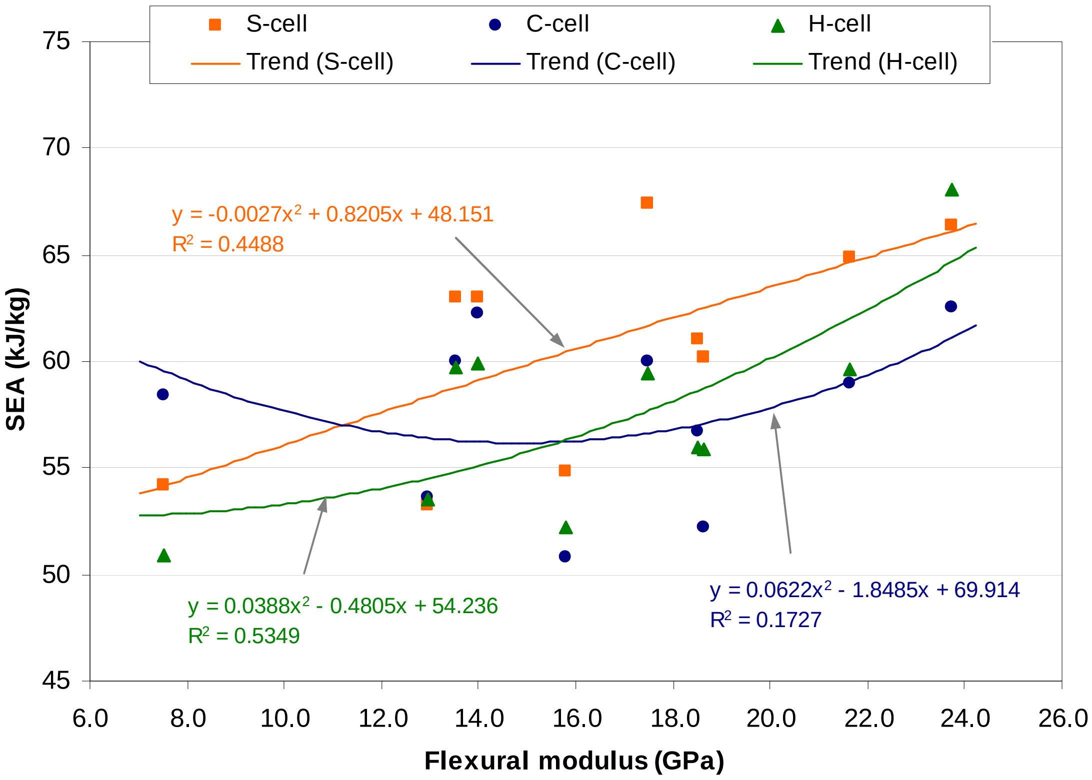

Figure 6.9 Data comparison of different geometries on SEA – flexural modulus curve

Furthermore, it has been concluded in last chapter that SEA levels increase with the increasing of thickness/Perimeter (t/P) ratio, where t = 2h (see Figure 5.1). It could be meaningful to consider both effects of materials property (flexural modulus) and scale (t/P ratio) together. Therefore, Figure 6.10 and Figure 6.11 are plotted below, where E/(t/P) is plotted against SEA for samples grouped according to cell geometry and lay-up.

It seems all data are located in a clearer region instead of dispersedly distributed in Figure 6.8 and Figure 6.9. Comparing Figure 6.10 with Figure 6.8, although triaxial samples have higher flexural moduli, data of these thinner triaxial samples in Figure 6.10 become closer to those thin biaxial samples. In addition, the trendline equations and R-squared values shown in Figure 6.11 fit the data better than those shown in Figure 6.9.

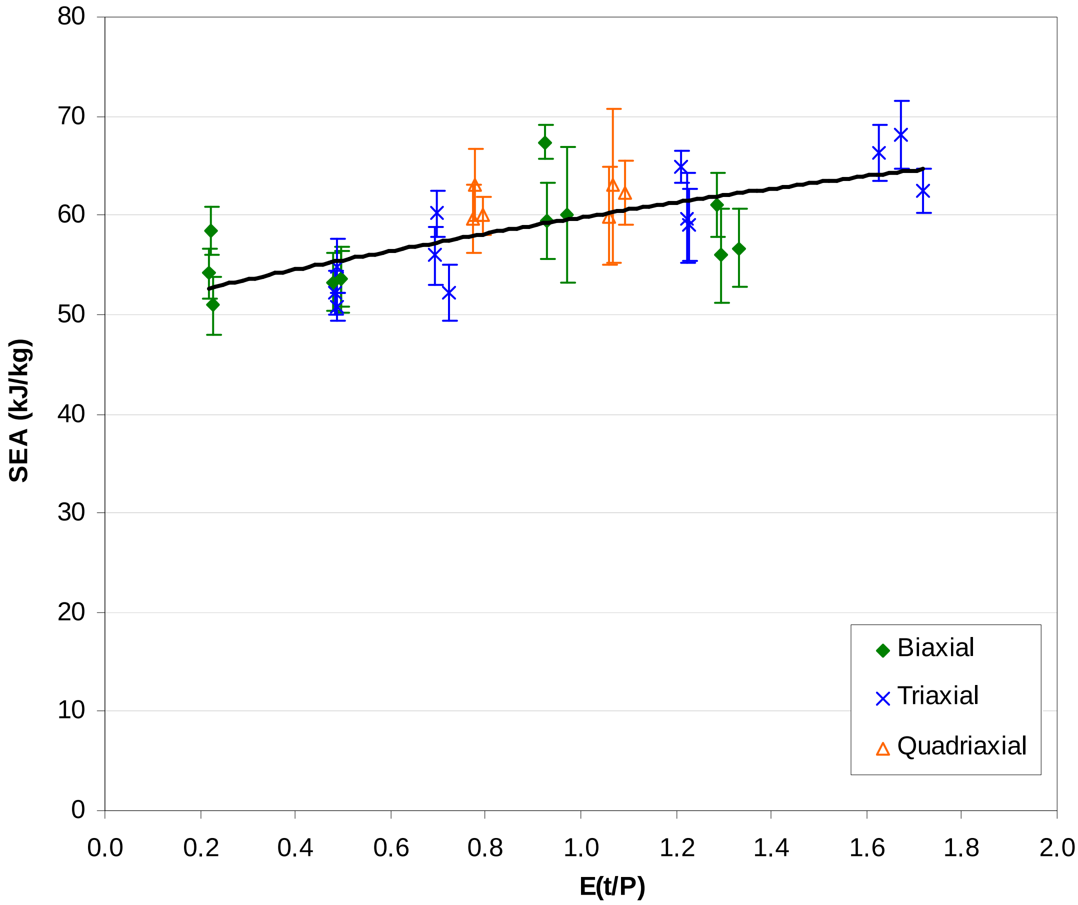

Figure 6.10 **Data comparison of different lay-ups on SEA – E*(t/P) curve**

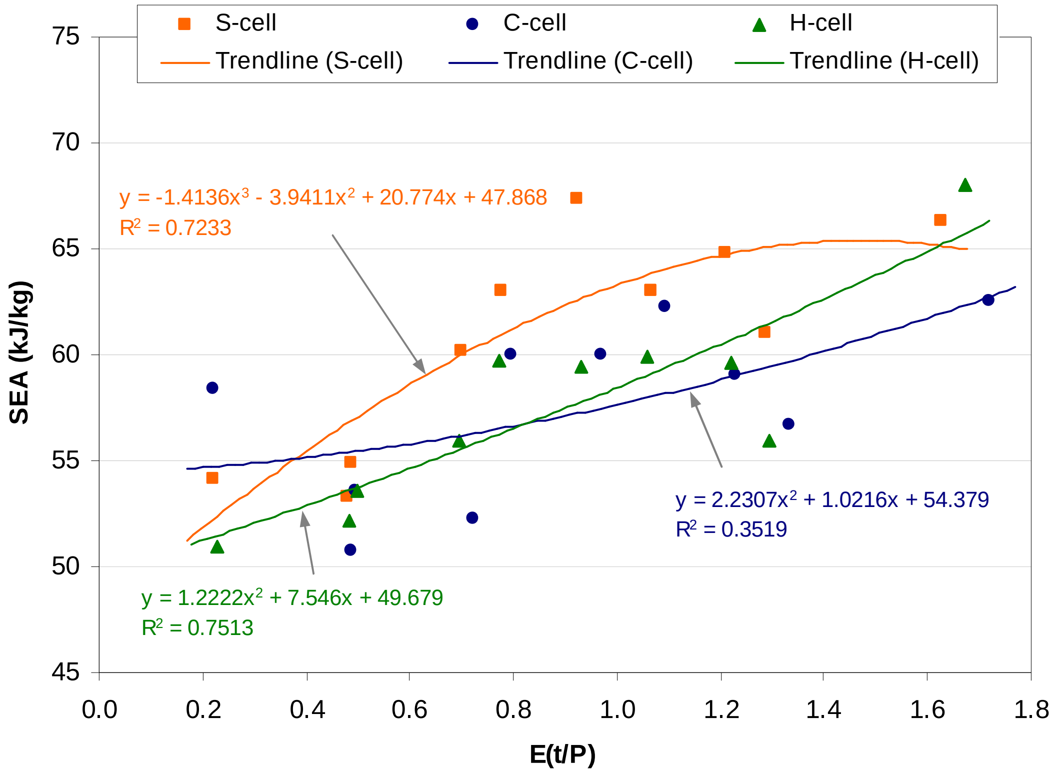

Figure 6.11 **Data comparison of different geometrical shapes on SEA – E*(t/P) curve**

Up to this point, the conclusion can be drawn that, the energy absorption capacity of a structural composite crushed in lamina bending mode is related to the bending radius of curvature of splaying fronds, dimensional scale and flexural modulus. Fundamentally, the flexural modulus of fibre-reinforced material is dominated by the content of 0° fibres and also the fibres which have small angle of orientation.

Therefore, the flexural rigidity of composite materials which involves both dimensional factors and flexural modulus should be considered in an evaluation of the energy absorption capacity of structural composite.

6.3.2. Relationship between SEA and flexural rigidity

The flexural rigidity, D, which is also known as bending stiffness, is a measure of stiffness of a structural member. It seems to play a critical role on the crushing forms. During crushing, tearing not only occurs along the stitches on the cell, but also takes place between the corrugated core and flat sides. Thus, the splaying fronds can be simply considered as a bent beam, which is demonstrated in Figure 6.12.

The flexural rigidity of the beam is defined as [109]:

$$D = EI \tag{6.2}$$

where E = flexural modulus,

I = second moment of area, and is frequently called moment of inertia of area.

In present study, the second moment of area, I, can be expressed as [110]:

$$I = \frac{bh^3}{12} \tag{6.3}$$

where b = width of the cross section area of the beam, and

h = thickness of the beam.

Substituting equation 6.3 into equation 6.2 we obtain,

$$D = \frac{Ebh^3}{12} \tag{6.4}$$

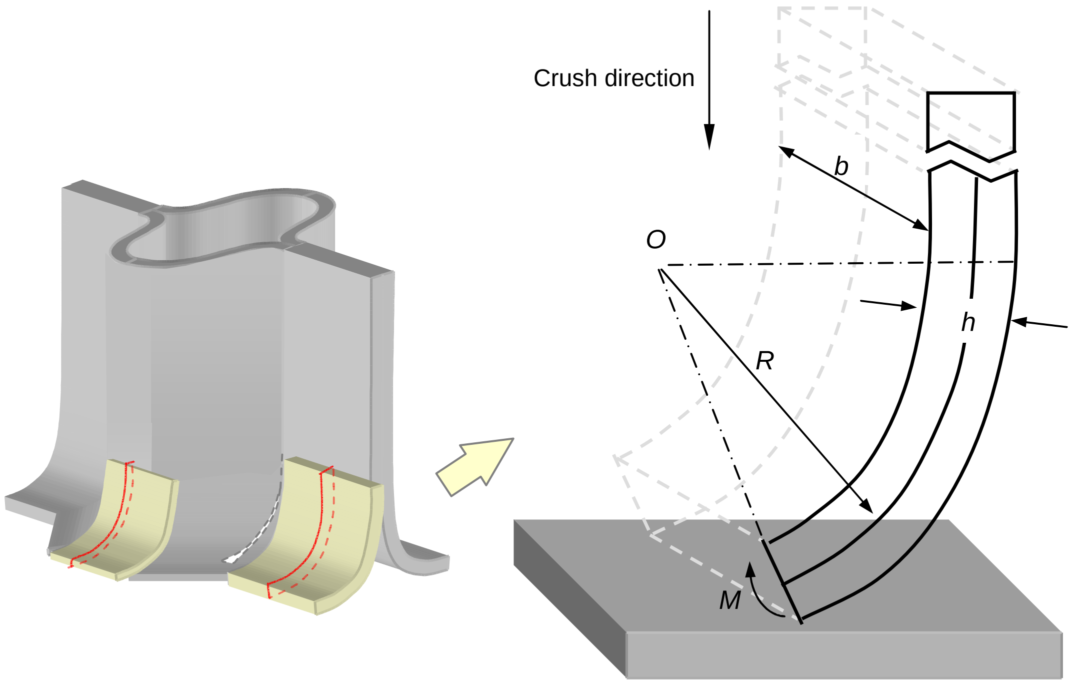

Figure 6.12 Schematic sketch of bending fronds

As can easily seen from equation 6.4, the flexural rigidity of a cell strongly relies on its flexural modulus, width of fronds, and especially the thickness of its laminate. Compared with the corrugated core section, the crushing forms of the section of flat side behaved in a complex fashion. Apart from the buckling issue, the energy absorption capability of cells could be significantly decreased if the laminate is too rigid to bend. When the laminate becomes more rigid, the crushing sample may not benefit from the energy absorbing mechanisms of Mode-II delaminations (U_{de}), bending of the fronds (U_{σ}), fibre fracture (U_{ff}), and friction within crushed fronds (U_{fr}), (see equation 2.5).

Due to the failure of the adhesive, stiffer (and normally thicker) cells tend not to bend at the section of the flat side after being triggered. Instead, the glued geometric cell splits itself back to two separated parts during crushing. This phenomenon also can also be seen in Figure 5.7a. Therefore, to achieve the best performance of these energy absorbing prototypes, the balance amongst thickness, modulus, and bonding effectiveness at flat sides must be optimised.

Furthermore, the radius of curvature is given by [109],

$$R = \frac{D}{M} \tag{6.5}$$

and is therefore directly proportional to the applied bending moment and inversely proportional to the flexural rigidity of the bending beam. To reduce the radius of curvature on the splaying fronds, bonding effectiveness between along the flat sides needs to be improved. A co-infusion process or high performance adhesive could be applied for this purpose. At the latter stage of this research, stitching mechanism is adopted to bond cell halves, as well as Taguchi method is used as the optimization technology. According all the conclusions stated above, the transition map of crushing forms for those geometric cells which were investigated in Chapter 5 is plotted in Figure 6.13.

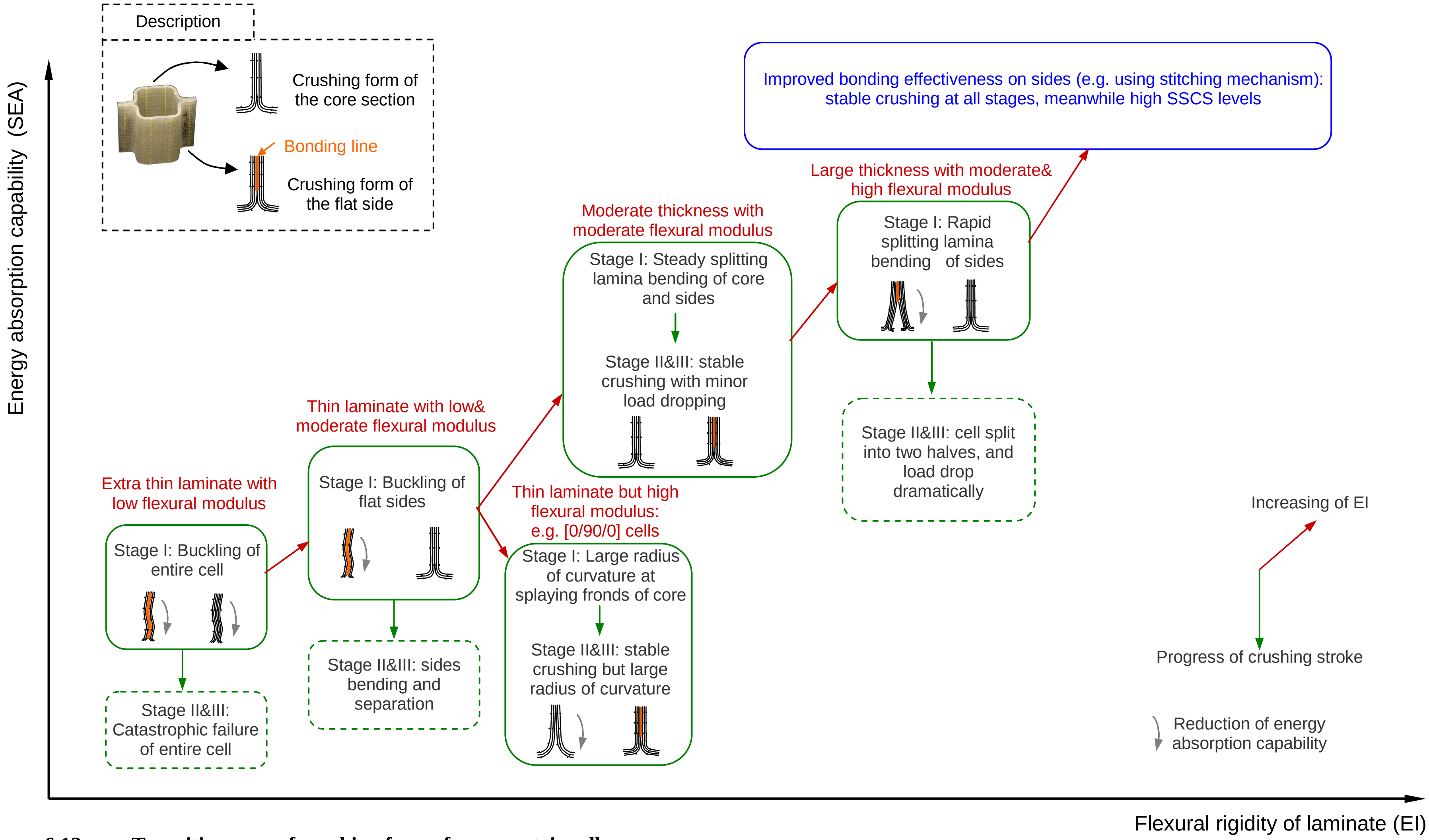

Figure 6.13 **Transition map of crushing forms for geometric cells**

6.3.3. Effects of matrix

The matrix system of all samples which were investigated before this section was polyester. It is believed that the matrix system has a measurable influence on the crushing behaviours of composite materials. In addition to polyester, two other widely used thermosetting matrices, vinyl ester resin and epoxy resin, were also investigated on triaxial ($[90/0_2]_S$) samples. The flexural moduli of these triaxial samples are shown in Figure 6.14.

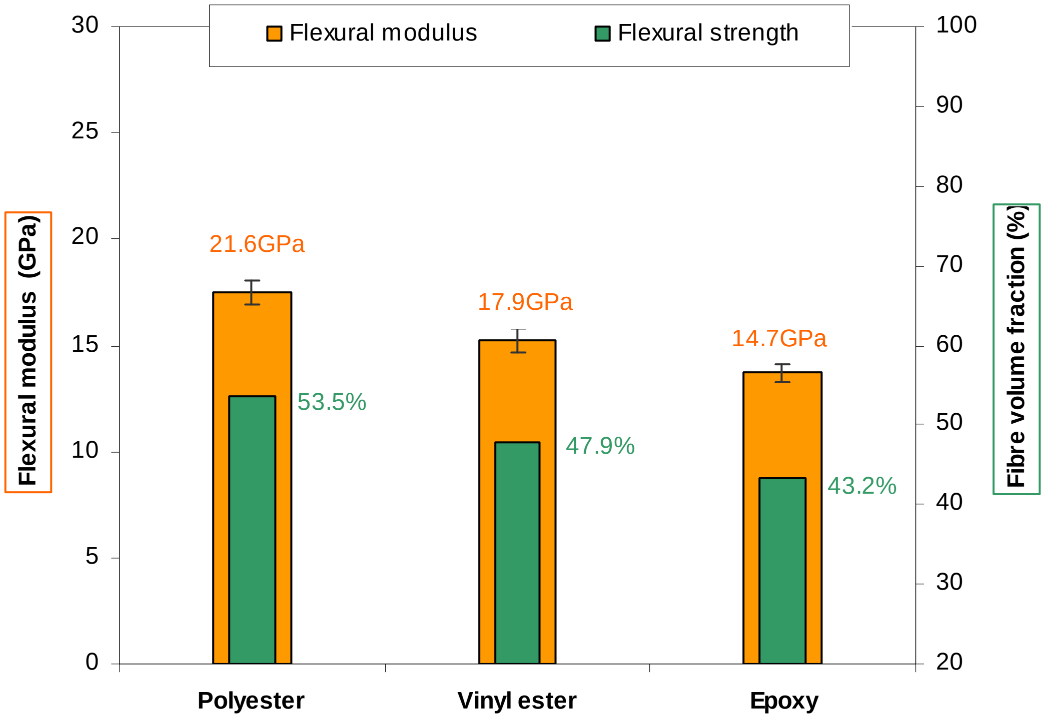

Figure 6.14 Effects of resin systems on triaxial ($[90/0_2]_S$) flexure samples

The reinforcement of resin with fibre to form a composite will produce a progressive increase in tensile properties, the increase following the rule of mixture. It is important to remember that the flexural modulus which is proportional to the tensile modulus, is also proportional to the fibre volume fraction [65].

The flexural modulus of composite laminates shown in Figure 6.14 seems not to be a function of the elastic modulus of their matrix system (see Table 3.3), but is proportional to their fibre volume fraction. It reveals in Figure 6.14 that the flexural modulus decreases linearly with the decreasing of fibre volume fraction of composite laminates. The relation between flexural modulus and fibre volume fraction for fibre-reinforced polymer composites also has been investigated by other researchers [65, 111-113], either experimentally or theoretically.

The rules of mixtures [103] and the expression of flexural modulus (Appendix A1.5) are written in following equation 6.6 and equation 6.7, respectively:

$$E_{11} = E_f V_f + E_m V_m \tag{6.6}$$

$$E_{ij}^{flex} = \frac{8}{n^3} \sum_{k=1}^{n/2} \left(\overline{Q}_{ij}\right)_k \left[k^3 - (k-1)^3\right], \qquad (i, j = 1, 2, 6) \tag{6.7}$$

where E_f and E_m are the elastic modulus of fibres and matrix, respectively. V_f and V_m are the volume fraction of fibres and matrix, respectively. The equation 6.7 is based on the usual assumption of classical theory of thin lamina in which a composite plate consists of many layers of transversely isotropic unidirectional lamina. When a tensile or compression load is applied to the certain direction (direction 1 in this case), it is assumed herein that the bond between matrix and fibre is perfect and the strain in matrix is the same as in fibre.

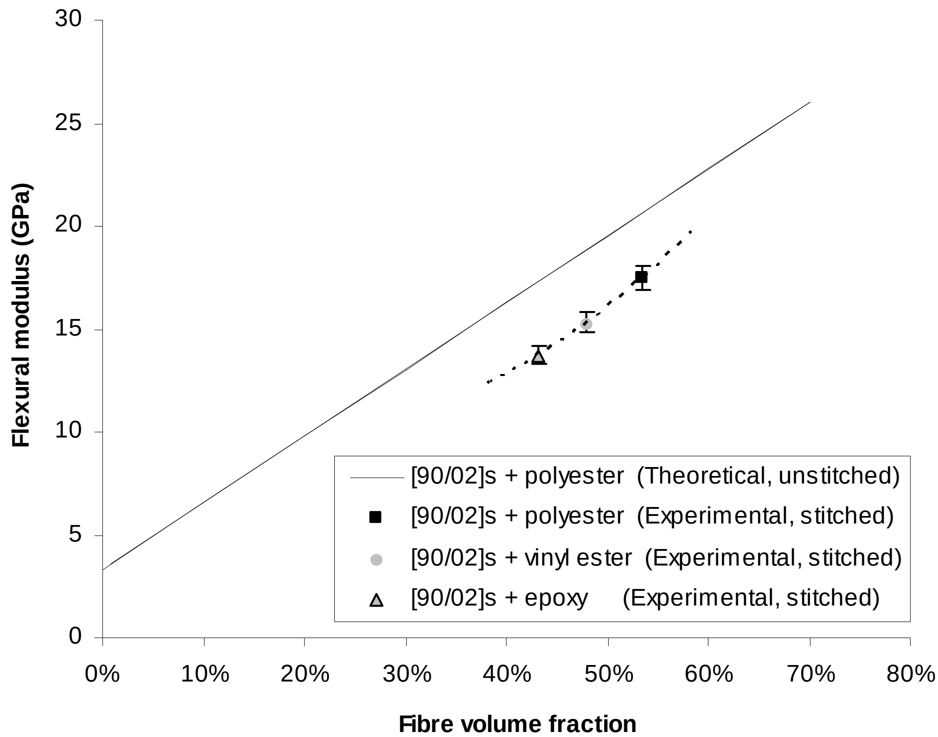

Figure 6.15 Comparisons between theoretical prediction and experiment results on flexural samples made of different resin types

The lamina elastic properties used in the calculation are based on the UD GFRP lamina. The UD GFRP composites which possess the fibre volume fraction of 53.8% have been listed previously in Table 3.5. By varying the volume fraction of fibres, a set of elastic moduli of the UD lamina with same materials are obtained. Then, for a multi-directional laminate with built up by this UD lamina, the flexural modulus can be also obtained once fibre volume fraction is predetermined.

Therefore, according to the rule of mixtures and the expression of flexural modulus for a composite laminate, the curve of the flexural modulus versus fibre volume fraction of the $[90/0_2]_S$ laminate is then plotted and shown in Figure 6.15. It clearly reveals that the trendline based on experimental data almost has the same slope as the trendline based on theoretical calculation, which is independent of resin type. In other words, in comparison to the properties of matrix, the fibre volume fraction plays more important role on the flexural modulus of composite laminates.

Equally important, the samples which are composed of polyester resin and are predicted by theoretic equations apparently have higher flexural moduli, than the samples composed of same materials and measured experimentally. Compared with the theoretic results, the reduction observed in the experimental data is probably due to the uniform distribution of fibres in the matrix, which was caused by through-thickness stitches.

This was also found in another research that the flexural modulus of the stitched laminates could be more than 15% lower than those of the unstitched laminate. Furthermore, this reduction would increase along with the increasing of stitching density [114].

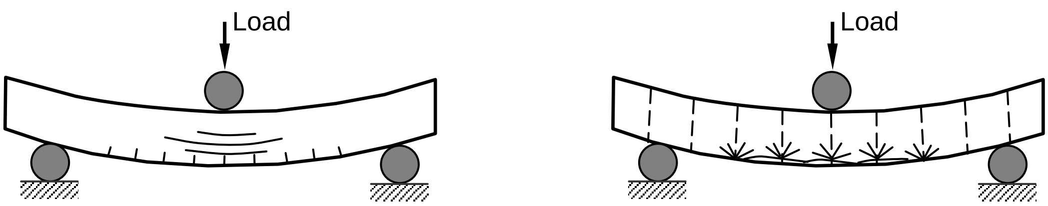

Figure 6.16 Schematic sketches of an unstitched flexural specimen (left) and a stitched flexural specimen (right) showing the locations of bending damages [114]

In general, the unstitched laminate failed by the rapid growth of delaminations combined with the compressive buckling of the fabric plies. To reach this, the flexural stress needs to be raised to a relatively higher level. Whereas, the stitched samples would start to generate damages around the stitching knots on the tensile side, instead of accumulating stresses for delaminations between plies. The comparison of flexural behaviours between unstitched and stitched samples are demonstrated Figure 6.16.

6.4. Summary

The flexural properties of composite materials are highly dependent on the content of 0° fibres, although the position of 0° fibres can also significantly impact the flexural performance. But it cannot be simply concluded that composite materials possessing more 0° fibres (or superior flexural modulus) must absorb more energy during crushing. A certain amount of crushing energy can be also consumed by fracturing of lateral fibres (90° fibres).

The relationship between flexural properties and energy absorption capability of composite materials is complicated. The SEA levels of composite materials increase non-linearly with increasing flexural modulus. However, a simpler relationship becomes apparent when the geometrical factors are introduced. In the other words, energy absorption capability seems to be controlled by the flexural rigidity of composite structures. This standpoint becomes more practically significant when composite samples made of different matrix systems are compared at the same time.

As mentioned in the literature review that the larger the radius of curvature, the lower energy would be absorbed by composite structure during crushing. It is interesting to note that composite cells possessing very high flexural rigidity generally crushed with early central crack growth. Consequently, their energy absorption capabilities are decreased due to early central crack growth.

Ideally, if two parts of a cell were perfectly glued or intensively bonded, the early central crack growth could be avoided during crushing. Thus, not only for the core section, stitching technology also ought to be introduced for binding two parts of the cell instead of adhesive.

Chapter 7. Fracture Toughness

In order to compare all DCB and 4-ENF testing results directly with the crushing results, the orientations and lay-ups were selected specifically. For comparison reasons, all these tests were performed on glass fibre and either polyester, vinyl ester or epoxy resins.

7.1. Fracture toughness tests: DCB and 4-ENF

Previous work based on composite plates [24], has shown that the SEA is related to the fracture toughness properties of the composites. It also revealed that this relationship is complicated and highly dependent on the interfacial performance between fibres and matrix. In order to achieve a higher SEA, rapid or early central crack must be avoided. This requires the Mode-I crack initiation value and the Mode-I crack propagation value between central laminas to be carefully controlled. Mode-II properties also show a strong correlation with the SEA indicating that shear cracking is an important factor in controlling the energy absorption of composite plates [24].

According to the evidence discussed in the literature and previous chapters, Mode-I and Mode-II fracture toughness properties can be optimised by varying stitching density [2]. Therefore, both Mode-I and Mode-II properties of stitched composite samples which have different fibre orientations were investigated. In addition, unstitched samples were compared with stitched samples so that the effectiveness of stitching could be evaluated.

For the purpose of directly comparing DCB/ENF results with crushing results in a parallel level, the selection of DCB and 4-ENF materials followed the configuration of the crushing samples. Thus, the Mode-I fracture toughness properties were measured in samples at the interface of 0/0, 90/0 and +45/-45, while Mode-II fracture toughness properties were only measured at the interfaces of 0/0, 90/0, +45/-45, 45/0, 45/90 and 0/plain woven.

7.1.1. DCB testing samples and testing results

In total, the eleven DCB sample types that are listed in Table 7.1 were tested. The first six samples were compared between stitched and unstitched samples by evaluating the effects of stitches on varying internal lay-ups.

Table 7.1 DCB testing Samples

Reference	Orientation	Matrix	Stitching	Thickness h (mm)	Width D (mm)	VF%
F1583_DCB	$[0_4\text{^}0_4]$	Polyester	No	2.976	19.91	53.3
F1595_DCB	$[0_3/90\text{^}0_4]$	Polyester	No	3.284	20.08	53.2
F1676_DCB	$[0_3/\pm45\text{^}\mp45/0_3]$	Polyester	No	3.416	20.06	48.2
F1680_DCB	$[0_4\text{^}0_4]$	Polyester	Yes	3.354	19.93	47.0
F1681_DCB	$[0_3/90\text{^}0_4]$	Polyester	Yes	3.347	19.98	47.8
F1682_DCB	$[0_3/\pm45\text{^}\mp45/0_3]$	Polyester	Yes	3.520	19.98	47.0
F1686_DCB	$[90/0_2\text{^}0_2/90]$	Polyester	Yes	2.309	20.03	51.0
F1687_DCB	$[\pm45/0_2\text{^}0_2/\mp45]$	Polyester	Yes	2.514	20.04	50.5
F1713_DCB	$[\pm45/0_2\text{^}0_2/\mp45]$	Vinyl ester	Yes	2.652	19.88	45.3
F1716_DCB	$[\pm45/0_2\text{^}0_2/\mp45]$	Epoxy	Yes	2.724	20.00	42.5
F1758_DCB	$[0_6/\pm45/0_2\text{^}0_2/\mp45/0_6]$	Epoxy	Yes	7.251	20.16	47.5

The symbol " ^ " indicates the position of insert film in fabrics; VF: Fibre volume fraction;

Practically, external fabrics might also affect the stitching effectiveness on the Mode-I failure mode, therefore samples F1686_DCB and F1687_DCB were selected as the references to sample F1583_DCB. Two tougher matrix systems, vinyl ester and epoxy, were also investigated.

In the design of a DCB sample, the opening sample arms are required to behave as linear elastic beams. This requires the DCB samples to have a large thickness. Therefore in most situations, if the DCB sample is not thick enough, it is stiffened with extra layers of 0° unidirectional fibres. However, approaches [92, 115] also have been developed for solving the non-linear problem of thin DCB samples. These approaches showed that the strain-energy release rate, G_I, could be accurately calculated, even if large deflections and rotations occurred during test.

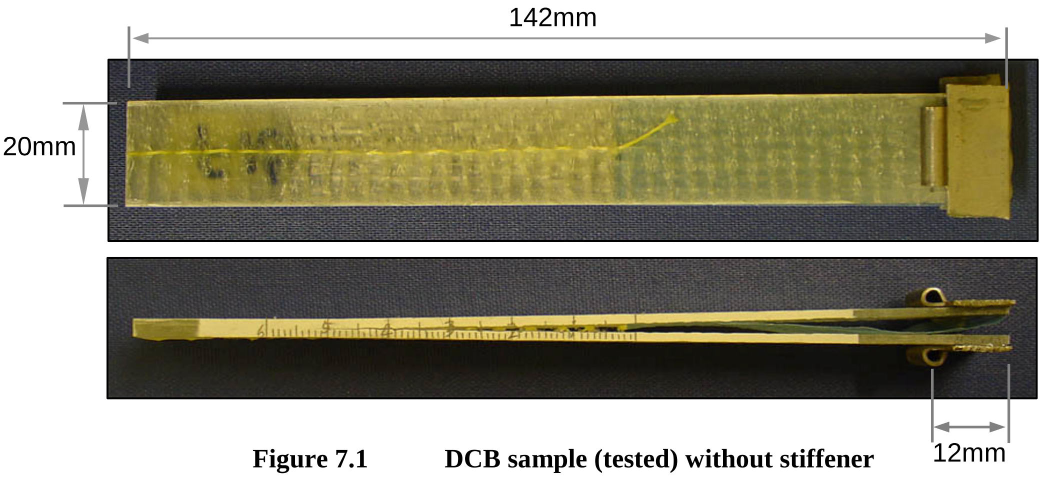

Figure 7.1 DCB sample (tested) without stiffener

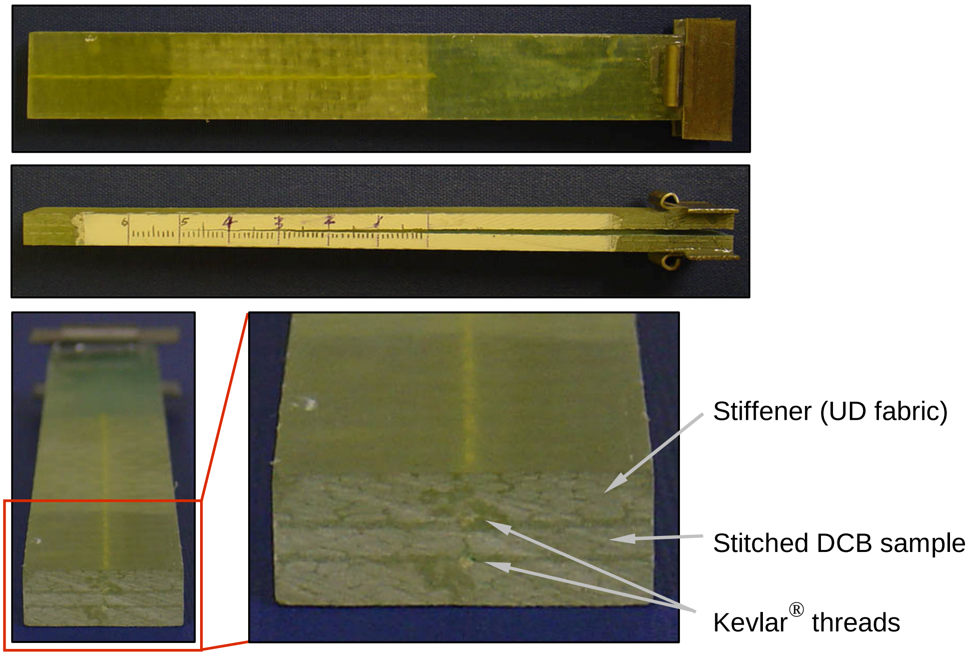

Figure 7.2 DCB sample (tested) with stiffener

Although it is more convenient to use thick samples to avoid theoretical or experimental drawbacks, in order to investigate the Mode-I fracturing behaviours under test conditions similar to practical cases, extra stiffening layers were not applied to most DCB samples. One of these non-stiffened DCB sample is shown in Figure 7.1.

In the calculation of G_I, large displacement effects for these thin samples were corrected by using a parameter, *F*, mentioned in ASTM D5528-01 [91]. This correction approach shows very similar results to the approach mentioned in Reference [92]. Furthermore, stiffened sample, F1758_DCB, were also tested for measuring the veracity of this correction. The stiffening materials (0° unidirectional fibres) were co-infused with stitched preforms during the manufacturing process. One of these stiffened DCB samples (F1758_DCB) is presented in Figure 7.2, and the location of stitches is identified.

Table 7.2 DCB testing results

Reference	Orientation	$G_{IC\text{-}VIS}$ (kJ/m^2)		$G_{IC\text{-}Prop}$ (kJ/m^2)	
		Average	Deviation	Average	Deviation
F1583_DCB	$[0_4$^$0_4]$ /PE*	0.332	0.037	0.451	0.071
F1595_DCB	$[0_3/90$^$0_4]$ /PE*	0.415	0.051	0.459	0.06
F1676_DCB	$[0_3/\pm45$^$\mp45/0_3]$ /PE*	0.793	0.085	0.994	0.141
F1680_DCB	$[0_4$^$0_4]$ /PE	0.335	0.037	1.223	0.191
F1681_DCB	$[0_3/90$^$0_4]$ /PE	0.521	0.095	1.564	0.133
F1682_DCB	$[0_3/\pm45$^$\mp45/0_3]$ /PE	0.978	0.158	1.681	0.181
F1686_DCB	$[90/0_2$^$0_2/90]$ /PE	0.263	0.106	0.789	0.204
F1687_DCB	$[\pm45/0_2$^$0_2/\mp45]$ /PE	0.524	0.094	1.192	0.071
F1713_DCB	$[\pm45/0_2$^$0_2/\mp45]$ /VE	1.105	0.258	1.482	0.12
F1716_DCB	$[\pm45/0_2$^$0_2/\mp45]$ /EP	1.284	0.266	1.543	0.21
F1758_DCB	$[0_6/\pm45/0_2$^$0_2/\mp45/0_6]$ /EP	1.124	0.266	1.497	0.146

* Non-stitched samples; the rest samples were stitched in the through-thickness direction;
The symbol " ^ " indicates the position of insert film in fabrics;
PE = Polyester; VE = Vinyl ester; EP = Epoxy.

The DCB testing results of the average propagation values ($G_{IC\text{-}Prop}$ and $G_{IIC\text{-}Prop}$) are shown in Table 7.2. The average propagation values were determined by approaches which are demonstrated in Figure 7.3. For some samples, their strain energy release rate (G_{IC} and G_{IIC}) on the Delamination Resistance Curve (R-curve) will also be reported in the latter Section 7.1.3.

Generally, if the interlaminar crack propagates evenly throughout the whole Mode-I opening process, a series of consistent $G_{IC\text{-}Prop}$ data form a plateau (see Figure 7.3, row A). But if the Mode-I crack becomes more difficult to propagate due to the fibre-bridging or stitching mechanism, the sample starts to bend. This means bent DCB sample would require further increments of displacement (see equation 3.1) to reach the next crack point. When the load is large enough to break down the bridged fibres or stitches, the crack propagates again at a higher plateau (see Figure 7.3, row B). In this case, consistent $G_{IC\text{-}Prop}$ data of both plateaus are taken account for calculating the average $G_{IC\text{-}prop}$ value. In some other situations, samples require more increments of displacement increment to reach the next crack point because the sample is bent too much due to bridged fibres or stitches. As a result, the R-curves tend to increases gradually instead of settling onto a plateau (see Figure 7.3, row C). Therefore, all G_{IC} data, which are behind the point where once the slope of R-curve drops, should be used for calculating the average $G_{IC\text{-}prop}$ value.

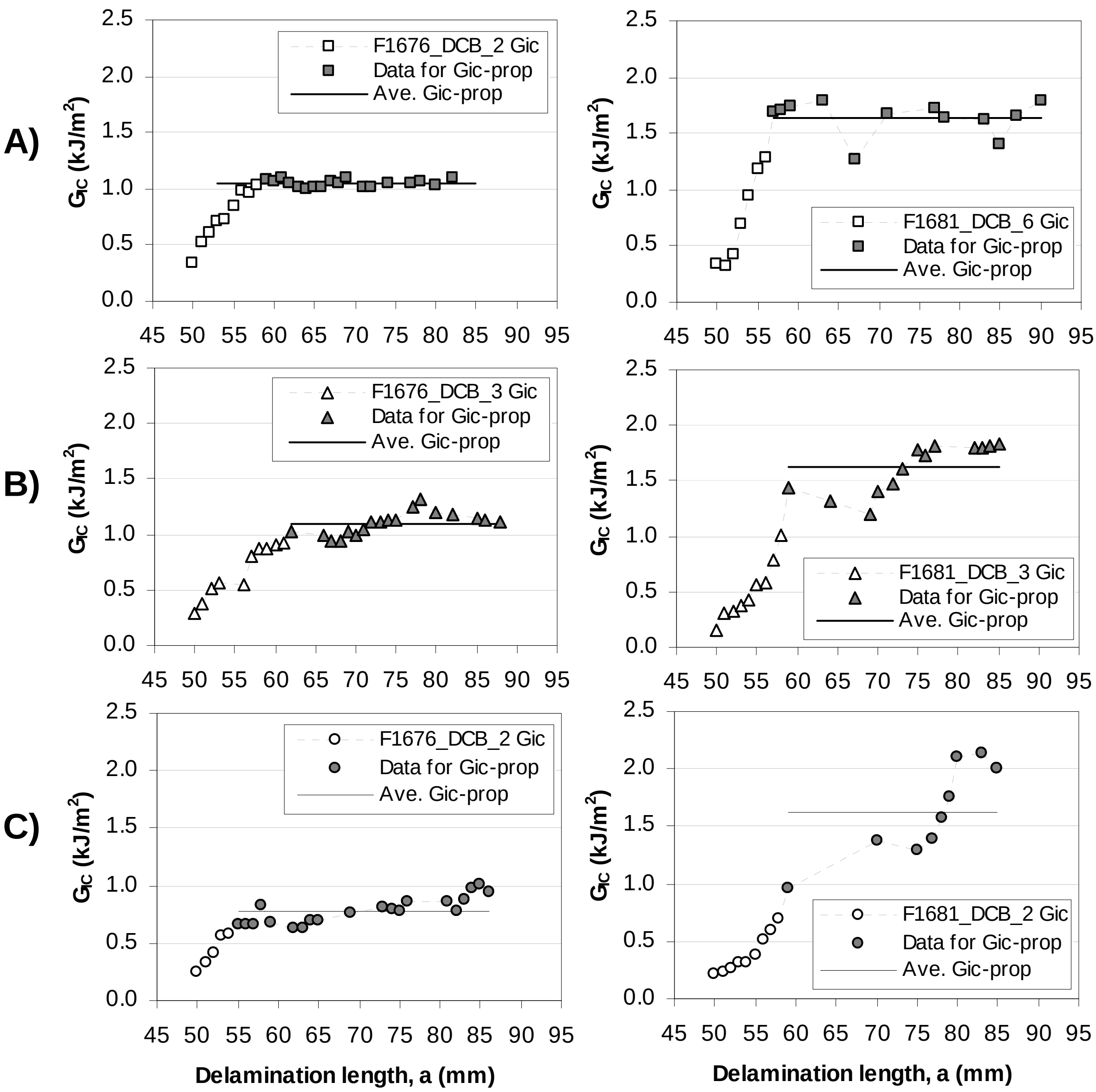

Figure 7.3 Determination of the average $G_{IC\text{-}prop}$ values on typical R-curves of Left) F1676_DCB unstitched $[0_3/\pm45$^$\mp45/0_3]$/Polyester; Right) 1681_DCB, stitched $[0_3/90^{\wedge}0_4]$/Polyester.

7.1.2. ENF testing samples and testing results

Similarly, six pairs of stitched/unstitched 4-ENF were compared at the early stage. These samples were selected to simulate and evaluate the Mode-II delamination behaviour within splaying fronds of crush samples.

Effects of resin toughness and external fabric layers were also measured for 4-ENF samples. In contrast to the DCB samples, all stitched 4-ENF samples were bonded with a stiffener on both sides. In samples without stiffeners it was found very difficult to generate delaminations during the 4-ENF test. A typical 4-ENF sample is shown in Figure 7.4.

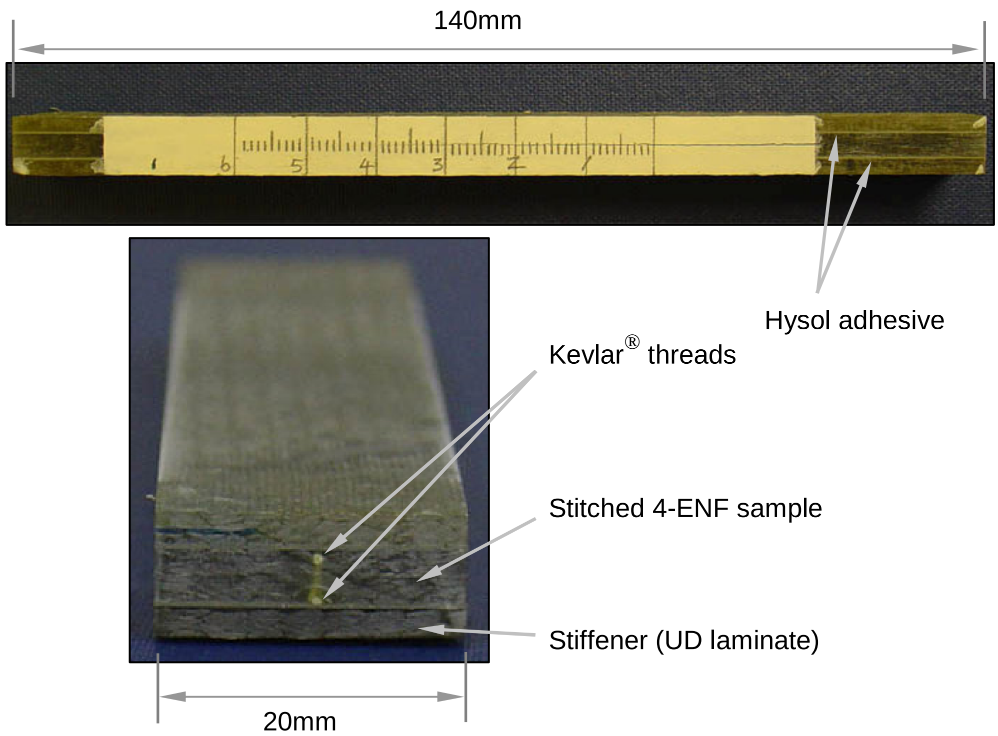

Figure 7.4 DCB sample (tested) bonded with stiffener

The details of 4-ENF testing samples and their testing results are listed in Table 7.3 and Table 7.4, respectively. Stiffener layers (six layers of UD laminates on each side) are not included in the expression of sample orientations.

Table 7.3 ENF testing Samples

Reference	Orientation	Matrix	Stitching	Width D (mm)	VF%
F1719_ENF	$[0_4$^$0_4]$	Polyester	No	20.13	53.1
F1595_ENF	$[0_3/90$^$0_4]$	Polyester	No	19.31	53.2
F1676_ENF	$[0_3/\pm45$^$\mp45/0_3]$	Polyester	No	20.03	48.2
F1677_ENF	$[0_3/\pm45$^$0_4]$	Polyester	No	20.02	47.3
F1678_ENF	$[0_3/\pm45$^$90/0_3]$	Polyester	No	19.97	46.8
F1679_ENF	$[0_3/PW$^$0_4]$	Polyester	No	19.99	47.5
F1680_ENF	$[0_4$^$0_4]$	Polyester	Yes	20.03	47.0
F1681_ENF	$[0_3/90$^$0_4]$	Polyester	Yes	19.96	47.8
F1682_ENF	$[0_3/\pm45$^$\mp45/0_3]$	Polyester	Yes	20.08	47.0
F1683_ENF	$[0_3/\pm45$^$0_4]$	Polyester	Yes	19.98	47.0
F1684_ENF	$[0_3/\pm45$^$90/0_3]$	Polyester	Yes	20.13	47.2
F1685_ENF	$[0_3/PW$^$0_4]$	Polyester	Yes	20.05	47.1
F1688_ENF	[90/±45/0^0/±45/90]	Polyester	Yes	20.12	51.0
F1686_ENF	$[90/0_2$^$0_2/90]$	Polyester	Yes	19.98	51.0
F1687_ENF	$[\pm45/0_2$^$0_2/\mp45]$	Polyester	Yes	20.09	50.5
F1713_ENF	$[\pm45/0_2$^$0_2/\mp45]$	Vinyl ester	Yes	19.76	45.3
F1716_ENF	$[\pm45/0_2$^$0_2/\mp45]$	Epoxy	Yes	19.56	42.5
F1721_ENF	$[0_3/\pm45$^$0_4]$	Vinyl ester	Yes	19.79	44.3
F1724_ENF	$[0_3/\pm45$^$0_4]$	Epoxy	Yes	19.61	43.3

The symbol " ^ " indicates the position of insert film in fabrics; VF: Fibre volume fraction;

Table 7.4 ENF testing results

Reference	Orientation	$G_{IIC-VIS}$ (kJ/m^2)		$G_{IIC-Prop}$ (kJ/m^2)	
		Average	Deviation	Average	Deviation
F1719_ENF	$[0_4$^$0_4]$ /PE*	1.374	0.624	1.949	0.268
F1595_ENF	$[0_3/90$^$0_4]$ /PE*	1.000	0.167	1.658	0.112
F1676_ENF	$[0_3/\pm45$^$\mp45/0_3]$ /PE*	2.306	0.067	3.353	0.150
F1677_ENF	$[0_3/\pm45$^$0_4]$ /PE*	1.706	0.484	2.518	0.193
F1678_ENF	$[0_3/\pm45$^$90/0_3]$ /PE*	2.221	0.592	2.873	0.381
F1679_ENF	$[0_3$/PW^$0_4]$ /PE*	1.206	0.310	2.014	0.082
F1680_ENF	$[0_4$^$0_4]$ /PE	1.241	0.067	2.078	0.058
F1681_ENF	$[0_3/90$^$0_4]$ /PE	0.629	0.192	2.076	0.357
F1682_ENF	$[0_3/\pm45$^$\mp45/0_3]$ /PE	1.937	0.235	2.820	0.412
F1683_ENF	$[0_3/\pm45$^$0_4]$ /PE	1.230	0.207	1.990	0.174
F1684_ENF	$[0_3/\pm45$^$90/0_3]$ /PE	1.538	0.301	2.428	0.132
F1685_ENF	$[0_3$/PW^$0_4]$ /PE	1.124	0.263	1.876	0.182
F1688_ENF	[90/±45/0^0/±45/90] /PE	1.097	0.235	1.877	0.172
F1686_ENF	$[90/0_2$^$0_2/90]$ /PE	1.063	0.246	1.748	0.104
F1687_ENF	$[\pm45/0_2$^$0_2/\mp45]$ /PE	1.228	0.186	2.044	0.073
F1713_ENF	$[\pm45/0_2$^$0_2/\mp45]$ /VE	2.140	0.580	3.521	0.289
F1716_ENF	$[\pm45/0_2$^$0_2/\mp45]$ /EP	1.876	0.074	3.299	0.251
F1721_ENF	$[0_3/\pm45$^$0_4]$ /VE	2.239	0.326	3.339	0.251
F1724_ENF	$[0_3/\pm45$^$0_4]$ /EP	1.794	0.261	2.983	0.373

* Non-stitced samples; PE = Polyester; VE = Vinyl ester; EP = Epoxy.

7.1.3. Comparison between stitched and unstitched samples

Under Mode-I loading, researchers [2, 46, 107] found that the delamination resistance (G_{IC}) of composite materials is improved by through-thickness stitches. However, these through-thickness stitches hardly affect the delamination resistance under Mode-II loading (G_{IIC}). The Mode-I and Mode-II testing results obtained in this section are mainly for the evaluation of energy absorption caused by delaminations during composite crushing.

7.1.3.1. *Stitching influences on Mode-I fracture toughness*

Typical R-curves calculated by the MBT (see 3.4.2.1 in Chapter 3) method for both stitched and unstitched samples are shown in Figure 7.7. It can be seen that the initiation values for all DCB samples are very similar (between 0.2 - 0.4 kJ/m^2). Within [0_3/90^0_4] specimens, the delamination was initiated between 0° and 90° layers. Because the fracture energy generated by 0°-90° delamination is very small, the delamination would not necessary propagate between the layers where the pre-crack was created. In fact, the crack could propagate at either side of 90° fibres. Figure 7.5 shows the crack did not follow the pre-crack line which was on the top of 90° fibres. Instead, the crack jumped to the bottom of 90° fibres and continued to grow. The R-curve of the unstitched [0_4^0_4] samples and R-curve of unstitched [0_3/90^0_4] samples are almost the same (see Figure 7.7).

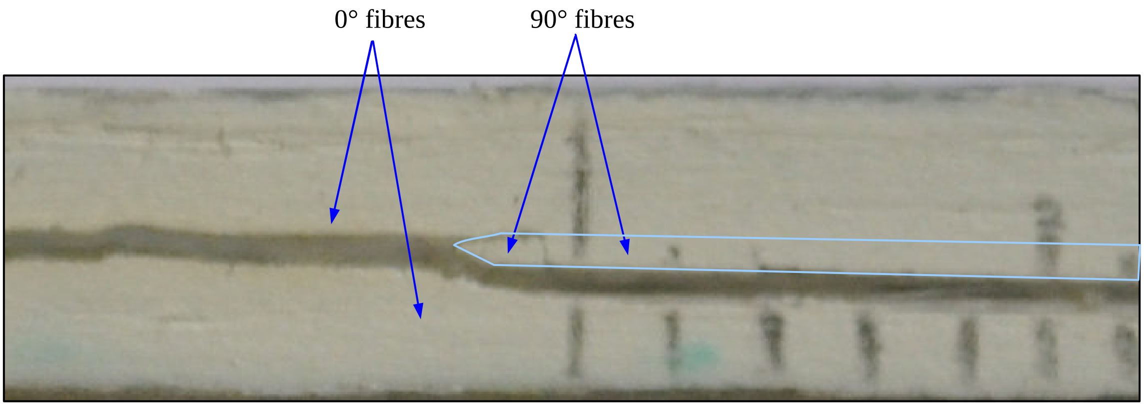

Figure 7.5 Photograph of crack propagation in a typical [0_3/90^0_4] DCB sample

In the unstitched [0_3/±45^∓45/0_3] sample, the crack grew right in the middle of laminate, which is between -45° and +45° fabrics. Compared with the unstitched [0_4^0_4] and [0_3/90^0_4] samples, unstitched [0_3/±45^∓45/0_3] sample achieved almost two times higher propagation value ($G_{IC\text{-}Prop}$). This difference can be attributed to fibre bridging in [0_3/±45^∓45/0_3] sample. It is also interesting to note that the crack did not only propagate between the layers where pre-crack was created, but also propagated at the adjacent +45 (or -45) layers due to fibre bridging and fibre pull-out. This phenomenon is presented in Figure 7.6

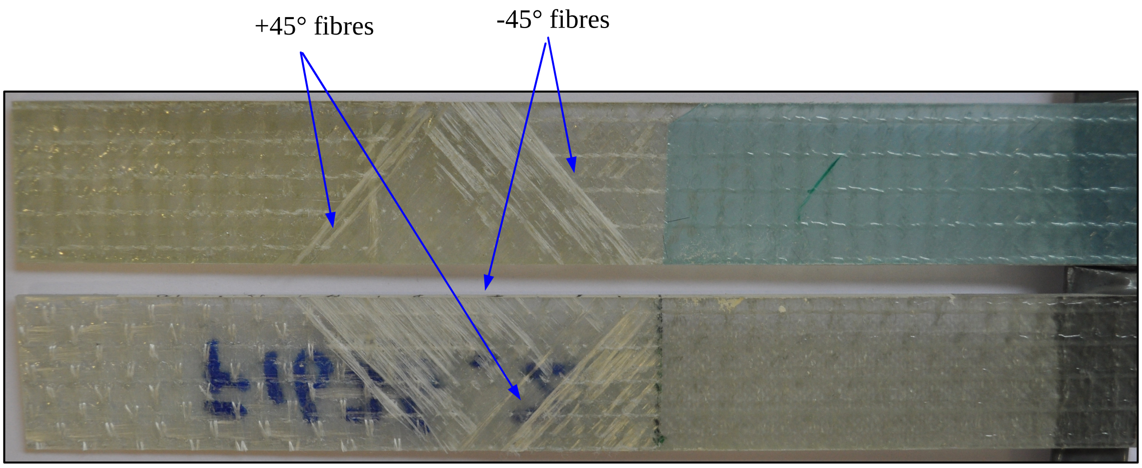

Figure 7.6 Photograph of crack propagation in a typical [0_3/90^0_4] DCB sample

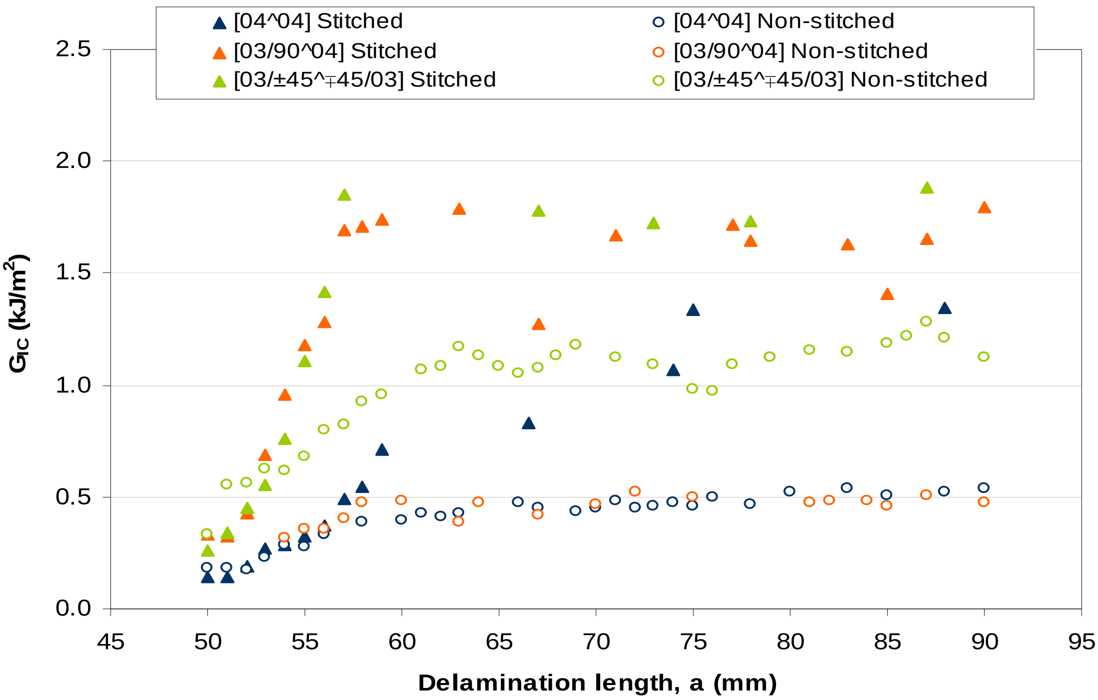

Figure 7.7 R-curves for DCB testing of stitched and unstitched samples

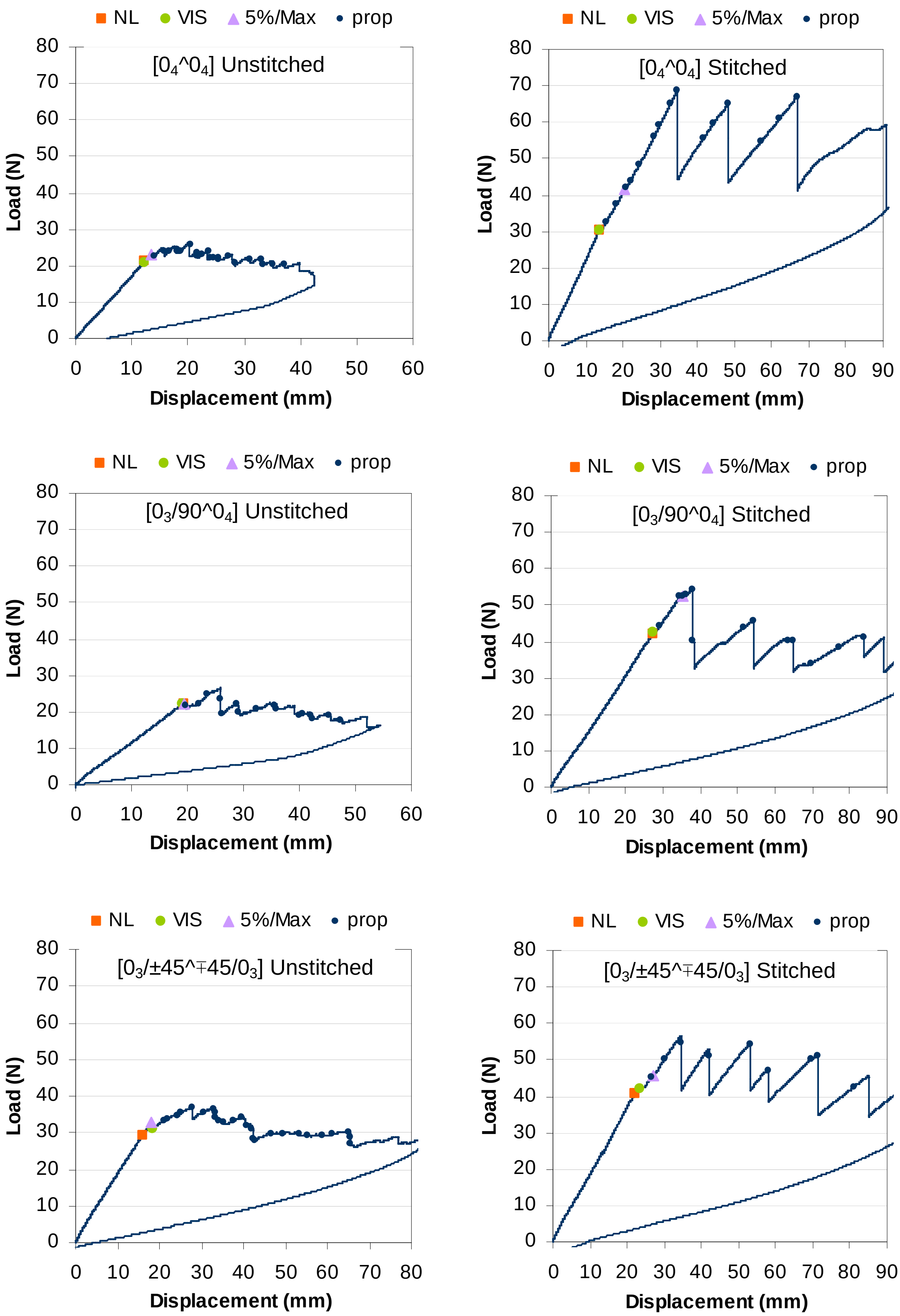

Figure 7.8 **Load-displacement curves for DCB testing of stitched and unstitched samples**

As for those stitched DCB samples, it seems the stitching mechanism dominates the fracture toughness properties. The R-curves and propagation values of stitched

$[0_3/90^\wedge 0_4]$ sample and $[0_3/\pm 45^\wedge \mp 45/0_3]$ sample are very similar, while the G_{IC} of stitched $[0_4{}^\wedge 0_4]$ sample was slightly lower.

The load-displacement curves for both stitched and unstitched samples are also shown in Figure 7.8. They indicate that the stitched samples are 1.5-2.8 times stronger than the unstitched samples according to their maximum loads. It also can be found that he distance between two adjacent load peaks is multiple of 1/5 inch (about 5mm) in general. The gap between two stitches is 1/5 inch. The reason of this is the stressed opening load releases and the crack propagates after stitch breaks.

Equally important, the delamination initiation calculated by using three different approaches (G_{IC-VIS}, G_{IC-NL} and $G_{IC-5\%/Max}$) presents very similar results. Specially, the difference between G_{IC-VIS} and G_{IC-NL} values that are shown in Figure 7.8 is very small for all samples shown in Figure 7.8. This result can also be seen in Figure 7.9 more clearly. Accordingly, the G_{IC-VIS} value will be used as the delamination initiation for DCB samples throughout the rest of the thesis.

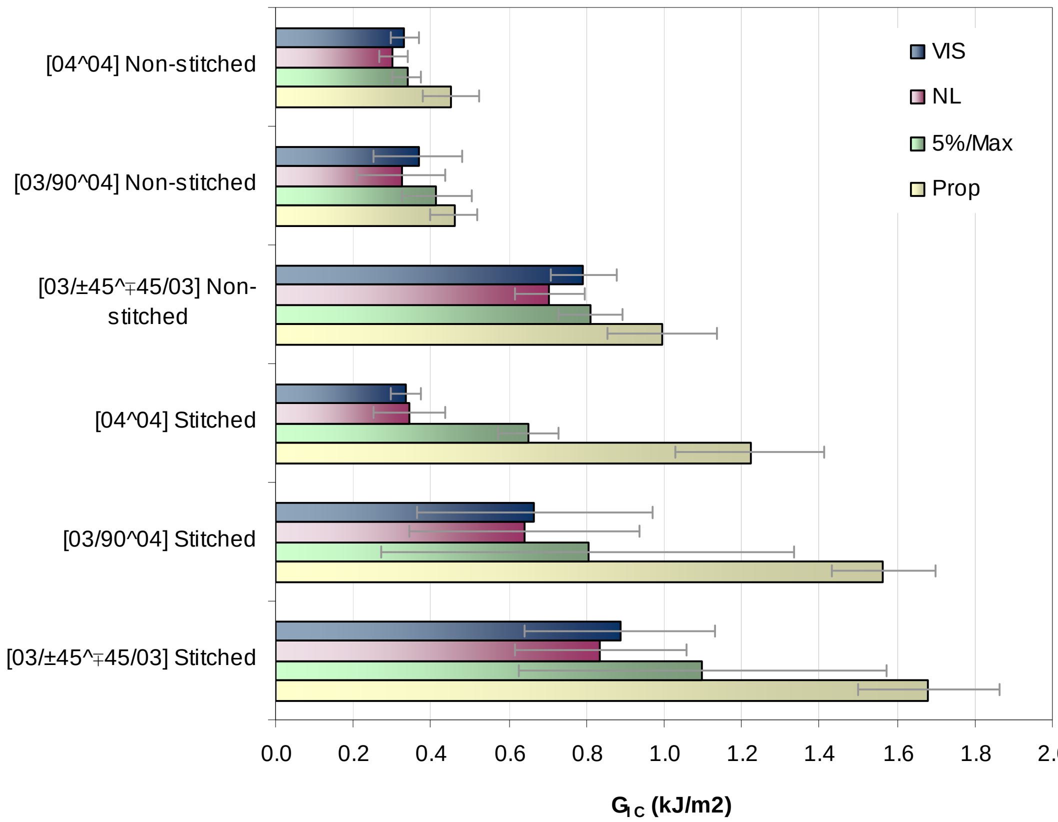

Figure 7.9 Comparison of results calculated by the different methods for DCB samples

7.1.3.2. *Stitching influences on Mode-II fracture toughness*

Glass fibre damage and fabric penetration caused by the stitching process degrade the Mode-II fracture toughness properties of most samples. As an example, the laminate $[0_3/\pm45^\wedge0_4]$ requires a higher load to propagate cracks for stitched F1677_ENF sample compared with unstitched F1683_ENF sample (see Figure 7.10).

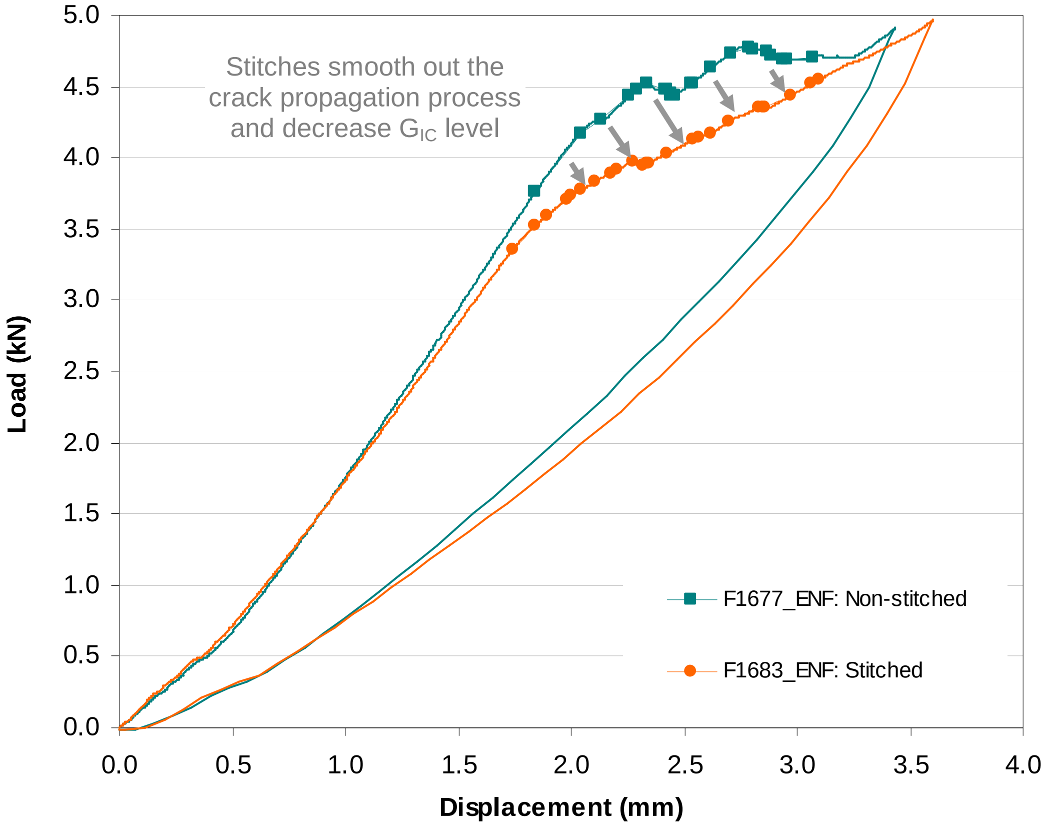

Figure 7.10 Load-displacement curves for stitched and unstitched $[0_3/\pm45^\wedge0_4]$ samples

R-curves for these two samples are also shown in Figure 7.11. The comparisons between other stitched and unstitched 4-ENF samples are shown in Figure 7.12 on their average propagation values, $G_{IIC\text{-}Prop}$. It indicates that most G_{IIC} values of stitched samples are below their corresponding unstitched samples, except for the $[0_3/90^\wedge0_4]$ samples.

Furthermore, in Figure 7.12, it also can be found that F1688_ENF ($[90/\pm45/0]_S$) has a very similar $G_{IIC\text{-}Prop}$ level as F1719-ENF ($[0]_8$). But as for calculating the energy absorption in the latter parts, only the $G_{IIC\text{-}Prop}$ value of F1719-ENF is considered as a proper average energy release rate under Mode-II deformation for the delamination between two 0° fabric layers.

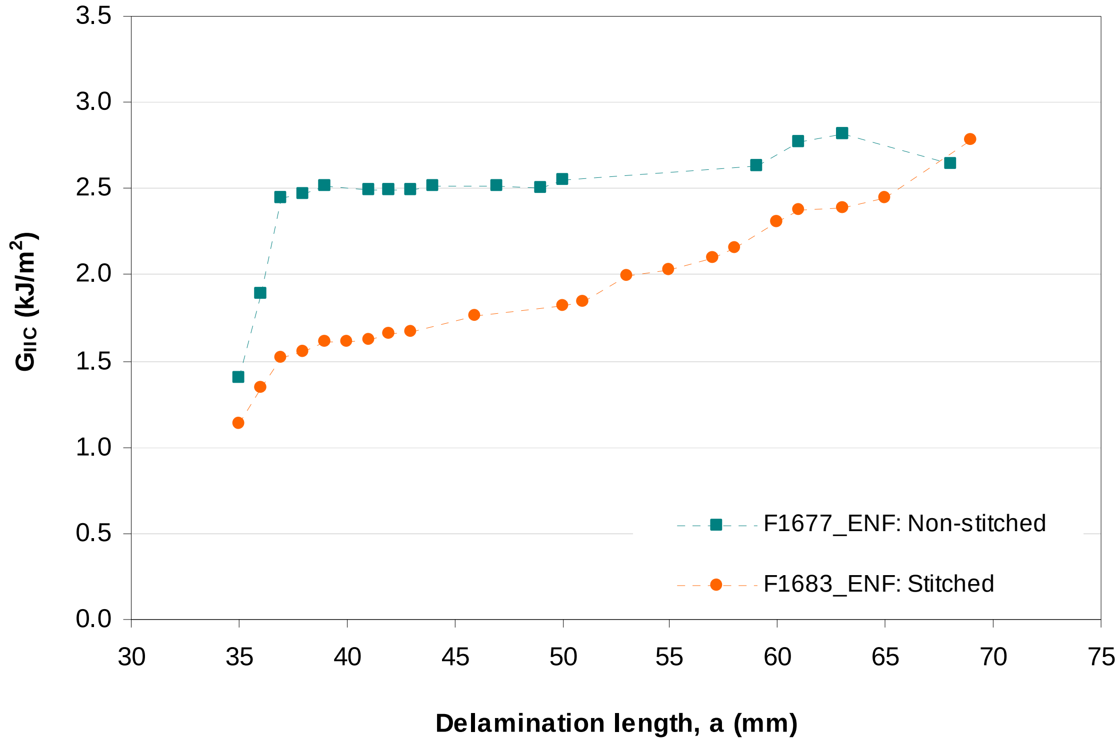

Figure 7.11 R-curves for 4-ENF testing of stitched and unstitched samples

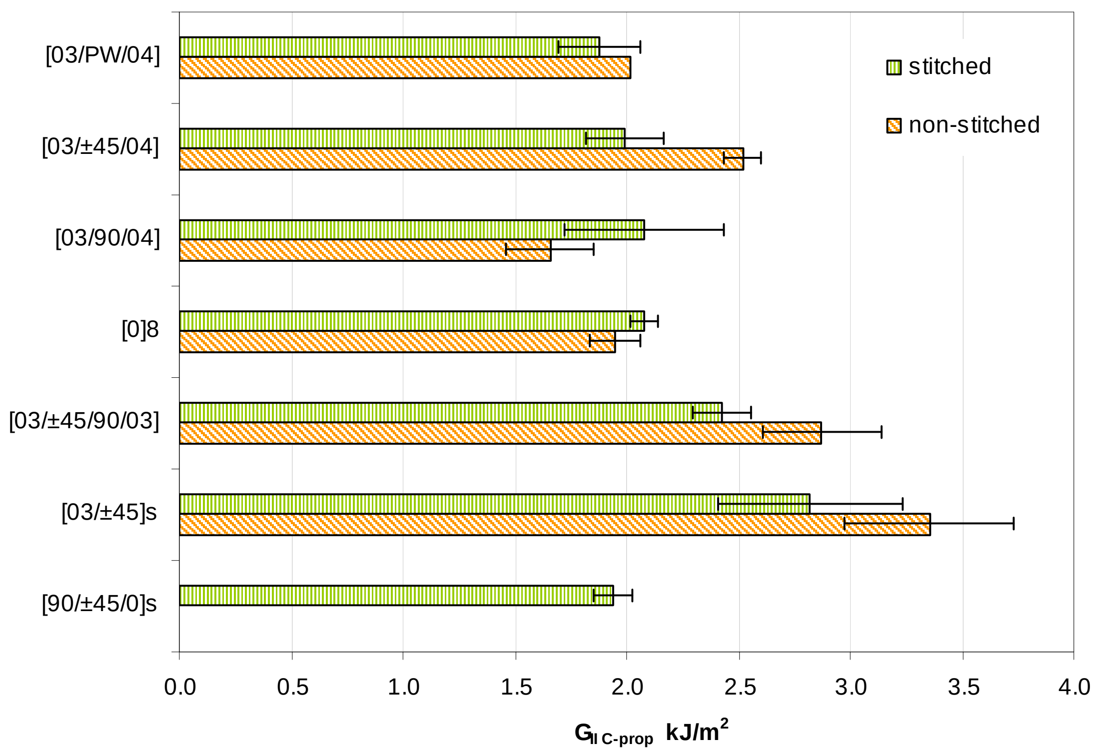

Figure 7.12 Comparison of results calculated by the different methods for DCB samples

7.2. Effect of resin toughness on DCB and 4-ENF tests

The results of Mode-I strain energy release rate of stitched DCB samples are compared in Figure 7.13. It shows that the laminates composed of vinyl ester resin and epoxy resin achieved the $G_{IC\text{-}Prog}$ value about 20% higher than the laminate composed of polyester resin.

Furthermore, the comparison between non-stiffened (F1716_DCB) and stiffened (F1758_DCB) samples is also indicated in Figure 7.13. There is almost no difference can be found between non-stiffened and stiffened DCB samples.

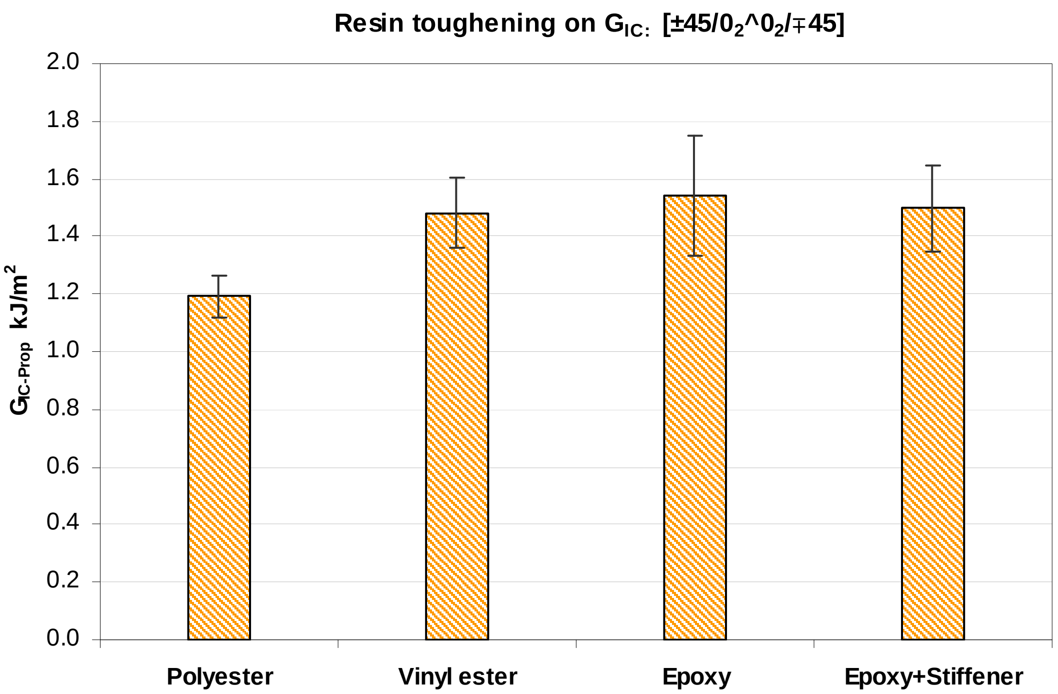

Figure 7.13 Comparison of different resin systems on stitched DCB samples

For stitched DCB samples, epoxy resin presents the best fracture toughening mechanism in Mode-I opening failure. However, in shearing failure mode (Mode-II), epoxy resin exhibits worse G_{IIC} than vinyl ester. This result is shown in Figure 7.14 by comparing stitched $[\pm45/0_2$^$0_2/\pm45]$ and $0_3/\pm45$^$0_4]$ 4-ENF samples.

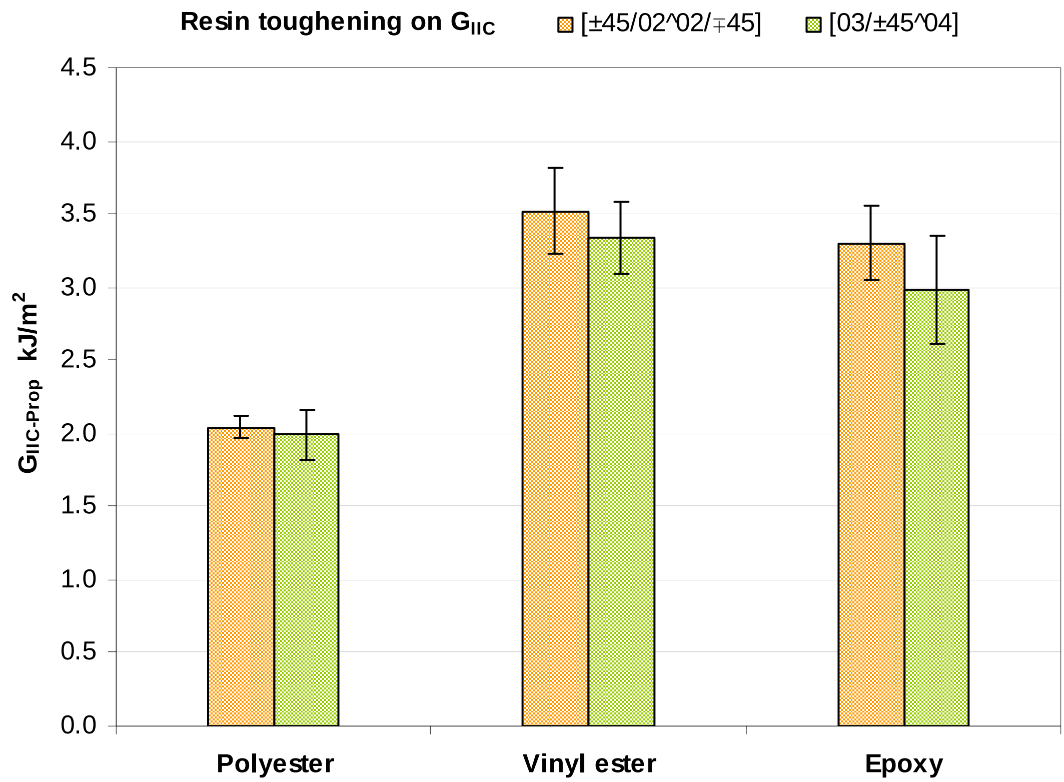

Figure 7.14 **Comparison of different resin systems on stitched 4-ENF samples**

7.3. Discussion on the relation between fracture toughness and SEA

The purpose of conducting DCB and 4-ENF tests was to evaluate the effectiveness of Mode-I and Mode-II fracture toughness in the crushing samples investigated in Chapter 5. In an ideal lamina bending crushing mode, a composite structure reaches its maximum energy absorbing capacity by exerting all crushing mechanisms (see Figure 2.9) to the utmost. As the result, the delaminations should be assumed to occur between every two adjacent laminas and delaminate thoroughly.

Considering the potential energy absorption capacity of geometric cells as their maximum energy absorption capacity, the fraction of energy absorption of U_{IC}, U_{sp} and U_{de} (see equation 2.5) can be thus derived from Mode-I and Mode-II testing results. To simplify the calculation process, the crushing samples are assumed to stroke 10mm on potential energy absorption levels and their corresponding DCB/ENF samples are assumed to delaminate 10mm on $G_{IC\text{-}Prog}$ and $G_{IIC\text{-}Prog}$ values.

The geometric cell is divided into two sections. The energy absorption mechanisms related to Mode-I and Mode-II failures in each section are demonstrated in the Figure 7.15. The $G_{IC\text{-}Prog}$ and $G_{IIC\text{-}Prog}$ values applied in the calculation for both sections are listed in the Table 7.5 and Table 7.6, respectively.

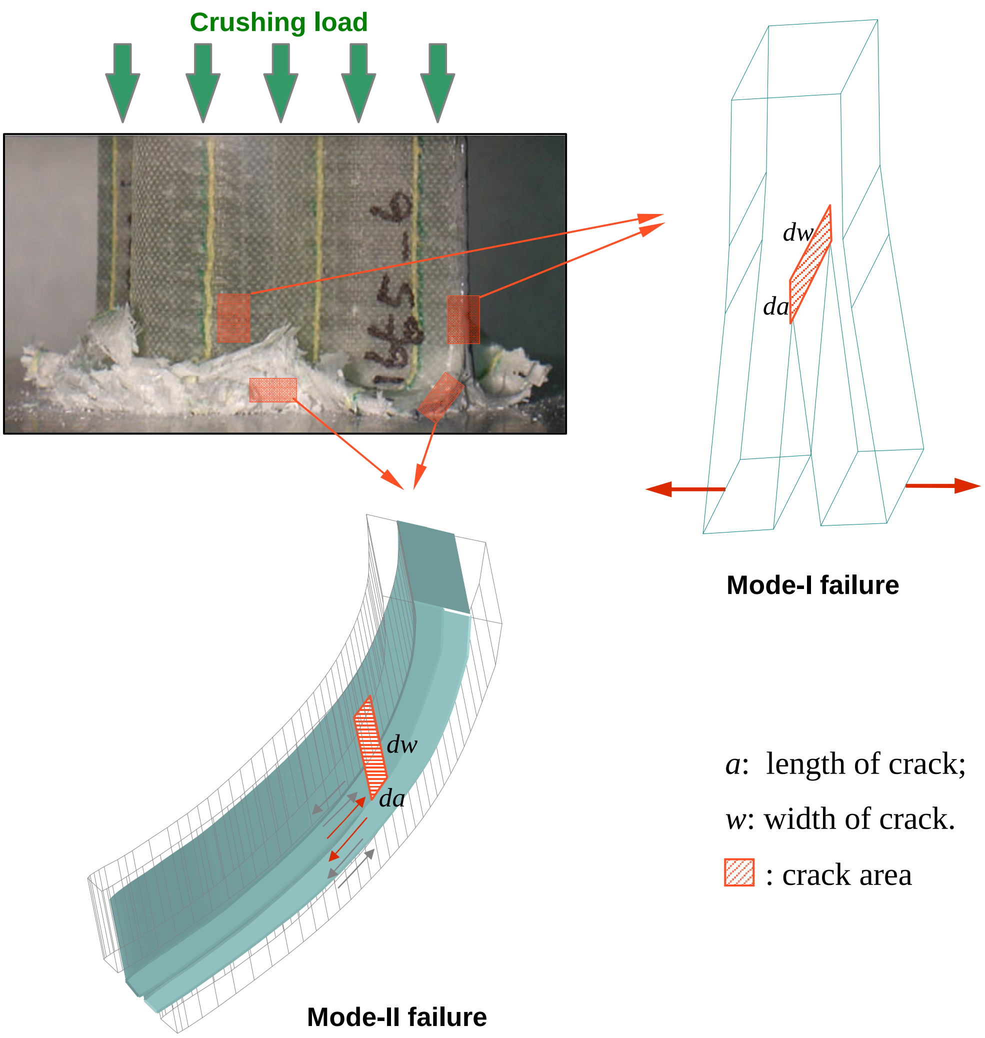

Figure 7.15 Energy absorption mechanisms referring to Mode-I and Mode-II failures at the flat sides and core section of a typical geometric cell (F1655_C, [±45/0]$_S$)

The energy absorption caused by Mode-I & II failure mechanisms within geometric cells, $U_{IC,IIC}$, can be written as:

$$U_{IC,IIC} = U_{IC,IIC}^{Sides} + U_{IC,IIC}^{Core} \tag{7.1}$$

where the $U_{IC,IIC}^{Sides}$ is the energy absorption caused by Mode-I & II at flat sides of cells, the $U_{IC,IIC}^{Core}$ is the energy absorption caused by Mode-I & II at core section of cells. Both components can be calculated by the following equations:

$$U_{IC,IIC}^{Sides} = U_{IC}^{Sides} + U_{IIC}^{Sides} = \xi \cdot L \cdot \left\{ \sum_{p=1}^{m} \left[(G_{IC})_p \alpha_p \right] + \sum_{q=1}^{n} \left[(G_{IIC})_q \beta_q \right] \right\} \tag{7.2}$$

$$U_{IC,IIC}^{Core} = U_{IC}^{Core} + U_{IIC}^{Core} = \xi \cdot P \cdot \left\{ \sum_{p=1}^{m} \left[(G_{IC})_p \alpha_p \right] + \sum_{q=1}^{n} \left[(G_{IIC})_q \beta_q \right] \right\} \tag{7.3}$$

where ξ is the stroke that DCB/ENF samples experienced (set as 100mm during present calculations). L and P indicate the length of flat sides and the perimeter of core section of geometric cell, respectively. L and P can be obtained in Chapter 5. m and n indicate the number of different fracture toughness values in Mode-I and Mode-II failures, respectively. α and ß indicate the quantity of same Mode-I and Mode-II failure within a laminate, respectively.

The values of both *α* and *ß* are listed in Table 7.5 and Table 7.6. The analysing results of $U_{IC,IIC}$ of geometric cells are shown in Table 7.7. However, it is important to note that the above calculation is based on several assumptions. The real relationship between fracture toughness and energy absorption capacity of geometric cells could be slightly different.

In Figure 7.16, it shows that the failure mechanisms of central crack (Mode-I), intralaminar delamination and splitting (Mode-I) only contribute 3% - 7% into the total crushing energy of geometric cells. Especially for composite laminates consist of biaxial or triaxial lay-ups, their energy absorption caused by Mode-I and Mode-II failure mechanisms take up more than 5% within total crushing energy.

Within the same materials, the normalized energy absorption capacities related to the Mode-I and Mode-II delaminations were also listed in Table 7.8 to compare the SEA values. In addition, these comparisons are also plotted in Figure 7.17, Figure 7.18 and Figure 7.19 for C-cells, H-cells and S-cells, respectively.

Table 7.5 Mode-I and Mode-II fracture mechanisms at the flat sides of geometric cells

Crushing sample	$G_{IC\text{-}Prop}$ values and corresponding α	$G_{IIC\text{-}Prop}$ values and corresponding β					
	0.40 kJ/m^2 (assumed)*	*0^0 F1680_ENF*	*0^90 F1681_ENF*	*+45^-45 F1682_ENF*	*0^45 F1683_ENF*	*45^90 F1684_ENF*	*PW^0 F1685_ENF*
[90/0/90]	1		4				
[0/90/0]	1		4				
$[90/0]_S$	1		4				
$[\pm45/0]_S$	1	2		4	4		
$[PW400/0]_S$	1	2					4
$[90/0_2]_S$	1	6	4				
$[\pm45/0_2]_S$	1	6		4	4		
$[90/\pm45/0]_S$	1	2		4	4	4	
$[90/0]_{2S}$	1	2	12				
$[\pm45/0_3]_S$	1	10		4	4		
$[90/\pm45/0_2]_S$	1	6		4	4	4	

^ : presents the position in laminate where the delamination propagates
* : Adhesive debonding along the glued areas

Table 7.6 Mode-I and Mode-II fracture mechanisms at the core section of geometric cells

Crushing sample	$G_{IC\text{-}Prop}$ values and corresponding α		$G_{IIC\text{-}Prop}$ values and corresponding β					
	0^0 F1680_DCB	*0^90 F1681_DCB*	*0^0 F1680_ENF*	*0^90 F1681_ENF*	*+45^-45 F1682_ENF*	*0^45 F1683_ENF*	*45^90 F1684_ENF*	*PW^0 F1685_ENF*
[90/0/90]		1		2				
[0/90/0]		1		2				
$[90/0]_S$	1			2				
$[\pm45/0]_S$	1				2	2		
[PW400/0]	1							2
$[90/0_2]_S$	1		2	2				
$[\pm45/0_2]_S$	1		2		2	2		
$[90/\pm45/0]_S$	1				2	2	2	
$[90/0]_{2S}$	1			6				
$[\pm45/0_3]_S$	1		4		2	2		
$[90/\pm45/0_2]$	1		2		2	2	2	

^ : presents the position in laminate where the delamination propagates

Table 7.7 Energy absorbed by Mode-I & II delaminations in crushing samples

Sample orientation	Energy absorbed in crush /J (10mm stroke on Potential SEA)			Energy absorption contributed by Mode-I and Mode-II delaminations /J (10mm crack length on $G_{C\text{-}Prop}$)		
	S-Cell	C-Cell	H-Cell	Mode-I	Mode-II	Mode-I & II
[90/0/90]	195.6	205.6	196.7	2.126	3.445	5.571
[0/90/0]	161.9	178.6	148.0	2.214	3.434	5.558
$[90/0]_S$	250.8	253.4	263.8	1.696	7.712	9.408
$[\pm45/0]_S$	298.1	262.3	287.4	1.695	16.728	18.423
$[PW400/0]_S$	263.7	261.2	251.5	1.695	7.031	8.726
$[90/0_2]_S$	454.8	413.7	425.5	1.696	14.598	16.295
$[\pm45/0_2]_S$	476.2	438.0	463.9	1.698	23.762	25.424
$[90/\pm45/0]_S$	483.9	451.2	470.5	1.698	24.878	26.576
$[90/0]_{2S}$	546.8	521.7	527.1	1.696	21.443	23.139
$[\pm45/0_3]_S$	602.6	586.6	656.2	1.697	30.552	32.249
$[90/\pm45/0_2]_S$	608.2	612.6	607.3	1.693	31.547	33.240

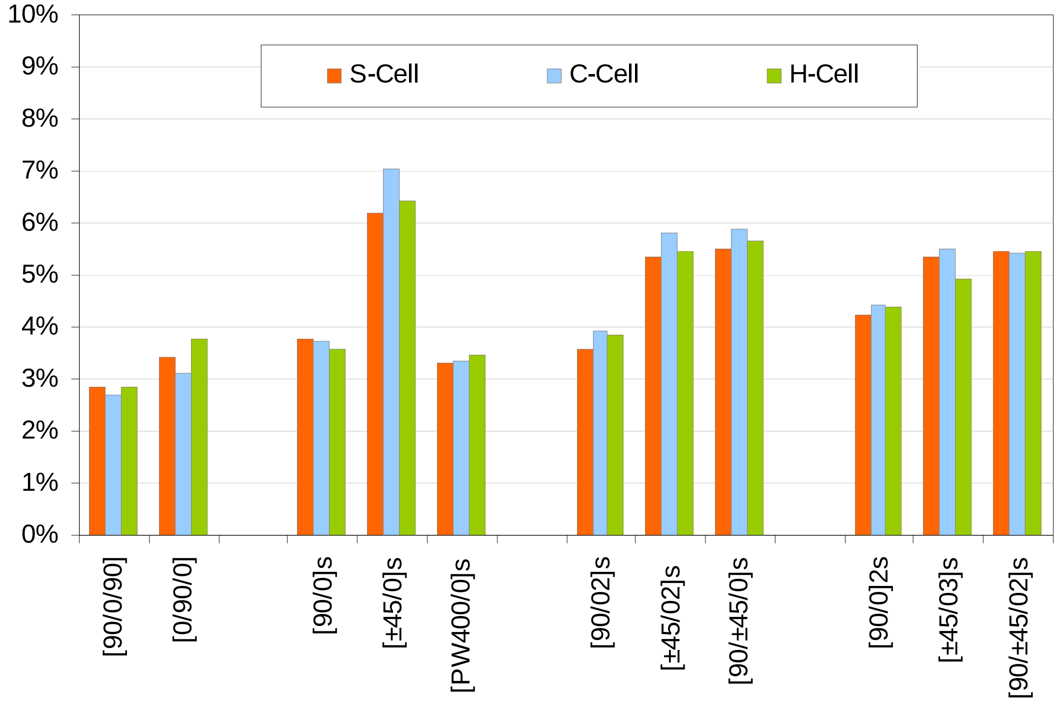

Figure 7.16 Percentages of energy absorption caused by Mode-I and Mode-II failures for geometric cells within the ideal crushing process

Table 7.8 Normalized energy absorption capacity related to the Mode-I & II delaminations in crushing samples

Sample orientation	Normalized energy absorption in S-Cell (kJ/kg)			Normalized energy absorption in C-Cell (kJ/kg)			Normalized energy absorption in H-Cell (kJ/kg)		
	Mode-I	Mode-II	Mode-I & II	Mode-I	Mode-II	Mode-I & II	Mode-I	Mode-II	Mode-I & II
[90/0/90]	0.566	0.954	1.520	0.581	0.979	1.561	0.529	0.892	1.421
[0/90/0]	0.585	0.982	1.567	0.570	0.957	1.527	0.546	0.918	1.464
$[90/0]_S$	0.343	1.638	1.982	0.342	1.631	1.972	0.328	1.566	1.894
$[\pm45/0]_S$	0.326	3.378	3.704	0.322	3.331	3.652	0.314	3.255	3.570
$[PW400/0]_S$	0.407	1.770	2.176	0.399	1.735	2.134	0.382	1.662	2.043
$[90/0_2]_S$	0.239	2.163	2.402	0.234	2.118	2.353	0.226	2.039	2.265
$[\pm45/0_2]_S$	0.220	3.230	3.451	0.218	3.196	3.414	0.208	3.051	3.259
$[90/\pm45/0]_S$	0.211	3.241	3.451	0.215	3.306	3.521	0.205	3.156	3.361
$[90/0]_{2S}$	0.180	2.394	2.574	0.176	2.330	2.506	0.171	2.276	2.447
$[\pm45/0_3]_S$	0.178	3.363	3.541	0.172	3.256	3.428	0.168	3.169	3.337
$[90/\pm45/0_2]_S$	0.167	3.269	3.437	0.164	3.206	3.370	0.159	3.112	3.272

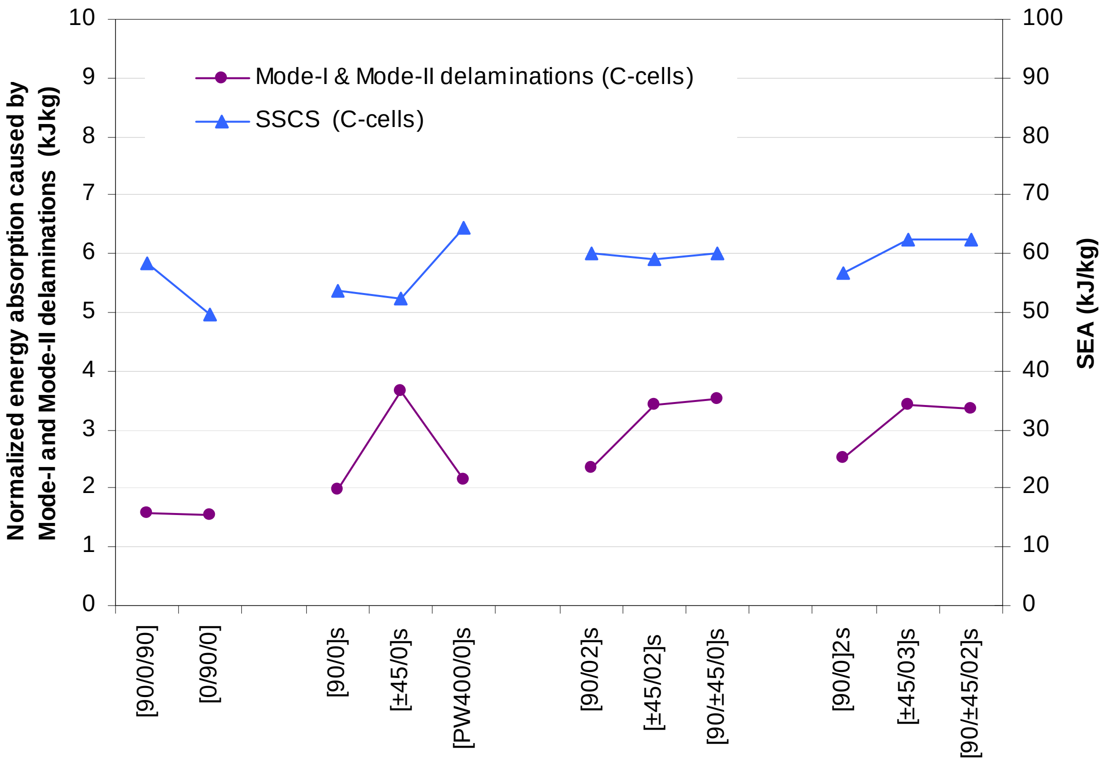

Figure 7.17 Comparisons between energy absorption capacity of C-cells and the energy fraction absorbed by Mode-I and Mode-II delaminations.

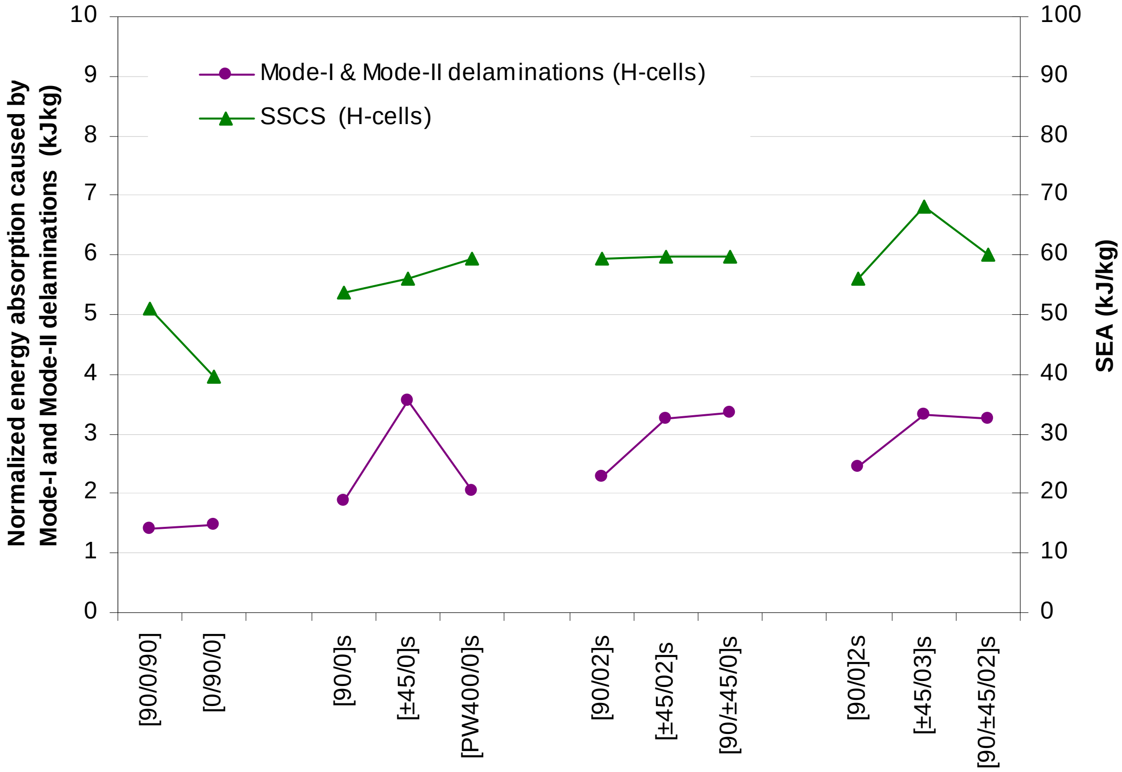

Figure 7.18 Comparisons between energy absorption capacity of H-cells and the energy fraction absorbed by Mode-I and Mode-II delaminations.

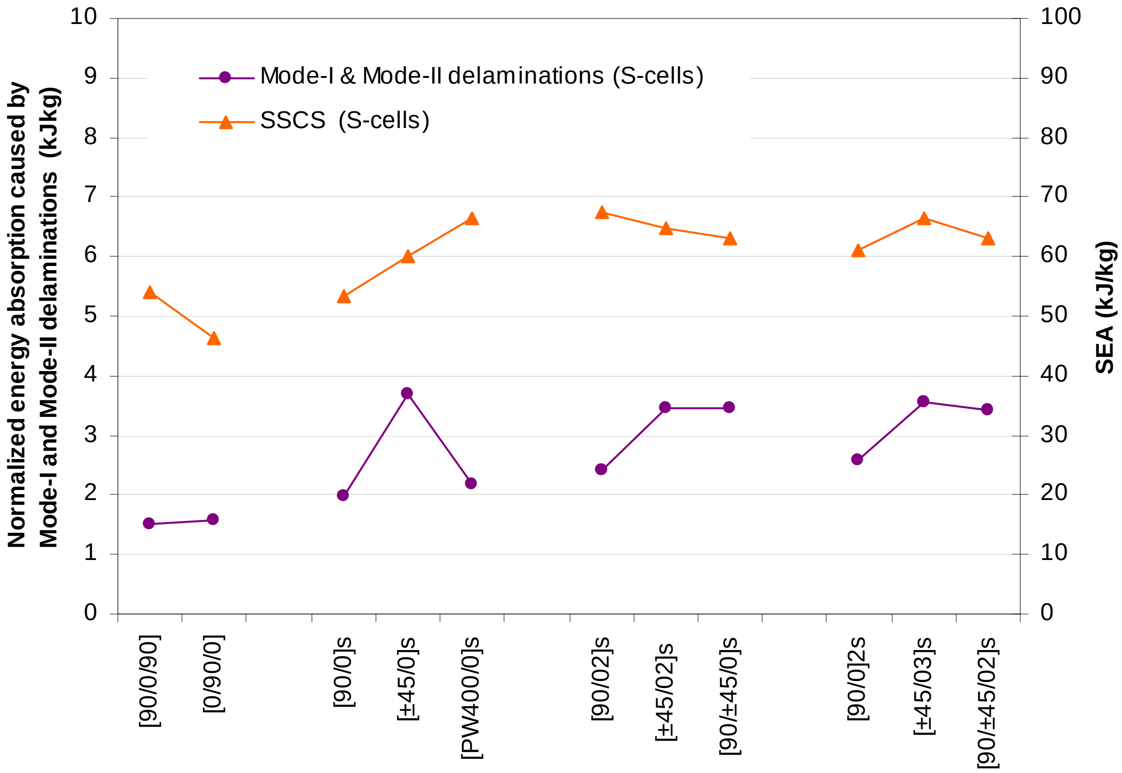

Figure 7.19 **Comparisons between energy absorption capacity of S-cells and the energy fraction absorbed by Mode-I and Mode-II delaminations.**

As the energy absorbed by delaminations contributes very small amount to the total energy absorption capability of composite materials, the variation of normalized delamination energy does not apparently impact the SEA results. Compared with the other material factors, the Mode-I and Mode-II delaminations contribute relatively small proportion to the total energy absorption of composite materials in crushing process.

7.4. Summary

In comparison to the other lay-up configurations, the best properties of both Mode-I and Mode-II fracture toughness were found between +45 and -45 fibres because of fibre pull-off and fibre bridging. All DCB and 4-ENF testing results are compared in Figure 7.20 and Figure 7.21, respectively.

Through-thickness stitching has significant effect on Mode-I fracture toughness properties of composite laminates. In this study, the $G_{IC\text{-}Prop}$ values of the unstitched $[0_4$^$0_4]$ and $[0_3/90$^$0_4]$ DCB samples only reached slightly higher than $0.4 kJ/m^2$, while the $G_{IC\text{-}Prop}$ values of their stitched DCB samples can achieve more than $1.2\ kJ/m^2$.

This result implies that during Mode-I opening failure, the fracture toughness properties of composite laminates mainly rely on the properties of fibres that bridge laminate. Thus the strength of stitching material and stitching density could also significantly affect the Mode-I fracture toughness properties of composite laminates.

In contrast to Mode-I, in Mode-II stitching degrades the fracture toughness properties of most samples due to glass fibre damage and fabric penetration caused by stitching process. It seems the stitching mechanism is less important than the fibre architecture and the fibre alignment around the delamination area.

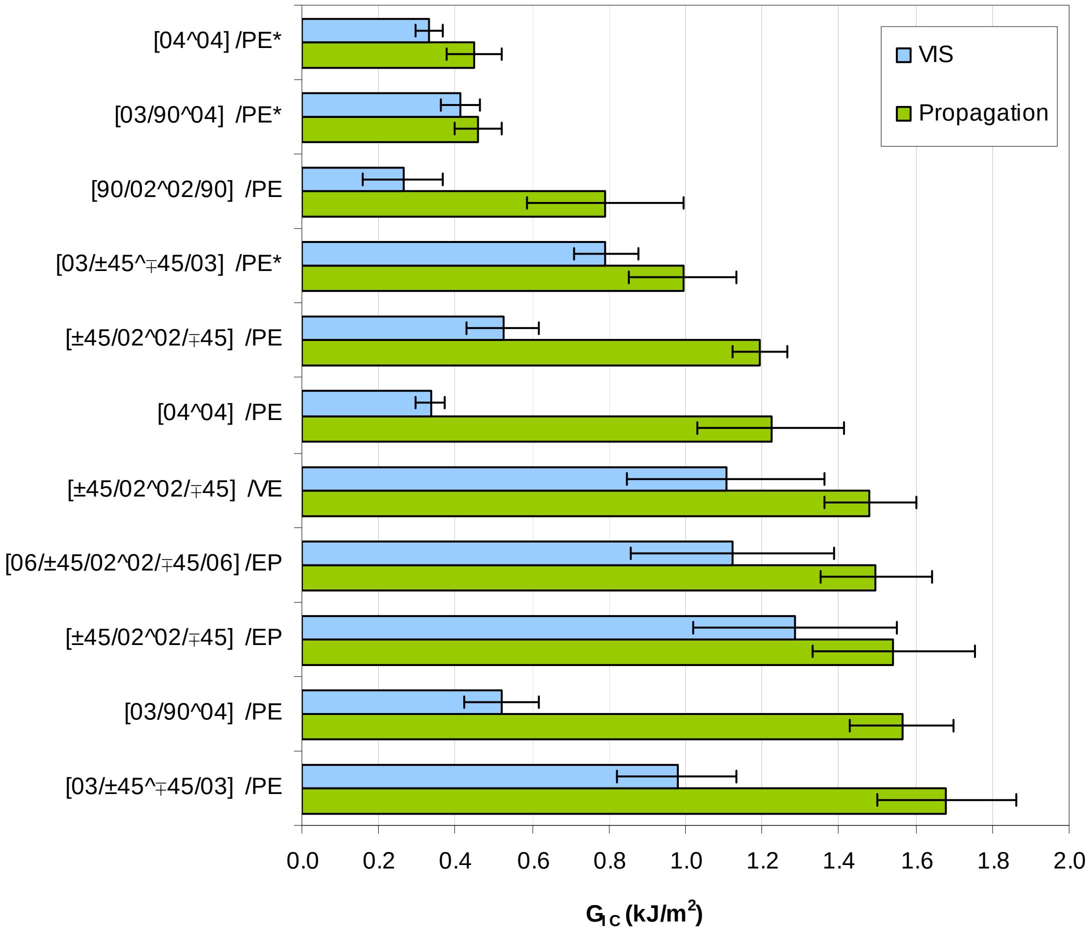

* Non-stitced samples; the rest samples were stitched in the through-thickness direction;

Figure 7.20 Comparison of all DCB testing results

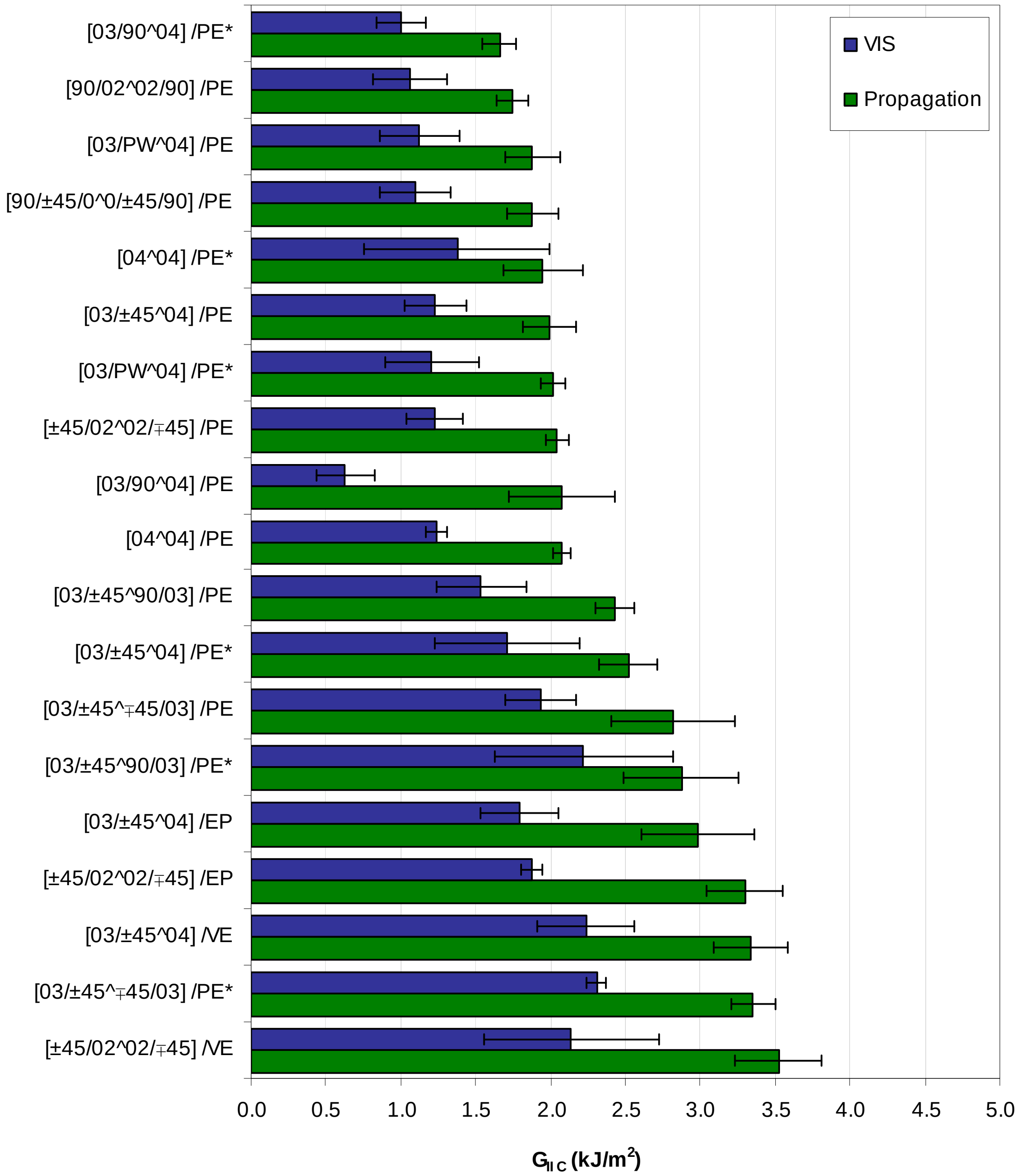

* Non-stitced samples; the rest samples were stitched in the through-thickness direction;

Figure 7.21 Comparison of all 4-ENF testing results

The comparison of matrices shows that the $G_{IC\text{-}Prog}$ values of laminates made of vinyl ester resin and epoxy resin are 20% higher than the laminates made of polyester resin. More importantly, by using vinyl ester or epoxy resin, the $G_{IIC\text{-}Prog}$ values of laminates can be increased by 50% higher than the laminated composed of polyester resin.

In the next stage, different resin systems will be investigated for crushing samples, although some reduction were found in the flexural testing results in last chapter. It was found that the through-thickness stitching did not significantly benefit the total energy absorption, but it seems that the improved Mode-I properties can indirectly increase the crushing performance by preventing the central crack from growing too rapidly. Therefore, in order to prevent premature failure from weak and rapid adhesive debonding, stitches are also applied on both flat sides of geometric cells instead of using adhesive. Co-infusion process is used for make whole cell after the neat fabrics are stitched together.

Chapter 8. Optimization Process

Optimization of the crushing characteristics of composite structures could become very complicated if too many variations are involved in the experiments. Therefore, an optimization approach based on the robust engineering methods (or Taguchi methods) was utilised in order to statistically determine the relationship and assist in evaluating the contribution of each factor on the crushing properties. This robust engineering method is a statistical methodology used for optimizing the product and process conditions which are minimally sensitive to the various causes of variation, and that produce high-quality products with low development and manufacturing costs [80]. The aim of this stage is to identify the most significant factors that influence the crushing performance of structural composites, and consequently to improve the crushing performance.

8.1. Sample configurations

To improve the bonding effectiveness, through-thickness stitching was thus applied instead of adhesive on the flat sides of the corrugated cells. Moreover, two symmetric half cells were co-infused by the resin infusion process. Following a similar process used for optimizing the crushing performance of composite plates [116], stitching characteristics of the corrugated cells were optimised at this stage. Other parameters including resin type, fibre architecture, geometric effect, and crushing speed were also scaled in several levels in a modified geometric structure.

8.1.1. Modification of cross-sectional geometry

According to the crushing results of geometric structures in Chapter 5, S-cells were found to possess the best potential energy absorption capacity but the worst sustained structural efficiency, while C-cells possessed the best sustained structural efficiency but moderate potential energy absorption capacity. Therefore, a modified cross-sectional shape (see Figure 8.1) combining the structural advantages of C-cell and S-cell were created and examined at this stage.

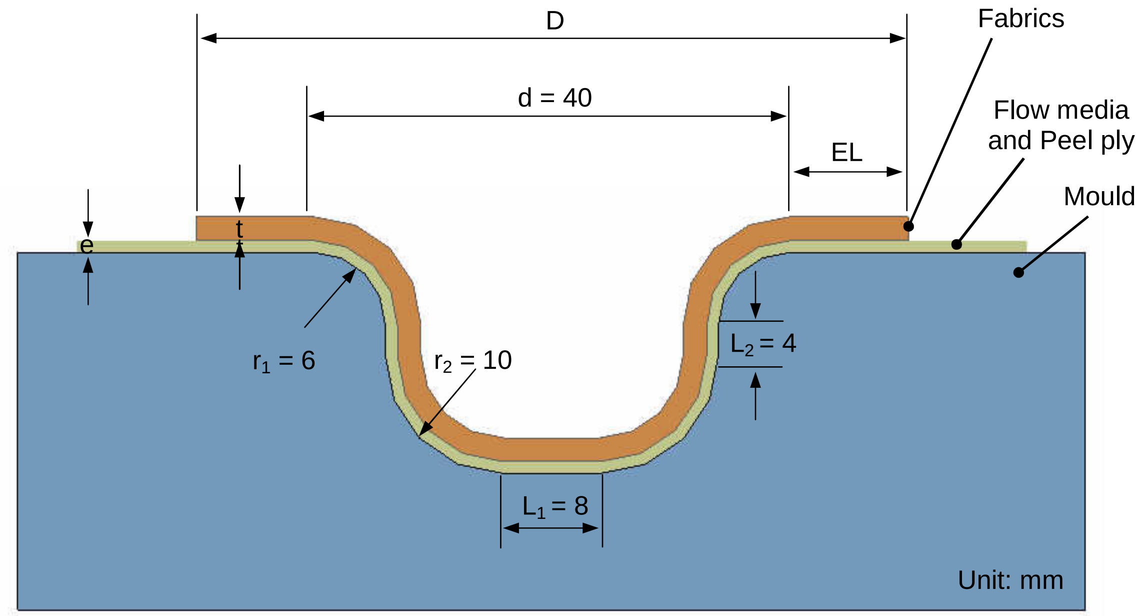

Figure 8.1 **Schematic sketch of the cross-sectional area of modified cell**

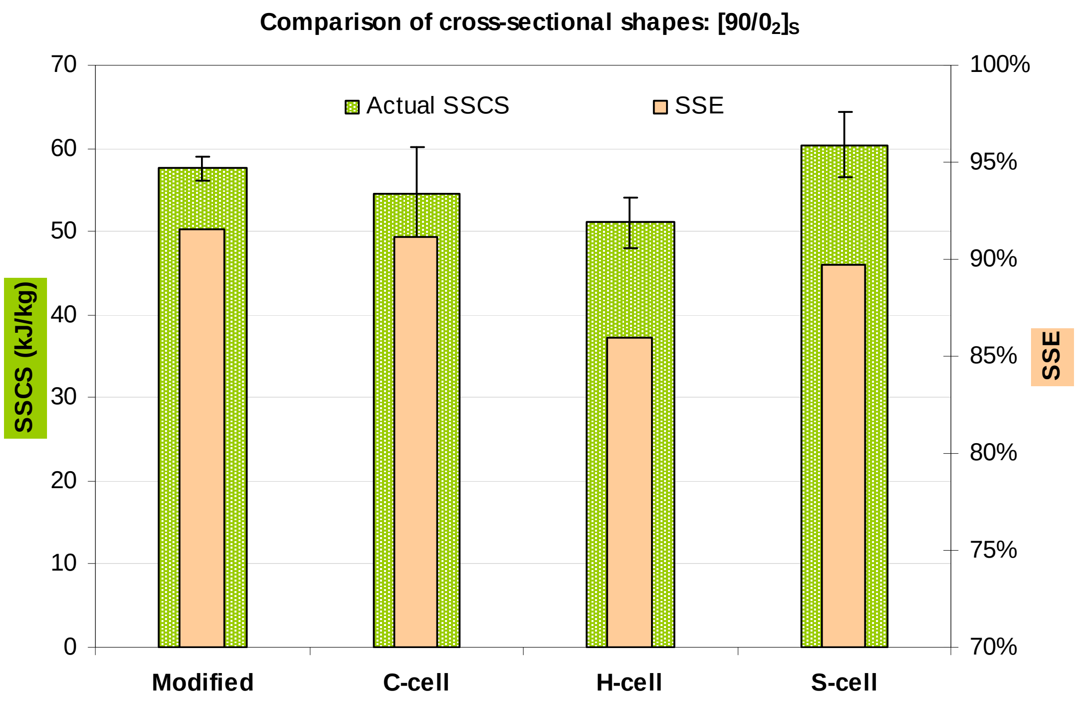

Figure 8.2 **Comparisons of crushing results between modified cell and other cells**

The crushing results of the modified sample are also compared with other cells (Figure 8.2). All cells compared in Figure 8.2 were made of $[90/0_2]_S$ glass fabric and polyester resin. In order to compare the modified cell with previously results in a parallel level, up to this step, these cells were still consisted of two symmetric half cells bonded together by adhesive. The results indicate that modified composite cell achieve slightly lower SEA than the S-cell, but meanwhile remain relatively higher SSE than the S-cell.

The modified geometry also can be regarded as a square cell possessing round corners of a large radius. It was shown in previous crushing experiments that if the radius of round corner is too small, compression stresses normally concentrate at the corner. As a result, the laminate lost its stability and would not continue crushing perpendicularly on the platen. And the laminates bend, resulting in premature failure.

8.1.2. Manufacturing process

After this point, through-thickness stitches were applied on the flat sides of the corrugated cells instead of adhesive bonding. The manufacturing process of side-stitched samples can be divided into six steps, which are demonstrated on Figure 8.3 and described as following:

Step I: Prepare two pieces of corrugated laminates on the aluminium mould by resin infusion process (Figure 8.3A).

Step II: Hold these two pieces of corrugated laminate together symmetrically and seal the edges around the tubular cylinder except one end of the cylinder (Figure 8.3B). Then pull a certain amount of silica rubber liquid in to the hollow cylinder and cast an mandrel mould (Figure 8.3C).

Step III: Prepare the two layers of neat fabrics according to requested lay-up. Put these two layers of fabrics together symmetrically and stitch the edges by using Kevlar® threads (Figure 8.3D). It must be noted that the crushing triggers, either 90C fibres or chamfers by fibre drop-off, are already embedded into the neat fabrics on this step.

Step IV: Insert the silicon rubber mandrel inside the stitched fabrics (Figure 8.3E).

Step V: Transfer the fabrics together with mandrel back to aluminium female mould, then manufacture the side-stitched tube by resin infusion process (Figure 8.3F). To remain both top and bottom parts of side-stitched tube having the same geometric

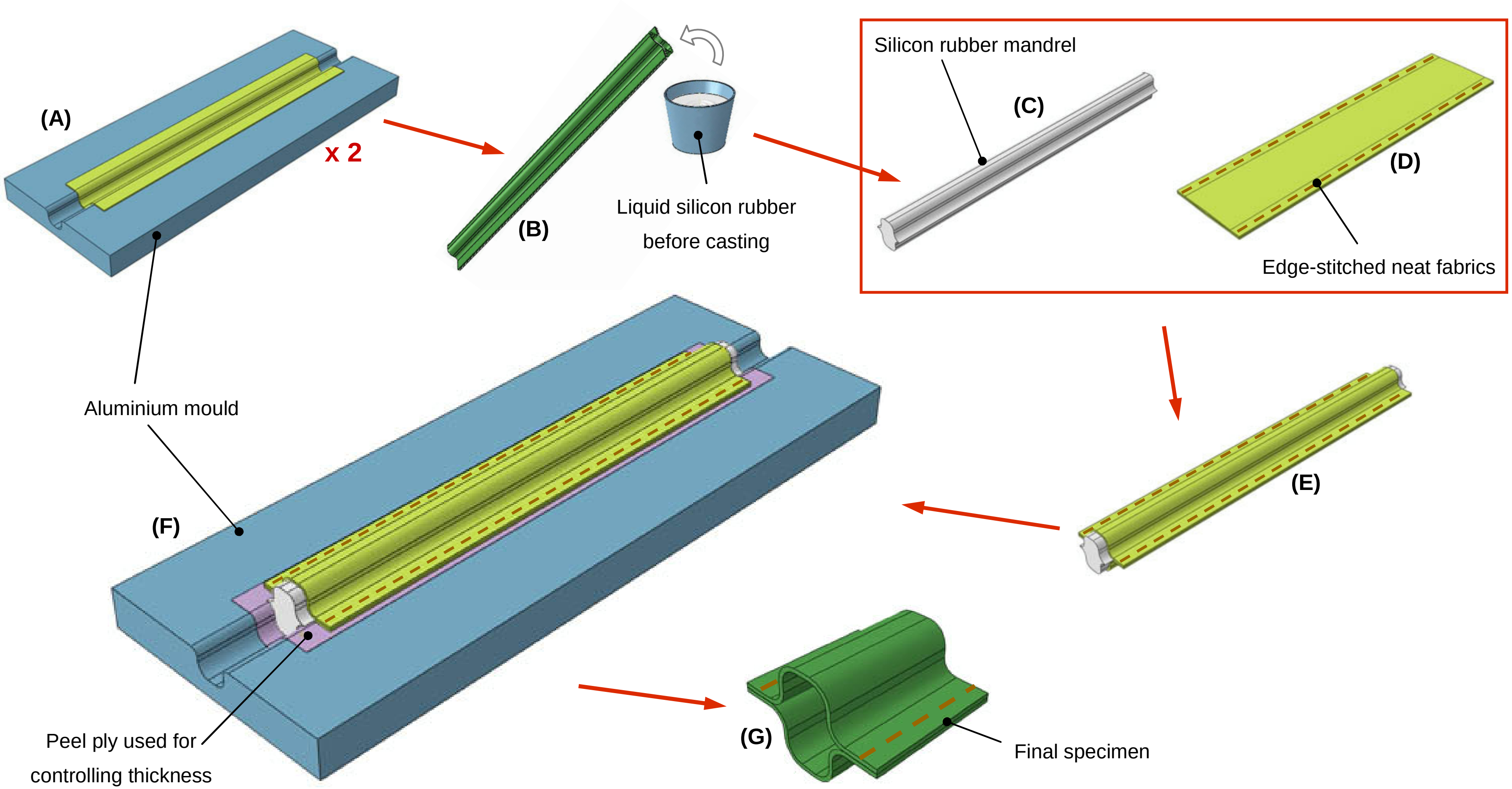

Figure 8.3 Manufacturing process of side-stitched crushing sample

shape, when it is applicable the peel ply are used to control the wall thickness of bottom laminate.

Step VI: Once the stitched tube is demoulded, pull the silicon rubber out and cut the tube into smaller sample size with required dimensions (Figure 8.3G).

8.1.3. Selection of control factors and levels

Conducting matrix experiments using special matrices, called orthogonal arrays is an important technique in Robust Design. It allows the effects of several parameters to be determined efficiently [78]. A *matrix experiment* consists of a set of experiments where the settings of several product or process parameters to be studied are changed from one experiment to another. The product or process parameters are also called *factors*, and parameter settings are also called *levels* [78].

The factors and levels must be carefully selected. The factors in experiments can be divided into two types: fixed and random. The fixed factors also can be subdivided into three classes: control factors, indicative factors and signal factors. In this study, the factors concerned in the matrix experiments are all control factors. The selection of the number of factor levels can have a significant impact on the size of matrix experiments. These factors and corresponding levels are described as following.

8.1.3.1. Trigger system

Apart from the trigger which is made of 90° lateral fibres used for geometric cells (Figure 5.6), a new trigger system that is similar to the steeple chamfer (Figure 4.1) was also introduced at this stage. However, this trigger is also different from the steeple chamfer as it is very difficult to evenly machine a chamfered trigger on corrugated laminate edge. Therefore, this trigger was manufactured by ply drop-off during lay-up process. The gap of the drop-off between two fabric edges is controlled to 1mm, approximately. The image and schematic sketch of this trigger system are shown in Figure 8.4.

The crushing behaviours of the structural composites which are triggered by different trigger systems have been discussed separately during previous chapters. The structural composites triggered by 90° lateral fibres and ply drop-off chamfer are compared in Figure 8.5.

On one hand, the advantage of using a chamfered trigger is to avoid large peak loads and sudden reductions in crushing load. But on the other hand, it becomes more difficult to connect the core section that is triggered by chamfers to the surface materials in a panel type composite structure. In this case, it is easy to see the benefits of the trigger fabricated by 90° fibres. Therefore, it is necessary to involve these two triggers in the further optimization process.

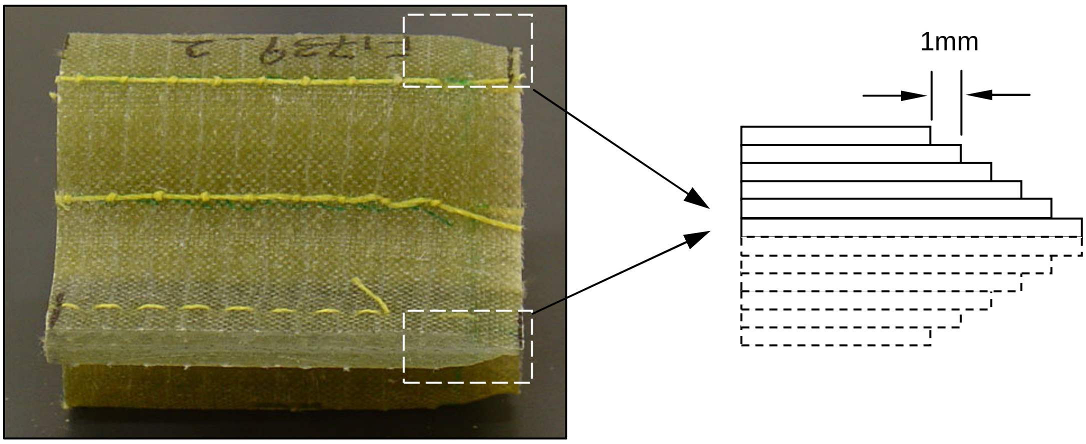

Figure 8.4 Demonstration of the trigger which is made by ply drop-off

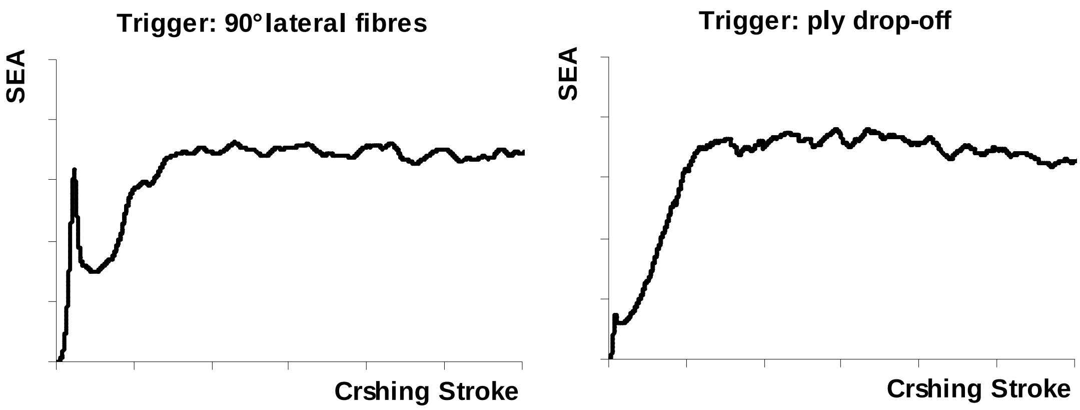

Figure 8.5 Comparisons of typical crushing behaviour between the samples triggered by lateral fibres and the samples triggered by ply drop-off chamfer

Accordingly, the first factor was assigned two levels for trigger system:

Factor A, Level 1: Lateral fibres

Factor A, Level 2: Ply drop-off

8.1.3.2. Fabric type and orientation

In previous work [2], Cauchi-Savona also applied Taguchi methods to compare carbon fibres and E-glass fibres on crushing performance of stitched composite plates. Although carbon fabrics exhibit slightly better crushing results than E-glass fabrics, he found that fabric type is less important compared with the other - orientation, resin type and stitching configurations.

It was found that the most significant factor is the fabric orientation. According to the crushing results of adhesive bonded cells (see Figure 5.16), biaxial $[90/0_2]_S$, triaxial $[\pm45/0_3]_S$, and woven fabric $[PW400/0]_S$, all can achieve the best potential energy absorption capacity. Besides, some other lay-up orientations, such as triaxial $[90/\pm45/0]_S$ and $[90/\pm45/0_2]_S$, and triaxial $[\pm45/0_2]_S$ also showed very remarkable crushing performance.

In order to find out the best configuration for the modified structural composite, three different fabric types and orientations are compared at this stage:

Factor B, Level 1: $[\pm45/0_2]_S$

Factor B, Level 2: $[90/0_2]_S$

Factor B, Level 3: $[PW400/0_2]_S$

The purpose of choosing above fabric orientations is to obtain similar thickness, and thus the effects from their perimeter/thickness (P/t) ratio could be minimized. Meanwhile, every lay-up orientation contains four layers of 0° fabric so that the effect of the content of 0° fibres also can be minimized.

8.1.3.3. Matrix system

Compared with polyester resin, vinyl ester and epoxy resins can significantly benefits the fracture toughness properties of composite materials (Figure 7.14). Whereas, the volume fraction of matrix also can dramatically lower the flexural properties of composite materials even if a tougher resin is used.

In comparison with other factors, the matrix system seems to have a more complex influence on the energy absorption capability of composite materials. Accordingly, the effects of the resins which have been introduced during previous chapters need to be investigated as well on crushing samples:

Factor C, Level 1: Polyester resin (Crystic®489PA)

Factor C, Level 2: Vinyl ester resin (Dion® 9102-500)

Factor C, Level 3: Epoxy resin (Araldite® LY564)

8.1.3.4. Beam web length

It is important to note that the main purpose of investigating geometric cells is to lead to an optimised design of panel type composite structure where the cell units are connected by beam webs. The length/thickness ratio of the flat beam webs are also expected to influence the energy absorption capacity of the entire structure.

To the geometric cell, Farley's concluded [62] that the total energy absorption of a composite structure is the combination of characteristic elements and structural elements (see equation 2.19). The energy absorption contributed by the beam webs is proportional to the cross-sectional area of beam webs in entire structure. The precondition is that the entire structure does not fail by buckling instead of crushing.

Furthermore, changing the length of the beam webs also varies the areal density of the panel type structure. This can significantly affect the performance of those structural composites that are subjected to impact or blast loadings. In order to balance the energy absorption capability with areal density in a modified cell, three levels of the length of beam web are chosen within this design:

Factor D, Level 1: BWL-9 (beam web length - 9mm)

Factor D, Level 2: BWL-15 (beam web length - 15mm)

Factor D, Level 3: BWL-21 (beam web length - 21mm)

8.1.3.5. Stitching gap on beam webs

Applying an appropriate stitching density on a composite laminate can increase its energy absorption capability by maximizing the properties of interlaminar fracture toughness. However, stitches also introduce defects in laminate by penetrating and disordering the original architecture of fabric. It is very necessary to avoid superfluous stitching by monitoring the stitching density.

Because the maximum distance between stitches in the same line is 5mm (see Figure 5.3), the stitching density is thus controlled by varying the gap between two stitching lines. For the core section, the stitching gap between lines was followed by previous parameters mentioned in Chapter 5, i.e. 15mm separation between lines. Because the laminate thickness of beam webs is relatively large, three levels of stitching gap were chosen to control the stitching densities on beam webs:

Factor E, Level 1: **StiGap-4 (Stitching gap - 4mm)**

Factor E, Level 2: **StiGap-8 (Stitching gap - 8mm)**

Factor E, Level 3: **StiGap-12 (Stitching gap - 12mm)**

Combined with the beam web length, the stitching gap is schematically sketched in Table 8.1. Unstitched beam webs are also investigated. One ninth samples which possess beam web length of 9mm remain unstitched. In contrast to the geometric cells studied previously, these unstitched (at beam webs) samples followed the sample manufacturing process that were shown in Figure 8.3 and bond two parts of symmetric fabrics via co-infusion process.

Table 8.1 **Schematic sketches of stitching gap combined with beam web length**

Factor E / Factor D	Stitching gap on beam webs		
Beam web length	4mm	8mm	12mm
9mm			
15mm			
21mm			

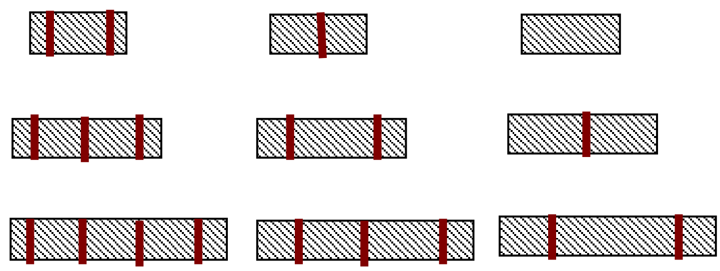

: Beam web   : Stitching line

8.1.3.6. *Crushing speed (crushing strain rate)*

The crushing speed, which sometimes is referred to as crushing strain rate, is also expected to have a minor effect on energy absorption of composites. Based on the inconsistent conclusions obtained from other researchers, it is still difficult to judge whether the energy absorption capability of this structure should increase with increasing crushing speed. Moreover, it is also interesting to know whether the factor of crushing speed is more effective than other factors, such as the stitching parameters. Thus, three crushing speed levels were implemented on the crushing samples:

Factor F, Level 1: 1mm/minute

Factor F, Level 2: 20mm/minute

Factor F, Level 3: 400mm/minute

Although dynamic crushing testes were not carried out in this study due to the limits of the testing facility, the investigation on above speed levels still could be valuable for the further applications.

8.1.4. Selection of orthogonal array

The six factors described above including one 2-level factor and five 3-level factors, are introduced for the Robust Design. These factors and their levels are indicated on a typical crushing sample that is shown in Figure 8.6.

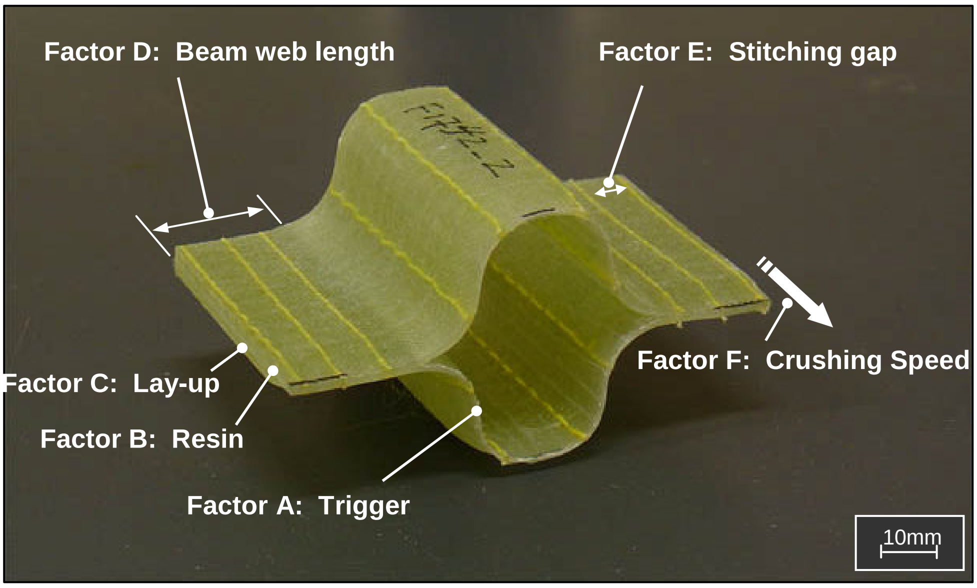

Figure 8.6 Six factors which indicated on a typical crushing sample for the Robust Design

According to the standard orthogonal arrays recommended by Taguchi (see Table 2.1), there are several options of selecting a suitable orthogonal array. One option is to select an orthogonal array which entirely consists of 3-level factors, and then to convert the 2-level factor into a 3-level factor, by using a dummy factor. The problem with this technique is that the dummy factor ends up being investigated more than the other factors [78]. The other option is to select an "levels-mixed" orthogonal array.

In this study, the L_{18} (2^1 x3^7) was selected. A full original L_{18} (2^1 x3^7) can be found in Table 2.2, Chapter 2. As a summary, these six factors and their levels as well as an L_{18} (2^1 x3^7) orthogonal array where these factors and levels are assigned are listed in Table 8.2 and Table 8.3, respectively.

Table 8.2 Control factors and their levels for the Robust Design

	Levels			
Factors	**1**	**2**	**3**	**DOF***
A - Trigger	90D Fibres	Ply drop-off chamfer		1
B - Resin	Polyester	Vinyl ester	Epoxy	2
C - Lay-up	[+45,-45/02]s	[90/02]s	$[PW/0_2]_S$	2
D - Beam web length	BWL-9mm	BWL-15mm	BWL-21mm	2
E - Stitching gap	StiGap-4mm	StiGap-8mm	StiGap-12mm	2
F - Crush Speed	1mm/min	20mm/min	400mm/min	2

** DOF: degree of freedom*

Table 8.3 shows that the experimental run consists of 18 experiments. Each experiment presents a combination of different levels in a crushing sample. Five specimens were prepared and tested for each experiment. As a result, each experiment will achieve an SEA level. The SEA level is the response of a product in the Robust Design. Because only six factors are studied, G and H are conducted as dummy factors in the L_{18} (2^1 x3^7) array. To analyse the obtained SEA results, a number of statistic methods that have been introduced in Chapter 2 are used at this stage.

Table 8.3 **Parameters for each experiment in the Robust Design using the L_{18} (2^1 x3^7) orthogonal array**

Ref.	Expt. No.	Factors							
		Trigger	Resin	Lay-up	Beam web length	Edge stitching density	Test Speed	G*	H*
F1727	1	90D Fibres	Polyester	[+45,-45/02]s	BWL-9mm	STIGAP-4mm	1mm/min	1	1
F1728	2	90D Fibres	Polyester	[90/02]s	BWL-15mm	STIGAP-8mm	20mm/min	2	2
F1729	3	90D Fibres	Polyester	[PW/02]s	BWL-21mm	STIGAP-12mm	400mm/min	3	3
F1730	4	90D Fibres	Vinyl ester	[+45,-45/02]s	BWL-9mm	STIGAP-8mm	20mm/min	3	3
F1731	5	90D Fibres	Vinyl ester	[90/02]s	BWL-15mm	STIGAP-12mm	400mm/min	1	1
F1732	6	90D Fibres	Vinyl ester	[PW/02]s	BWL-21mm	STIGAP-4mm	1mm/min	2	2
F1733	7	90D Fibres	Epoxy	[+45,-45/02]s	BWL-15mm	STIGAP-4mm	400mm/min	2	3
F1734	8	90D Fibres	Epoxy	[90/02]s	BWL-21mm	STIGAP-8mm	1mm/min	3	1
F1735	9	90D Fibres	Epoxy	[PW/02]s	BWL-9mm	STIGAP-12mm	20mm/min	1	2
F1736	10	45D Chamfer	Polyester	[+45,-45/02]s	BWL-21mm	STIGAP-12mm	20mm/min	2	1
F1737	11	45D Chamfer	Polyester	[90/02]s	BWL-9mm	STIGAP-4mm	400mm/min	3	2
F1738	12	45D Chamfer	Polyester	[PW/02]s	BWL-15mm	STIGAP-8mm	1mm/min	1	3
F1739	13	45D Chamfer	Vinyl ester	[+45,-45/02]s	BWL-15mm	STIGAP-12mm	1mm/min	3	2
F1740	14	45D Chamfer	Vinyl ester	[90/02]s	BWL-21mm	STIGAP-4mm	20mm/min	1	3
F1741	15	45D Chamfer	Vinyl ester	[PW/02]s	BWL-9mm	STIGAP-8mm	400mm/min	2	1
F1742	16	45D Chamfer	Epoxy	[+45,-45/02]s	BWL-21mm	STIGAP-8mm	400mm/min	1	2
F1743	17	45D Chamfer	Epoxy	[90/02]s	BWL-9mm	STIGAP-12mm	1mm/min	2	3
F1744	18	45D Chamfer	Epoxy	[PW/02]s	BWL-15mm	STIGAP-4mm	20mm/min	3	1

** G and H are conducted as dummy factors*

Table 8.4 Crushing results of Robust Design

	SEA Results									VF%
Expt. No.	1	2	3	4	5	Mean, $\bar{y}_i$	Deviation	CV%	S/N ratio, η	
1	60.77	60.39	60.16	58.42	60.64	60.07	0.96	1.59	35.57	53.96%
2	65.45	60.44	61.74	62.01	61.74	62.27	1.88	3.01	35.88	50.89%
3	68.56	63.44	68.72	68.43	62.63	66.36	3.05	4.59	36.42	52.72%
4	69.46	70.74	69.50	74.34	68.96	70.60	2.19	3.11	36.97	49.94%
5	68.36	66.02	68.92	69.59	66.19	67.82	1.62	2.39	36.62	47.40%
6	80.96	77.29	75.37	78.85	79.35	78.37	2.12	2.71	37.87	46.73%
7	77.32	73.17	71.97	67.16	78.17	73.56	4.45	6.04	37.29	44.82%
8	60.89	55.30	57.43	58.16	56.78	57.71	2.06	3.57	35.21	48.52%
9	70.30	67.82	72.81	74.72	71.93	71.51	2.61	3.65	37.07	49.61%
10	56.15	56.34	55.26	56.33	56.80	56.18	0.56	1.01	34.99	54.68%
11	59.20	54.42	51.05	58.48	55.81	55.79	3.29	5.89	34.89	54.80%
12	65.59	67.74	66.82	65.55	65.35	66.21	1.04	1.57	36.42	55.14%
13	73.10	72.58	68.13	71.08	67.37	70.45	2.59	3.67	36.94	51.76%
14	58.00	60.69	58.78	62.49	60.10	60.01	1.75	2.91	35.56	49.09%
15	82.81	87.03	87.45	86.86	80.20	84.87	3.22	3.79	38.56	47.03%
16	66.44	68.67	71.59	65.84	71.36	68.78	2.68	3.89	36.73	48.88%
17	67.52	62.64	67.33	63.29	63.26	64.81	2.40	3.71	36.22	44.36%
18	72.78	74.18	75.96	74.06	72.05	73.81	1.50	2.03	37.36	47.30%

8.2. Results of Robust Design

The crushing results of the Robust Design experiments are shown in Table 8.4. As the characteristic of the SEA results is "Larger-the-better", the S/N ratios then were calculated by applying equation 2.31. Two statistical approaches, response table and ANOVA method, are applied for analysing the results produced through the orthogonal array. Both mean values and S/N ratios which are listed in Table 8.4 are calculated by using those statistical approaches.

8.2.1. Response Tables

By taking the numerical values of the mean ($\bar{y}_i$) and S/N ratios (η) that are listed in Table 8.4, the average $\bar{y}_i$ and η for each level of the six factors can be obtained as listed in Table 8.5 and Table 8.6, respectively. It reveals that the most significant factor is the fabric type and orientation, while the least significant factor is the trigger system.

These averages are shown graphically in Figure 8.7 and Figure 8.8, respectively. The average line has also been drawn in these figures. The response graph is used to visualize the data from the response table and identify factors that have large effects on the average values. As the differences between the best and worst parameters are clearly shown, it is easy to choose the best combination of parameters for crushing sample. Furthermore, the confidence intervals (CI_1) around the average $\bar{y}_i$ and η for each level of these factors are also plotted as the error bars in Figure 8.7 and Figure 8.8.

Table 8.5 The Response Table of the crushing results: Mean

	Factors					
	A	B	C	D	E	F
Level 1	67.59	61.15	66.61	67.94	66.93	66.27
Level 2	66.77	72.02	61.40	69.02	68.41	65.73
Level 3	-	68.36	73.52	64.57	66.19	69.53
Difference	0.82	10.87	12.12	4.45	2.22	3.80
Rank	6	2	1	3	5	4
Optimum	90D Fibres	Vinyl ester	[PW/0$_2$]s	BWL-15mm	StiGap-8mm	400mm/min

Table 8.6 **The Response Table of the crushing results: S/N ratio**

	Factors					
	A	B	C	D	E	F
Level 1	36.54	35.69	36.42	36.55	36.42	36.37
Level 2	36.41	37.09	35.73	36.75	36.63	36.30
Level 3	-	36.65	37.28	36.13	36.38	36.75
Difference	0.14	1.39	1.55	0.62	0.25	0.45
Rank	6	2	1	3	5	4
Optimum	90D Fibres	Vinyl ester	[PW/0$_2$]s	BWL-15mm	StiGap-8mm	400mm/min

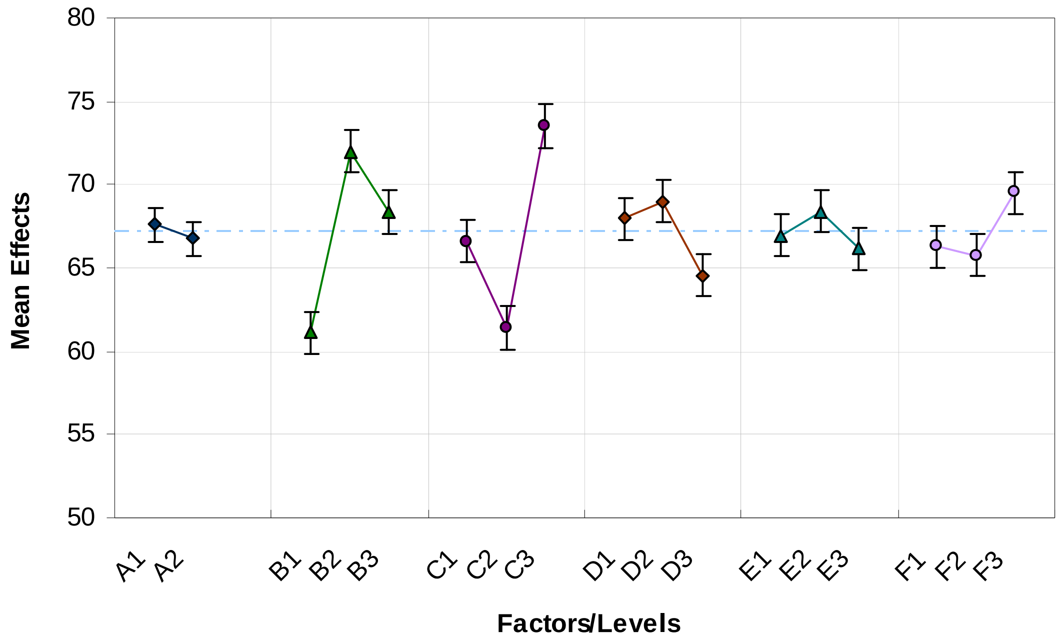

Figure 8.7 **Response graph of SEA results for mean values (Error deviation = CI$_1$; confidence level = 95%)**

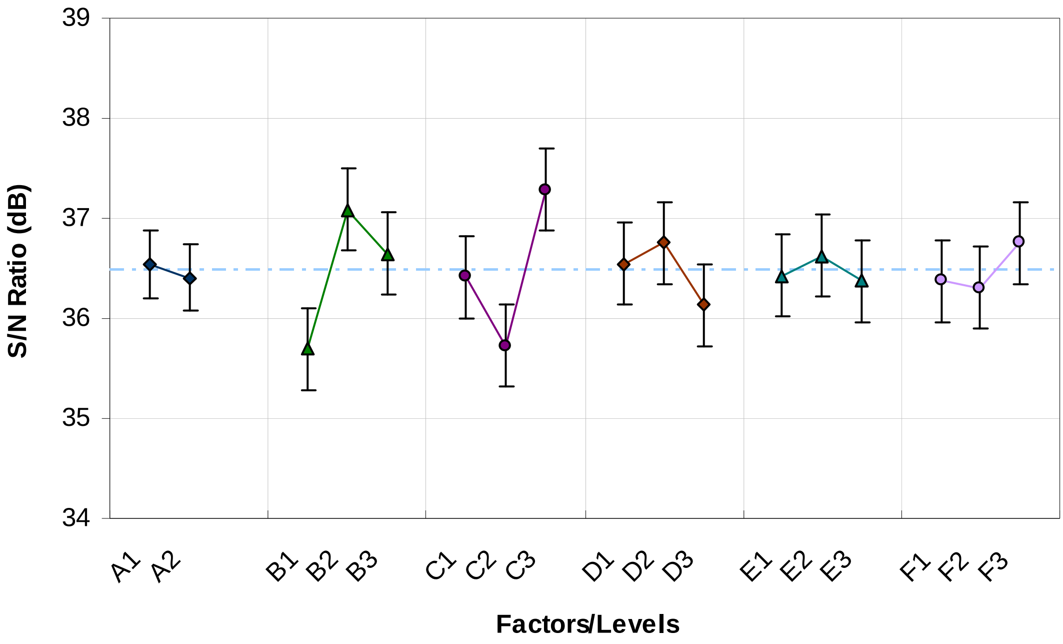

Figure 8.8 **Response graph of SEA results for S/N ratios (Error deviation = CI_1; confidence level = 95%)**

8.2.2. ANOVA method

Above results are further confirmed by the ANOVA results that are shown in Table 8.7 and Table 8.8. In the ANOVA results, factor A and factor E results have been pooled into the error since these particular factors showed a high degree of error within themselves. This does have the adverse influence of increasing the total error.

The S/N ratio results are practically identical to the analysis of means for the unpooled factors. In both cases, the fabric type and the matrix type are the most significant factors while the pooled error proves to be greater than the influences of the remaining factors. This result implies that there was a reasonable degree of error that affects the prediction. The alpha mistake is probably made in this case. In other words, some factors do not improve the energy absorption capability of crushing sample.

In Table 8.7 and Table 8.8, the percentage contribution of each important factor to the improvement of the SEA is plotted. The error can be seen to be significant, and it is even more significant than the effects of beam web length and crushing speed on SEA results. The contribution of these factors for the mean values and S/N ratios are also plotted in Figure 8.9 and Figure 8.10, respectively. It is interesting to note that the effect of crushing speed becomes negligible in the ANOVA of S/N ratios.

Table 8.7 ANOVA table for pooled mean values

Source	Pool	*SSq*	*DOF*	*Variance*	*F'-ratio*	$F_{a,D1,D2}$ (α=5%)	*Contribution %*
Factor A	Y	15.1	1	15.07	1.21	3.96	
Factor B	-	1836.3	2	918.15	73.49	3.11	32.25
Factor C	-	2217.2	2	1108.59	88.74	3.11	39.03
Factor D	-	323.8	2	161.92	12.96	3.11	5.33
Factor E	Y	76.6	2	38.29	3.14	3.11	
Factor F	-	253.4	2	126.69	10.14	3.11	4.08
Factor G*	Y	361.0	2	-	-	-	
Factor H*	Y	21.7	2	-	-	-	
Error	-	512.6	74	6.93	1.00	1.46	
Pooled Error	-	986.9	79	12.49	1.80	1.45	19.30
Mean	-	406139.5	1	-	-	-	-
Total	-	5617.7	89	-	-	-	100.00

* Factor was run as a dummy

Table 8.8 ANOVA table for pooled S/N ratio

Source	Pool	*SSq*	*DOF*	*Variance*	*F'-ratio*	$F_{a,D1,D2}$ (α=5%)	*Contribution %*
Factor A	Y	0.08	1	0.08	0.43	5.12	
Factor B	-	6.09	2	3.04	15.28	4.26	33.360
Factor C	-	7.27	2	3.63	18.25	4.26	40.286
Factor D	-	1.20	2	0.60	3.02	4.26	4.718
Factor E	Y	0.21	2	0.11	0.53	4.26	
Factor F	-	0.70	2	0.35	1.76	4.26	1.782
Factor G*	Y	0.96	2	-	-	-	
Factor H*	Y	0.10	2	-	-	-	
Error	-	0.44	2	0.22	1.10	3.11	
Pooled Error	-	1.79	9	0.20	0.03	2.00	19.85
Mean	-	23949.34	1	-	-	-	-
Total	-	17.05	17	-	-	-	100.00

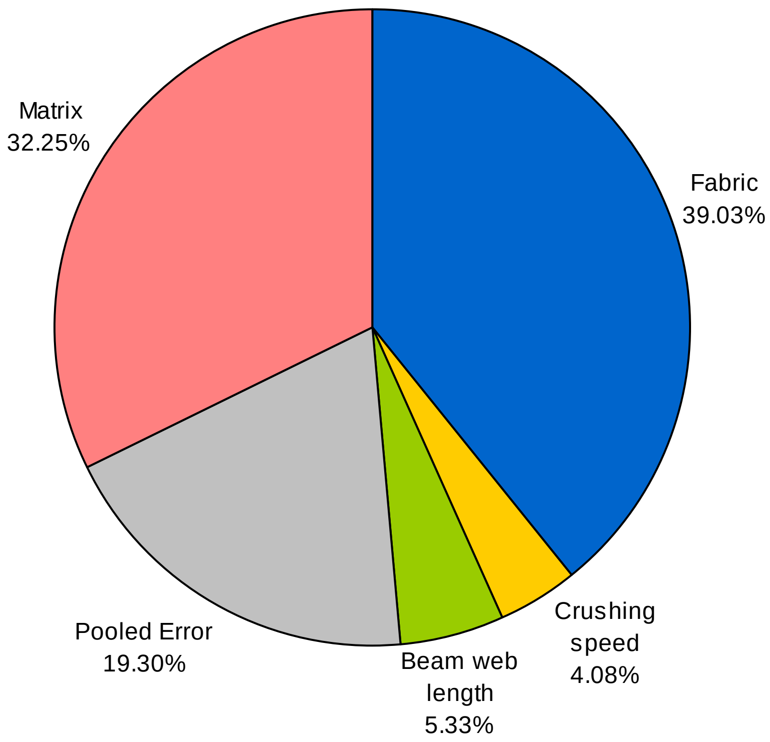

Figure 8.9 **Percentage contributions of factors for the ANOVA of mean values**

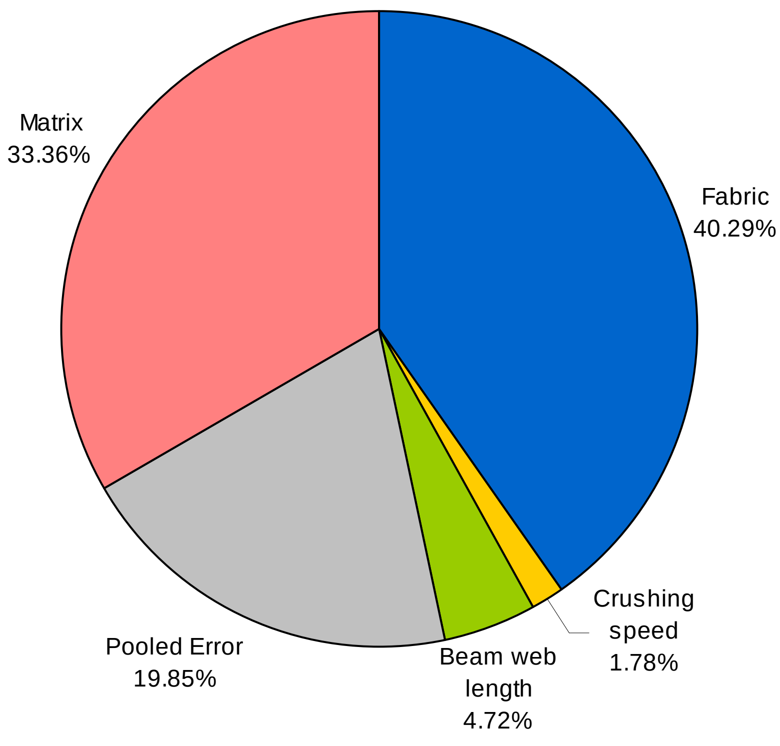

Figure 8.10 **Percentage contributions of factors for the ANOVA of S/N ratios**

8.2.3. Confirmation experiment

Therefore, according to the crushing results analysed in Section 8.2.1 , the confirmation experiment was performed. The optimised samples were made of the optimum levels that were listed in Table 8.5 and Table 8.6. It is important to note that the vinyl ester resin used for the confirmation test is slightly different from the vinyl ester resin used for optimization process. The vinyl ester resin used in previous stages was expired and was unobtainable. The new vinyl ester resin, Dion® 9102, was also supplied by Reichhold (UK) Ltd. But it was not a preaccelerated product. Therefore, an cobalt solution (0.1%) supplied by Glasplies Limited (UK) was used as the accelerator for Dion® 9102.

The average of SEA level obtained from the confirmation experiment is 77.28 kJ/kg. The results of confirmation experiment of are compared with the mean of entire experimental results ($\bar{y}$, see equation 2.32) and the estimated mean ($\hat{y}$, see equation 2.53). These comparisons for average SEA levels and average S/N ratios are shown in Table 8.9 and Table 8.10 respectively.

Table 8.9 Predicted values and confidence intervals for factors

Prediction and confirmation results	Confidence intervals
Average of entire experimental results, $\bar{y}$ = 67.18	CI_1 (factor A) = ±1.04
	CI_1 (factor B-F) = ±1.27
Average of prediction, $\hat{y}$ = 83.79	CI_2 = ±2.43
Average of confirmation experiment = 77.28	CI_3 = ±3.94

Confidence level = 95%

Table 8.10 Prediction and confirmation regarding to S/N ratio

Prediction and confirmation results	Confidence intervals
Average of entire experimental results, $\bar{y}$ = 36.48	CI_1 (factor A) = ±0.34
	CI_1 (factor B-F) = ±0.41
Average of prediction, $\hat{y}$ = 38.44	CI_2 = ±0.71
Average of confirmation experiment = 37.36	CI_3 = ±0.84

Confidence level = 95%

The SEA results of optimised samples are approximately 15% higher than the SEA average results of 18 experimental observations (see Table 8.4). According to the estimated means, the confirmation samples combined with optimised parameters could achieve a bit higher SEA than the real results that were obtained in confirmation experiment. It implies that some significant factors experimental and environmental factors could be neglected according to above results. One possibility is that the mechanical properties of vinyl ester resin that was used for confirmation test might be slightly decreased. While other factors, such as machining methods and testing conditions also might affect the confirmation results. All these factors are worthy of being measured in the further step of Robust Design.

8.3. Summary

Compared with the three geometric cells which were previously investigated in Chapter 5, the optimised cells show a very remarkable increase on the crushing performance. These results indicate that the SEA level of a panel type structural composite potentially is able to achieve more than 80kJ/kg, if the configuration parameters are chosen properly. Robust engineering methods which are applied in this research are proved as an effective and efficient tool for the design of experiment and products. Materials and labour were thus considerably reduced by using those methods.

The resin and fabric types are the main factors which determine crushing performance of composites cells. Together they contribute about 71% energy absorption capacity to composite cells. The enhancement of bonding two half cells by using stitching and co-infusion processes can also significantly improve the crushing performance. But this was mainly achieved by avoiding rapid and unstable central crack along bonding area. The stitches themselves actually did not improve the energy absorption capacity during the crushing of cells.

Chapter 9. Discussion

The failure mechanisms for structural composites which were investigated in this research have been described briefly in previous chapters. The failure modes of energy absorbing composites are dependent on a large number of factors, including boundary conditions, geometric shapes, triggers and material types, etc. Researchers [14-16] have found that the lamina bending is the most efficient crushing mode for fibre-reinforced composite laminates. The main purpose of this chapter is to analyse the geometric and scale effects on energy absorption of structural composites. The failure mechanisms of these structural composites are discussed.

9.1. Failure mechanism of intersecting square cells

In Figure 9.1, the SEA values of intersecting square cells were plotted against the ratio of separation width (SD) to thickness (h). A trendline was then drawn over all these crushing data. It seems the energy absorption capability of intersecting square cell increases when the SD/h ratio decreases.

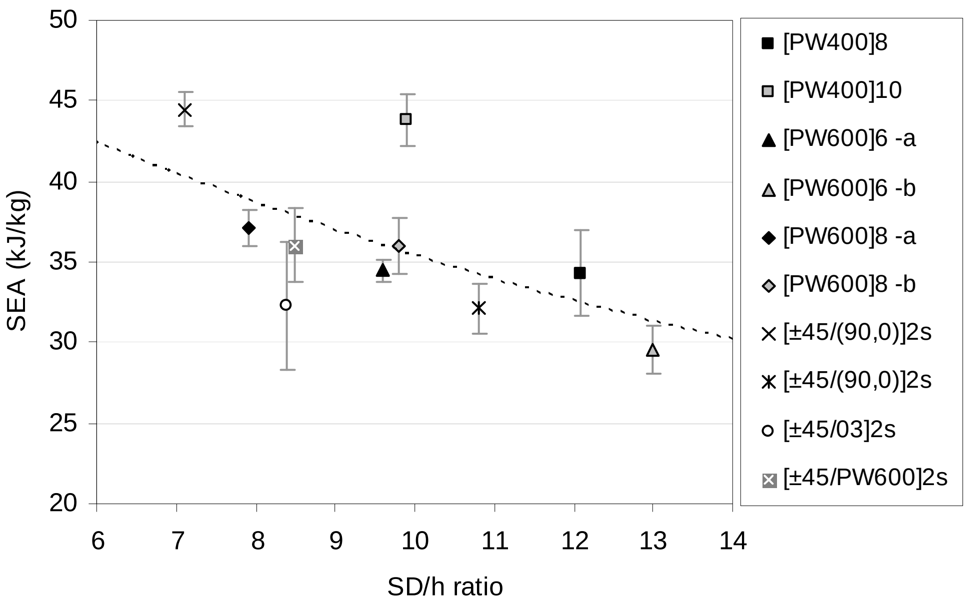

Figure 9.1 SEA vs. separation width/thickness (SD/h) for all intersecting square cells

It is important to mention that the SD/h ratios of the intersecting square cells were scaled by varying the fabric type and the number of fabric layers. The relationship between SEA and SD/h ratio, which was presented in Figure 9.1, becomes more straightforward if the data are categorized by the fibre architecture. This result can be found in Figure 9.2.

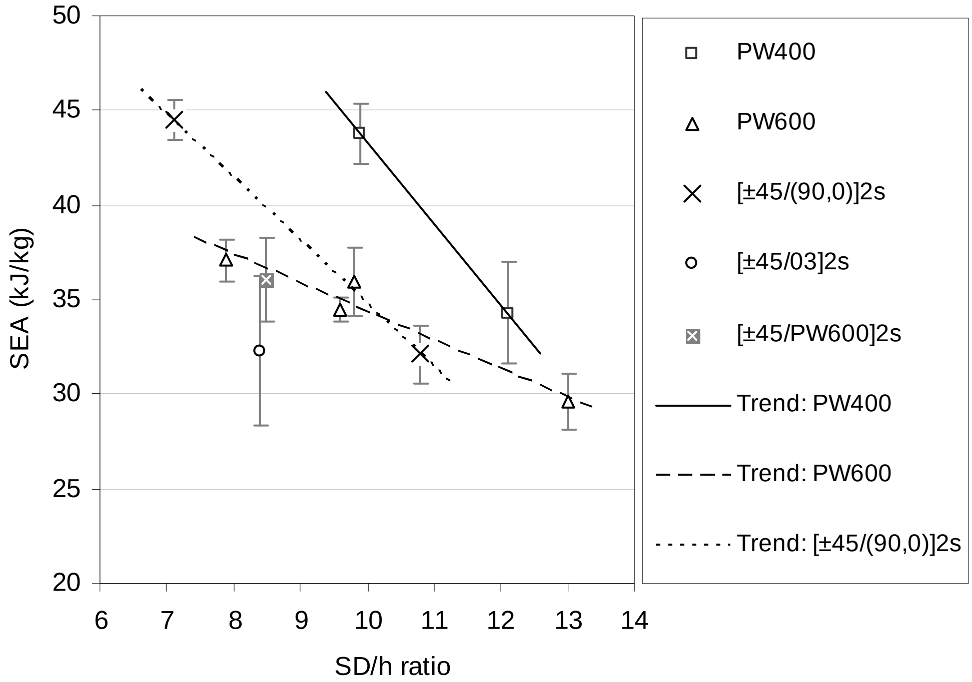

Figure 9.2 SEA vs. separation width/thickness (SD/h) for all intersecting square cells which were categorized by the fibre architecture

Therefore, apart from the geometric effects, the energy absorption capability of structure composites is also affected by the fibre architecture. For example, sample F1537_ISC which was made of $[PW400]_{10}$ achieved a much higher SEA level with SD/h ratio of 9.9 than most samples that possessed smaller SD/h ratios. Furthermore, the energy absorption capability of sample $[\pm 45/0_3]_{2S}$ seems to be lowered by placing stiffer 0° fibre in the middle of laminate, compared with sample $[\pm 45/PW600]_{2S}$.

Increasing the proportion of 0° fibres can increase the compressive strength of laminate, but poor interlaminar fracture toughness properties between 0° fabrics could also reduce the energy absorption capability. Because of their high stiffness, these bundles of 0° fibre can hardly be bent during crushing. This phenomenon can be found on the pictures of $[\pm45/0_3]_{2S}$ crushing sample that are shown in Figure 9.3 (top). As a result, the energy absorbing effectiveness caused by interlaminar friction and fronds bending could be reduced.

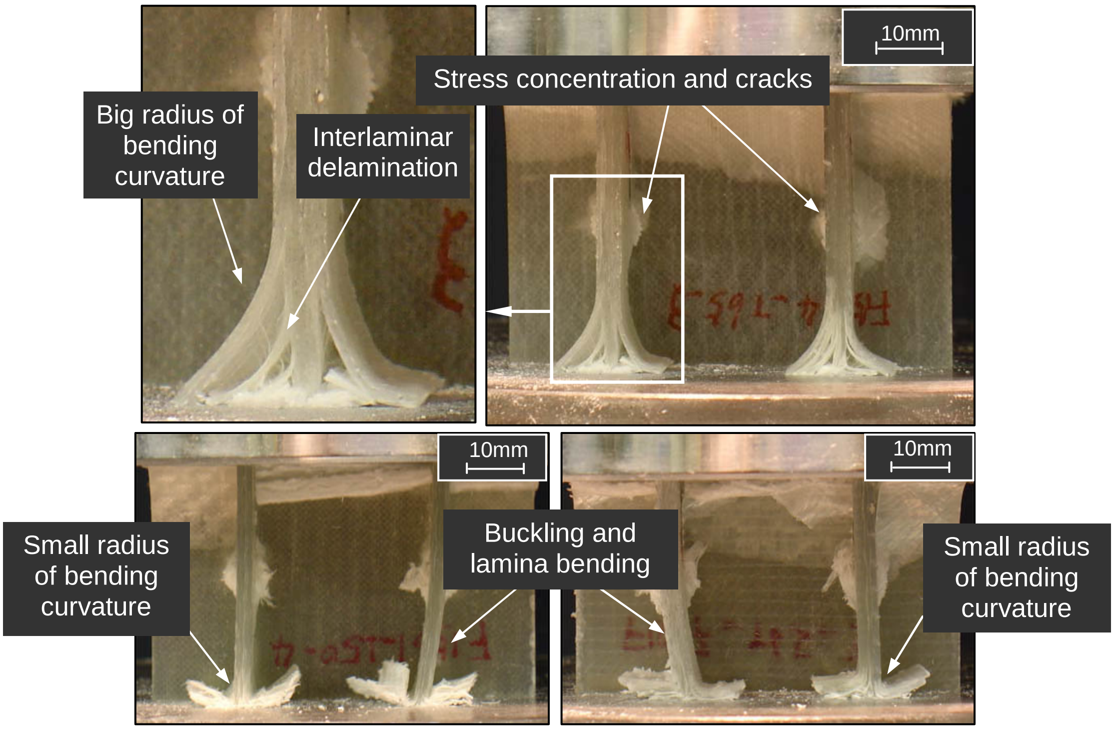

Figure 9.3 Photographs of intersecting square cells during crushing: $[\pm45/0_3]_{2S}$ (F1564_ISC top), $[PW400]_{10}$ (F1537_ISC, bottom left) and $[\pm45/PW600]_{2S}$ (F1567_ISC, bottom right)

In contrast, $[\pm45/PW600]_{2S}$ as well as other laminates that were made of woven fabrics crushed with much smaller radius of bending curvature in the splayed fronds. In addition to interlaminar friction and the bending of the fronds, extra energy could be absorbed by the fragmentation fracture of woven fibres bundles during crushing. This phenomenon also can be found in Figure 9.3 (bottom).

Furthermore, it is important to note that most ISC samples failed in an unstable crushing mode compared with simply-supported plates. Due to the freely-supported boundary conditions, buckling and the "single-direction lamina bending", which differs from the laminar bending mode with symmetric splaying fronds, would easily occur during crushing (also see Figure 9.3).

Therefore, in some cases, cumulated buckling stresses would generate lateral cracks on laminates around end of slots. As a result, these intersecting laminates failed in a much less efficient crushing mode which accompanied with laminate buckling and folding as well as unsymmetrical splaying fronds (see crushed $[\pm 45/(90,0)]_{2S}$ sample shown in Figure 9.4).

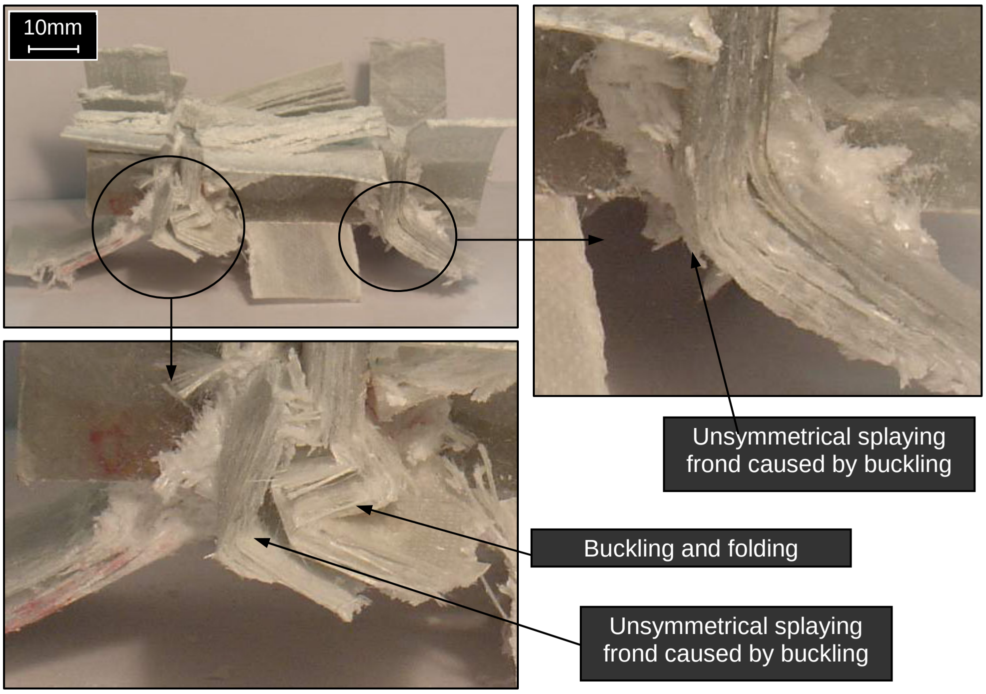

Figure 9.4 Photographs of crushed $[\pm 45/(90,0)]_{2S}$ sample (F1535_ISC)

The energy absorption capability of intersecting square cells is dominated by the geometric scale and fibre architecture as well as the crushing mode. Unlike the tubular and simply-supported plates, structural stability played a crucial role in this intersecting structure. Because of the freely-supported boundary conditions along the intersecting edges of laminate plates, the plates tend to fracture and crack after the accumulated compression stresses exceeded the critical buckling stresses of laminate. Therefore corrugated cells were investigated as a more efficient energy absorbing unit in the design of panel type structures.

9.2. Failure mechanism of three geometric cells

The crushing failure mode and energy absorption capability of the modified geometric cells are influenced by structural geometric shape, bonding effectiveness, fabric lay-ups as well as laminate thickness. The failure mechanism of the geometric cells becomes more complicated than that of intersecting square cells.

Due to different thicknesses and boundary conditions, the corrugated core section and the section of flat side of a geometric cell present different deformation forms during crushing. These crushing forms are demonstrated schematically in Figure 9.5. Accordingly, the crushing forms of both core and flat side for each sample were recorded during the test. They are listed in Table 9.1. It is important to note that the S-cells and H-cells, which have the same fibre architecture, crushed in the same form. Compared with H-/S-cells, C-cells exhibit more effective crushing forms at the flat edge area.

It is revealed in Table 9.1 that almost all specimens crushed by lamina bending mode in the section of corrugated core. Although all [0/90/0] cells also crushed by lamina bending mode in the core section, their splaying fronds exhibited fairly large bending radius so that all [0/90/0] cells failed in relatively low SEA levels. This result is a consequence of the early central crack growth and small Mode-I strain energy release rate (G_{IC}). When the modified lock stitches were applied to the [0/90/0] fabrics, stitches actually were not hooked around the exterior 0° fibres as the stitching direction is parallel to the 0° direction. Therefore, without constraining the propagation of central crack, the exterior 0° fibres did not bend during crushing due to their high stiffness. The 90° fibres in the middle contribute very limited energy absorption effectiveness due to their low compression strength.

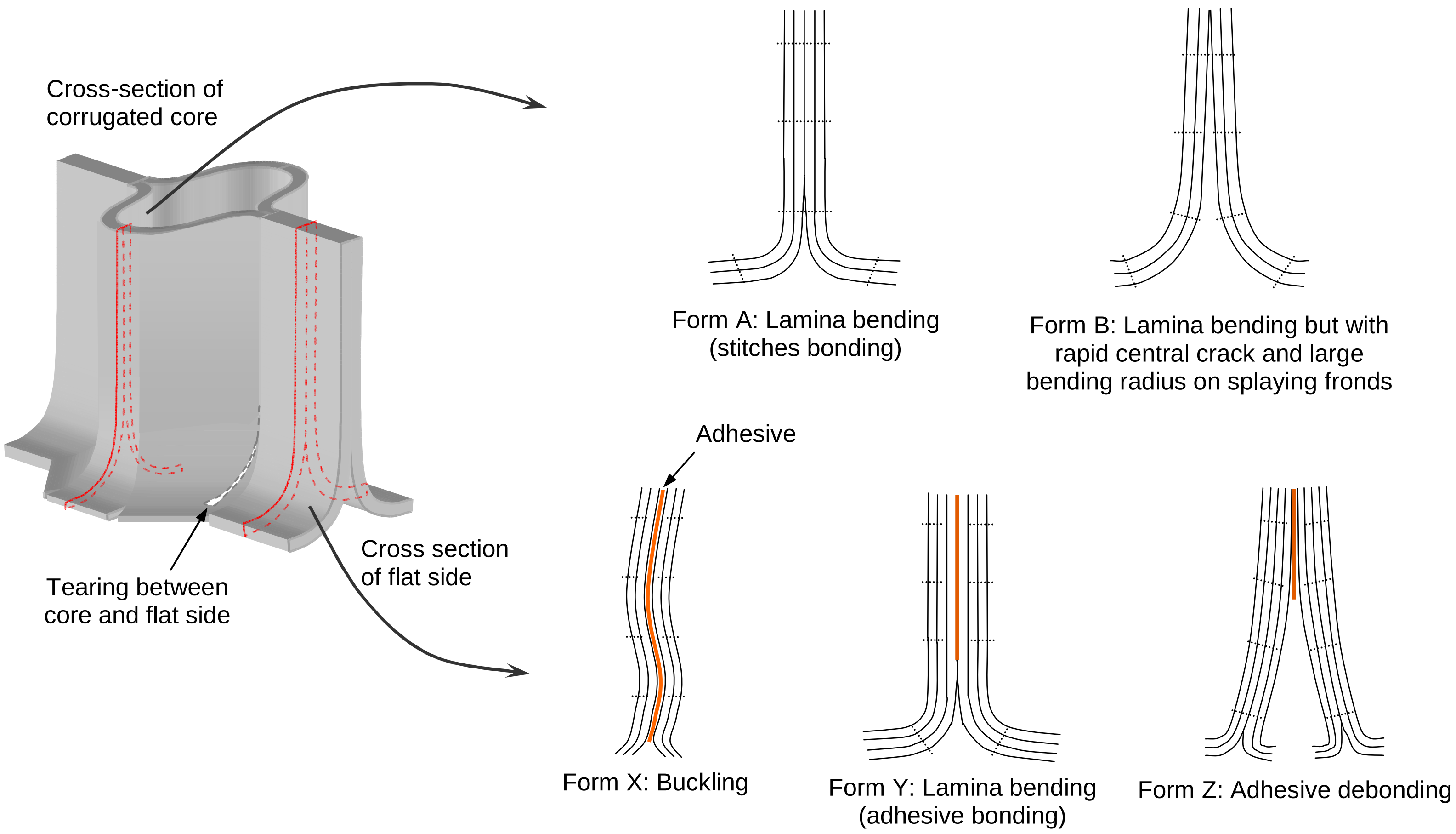

Figure 9.5 **Schematic sketch of crushing forms**

Table 9.1 **Crushing forms for all geometric cells**

Lay-up	Crushing forms: S-cells					Crushing forms: C-cells					Crushing forms: H-cells				
	A	B	X	Y	Z	A	B	X	Y	Z	A	B	X	Y	Z
[90/0/90]	Primary		Primary	Secondary		Primary			Primary		Primary		Primary	Secondary	
[0/90/0]		Primary		Primary			Primary		Primary			Primary		Primary	
$[90/0]_S$	Primary			Primary		Primary			Primary		Primary			Primary	
$[90/0_2]_S$	Primary			Secondary	Primary	Primary			Primary		Primary			Secondary	Primary
$[90/0]_{2S}$	Primary				Primary	Primary			Primary		Primary				Primary
[±45/0/±45]	Primary		Secondary	Primary		Primary		Secondary	Primary		Primary		Secondary	Primary	
$[\pm 45/0]_S$	Primary			Primary		Primary			Primary		Primary			Primary	
$[\pm 45/0_2]_S$	Primary				Primary	Primary			Primary	Secondary	Primary				Primary
$[\pm 45/0_3]_S$	Primary				Primary	Primary			Primary	Secondary	Primary				Primary
$[90/\pm 45/0]_S$	Primary				Primary	Primary			Primary	Secondary	Primary				Primary
$[90/\pm 45/0_2]_S$	Primary				Primary	Primary			Secondary	Primary	Primary				Primary
$[PW400/0]_S$	Primary			Primary		Primary			Primary		Primary			Primary	

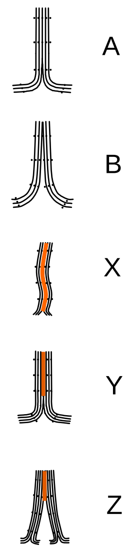

Primary

Secondary

9.2.1. Effect of the content of 0° fibres

In the same way as other fibre-reinforced composite structures, the energy absorption capabilities of the geometric cells are highly sensitive to the proportion of 0° fibres in the middle of the laminate. It was found the SEA levels of biaxial and triaxial cells increases with increasing the content of 0° fibres placed in the middle of the laminate, whether by actual energy absorption data or by potential energy absorption data. Figure 9.6 and Figure 9.7 demonstrate this trend on potential energy absorption data of biaxial and triaxial cells, respectively. Especially for triaxial cells, a clear tendency and separated boundaries between geometric shapes can be seen on these triaxial data.

However, it has been discussed previously that the [0/90/0] sample is an exception. It seems the stitches did not prevent the [0/90/0] sample from rapid central cracking during crushing. Their 0° fibres proportion reaches almost 67% by weight, but their energy absorption capabilities has been proved as the poorest (see Figure 5.15 and Figure 5.16 in Chapter 5).

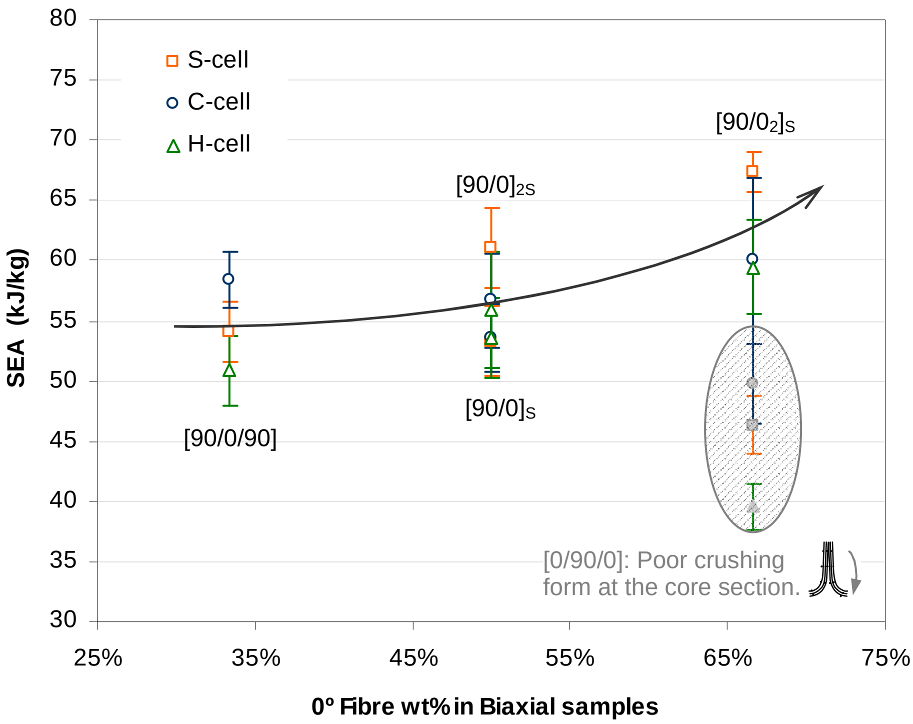

Figure 9.6 Potential energy absorption capability of biaxial cells affected by the weight proportion of longitudinal 0° fibres.

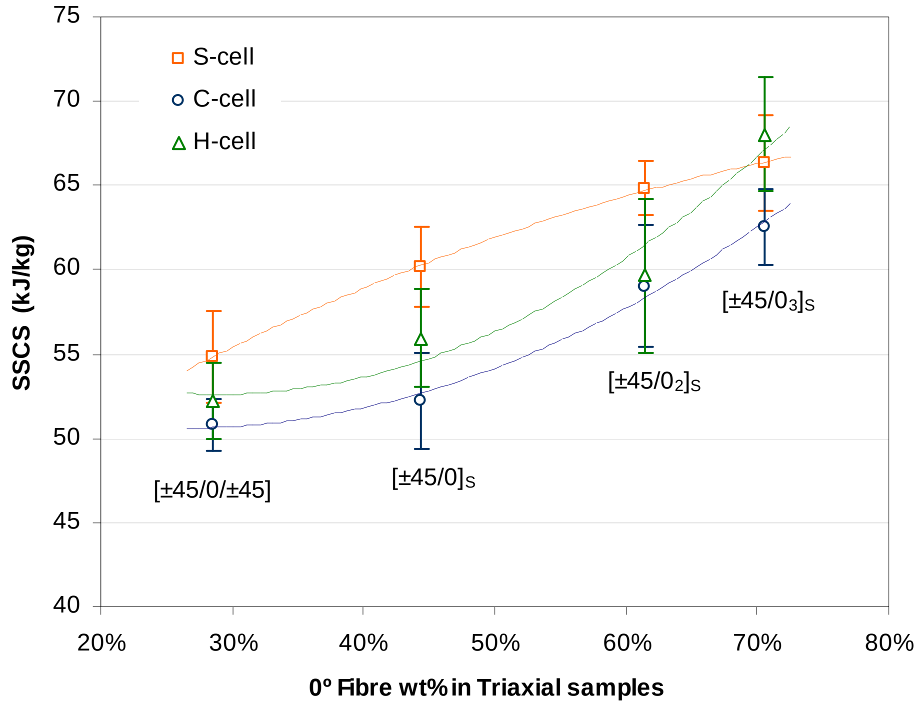

Figure 9.7 Potential energy absorption capability of triaxial cells affected by the weight proportion of longitudinal 0° fibres

It is important to note here that stitches were stitched along 0°, the crushing result for [0/90/0] sample with 90° stitches might be different. Moreover, for some other structural composites, increasing of 0° fibres proportion would not definitely increase energy absorption capabilities of structures. For example, the $[\pm45/0_3]_{2S}$ intersecting square cells achieved lower SEA level than $[\pm45/PW600]_{2S}$ cells (see Table 4.1).

In contrast, the $[90/0_2]_S$ samples which possess as similar proportion of 0° fibres as the [0/90/0] samples, exhibited much better energy absorbing capability. They crushed in a lamina bending mode in the core section and exhibit much more effective crushing forms with a small bending radius for the fronds. In this region, photos of crushed [0/90/0] and $[90/0_2]_S$ samples are shown in Figure 9.8 and Figure 9.9, respectively. Even though some $[90/0_2]_S$ S-/H-cells split or separated on the flat side parts, the stable core section crushing still guarantees $[90/0_2]_S$ cells a superior energy absorbing capability over $[0/90/0]_S$ cells.

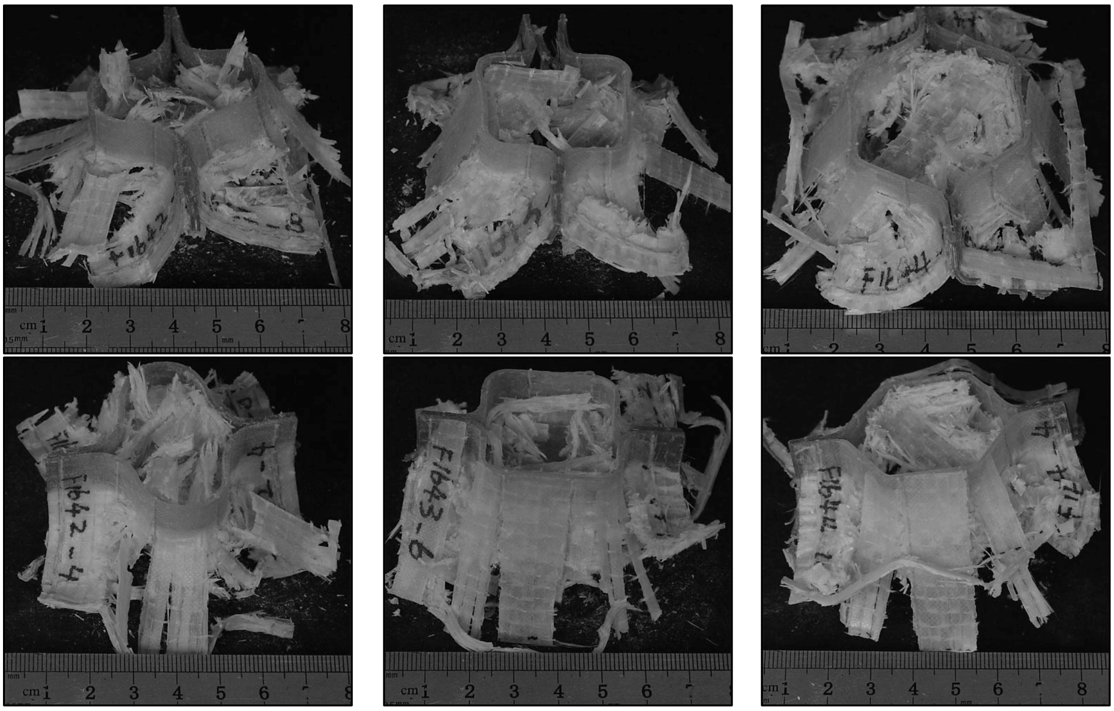

Figure 9.8 **Photographs of crushed [0/90/0] C-cells (left), S-cells (middle) and H-cells (right)**

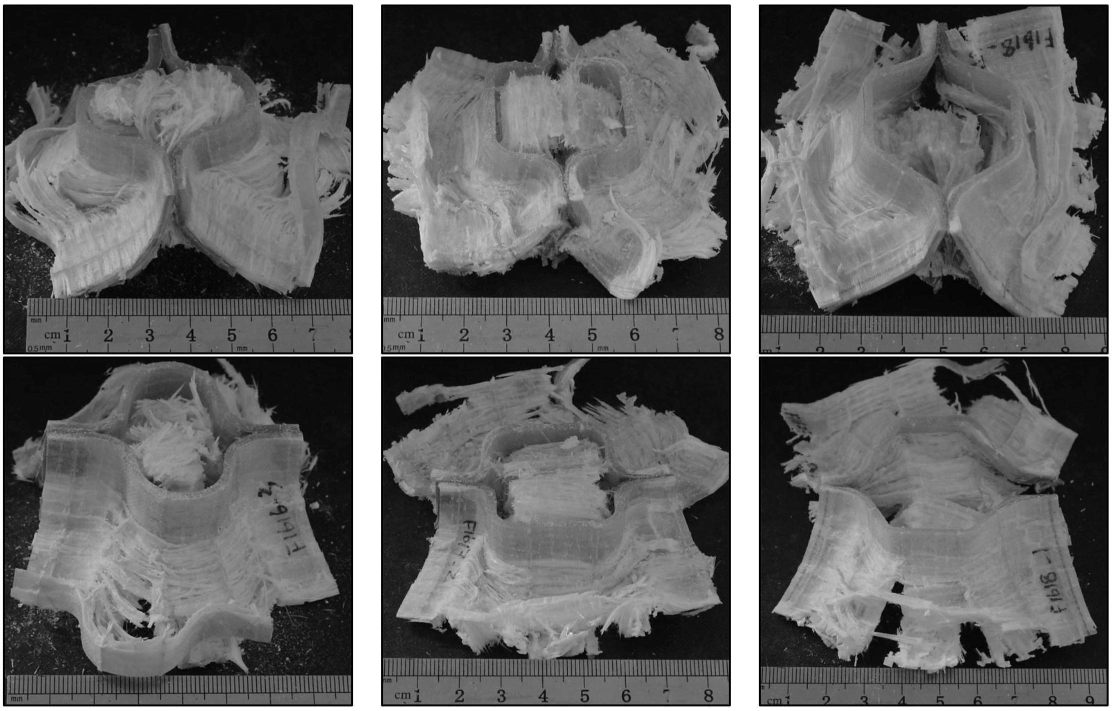

Figure 9.9 **Photographs of crushed $[90/0_2]_S$ C-cells (left), S-cells (middle) and H-cells (right)**

On the other hand, this result also indicates the contribution towards energy absorption offered by core section is more significant than that of flat edge section. This argument can also be proved by comparing $[0/90/0]_S$ cells with $[90/0/90]_S$ cells. Listed on Table 9.1, [90/0/90] crushed by lamina bending mode (with small bending radius) in the core section, but buckled in the flat sides. As discussed in the last chapter, the buckling issue could significantly decrease the energy absorbing capability of composite structures. However, the [90/0/90] cells achieved an averagely higher SEA level than [0/90/0] cells, especially for the C-cells (also see Figure 5.10 in Chapter 5).

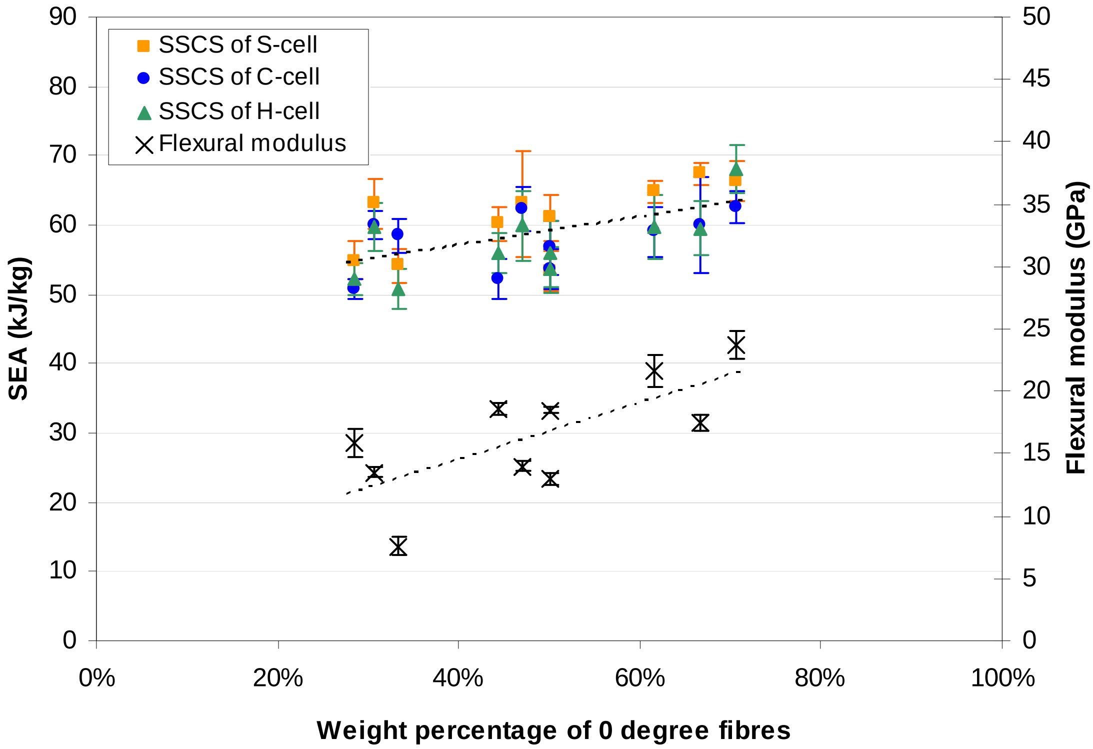

Figure 9.10 **Effect of the content of 0° fibres on crushing performance and flexural modulus**

As presented previously in Chapter 6, increasing the content of 0° fibres also increases the flexural modulus. The effect of the content of 0° fibres on both crushing performance and flexural modulus is shown together in Figure 9.10. It reveals that, generally, when the weight percentage of 0° fibres of a composite material is increased from 30% to 70%, its flexural modulus increases about two times, while its crushing performance increases only about 15%.

Furthermore, the flexural rigidity (EI) of the crushing samples should not be ignored. It is believed that thicker $[90/0_2]_S$ cells gain more benefit from flexural rigidity (EI) than thinner [0/90/0] cells, according to the equation 6.3 in Chapter 6. This also might be the reason of that the $[90/0]_{2S}$ cells behaved slightly better crushing performance than the $[90/0]_S$ cells.

9.2.2. Failure mechanism map for three geometric cells

The potential energy absorption capacities of all cells are presented in Figure 9.11. Trendline and data distribution of the cells made of NCFs are also plotted in Figure 9.11. They indicate these NCF cells also follow the same geometry-SEA rule as simply-supported plate [16] and intersecting square cells, i.e. SEA levels of NCF structural cells decrease with the increasing of the Perimeter/thickness (P/t) ratio, where t = 2h (see Figure 5.1).

Compared with the specimens made of NCFs, the $[PW400/0]_S$ samples which have plain woven fabrics placed as the exterior layers present superior energy absorption capabilities. Under similar P/t ratio or thickness, the SEA levels of $[PW400/0]_S$ cells are increased about 30% than that of NCF cells.

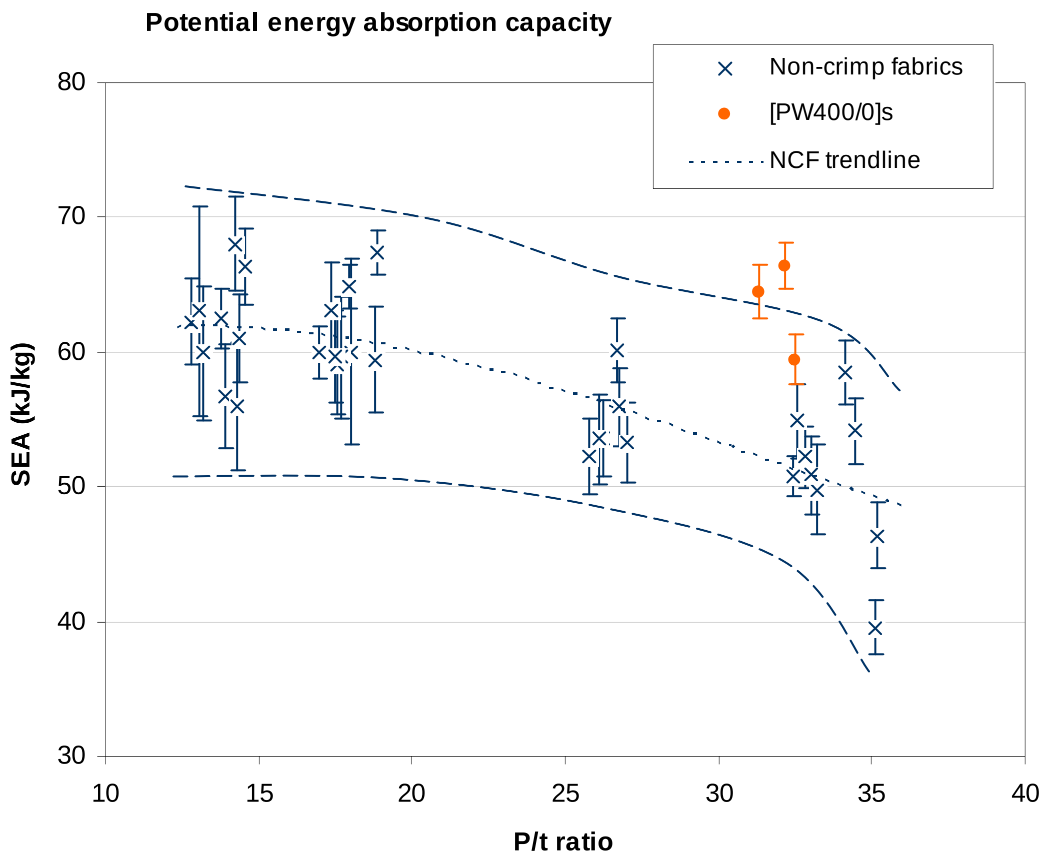

Figure 9.11 Potential energy absorption capacity vs. P/t ratio of all modified cells

It can be attributed to the crimped fibres in the plain-woven fabric that can easily cause micro-fracturing under crushing load. In Figure 9.12, it schematically shows the crushing mechanism of $[PW400/0]_S$ laminates around the core section. Furthermore, composite laminate consists of woven fabrics in general generate very stable crushing, which results in $[PW400/0]_S$ cells achieve higher SSE (see equation 5.1) than most non-crimp cells.

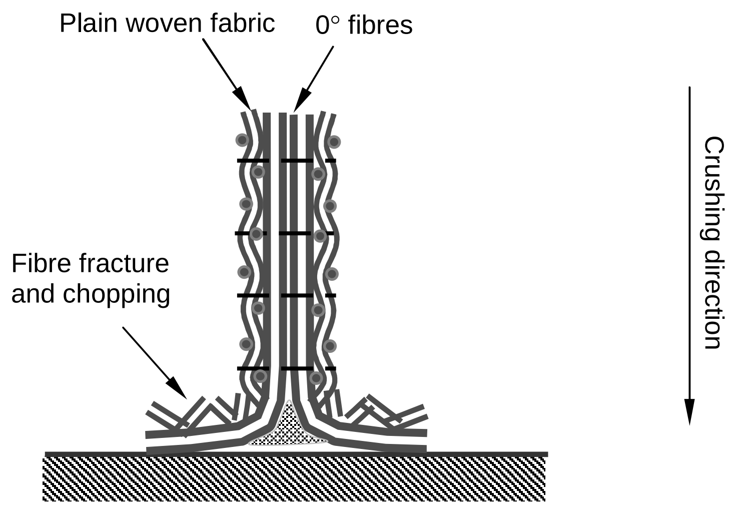

Figure 9.12 Schematic sketch of crushing mechanisms in the core section of [PW400/0]S cells

It can be concluded from Figure 9.11 that, potentially, the SEA values of specimens increase as the P/t ratio decreases. However, this trend becomes slightly inconspicuous in the actual energy absorption capacity data, which are shown in Figure 9.13. This difference is caused by the loss of energy absorption on flat sides due to imperfect bonding and freely-supported boundary condition.

In addition, Figure 9.13 also reveals that the energy absorption capability mainly depends on the laminate properties of core section. If the core section failed in a low effectiveness crushing mode, the reduction of energy absorption capability on the entire structural would be enormous.

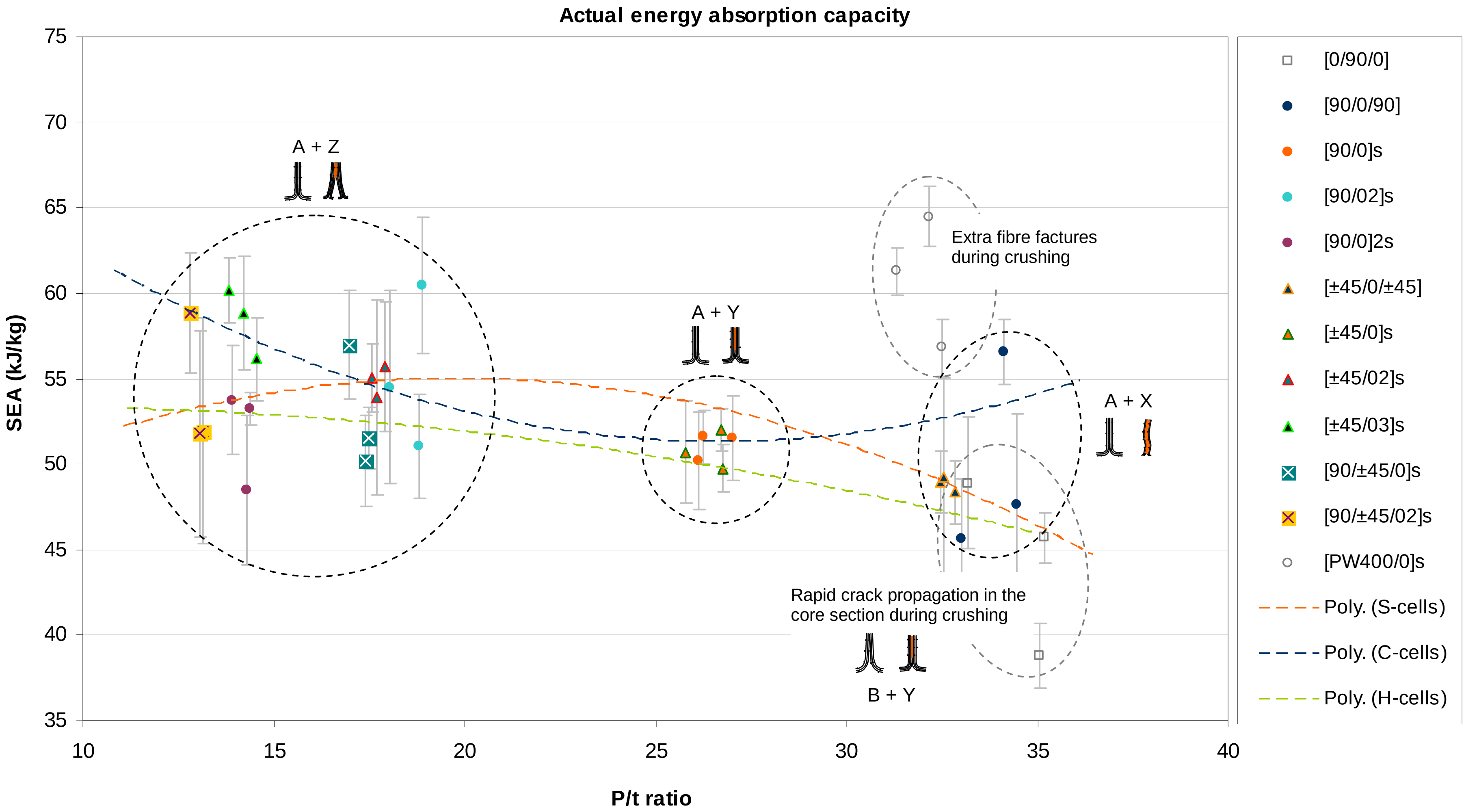

Figure 9.13 SEA vs. perimeter/thickness (P/t) ratio for all geometric cells basing on actual energy absorption data

9.3. Failure mechanism of modified geometric cells

For the modified geometric cells at the last stage, stitching and co-infusion methods were used to bond two half cells together. Thanks to these bonding mechanisms, all modified cells could crush by more stable and effective failure mode – lamina bending with small radius of bending curvature at fronds – on both core and flat side sections.

9.4. Comparisons of failure mechanisms for all samples

Figure 9.14 summaries the distribution of crushing modes of all structural composites that were investigated in this research. On the same plot, the crushing modes of simply-supported composite plates which were previously investigated are also presented [16, 116]. In order to compare different structures at the same manner, the term "Normalized width" was introduced. For each investigated structure, it is described as:

i) Normalized width for intersecting square cell:

= total width of sample;

ii) Normalized width for geometric cell:

= total length of flat sides + perimeter of a half cell; (see Figure 5.1)

While the thickness for geometric cell:

= thickness of flat side after bonded = 2 × thickness of core section;

iii) Normalized width for simply-supported plate:

= separation width between knife-edge clamps [16]

In Figure 9.14, it clearly shows that the samples crushed by the failure of buckling generally possess poorer energy absorption capacity. In contrast, the energy absorption capacity of structural composites increases with increasing of the intensity of bending at splayed lamina fronds. Most of stitched samples crush by intensive lamina bending mode. Especially, when the appropriate stitching configuration was chosen, remarkable energy absorption capacity then can be achieved by controlling the balance between the flexural stiffness and Mode-I crack speed during the crushing process.

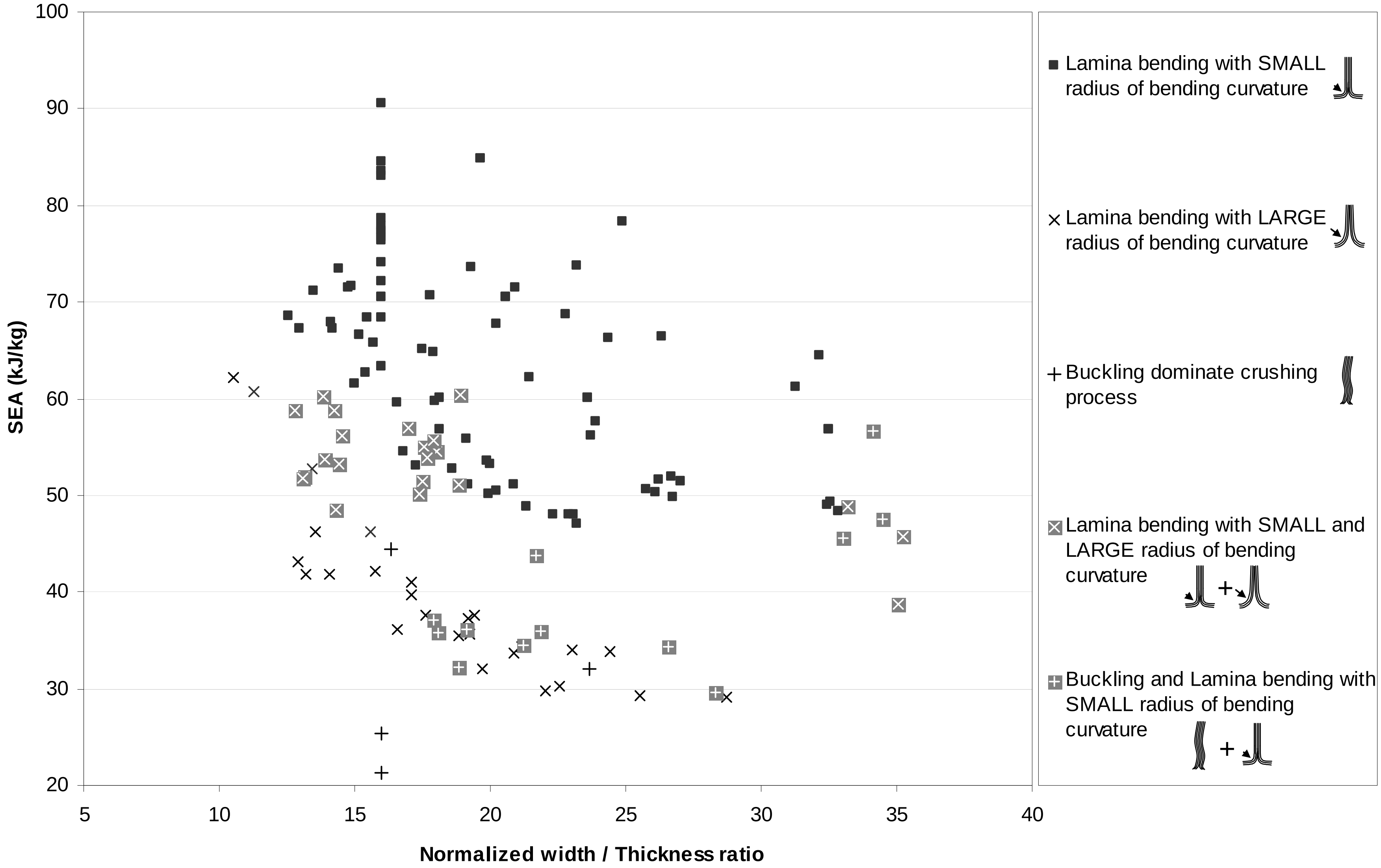

Figure 9.14 The distribution of crushing mechanisms for composite laminate (date for plates are obtained from Ref [16, 116])

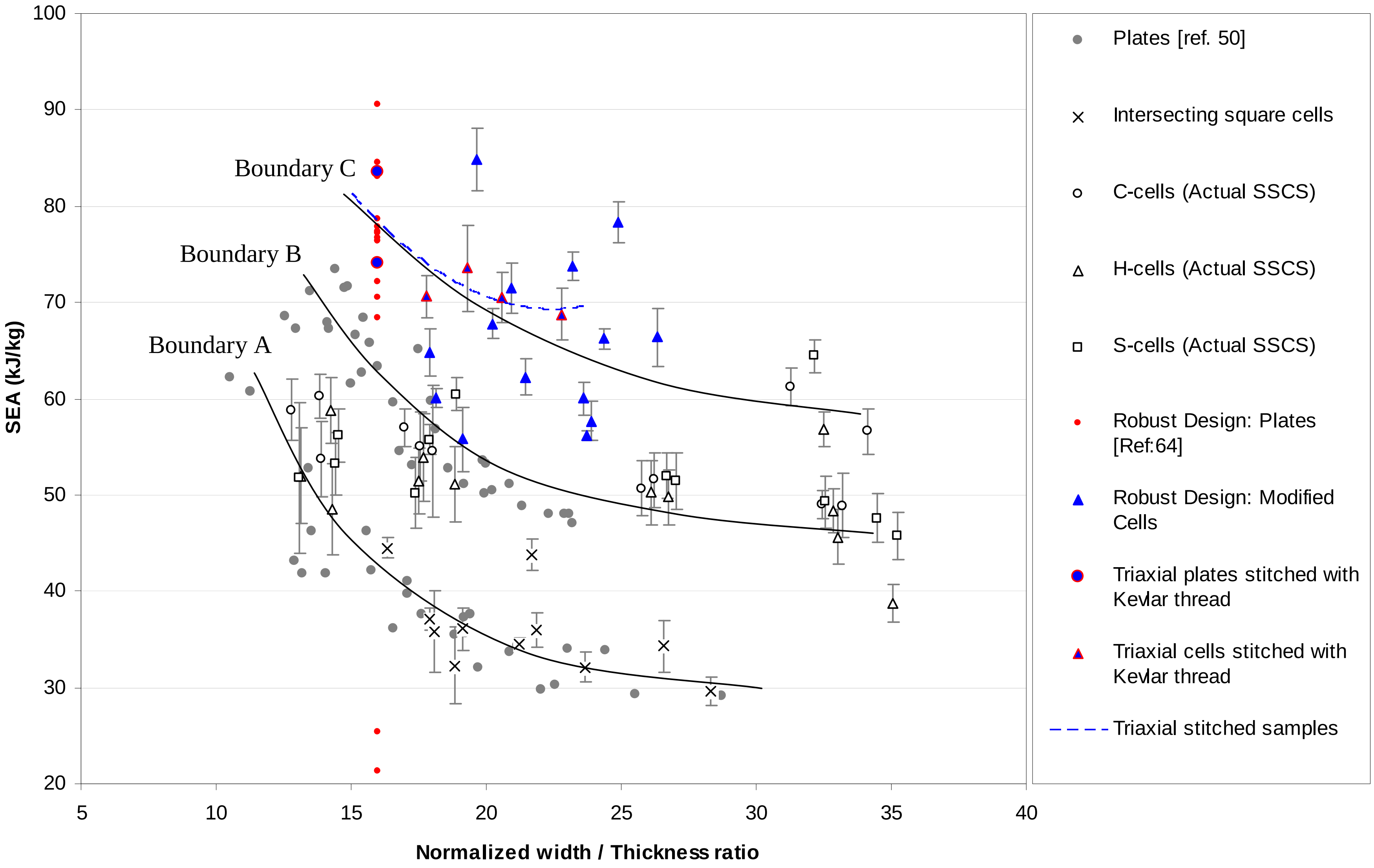

Figure 9.15 **Comparison between plates and all geometric cells that investigated in this research**

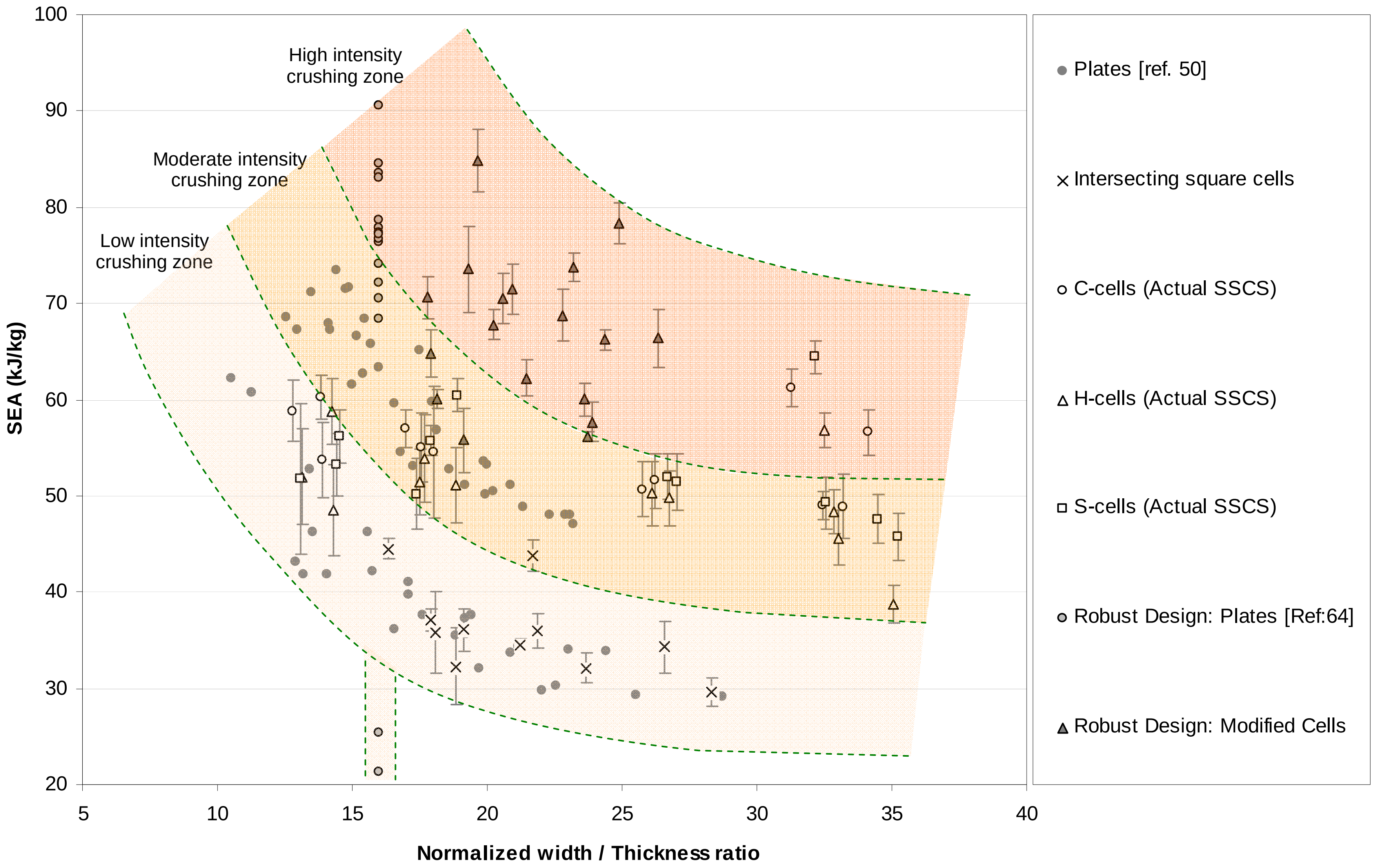

Figure 9.16 **SEA vs. D/t ratio for both plates and geometric cells showing the general behaviour of the data**

Moreover, the crushing performance of all composite structures which were investigated in this research is plotted in Figure 9.15. As a reference, the crushing result of composites plates [16] is also added into this figure. Accordingly, three boundaries (A, B and C) are drawn in Figure 9.15. Because each modified cell consist of different factors and levels, only modified triaxial cells are taken into account for plotting the boundary C. In this figure, the results of most intersecting square cells are located around the boundary A, which is the lower energy absorbing boundary for simply-supported plates [16].

It also indicates that the distribution of crushing results of three geometric cells (C-cells, S-cells and H-cells) are more scattered in Figure 9.15. The data of actual energy absorption capacity are applied for them. It seems the crushing results of these geometric cells do not belong to any boundary. This could be attributed to unstable crushing caused by poor bonding effectiveness between two symmetric corrugated laminates, especially for the cells with lower width/thickness ratios.

However, the crushing results of stitched samples follow the similar trends as the Boundary A and B. For example, a trendline which is the blue dash line in Figure 9.15 is drawn for the stitched triaxial laminates.

Combining the results shown in Figure 9.14 and Figure 9.15, the crushing data for structural composites also can be categorized into three zones by crushing intensity of composite samples. They are:

1) **Low intensity crushing zone**: The samples mainly failed by buckling, buckling dominated crushing mode, or lamina bending mode with large radius of bending curvature. Unexpected early central cracks were often found in samples during crushing.
2) **Moderate intensity crushing zone**: The lamina bending mode with small radius of bending curvature is the main failure mode in this crushing zone. But some samples also have minor effects from buckling mode and lamina bending mode with large radius of bending curvature. The energy absorption capacity of composite materials could be improved by further optimization.
3) **High intensity crushing zone:** All samples failed by lamina bending mode with

small radius of bending curvature. The energy absorption capacity of composite materials is intensively improved by optimizing the internal and external factors. In this case, stitching parameters and material properties should be carefully chosen.

Furthermore, the materials which fail at the same SEA level have the same failure mechanism that dominates their crushing process. This relationship is schematically plotted in Figure 9.17. For example, the samples that have higher critical failure stresses and fall into Boundary B, crush by the same crushing mode (lamina bending with small radius of bending curvature) as the samples that have lower critical failure stresses but fall into Boundary C. The critical stress is equal to the crushing strength of laminar bending failure mode or critical buckling stress in buckling failure mode. In general, the energy absorption capacity of structural composites increases as the increasing of the critical failure stress. Buckling failure mode was found as the poorest energy absorbing mode in this research.

It also demonstrates in Figure 9.17 that the energy absorption capacity of structural composites is not only affected by sample geometry and scale, but also affected by the balance between the flexural properties and fracture toughness properties of materials. By increasing the content of 0° fibres, it can directly increase the bending stiffness of laminate. As a result, the crushing strength and sustained crushing stress are thus increased. Once the laminate is too stiff to bend, it turns to rapid splitting or central cracking at the vertical direction. Therefore, its energy absorption capacity drops.

Stitching is a very efficient method to improve the Mode-I fracture toughness properties of laminates and avoid rapid central cracks. However, the through-thickness stitches also introduce defects into the laminate. If the stitching intensity or stitching density exceeds a certain limit, the laminate is then not more able to overcome the strength of those stitches for a lamina bending mode. Eventually, laminate fails catastrophically by squashing and buckling modes at a relatively low SEA level.

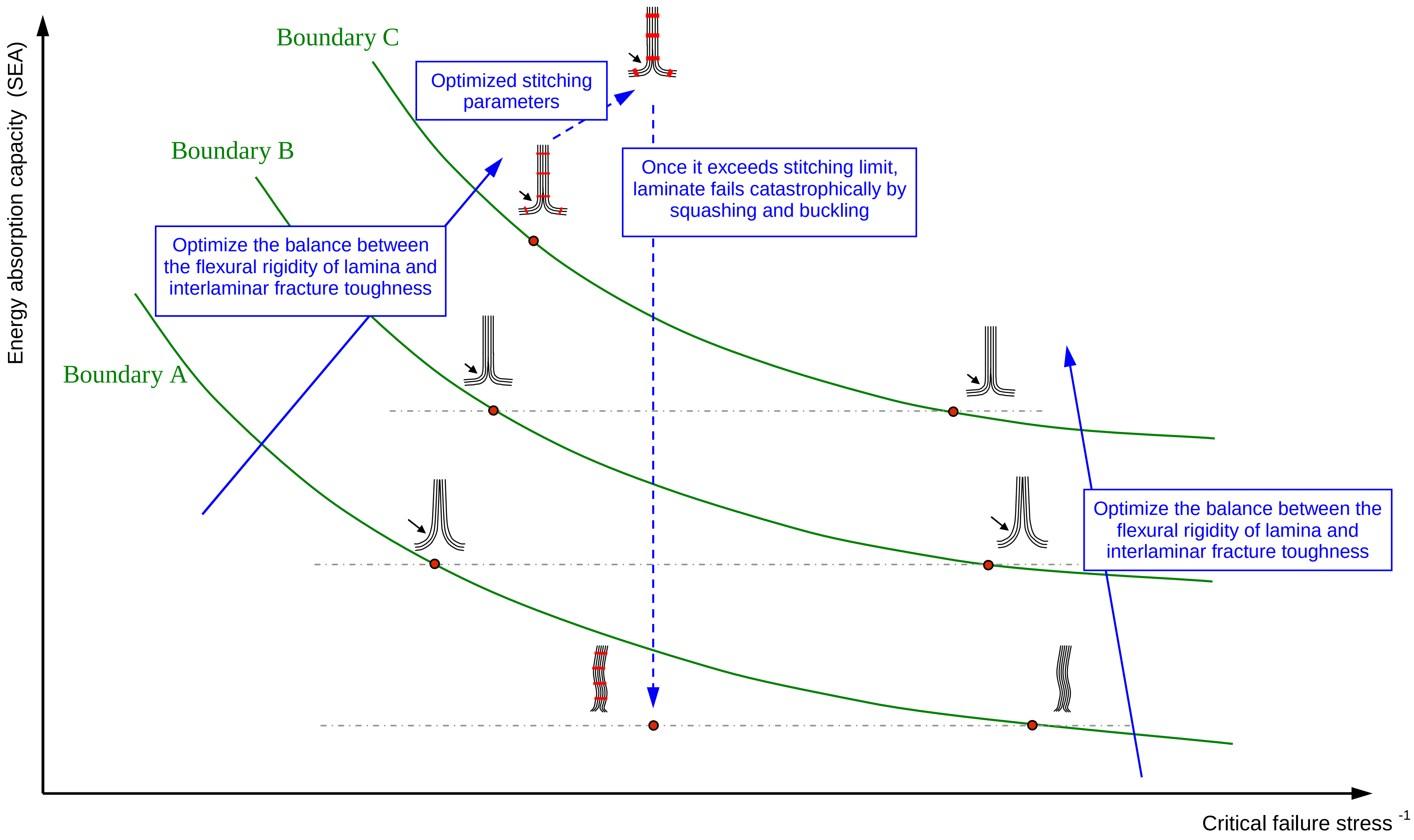

Figure 9.17 **Summary the relationship between crushing behaviour and geometric and scale effects for structural composites**

9.5. *Prediction of energy absorption capacities of composites panels*

In application to a real energy absorbing system, each type of composite cell investigated in this research needs to be manufactured as a side-by-side and row-by-row structure. Five schematic sketches which are shown in Figure 9.18 present the eventual figures of cross section for these cells. Therefore, if it is assumed that each unit cell in the relative panel type structure (or sandwich structure) would absorb the same amount energy as an individual cell, then the crushing data for all composite cells can be normalized.

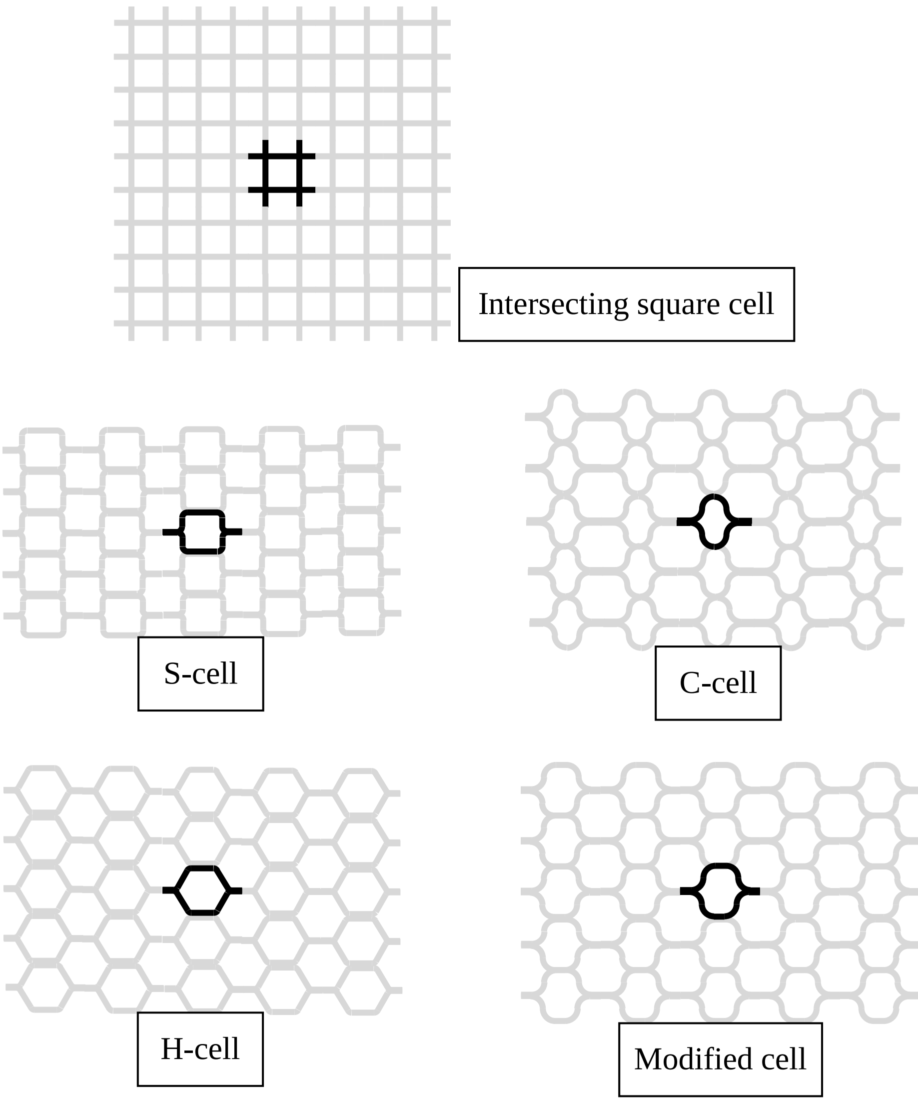

Figure 9.18 Schematic sketches of panel type energy absorbers for different composite cells

9.5.1. Crushing properties of the panel type structure with thickness of 50mm

In order to compare all composite cells at a parallel weight level, the height of every composite cell, which is also the thickness of the panel type structure, was set to 50mm. These normalized data are plotted in Figure 9.19. The actual energy absorption capacity of structure (see equation 5.1) was used. Accordingly, there are two approaches can be used in the design of an energy absorbing structure in this case:

1) When the density of a structure is crucial, only the normalized panel weight on x-axis needs to be considered. For example, if a structure requires the minimum energy absorption capacity of 70kJ/kg, but also is required to not exceed 12kg/m^2 in density, the cell, 'a', is then the best choice (see Figure 9.19).

2) When the density of a structure is not crucial but a secondary factor, the dashed lines shown in Figure 9.18 should be followed. For example, if the structure requires to absorb the energy of 800kJ, any cell which is located between the dashed line '800kJ/m^2' and '1,200kJ/m^2' could be an option.

9.5.2. Crushing properties of the panel type structure with various thickness

In many situations, researchers and engineers might require a wider dimensional scale in order to satisfy the design criterion of energy absorbing structures. Assuming the thickness of panel (or length of cell) does not affect the crushing performance, then the normalized data presented in Figure 9.19 can be extended by increasing or decreasing the thickness of panel.

Consequently, the weight per unit area of the panel is also varied. The extended crushing data are plotted into a three-dimensional (3D) figure as well as two figures for its side views. They are shown in Figure 9.20 and Figure 9.21, respectively. The total energy absorption of a unit area and the SEA levels are also compared.

Figure 9.21(A) can be considered as an alternative aspect to the Figure 9.19, while normalized data with other thicknesses, apart from 50mm, are also added. The slopes of the trendlines plotted in Figure 9.21(B) exhibit the average energy absorption capacity for different structures.

In these figures, the thicknesses for all samples were assumed to be 30mm, 40mm, 50mm, 60mm, 70mm, 80mm, 90mm, and 100mm. Moreover, the thicknesses of 110mm and 120mm were also added to the samples studied in Robust Design. To absorb the same amount of crushing energy, the structure consists of intersecting square cells need to be heavier than other structures. But the structure of the ISC still achieves 2000kJ/m^2 when it is 100mm thick. If the weight of structure is not considered in the design, the intersecting plates could be an ideal option. They are easy and quick to make, transport and assemble.

On the other hand, the structure consists of geometric cells optimised by Robust Design process reduces the weight more than 50%, compared with the structure consists of intersecting plates. However, this type of structure is more difficult to manufacture. The whole manufacturing process becomes complex especially because it requires an extra step to stitch the dry fabrics along the flat sides. The metallic female mould (see Figure 8.3F) can not be used for the panel type structure any more. Accordingly, the inner mandrels must be made of stiffer materials, rather than silicon rubber.

Potentially, using rigid polymer foam as the mandrel could be a good solution. Co-infused with fabrics, the polymer foam does not need to be removed afterwards. The polymer foam could also offer many other benefits to the sandwich structure. It can increase the bonding surface between the core and skins. It also can reduce the moisture trapped in the honeycomb cells, especially, when the closed-cell foams are used. Therefore, the honeycomb water corrosion can be reduced or avoided.

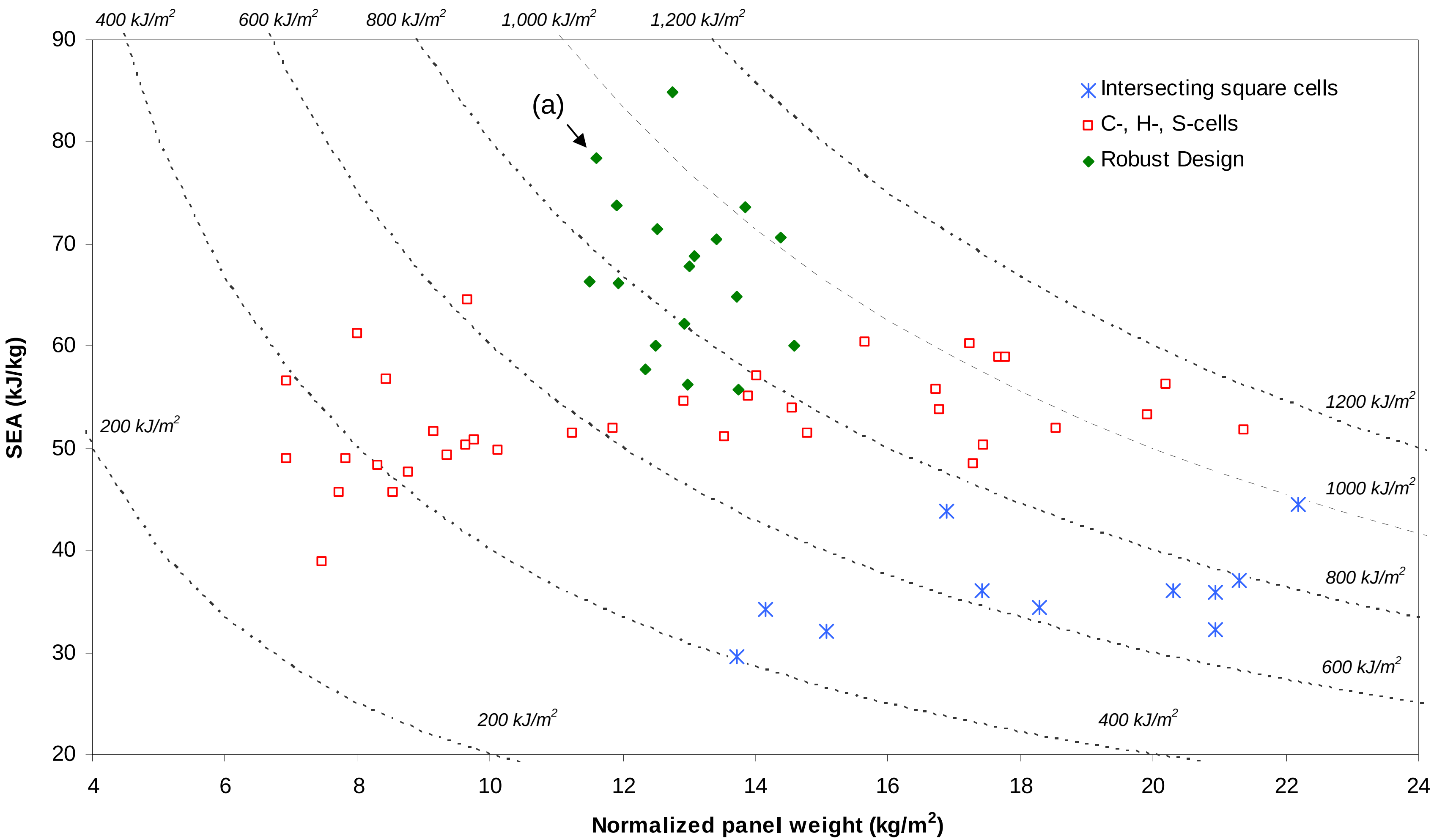

Figure 9.19 **Geometric and scale effects on SEA levels for all samples measured in this research: SEA vs. normalized panel weight.**

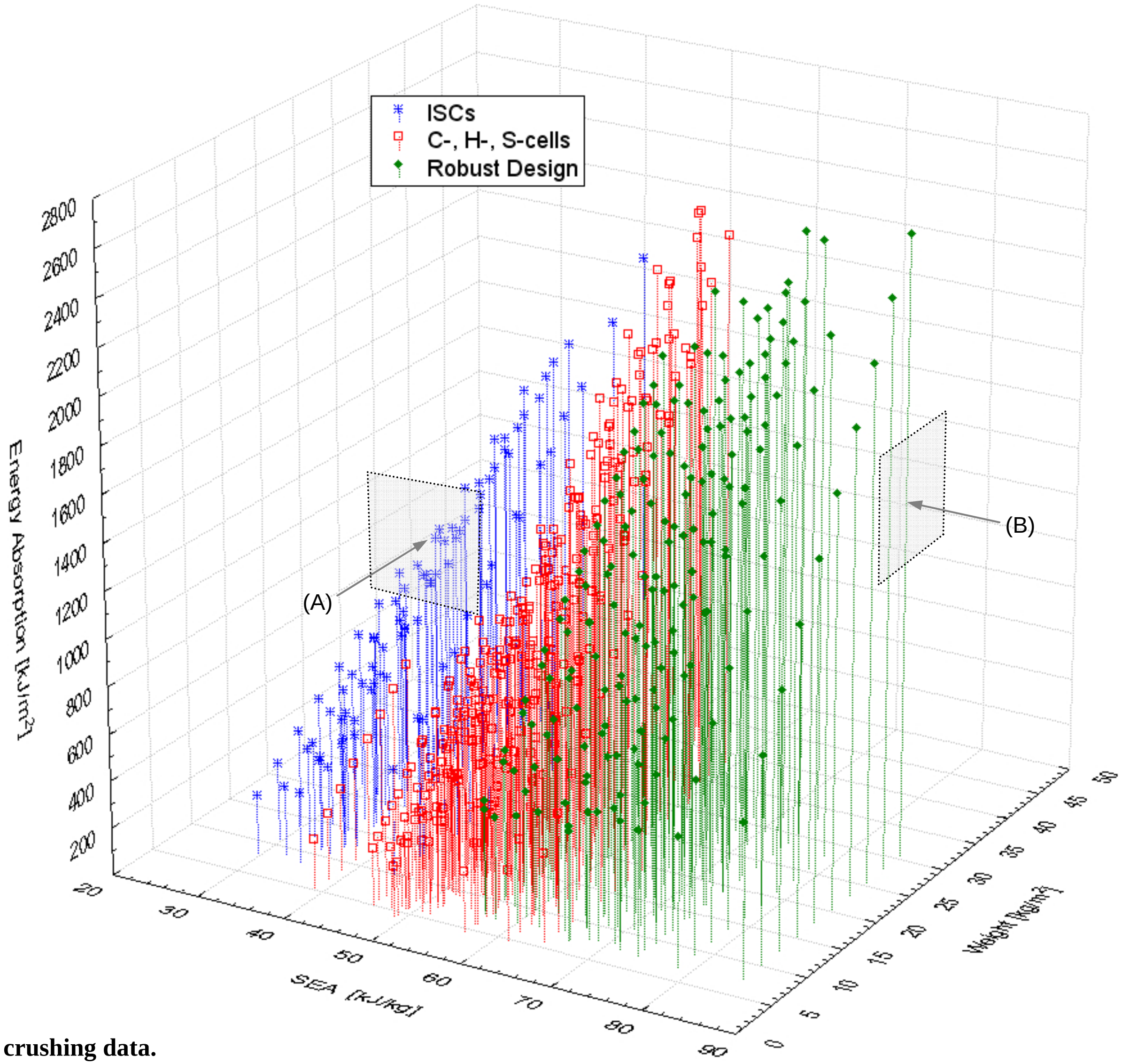

Figure 9.20 **3D view of normalized crushing data.**

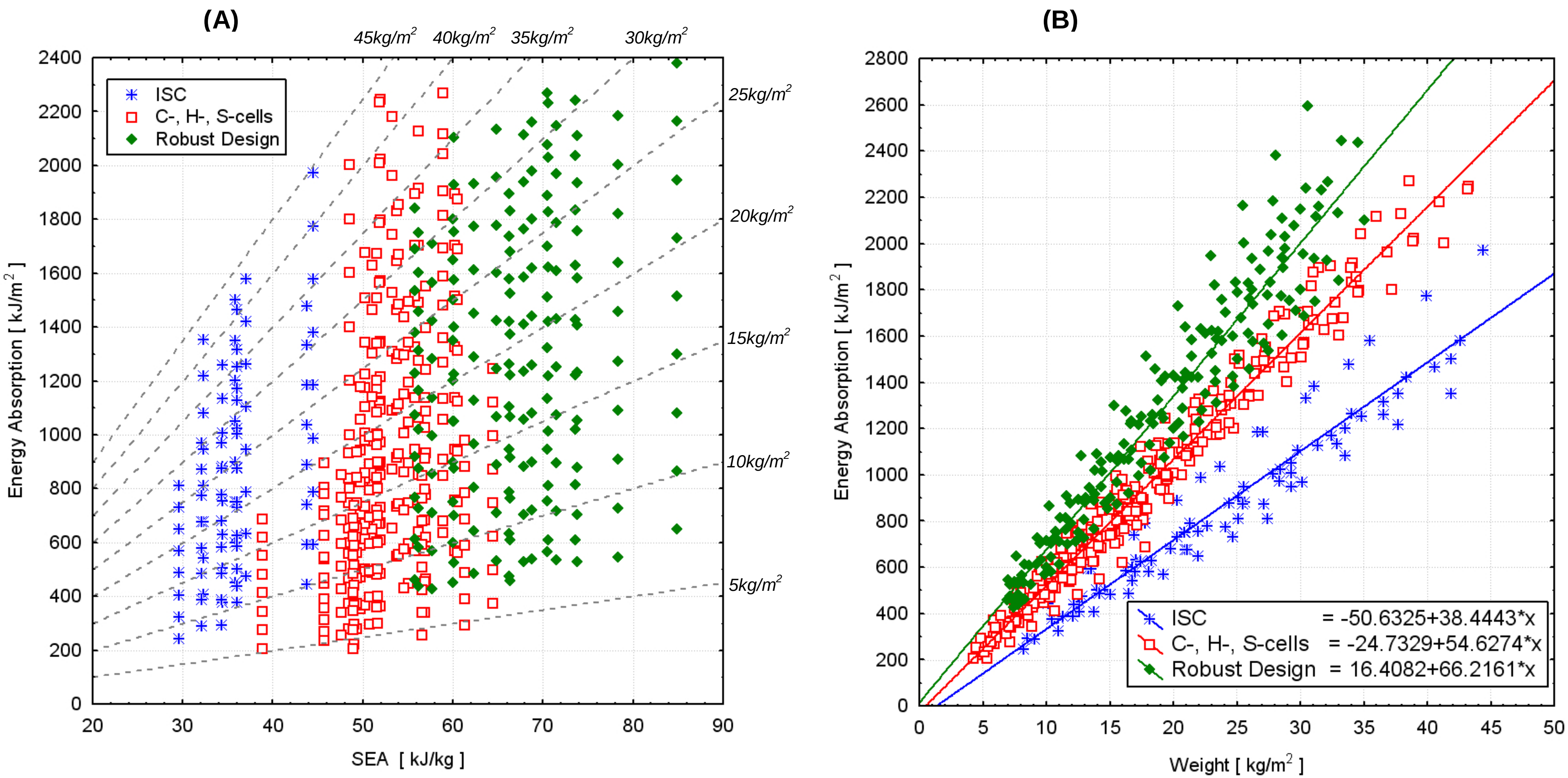

Figure 9.21 **Side views of normalized crushing data corresponding to Figure 9.20.**

Chapter 10. Conclusions

- The energy absorption capability of intersecting square cells is dominated by the geometric scale and fibre architecture as well as the crushing mode. Unlike the tubular and simply-supported plates, structural stability played a crucial role in this intersecting structure. Because of freely-supported boundary condition along the intersecting edges of laminate plates, the plates tend to fracture and crack after the cumulated buckling stresses triggered laminar to bend. However, these intersecting square cells achieved a very outstanding crushing performance (between 29.58 and 44.47 kJ/kg), compared with the egg-box [67] (between 1 and 7 kJ/kg) and aluminium honeycombs [74] (between 22 and 39 kJ/kg).
- With the improved critical buckling stress, these three geometric cells developed in this work have achieved greater energy absorbing levels than those intersecting square cells. The section of corrugated core prevents the structural composites from buckling during crushing. As a result, the energy absorption capabilities of composite samples with geometrical shapes are significantly improved. However, due to the weak bonding effectiveness at the edges of cells, some samples failed with very low crushing efficiency. The square cells achieved the highest potential energy absorption capacity, while the circular cells presented slightly more stable crushing process than other cells.
- The energy absorption capability of structural composites is not only controlled by geometrical shape of cross section of cells, but all is controlled by the flexural properties of composite materials. Moreover, the flexural properties of composite materials are highly dominated by the content of the 0° fibres within laminate. Accordingly, we can conclude that the flexural modulus and width/thickness ratio are main factors but the precondition is that when the composite sample crushes stably central crack propagates progressively.

- Through-thickness stitching has significant effect on Mode-I fracture toughness properties of composite laminates. Stitching mechanism has been used as a very efficient tool that can control the propagation process of central crack of laminates during the crushing. Different from Mode-I, because glass fibre damage and fabric penetration were caused by stitching process, through-thickness stitches degraded the Mode-II fracture toughness of most samples. Compared with the other material factors, the Mode-I and Mode-II delaminations contribute a relative small proportion to the total energy absorption of composite materials in crushing process.
- Compared with the three geometric cells, the optimised cells show a very remarkable increase on the crushing performance. The energy absorbing performance of a composite structure can be improved very significantly by selecting the right combinations of factors with correct levels, which is able to achieve an SEA level of 84.6 kJ/kg. Eventually, the optimum configuration provides energy absorption of 1100kJ/m^2 with a weight of only 13kg/m^2.
- According to the results of Robust Design, the resin and fabric types are found as the main factors controlling crushing performance of composites cells. Together they contribute about 71% energy absorption capacity to geometric cells. Unlike the most investigations of energy absorption of composite materials, this study revealed the significance of different material properties in the energy absorption.
- Finer stitching yarns and finer stitching needles could also potentially improve the energy absorbing capacity of composites, because the damages caused by through-thickness stitching would be eased. Z-pinning [117] and tufting techniques [118] also could be very promising methods of increasing energy absorption capacity of composites, while minimizing the damages caused by added materials. 3D textile composites could benefit the crushing performance through the through-thickness yarns.

Appendix 1. Classical laminate theory and buckling

Classical laminate theory has been described and discussed in many early textbooks [9, 103, 119-121]. In most situations, the anisotropic composite associated with simple laminate construction is considered as an orthotropic body, which has three mutually perpendicular planes of materials symmetry and the properties at any point are different in three mutually perpendicular directions.

A1.1. Basic conceptions of orthotropic elasticity

Consider an elastic body of any general shape, and assume it is composed of an infinity of material points in the interior of the elastic body. If one assigns a Cartesian reference frame with axes x, y, and z to the elastic body illustrated in Figure A10.1 , then it is convenient to assign a rectangular parallelepiped shape to the material point, and call it a control element of dimensions dx, dy, and dz.

On the surface of the control element there can exist both normal stresses (those perpendicular to the plane of the face) and shear stresses (those parallel to the plane of the face). On any one face the three mutually orthogonal stress components comprise a vector, called a surface traction.

It is important to note the sign convention and the meaning of the subscripts of these surface stresses. For a stress component on a positive face whose outward normal is in the direction of a positive axis, the stress component is positive when it is in the direction of a positive axis. Conversely, when a stress component is on a face whose outward normal is in the direction of a negative axis, the stress component is positive when it is directed in the negative axis direction.

As shown in Figure A10.1, there are three normal stresses σ_{xx}, σ_{yy}, σ_{zz}, and six shear stresses σ_{yz}, σ_{zx}, σ_{xy}, σ_{zy}, σ_{xz}, σ_{yx} (these suffixes x, y, z can be replaced by number 1, 2, 3 respectively). The first suffix of any stress component on any face of the control element signifies the direction normal to the plane in which the stress is acting. The second suffix refers to the direction in which the stress is acting. Correspondingly, there are two types of strains, three extensional strain tensors ε_{xx}, ε_{yy}, ε_{zz}, and shear strain tensors ε_{yz}, ε_{zx}, ε_{xy}, ε_{zy}, ε_{xz}, ε_{yx}. It is important to note that in some texts and papers, the shear strain is defined as γ. Here $\varepsilon_{ij} = ½\ \gamma_{ij}$.

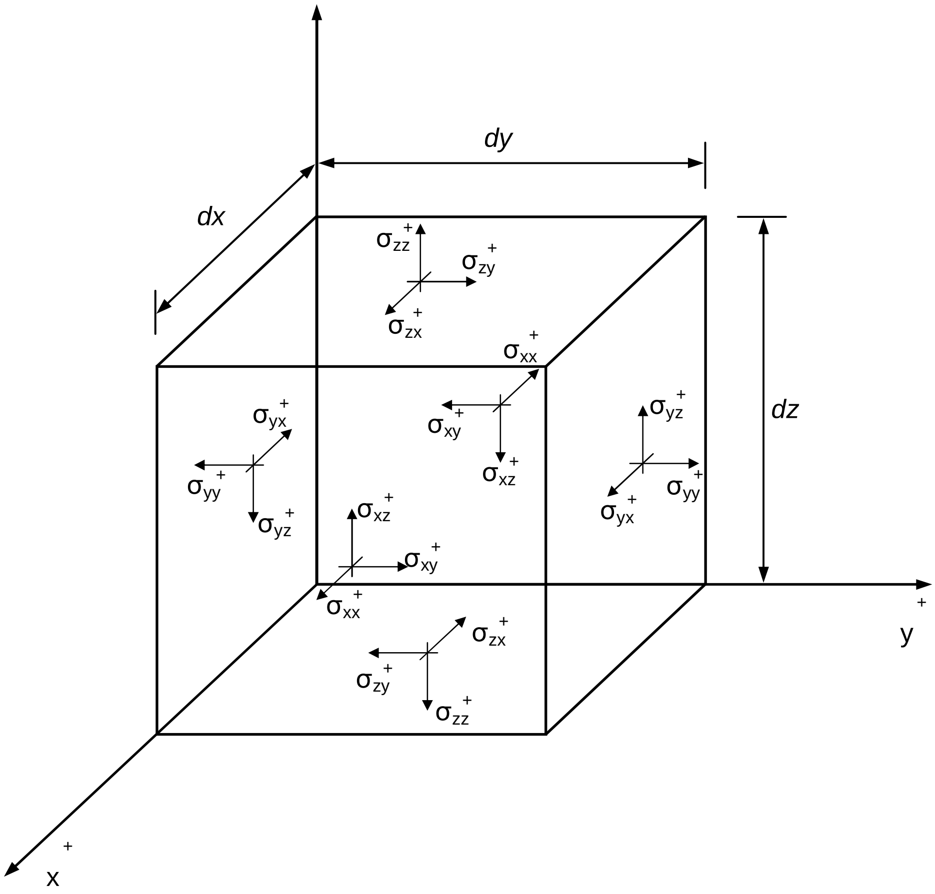

Figure A10.1. Control element in an elastic body

For an equilibrium state at any point, both the stresses and strain tensors are symmetric through the element of unit cube, which means $\sigma_{ij} = \sigma_{ji}$, and $\varepsilon_{ij} = \varepsilon_{ji}$. Using the following shorthand notation,

$$\left.\begin{array}{lll} \sigma_{11} = \sigma_1 & \sigma_{22} = \sigma_2 & \sigma_{33} = \sigma_3 \\ \sigma_{23} = \sigma_4 & \sigma_{31} = \sigma_5 & \sigma_{12} = \sigma_6 \\ \varepsilon_{11} = \varepsilon_1 & \varepsilon_{22} = \varepsilon_2 & \varepsilon_{33} = \varepsilon_3 \\ \varepsilon_{23} = \sigma_4 & \varepsilon_{31} = \varepsilon_5 & \varepsilon_{12} = \varepsilon_6 \end{array}\right\} \qquad (A1.1)$$

According to Hooke's law, the well-known elasticity equation is written as,

$$\sigma_{ij} = C_{ijkl}\,\varepsilon_{ij} \qquad (i, j, k, l = 1, 2, 3) \qquad (A1.2)$$

where C_{ijkl} is called the stiffness matrix. It can be shown that $C_{ijkl} = C_{klij}$, or in the shorthand notation, $C_{ij} = C_{ji}$.

Therefore, the elasticity equation can be expressed as:

$$\begin{bmatrix} \sigma_1 \\ \sigma_2 \\ \sigma_3 \\ \sigma_4 \\ \sigma_5 \\ \sigma_6 \end{bmatrix} = \begin{bmatrix} C_{11} & C_{12} & C_{13} & C_{14} & C_{15} & C_{16} \\ C_{12} & C_{22} & C_{23} & C_{24} & C_{25} & C_{26} \\ C_{13} & C_{23} & C_{33} & C_{34} & C_{35} & C_{36} \\ C_{14} & C_{24} & C_{34} & C_{44} & C_{45} & C_{46} \\ C_{15} & C_{25} & C_{35} & C_{45} & C_{55} & C_{56} \\ C_{16} & C_{26} & C_{36} & C_{46} & C_{56} & C_{66} \end{bmatrix} \begin{bmatrix} \varepsilon_1 \\ \varepsilon_2 \\ \varepsilon_3 \\ \varepsilon_4 \\ \varepsilon_5 \\ \varepsilon_6 \end{bmatrix} \qquad \text{(A1.3)}$$

Moreover, consider an elastic body symmetric in properties with respect to one plane, say the x_1-x_2 plane. Thus the symmetry can be expressed by the face that the C_{ij}'s discussed above are invariant under the transformation $x_1 = x_1'$, $x_2 = x_2'$, and $x_3 = -x_3'$, which show in Figure A10.2. Also, the direction cosines, t, associated with this transformation are shown in the table. The stresses and strain tensors of the prime co-ordinate system are related to those of the original co-ordinate system by:

$$\sigma'_{\alpha\beta} = t_{\alpha i} t_{\beta j} \sigma_{ij} \quad \textit{and} \quad \varepsilon'_{\alpha\beta} = t_{\alpha i} t_{\beta j} \varepsilon_{ij} \quad (\alpha, \beta, i = 1,2,3,6) \qquad \text{(A1.4)}$$

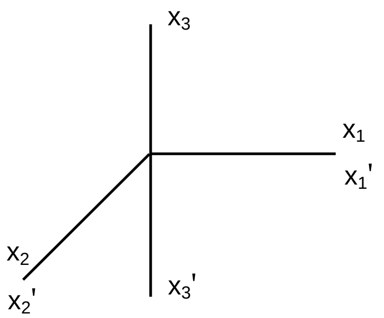

	x_1	x_2	x_3
x_1'	1	0	0
x_2'	0	1	0
x_3'	0	0	-1

Figure A10.2. $x_1 - x_2$ plane of symmetry

By considering the relationship of stresses and strain tensors in equation A1.4, it can be derived that:

$C_{14} = C_{15} = C_{16} = C_{24} = C_{34} = C_{41} = C_{42} = C_{43} = C_{46} = C_{51} = C_{52} = C_{53} = C_{56} = C_{65} = 0$

Similarly, orthotropic materials are symmetric in properties with respect to the x_1-x_3 and x_2-x_3 plane. Hence, other terms in the elasticity matrix are also zero, i.e.:

$$C_{16} = C_{26} = C_{36} = C_{45} = 0$$

So, for orthotropic materials the number of elastic constants can be reduced from 36 (6×6=36) to 9, which is expressed below, remembering that $C_{ij} = C_{ji}$:

$$C_{ij} = \begin{bmatrix} C_{11} & C_{12} & C_{13} & 0 & 0 & 0 \\ C_{12} & C_{22} & C_{23} & 0 & 0 & 0 \\ C_{13} & C_{23} & C_{33} & 0 & 0 & 0 \\ 0 & 0 & 0 & C_{44} & 0 & 0 \\ 0 & 0 & 0 & 0 & C_{55} & 0 \\ 0 & 0 & 0 & 0 & 0 & C_{66} \end{bmatrix} \qquad \text{(A1.5)}$$

A1.2. Elastic properties of a unidirectional lamina

Consider a simple tensile or compression test for a unidirectional lamina wherein the specimen is stressed along the principal material direction x_1, which is presented in the Figure A10.3, the resulting stress and strain tensors are:

$$\sigma_{ij} = \begin{bmatrix} \sigma_1 & 0 & 0 \\ 0 & 0 & 0 \\ 0 & 0 & 0 \end{bmatrix} \qquad \varepsilon_{ij} = \begin{bmatrix} \varepsilon_1 & 0 & 0 \\ 0 & -\nu_{12}\varepsilon_1 & 0 \\ 0 & 0 & -\nu_{13}\varepsilon_1 \end{bmatrix} \qquad \text{(A1.6)}$$

Here υ_{ij} is the Poisson's ratio. It is defined as the negative of the ratio of the strain in the x_j direction to the strain in the x_i direction due to a stress in the x_i direction. In other word from equation above, $\upsilon_{12} = - \varepsilon_2 / \varepsilon_1$.

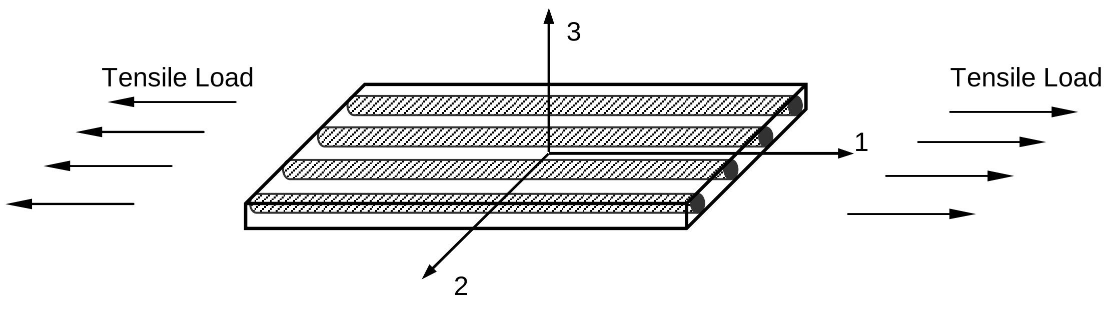

Figure A10.3. Unidirectional lamina is loaded along principal material direction

Similarly, a simple tensile test in the x_2 direction yields the following

$$\sigma_{ij}=\begin{bmatrix}0&0&0\\0&\sigma_2&0\\0&0&0\end{bmatrix}\qquad \varepsilon_{ij}=\begin{bmatrix}-\nu_{21}\varepsilon_2&0&0\\0&\varepsilon_2&0\\0&0&-\nu_{23}\varepsilon_{21}\end{bmatrix}\tag{A1.7}$$

According simple tensile test in three different directions, it also can be found a most important relationship for orthotropic materials [27]:

$$\frac{\nu_{ij}}{E_i}=\frac{\nu_{ji}}{E_j}\tag{A1.8}$$

where E is Young's modulus.

In the case of unidirectional laminae and laminates it assumed that they are sufficiently thin that the through-thickness stresses are zero, and transverse shear deformation and transverse normal stress are neglected, namely,

$$\sigma_3 = \sigma_{23} = \sigma_{31} = 0\tag{A1.9}$$

Therefore, the stress-strain relation for a unidirectional lamina is obtained:

$$\begin{bmatrix}\sigma_1\\\sigma_2\\\sigma_{12}\end{bmatrix}=\begin{bmatrix}Q_{11}&Q_{12}&0\\Q_{12}&Q_{22}&0\\0&0&2Q_{66}\end{bmatrix}\begin{bmatrix}\varepsilon_1\\\varepsilon_2\\\varepsilon_{12}\end{bmatrix}\tag{A1.10}$$

Q_{ij} is called reduced stiffnesses. In terms of the engineering constants, it can be expressed as:

$$\left.\begin{aligned}&Q_{11}=C_{11}=\frac{E_1}{1-\nu_{12}\nu_{21}}; &&Q_{22}=C_{22}=\frac{E_2}{1-\nu_{12}\nu_{21}}\\&Q_{12}=C_{12}=\frac{\nu_{12}E_2}{1-\nu_{12}\nu_{21}}=\frac{\nu_{21}E_1}{1-\nu_{12}\nu_{21}}; &&Q_{66}=\frac{1}{2}\left(C_{11}-C_{12}\right)=G_{12}\end{aligned}\right\}\tag{A1.11}$$

where G is shear modulus.

equation A1.10 indicates that orthotropic materials tested in tension or compression along the principal material directions exhibit that there is no coupling between tensile and shear strains [103]. This does not apply when the lamina is tested at arbitrary angle to the principal materials directions. Thus, consider a lamina tested in such a way that the new co-ordinate system x-y is at an angle, θ, to the principal materials directions as illustrated in Figure A10.4. Elasticity theory shows that the stress-strain relation becomes:

$$\begin{bmatrix}\sigma_x\\ \sigma_y\\ \sigma_{xy}\end{bmatrix} = \begin{bmatrix}\overline{Q}_{11} & \overline{Q}_{12} & 2\overline{Q}_{16}\\ \overline{Q}_{12} & \overline{Q}_{22} & 2\overline{Q}_{26}\\ \overline{Q}_{16} & \overline{Q}_{26} & 2\overline{Q}_{66}\end{bmatrix} \begin{bmatrix}\varepsilon_x\\ \varepsilon_y\\ \varepsilon_{xy}\end{bmatrix} \tag{A1.12}$$

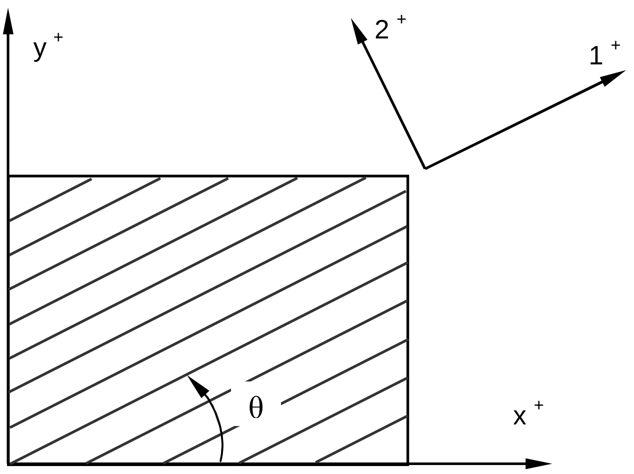

Figure A10.4. The rotated new co-ordinate system x-y from 1-2 at angle θ

The matrix $\overline{Q}_{ij}$ is called the transformed reduced stiffness matrix and the stiffnesses have the following values [120]:

$$\left.\begin{aligned}
\overline{Q}_{11} &= Q_{11}\cos^4\theta + 2(Q_{12}+2Q_{66})\sin^2\theta\cos^2\theta + Q_{22}\sin^4\theta\\
\overline{Q}_{12} &= (Q_{11}+Q_{22}-4Q_{66})\sin^2\theta\cos^2\theta + Q_{12}(\sin^4\theta+\cos^4\theta)\\
\overline{Q}_{22} &= Q_{11}\sin^4\theta + 2(Q_{12}+2Q_{66})\sin^2\theta\cos^2\theta + Q_{22}\cos^4\theta\\
\overline{Q}_{16} &= (Q_{11}-Q_{12}-2Q_{66})\sin\theta\cos^3\theta + (Q_{12}-Q_{22}+2Q_{66})\sin^3\theta\cos\theta\\
\overline{Q}_{26} &= (Q_{11}-Q_{12}-2Q_{66})\sin^3\theta\cos\theta + (Q_{12}-Q_{22}+2Q_{66})\sin\theta\cos^3\theta\\
\overline{Q}_{66} &= (Q_{11}+Q_{22}-2Q_{12}-2Q_{66})\sin^2\theta\cos^2\theta + Q_{66}(\sin^4\theta+\cos^4\theta)
\end{aligned}\right\} \tag{A1.13}$$

A1.3. Elastic properties of multi-directional laminates

The elastic properties of the multi-directional laminates depend on the properties of the unidirectional laminae. According to the assumptions in lamination theory, the laminae are considered that they are perfectly bonded and don not slip relative each other and the bond between the laminae is infinitely thin, so that the laminate is treated as a thin elastic plate [103].

In the case of unidirectional lamina, the transverse shear deformation and transverse normal stress are neglected for deriving its stress-strain relation (see equation A1.10). However, due to the multi-directional laminates or plate is very weak in transverse shear resistance and the effects of transverse shear deformation are significant, it is necessary to include transverse shear deformation in the analysis of most plate structures composed of composite materials. Therefore in this case, equation A1.10 is modified to be:

$$\begin{bmatrix} \sigma_1 \\ \sigma_2 \\ \sigma_{23} \\ \sigma_{31} \\ \sigma_{12} \end{bmatrix} = \begin{bmatrix} Q_{11} & Q_{12} & 0 & 0 & 0 \\ Q_{12} & Q_{22} & 0 & 0 & 0 \\ 0 & 0 & 2Q_{44} & 0 & 0 \\ 0 & 0 & 0 & 2Q_{55} & 0 \\ 0 & 0 & 0 & 0 & 2Q_{66} \end{bmatrix} \begin{bmatrix} \varepsilon_1 \\ \varepsilon_2 \\ \varepsilon_{23} \\ \varepsilon_{31} \\ \varepsilon_{12} \end{bmatrix} \qquad \text{(A1.14)}$$

Here, Q_{11}, Q_{22}, Q_{12} and Q_{66} are given by equation A1.11, and Q_{44} and Q_{55} are expressed as:

$$Q_{44} = G_{23} \qquad Q_{55} = G_{31} \qquad \text{(A1.15)}$$

Following by the equation A1.12 and (A1.13), the stress-strain relations for a generally orthotropic lamina of k^{th} layer including transverse shear deformation can be written as:

$$\begin{bmatrix} \sigma_x \\ \sigma_y \\ \sigma_{yz} \\ \sigma_{zx} \\ \sigma_{xy} \end{bmatrix}_k = \begin{bmatrix} \overline{Q}_{11} & \overline{Q}_{12} & 0 & 0 & 2\overline{Q}_{16} \\ \overline{Q}_{12} & \overline{Q}_{22} & 0 & 0 & 2\overline{Q}_{26} \\ 0 & 0 & 2\overline{Q}_{44} & 2\overline{Q}_{45} & 0 \\ 0 & 0 & 2\overline{Q}_{45} & 2\overline{Q}_{55} & 0 \\ \overline{Q}_{16} & \overline{Q}_{26} & 0 & 0 & 2\overline{Q}_{66} \end{bmatrix}_k \begin{bmatrix} \varepsilon_1 \\ \varepsilon_2 \\ \varepsilon_{23} \\ \varepsilon_{31} \\ \varepsilon_{12} \end{bmatrix} \qquad \text{(A1.16)}$$

And also, the new transformed reduced stiffnesses have the following values:

$$\left.\begin{aligned}\overline{Q}_{44} &= Q_{44}\cos^2\theta + Q_{55}\sin^2\theta \\ \overline{Q}_{55} &= Q_{44}\sin^2\theta + Q_{55}\cos^2\theta \\ \overline{Q}_{45} &= (Q_{55} - Q_{44})\sin\theta\cos\theta\end{aligned}\right\} \tag{A1.17}$$

To derive the constitutive relations accruing from bonding several laminae together, a laminated plate of thickness h is illustrated in the following Figure A10.5 when it is subjected to lateral and shearing load.

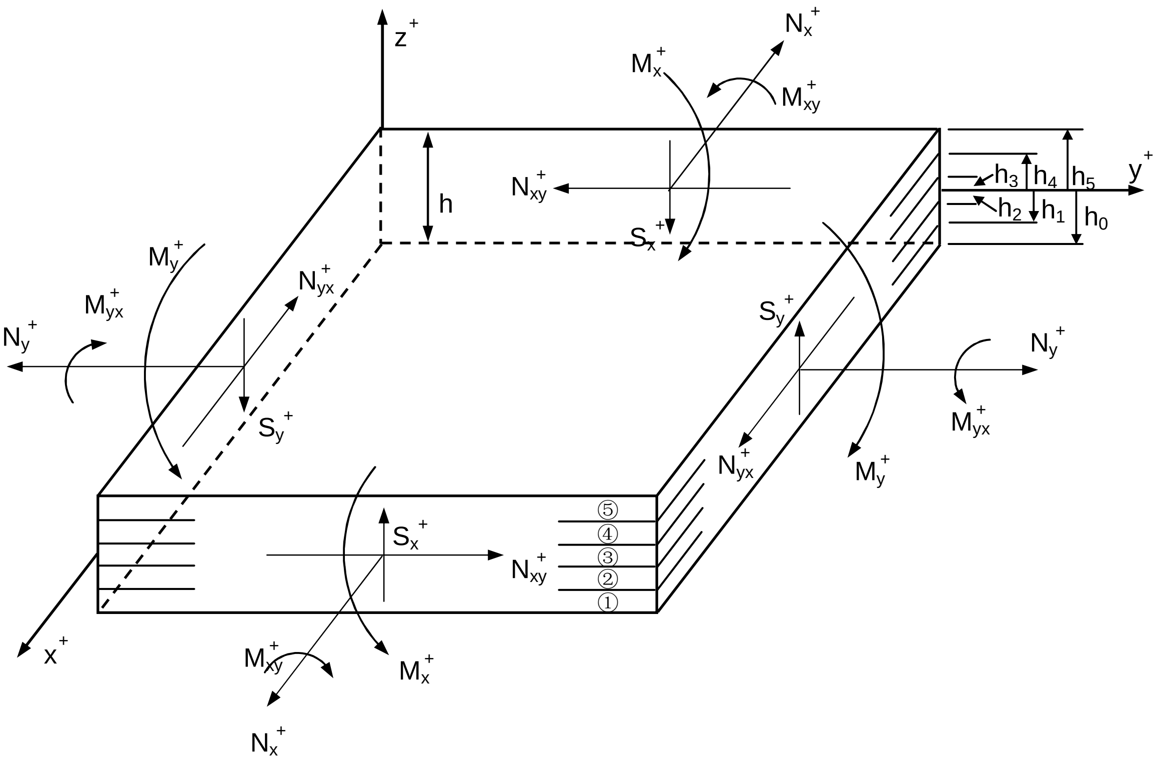

Figure A10.5. Positive directions for stress resultants and couples in multilayer plate

It is seen that h_k is the vectorial distance from the plate mid-plane. Any dimension below the mid-surface is a negative dimension and any dimension above the mid-surface is positive. Also, in classical laminate theory, it uses the following stress resultants and couples for the overall plate regardless of the number and the orientation of the laminae:

- Normal stress resultant, *N*, which has unit of force per unit length,
- Shear stress resultant, *S*, which also has unit of force per unit length, and,
- Stress couples, *M*, which has unit of moment per unit length.

These stress resultants and couples of a plate of thickness h can be expressed as:

$$\begin{bmatrix} N_x \\ N_y \\ N_{xy} \\ S_x \\ S_y \end{bmatrix} = \int_{-h/2}^{+h/2} \begin{bmatrix} \sigma_x \\ \sigma_y \\ \sigma_{xy} \\ \sigma_{xz} \\ \sigma_{yz} \end{bmatrix} dz \qquad \begin{bmatrix} M_x \\ M_y \\ M_{xy} \end{bmatrix} = \int_{-h/2}^{+h/2} \begin{bmatrix} \sigma_x \\ \sigma_y \\ \sigma_{xy} \end{bmatrix} z \; dz \tag{A1.18}$$

However, for an n-layer multi-directional laminated plate, the stress components are integrated through the thickness of the plate are the sum of the stresses across each lamina [9, 119]. They can be written as:

$$\begin{bmatrix} N_x \\ N_y \\ N_{xy} \end{bmatrix} = \sum_{k=1}^{n} \int_{h_{k-1}}^{h_k} \begin{bmatrix} \sigma_x \\ \sigma_y \\ \sigma_{xy} \end{bmatrix}_k dz = \sum_{k=1}^{n} \left(\overline{Q}_{ij}\right)_k \left(h_k - h_{k-1}\right) \begin{bmatrix} \varepsilon_x^o \\ \varepsilon_y^o \\ \varepsilon_{xy}^o \end{bmatrix} + \frac{1}{2} \sum_{k=1}^{n} \left(\overline{Q}_{ij}\right)_k \left(h_k^2 - h_{k-1}^2\right) \begin{bmatrix} \kappa_x \\ \kappa_y \\ \frac{1}{2}\kappa_{xy} \end{bmatrix}$$

$$\begin{bmatrix} M_x \\ M_y \\ M_{xy} \end{bmatrix} = \sum_{k=1}^{n} \int_{h_{k-1}}^{h_k} \begin{bmatrix} \sigma_x \\ \sigma_y \\ \sigma_{xy} \end{bmatrix}_k z \; dz = \frac{1}{2} \sum_{k=1}^{n} \left(\overline{Q}_{ij}\right)_k \left(h_k^2 - h_{k-1}^2\right) \begin{bmatrix} \varepsilon_x^o \\ \varepsilon_y^o \\ \varepsilon_{xy}^o \end{bmatrix} + \frac{1}{3} \sum_{k=1}^{n} \left(\overline{Q}_{ij}\right)_k \left(h_k^3 - h_{k-1}^3\right) \begin{bmatrix} \kappa_x \\ \kappa_y \\ \kappa_{xy} \end{bmatrix}$$

$$S_x = \frac{5}{2} \sum_{k=1}^{n} \overline{Q}_{55}^{(k)} \left[h_k - h_{k-1} - \frac{4}{3} \frac{\left(h_k^3 - h_{k-1}^3\right)}{h^2} \right] \cdot \varepsilon_{xz} + \frac{5}{2} \sum_{k=1}^{n} \overline{Q}_{45}^{(k)} \left[h_k - h_{k-1} - \frac{4}{3} \frac{\left(h_k^3 - h_{k-1}^3\right)}{h^2} \right] \cdot \varepsilon_{yz}$$

$$S_y = \frac{5}{2} \sum_{k=1}^{n} \overline{Q}_{45}^{(k)} \left[h_k - h_{k-1} - \frac{4}{3} \frac{\left(h_k^3 - h_{k-1}^3\right)}{h^2} \right] \cdot \varepsilon_{xz} + \frac{5}{2} \sum_{k=1}^{n} \overline{Q}_{44}^{(k)} \left[h_k - h_{k-1} - \frac{4}{3} \frac{\left(h_k^3 - h_{k-1}^3\right)}{h^2} \right] \cdot \varepsilon_{yz}$$

$$(i, j = 1, 2, 6) \tag{A1.19}$$

where $$\varepsilon_x^o = \frac{\partial u_o}{\partial x}, \qquad \varepsilon_y^o = \frac{\partial v_o}{\partial y}, \qquad \varepsilon_{xy}^o = \frac{1}{2}\frac{\partial u_o}{\partial y} + \frac{\partial v_o}{\partial x} \tag{A1.20}$$

and $$\kappa_x = \frac{\partial^2 w}{\partial x^2}, \quad \kappa_y = -\frac{\partial^2 w}{\partial y^2}, \quad \kappa_{xy} = -2\frac{\partial^2 w}{\partial x \partial y} \tag{A1.21}$$

and where u_o, v_o, and w are the in-plane mid-surface displacement in the x direction, the in-plane mid-surface displacement in the y direction, and the lateral displacement of the laminated plate, respectively.

A1.4. Buckling of composite plates - Minimum Potential Energy

Many composite material structures not only involve anisotropy, multilayer considerations and transverse shear deformation, but also have hydrothermal effects, which must be included in final design. These thermal and moisture effects cause consideration difficulty, because with their inclusion few boundary conditions are homogeneous. Consequently, separation of variables, used throughout the plate and shell solution to this point, cannot be utilised straightforward [119].

More convenient energy principles, therefore, are developed for use in design and analysis of composite structures. In the following section, the Theorem of Minimum Potential Energy is introduced for the analysis of critical buckling in composite orthotropic plates. For any generalized elastic body, the potential energy, *V*, can be written as [9, 119]:

$$V = \int_R W dR - \int_{S_T} T_i u_i dS - \int_R F_i u_i dR \tag{A1.22}$$

where W = Strain energy density function

R = Volume of the elastic body

T_i = i^{th} component of the surface traction

u_i = i^{th} component of deformation

F_i = i^{th} component of the body force

S_t = Portion of the surface over which traction are prescribed

The first term on the right hand side is the strain energy of the body. The second and third are the work done by the surface tractions and the body forces, respectively.

The theorem of minimum potential energy can be stated as: “Of all displacements satisfying compatibility and the given boundary conditions, those which satisfy the equilibrium equations make the potential energy a minimum.” [9]

Mathematically, the operation, which is called variation, can be written as

$$\delta V = 0 \qquad \text{(A1.23)}$$

It can be explained as when the elastic body is under equilibrium state, it can have a variation. In the case of elastic stability, neglecting the effects body forces, the critical buckling state can be expressed as following:

$$\delta V = \delta \int_R W dR - \delta \int_{S_T} T_i u_i dS = 0 \qquad \text{(A1.24)}$$

In earlier research, the solutions for elastic stability of varied orthotropic composites are difficult and very seldom are found in closed form. However, in the case of crossply construction (θ = 0° or 90°), Vince and Chou [9] derived its potential energy expression including transverse shear deformation for the subject boundary condition.

Assume a rectangular plate simply-supported on all four edges in the region $0 \le x \le a$, $0 \le y \le b$, and $-h/2 \le z \le h/2$, and subjected to only an in-plane load N_x, which is illustrated in Figure A10.6. The governing equation can be written as the Navier form:

$$w(x, y) = \sum_{m=1}^{\infty} \sum_{n=1}^{\infty} A_{mn} \sin \frac{m\pi x}{a} \sin \frac{n\pi x}{b} \qquad \text{(A1.25)}$$

Here, *w(x,y)* is known as the lateral deflection function which satisfies all boundary conditions. A_{mn} can be expanded as:

$$A_{mn} = \frac{\frac{4}{ab} \int_0^a \int_0^b p(x, y) \sin \frac{m\pi x}{a} \sin \frac{n\pi x}{b} dydx}{D\pi^4 \left[\left(m^2 / a^2 \right) + \left(n^2 / b^2 \right) \right]} \qquad \text{(A1.26)}$$

where D is the flexural stiffness for the plate, *p(x,y)* is the lateral pressure function, and m and n represents the number of half sine wave in x and y direction respectively.

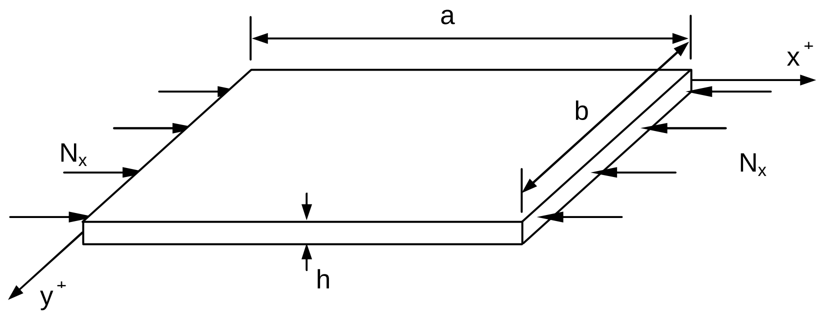

Figure A10.6. All four edges simply-supported plate subjected to in-plane load

Thus, taking variations with respect to A_{mn}, the potential energy expression mentioned in the earlier of this section can be written as following form for all four edges simply-supported orthotropic plate:

$$\delta V = \hat{N}_x^2 A + \hat{N}_x B + C = 0 \qquad \text{(A1.27)}$$

Prescribing compressive resultants $\overline{N}_x \equiv -N_x$ and $\overline{N}_y \equiv -N_y$, the dimensionless buckling load can be expressed as $\hat{N}_x = \dfrac{\overline{N}_x \pi^2}{G_{xz} h}$. And also here,

$$A = \left[\frac{3\pi^2}{500}\left(\frac{G_{xy}}{G_{xz}}\right)\left(\frac{E_x}{G_{xz}}\right)^2 \left(\frac{a}{b}\right)^2 n^2 + \frac{9\pi^2}{1500v'}\left(\frac{E_x}{G_{xz}}\right)^3 m^2 + \frac{3}{50}\left(\frac{E_x}{G_{xz}}\right)^2 \left(\frac{a}{h}\right)^2 \right]$$

$$B = \begin{bmatrix} -\dfrac{5}{\pi^2}\left(\dfrac{a}{h}\right)^6 \dfrac{1}{m^4} + \dfrac{\pi^2}{5}\left(\dfrac{G_{xy}}{G_{xz}}\right)\left(\dfrac{E_x}{G_{xz}}\right)\left(\dfrac{a}{b}\right)^2\left(\dfrac{a}{h}\right)^2 \dfrac{n^2}{m^2} - \dfrac{\pi^4}{100}\left(\dfrac{G_{xy}}{G_{xz}}\right)\left(\dfrac{E_x}{G_{xz}}\right)^2\left(\dfrac{a}{b}\right)^2 n^2 \\ -\dfrac{\pi^4}{100}\left(\dfrac{G_{xy}}{G_{xz}}\right)\left(\dfrac{E_x}{G_{xz}}\right)\left(\dfrac{E_y}{G_{yz}}\right)\left(\dfrac{a}{b}\right)^4 \dfrac{n^4}{m^2} - \dfrac{\pi^4}{100v'}\left(\dfrac{E_x}{G_{xz}}\right)^3 m^2 + \dfrac{\pi^2}{10v'}\left(\dfrac{E_x}{G_{xz}}\right)^2\left(\dfrac{a}{h}\right)^2 \\ -\dfrac{\pi^4}{100v'}v_{yx}\left(\dfrac{E_x}{G_{xz}}\right)\left(\dfrac{E_y}{G_{yz}}\right)\left(\dfrac{a}{b}\right)^4 \dfrac{n^4}{m^2} + \dfrac{\pi^2}{10v'}v_{yx}\left(\dfrac{E_x}{G_{xz}}\right)^2\left(\dfrac{a}{b}\right)^2\left(\dfrac{a}{h}\right)^2 \dfrac{n^2}{m^2} - \dfrac{\pi^2}{10}\left(\dfrac{E_x}{G_{xz}}\right)^2\left(\dfrac{a}{h}\right)^2 \end{bmatrix}$$

$$C=\begin{bmatrix} \frac{5\pi^2}{3}\left(\frac{G_{xy}}{G_{xz}}\right)\left(\frac{a}{b}\right)^2\left(\frac{a}{h}\right)^4\frac{n^2}{m^4}-\frac{\pi^4}{6}\left(\frac{G_{xy}}{G_{xz}}\right)\left(\frac{E_x}{G_{xz}}\right)\left(\frac{a}{b}\right)^2\left(\frac{a}{h}\right)^2\frac{n^2}{m^2} \\ -\frac{\pi^4}{6}\left(\frac{G_{xy}}{G_{xz}}\right)\left(\frac{E_y}{G_{yz}}\right)\left(\frac{a}{b}\right)^4\left(\frac{a}{h}\right)^2\frac{n^4}{m^4}+\frac{\pi^6}{240}\left(\frac{G_{xy}}{G_{xz}}\right)\left(\frac{E_x}{G_{xz}}\right)^2\left(\frac{a}{b}\right)^2 n^2 \\ +\frac{\pi^6}{240}\left(\frac{G_{xy}}{G_{xy}}\right)\left(\frac{E_y}{G_{yz}}\right)^2\left(\frac{a}{b}\right)^6\frac{n^6}{m^4}+\frac{5\pi^2}{12v'}\left(\frac{E_x}{G_{xz}}\right)\left(\frac{a}{h}\right)^4\frac{1}{m^2}+\frac{\pi^4}{24}\left(\frac{E_x}{G_{xz}}\right)^2\left(\frac{a}{h}\right)^2 \\ +\frac{\pi^6}{240v'}\left(\frac{E_x}{G_{xz}}\right)^3 m^2-\frac{\pi^4}{12v'}\left(\frac{E_x}{G_{xz}}\right)^2\left(\frac{a}{h}\right)^2+\frac{\pi^6}{120}\left(\frac{G_{xy}}{G_{xz}}\right)\left(\frac{E_x}{G_{xz}}\right)\left(\frac{E_y}{G_{yz}}\right)\left(\frac{a}{b}\right)^4\frac{n^4}{m^2} \\ +\frac{\pi^6}{120v'}v_{yx}\left(\frac{E_x}{G_{xz}}\right)^2\left(\frac{E_y}{G_{yz}}\right)\left(\frac{a}{b}\right)^4\frac{n^4}{m^2}-\frac{\pi^4}{12v'}v_{yx}\left(\frac{E_x}{G_{xz}}\right)^2\left(\frac{a}{b}\right)^2\left(\frac{a}{h}\right)^2\frac{n^2}{m^2} \\ -\frac{\pi^4}{12v'}v_{yx}\left(\frac{E_x}{G_{xz}}\right)\left(\frac{E_y}{G_{yz}}\right)\left(\frac{a}{b}\right)^4\left(\frac{a}{h}\right)^2\frac{n^4}{m^4}+\frac{5\pi^2}{6v'}v_{yx}\left(\frac{E_x}{G_{xz}}\right)\left(\frac{a}{b}\right)^2\left(\frac{a}{h}\right)^4\frac{n^2}{m^4} \\ +\frac{\pi^6}{240v'}\frac{v_{yx}}{v_{xy}}\left(\frac{E_x}{G_{xz}}\right)\left(\frac{E_y}{G_{yz}}\right)^2\left(\frac{a}{b}\right)^8\frac{n^8}{m^6}-\frac{\pi^4}{12v'}\frac{v_{yx}}{v_{xy}}\left(\frac{E_x}{G_{xz}}\right)\left(\frac{E_y}{G_{yz}}\right)\left(\frac{a}{b}\right)^6\left(\frac{a}{h}\right)^2\frac{n^6}{m^6} \\ +\frac{5\pi^2}{12v'}\frac{v_{yx}}{v_{xy}}\left(\frac{E_x}{G_{xz}}\right)\left(\frac{a}{b}\right)^4\left(\frac{a}{h}\right)^4\frac{n^4}{m^6}+\frac{\pi^4}{24}\frac{v_{yx}}{v_{xy}}\left(\frac{E_x}{G_{xz}}\right)\left(\frac{E_y}{G_{yz}}\right)\left(\frac{a}{b}\right)^6\left(\frac{a}{h}\right)^2\frac{n^6}{m^6} \end{bmatrix}$$

(A1.28)

where, $v'=1-v_{xy}v_{yx}$, engineering constants comprising moduli E_x, E_y, G_{xy}, G_{xz}, G_{yz} and Poisson's ratio v_{xy} and v_{xy} can be calculated by classical laminate theory . It can be seen that the minimum buckling load occurs when $n = 1$. However, the value of m, the wave number in the load direction will vary with the aspect ratio, *a/b*. Also, to cover the range of possible values for practical plates and practical materials systems, it requires [9]:

$$2\le\frac{E_x}{G_{xz}}\le 60 \qquad \frac{1}{3}\le\frac{a}{b}\le 3 \qquad \text{and} \qquad 10\le\frac{a}{h}\le 100$$

Therefore, the critical buckling load for an all edges simply-supported crossply orthotropic plate can be obtained by solving the quadratic equation A1.25 and equation A1.26.

A1.5. *Flexural modulus of a thin laminate*

The usual assumption of plane stress conditions for a thin composite laminate implies that the in-plane strains in the plate are linear functions of thickness. The normals to the undeformed planes in the plate would remain normal and undeformed in the deformed planes. Following the equation A1.19, the stress and moment resultants per unit length, *N* and *M*, at the mid-surface also can be written briefly as [111]:

$$\begin{bmatrix} N_i \\ M_i \end{bmatrix} = \begin{bmatrix} A_{ij} & B_{ij} \\ B_{ij} & D_{ij} \end{bmatrix} \begin{bmatrix} \varepsilon_j^o \\ \kappa_j \end{bmatrix} \quad , \qquad (i, j = 1, 2, 6) \qquad \text{(A1.29)}$$

or:

$$[N]_i = [A]_{ij}\left[\varepsilon^o\right]_j + [B]_{ij}[\kappa]_j$$

$$[M]_i = [B]_{ij}\left[\varepsilon^o\right]_j + [D]_{ij}[\kappa]_j \quad , \qquad (i, j = 1, 2, 6) \qquad \text{(A1.30)}$$

where ε^o are plane strains at mid-surface, κ are curvatures, and for the *k*th layer in an *n*-layer multidirectional laminate [111]:

$$A_{ij} = \sum_{k=1}^{n}\left(\overline{Q}_{ij}\right)_k \left(h_k - h_{k-1}\right)$$

$$B_{ij} = \frac{1}{2}\sum_{k=1}^{n}\left(\overline{Q}_{ij}\right)_k \left(h_k^2 - h_{k-1}^2\right)$$

$$D_{ij} = \frac{1}{3}\sum_{k=1}^{n}\left(\overline{Q}_{ij}\right)_k \left(h_k^3 - h_{k-1}^3\right), \qquad (i, j = 1, 2, 6) \qquad \text{(A1.31)}$$

where A_{ij} are extensional stiffnesses (or in-plane laminate moduli), which relates in-plane loads to in-plane strains. B_{ij} are coupling stiffnesses (or in-plane/flexure coupling laminate moduli), which relates in-plane loads to curvatures and moments to in-plane strains. If $B_{ij} \neq 0$, the in-plane forces produce the flexural and twisting deformations. D_{ij} are bending (or flexural) stiffnesses which relates moments to curvatures [122]. The h_k and h_{k-1} are the upper and lower co-ordinates of the *k*th layer (see Figure A10.5). In the absence of in-plane forces, equation A1.30 is then reduced to [111]:

$$[M]_i = [B]_{ij}\left[\varepsilon^o\right]_j + [D]_{ij}[\kappa]_j \quad (i, j = 1, 2, 6) \qquad \text{(A1.32)}$$

The in-plane coupling effect mutually induces in-plane stress and moments. However in symmetric laminates, this effect can be removed. Thus the equation A1.32 can be reduced to [111]:

$$[M]_i = [D]_{ij}[\kappa]_j \qquad (i, j = 1, 2, 6) \qquad \text{(A1.33)}$$

In the expression of the flexural moduli (equation A1.31), the reduced stiffness matrix $\overline{Q}_{ij}$ is independent of thickness within the *k*th lamina. In the case where every layer is of the same thickness, the bending stiffnesses D_{ij} of a symmetric laminate possessing total thickness of *h*, can be written as [111]:

$$D_{ij} = \frac{2h^3}{3n^3}\sum_{k=1}^{n/2}\left(\overline{Q}_{ij}\right)_k\left[k^3 - (k-1)^3\right], \qquad (i, j = 1, 2, 6) \qquad \text{(A1.34)}$$

The curvatures are given by equation A1.33 as:

$$[\kappa]_i = \frac{[M]_j}{[D]_{ij}} \qquad (i, j = 1, 2, 6) \qquad \text{(A1.35)}$$

If a laminate is subjected to the bending moment M_1, the deformation is referred to as "free flexure". In this case, if the assumption is made that application of the bending moment M_1 involves only one curvature along the "1" direction, κ_1, then equation A1.35 is reduced to:

$$[\kappa]_1 = \frac{[M]_1}{[D]_{11}} \qquad \text{(A1.36)}$$

In a laminate having rectangular cross section area, the bending stiffnesses, D_{ij}, and its flexural modulus E_{ij} has the following relation:

$$D_{ij} = E^{flex} I = \frac{E_{ij}^{flex} dh^3}{12}, \qquad (i, j = 1, 2, 6) \qquad \text{(A1.37)}$$

where d is the width of laminate, I is the second moment of inertia. Therefore, the flexural modulus of for a thin laminate per unit length and width (or normalised flexural modulus of a laminate) can be expressed as [111]:

$$E_{ij}^{flex} = \frac{8}{n^3}\sum_{k=1}^{n/2}\left(\overline{Q}_{ij}\right)_k\left[k^3 - (k-1)^3\right], \qquad (i, j = 1, 2, 6) \qquad \text{(A1.38)}$$

Appendix 2. F-ratio tables

Table A10.1 $F_{\alpha, v1,v2}$ **Values**

$F_{0.10, v1,v2}$ **90% confidence**

Degrees of freedom for the denominator (v_2)	Degrees of freedom for the numerator (v_1): 1	2	3	4	5	6	7	8	9	10
1	39.9	49.5	53.6	55.8	57.2	58.2	58.9	59.4	59.9	60.2
2	8.53	9.00	9.16	9.24	9.29	9.33	9.35	9.37	9.38	9.39
3	5.54	5.46	5.39	5.34	5.31	5.28	5.27	5.25	5.24	5.23
4	4.54	4.32	4.19	4.11	4.05	4.01	3.98	3.95	3.94	3.92
5	4.06	3.78	3.62	3.52	3.45	3.40	3.37	3.34	3.32	3.30
6	3.78	3.46	3.29	3.18	3.11	3.05	3.01	2.98	2.96	2.94
7	3.59	3.26	3.07	2.96	2.88	2.83	2.78	2.75	2.72	2.70
8	3.46	3.11	2.92	2.81	2.73	2.67	2.62	2.59	2.56	2.54
9	3.36	3.01	2.81	2.69	2.61	2.55	2.51	2.47	2.44	2.42
10	3.29	2.92	2.73	2.61	2.52	2.46	2.41	2.38	2.35	2.32

$F_{0.05, v1,v2}$ **95% confidence**

Degrees of freedom for the denominator (v_2)	Degrees of freedom for the numerator (v_1): 1	2	3	4	5	6	7	8	9	10
1	161	199	216	225	230	234	237	239	241	242
2	18.5	19.0	19.2	19.2	19.3	19.3	19.4	19.4	19.4	19.4
3	10.1	9.55	9.28	9.12	9.01	8.94	8.89	8.85	8.81	8.79
4	7.71	6.94	6.59	6.39	6.26	6.16	6.09	6.04	6.00	5.96
5	6.61	5.79	5.41	5.19	5.05	4.95	4.88	4.82	4.77	4.74
6	5.99	5.14	4.76	4.53	4.39	4.28	4.21	4.15	4.10	4.06
7	5.59	4.74	4.35	4.12	3.97	3.87	3.79	3.73	3.68	3.64
8	5.32	4.46	4.07	3.84	3.69	3.58	3.50	3.44	3.39	3.35
9	5.12	4.26	3.86	3.63	3.48	3.37	3.29	3.23	3.18	3.14
10	4.96	4.10	3.71	3.48	3.33	3.22	3.14	3.07	3.02	2.98

$F_{0.01, v1,v2}$ **99% confidence**

Degrees of freedom for the denominator (v_2)	Degrees of freedom for the numerator (v_1): 1	2	3	4	5	6	7	8	9	10
1	4052	4999	5403	5625	5764	5859	5928	5981	6022	6056
2	98.5	99.0	99.2	99.2	99.3	99.3	99.4	99.4	99.4	99.4
3	34.1	30.8	29.5	28.7	28.2	27.9	27.7	27.5	27.3	27.2
4	21.2	18.0	16.7	16.0	15.5	15.2	15.0	14.8	14.7	14.5
5	16.3	13.3	12.1	11.4	11.0	10.7	10.5	10.3	10.2	10.1
6	13.7	10.9	9.78	9.15	8.75	8.47	8.26	8.10	7.98	7.87
7	12.2	9.55	8.45	7.85	7.46	7.19	6.99	6.84	6.72	6.62
8	11.3	8.65	7.59	7.01	6.63	6.37	6.18	6.03	5.91	5.81
9	10.6	8.02	6.99	6.42	6.06	5.80	5.61	5.47	5.35	5.26
10	10.0	7.56	6.55	5.99	5.64	5.39	5.20	5.06	4.94	4.85

References

1. Lu, G. and T. Yu, *Energy absorption of structures and materials*. 2003: Woodhead Publishing Limited.

2. Cauchi-Savona, S., *Energy absorbing composites for crash energy management*. 2003, PhD Thesis, Queen Mary, University of London, Department of Materials.

3. Theobald, M.D. and G.N. Nurick, *Numerical investigation of the response of sandwich-type panels using thin-walled tubes subject to blast loads.* International Journal of Impact Engineering, 2007. 34(1): p. 134-156.

4. Hancock, S.G. and K.D. Potter, *Inverse drape modelling - an investigation of the set of shapes that can be formed from continuous aligned woven fibre reinforcements.* Composites Part A: Applied Science and Manufacturing, 2005. 36(7): p. 947-953.

5. Chung, J.G., S.H. Chang, and M.P.F. Sutcliffe, *Deformation and energy absorption of composite egg-box panels.* Composites Science and Technology, 2007. 67(11-12): p. 2342-2349.

6. Hosur, M.V., M. Abdullah, and S. Jeelani, *Manufacturing and low-velocity impact characterization of foam filled 3-D integrated core sandwich composites with hybrid face sheets.* Composite Structures, 2005. 69(2): p. 167-181.

7. Hosur, M.V., M. Abdullah, and S. Jeelani, *Manufacturing and low-velocity impact characterization of hollow integrated core sandwich composites with hybrid face sheets.* Composite Structures, 2004. 65(1): p. 103-115.

8. Taguchi, G., R. Jugulum, and S. Taguchi, *Computer-based robust engineering:essentials for DFSS*. 2004: American Society for Quality, Quality Press.

9. Vinson, J.R. and T.W. Chou, *Composite materials and their use in structures*. 1975, London: Applied Science Publishers Ltd.

10. Brush, D.O. and B.O. Almroth, *Buckling of bars, plates, and shells*. 1975: McGraw-Hill, Inc.

11. Price, J.N. and D. Hull, *How to apply advanced composites technology*, in *4th Conference on Advanced Composites*. 1988, ASM International: Dearborn, Michigan. p. 53-61.

12. Ramakrishna, S., *Microstructural design of composite materials for crashworthy structural applications.* Material and Design, 1997. 18 (3): p. 167-173.

13. Jiménez, M.A., et al., *Effect of trigger geometry on energy absorption in composite profiles.* Composite Structures, 2000. 48(1-3): p. 107 -111.

14. Farley, G.L., *Relationship between mechanical-property and enegy-absorption trends for composite tubes.* L-17087, NASA TP-3284, ARL-TR-29, Hampton,

VA: Vehicle Structures Directorate, U.S. Army Research Laboratory., 1992.

15. Hull, D., *A unified approach to progressive crushing of fibre-reinforced composite tubes.* Composites Science and Technology, 1991. 40 (4): p. 377-421.

16. Cauchi-Savona, S. and P.J. Hogg, *Investigation of plate geometry on the crushing of flat composite plates.* Composites Science and Technology, 2006. 66(11-12): p. 1639-1650.

17. Lavoie, J.A., J. Morton, and K. Jackson, *An evaluation of the energy-absorption of laminated composite plates.* Proceedings of the Institution of Mechanical Engineers Part G: Journal of Aerospace Engineering, 1995. 209(3): p. 185-194.

18. Thuis, H.G.S.J. and V.H. Metz, *The influence of trigger configurations and laminate lay-up on the failure mode of composite crush cylinders.* Composite Structures, 1994. 28(2): p. 131-137.

19. Czaplicki, M.J., R.E. Robertson, and P.H. Thornton, *Comparison of bevel and tulip triggered pultruded tubes for energy absorption.* Composites Science and Technology, 1991. 40(1): p. 31-46.

20. Sigalas, I., M. Kumosa, and D. Hull, *Trigger mechanism in energy-absorbing glass cloth epoxy tubes.* Composites Science and Technology, 1991. 40(3): p. 265-287.

21. Hamada, H., et al., *The crushing performance of a braided I-beam.* Composites Science and Technology, 1999. 59(12): p. 1881-1890.

22. Jackson, K., et al., *Scaling of energy absorbing composite plates.* Journal of the American Helicopter Society, 1994. 39(1): p. 17-23.

23. Harte, A.-M., N.A. Fleck, and M.F. Ashby, *Energy absorption of foam-filled circular tubes with braided composite walls.* European Journal of Mechanics - A/Solids, 2000. 19 (2000): p. 31-50.

24. Cauchi-Savona, S. and P.J. Hogg, *Effect of fracture toughness properties on the crushing of flat composite plates.* Composites Science and Technology, 2006. 66(13): p. 2317-2328.

25. Nakatani, T., K. Kameo, and H. Hamada, *Development of energy absorption parts with FRP tubes.* Advanced Composite Materials, 1999. 8 (4): p. 345-354.

26. Jacob, G.C., et al., *Effect of fiber volume fraction, fiber length and fiber tow size on the energy absorption of chopped carbon fiber-polymer composites.* Polymer Composites, 2005. 26(3): p. 293-305.

27. Karbhari, V.M. and J.E. Haller, *Rate and architecture effects on progressive crush of braided tubes.* Composite Structures, 1998. 43(2): p. 93-108.

28. Warrior, N.A., et al., *Effect of resin properties and processing parameters on crash energy absorbing composite structures made by RTM.* Composites: Part

A, 2003. 34(6): p. 543-550.

29. Hamada, H., et al., *Comparison of energy absorption of carbon-epoxy and carbon-PEEK composite tubes.* Composites, 1992. 23(4): p. 245-252.

30. Song, H.-W., X.-W. Du, and G.-F. Zhao, *Energy absorption behavior of doulbe-chamfer triggered glass/epoxy circular tubes.* Journal of Composite Materials, 2002. 36(18): p. 2183-2198.

31. Daniel, L., P.J. Hogg, and P.T. Curtis, *The relative effects of through-thickness properties and fibre orientation on energy absorption by continuous fibre composites.* Composites Part B: Engineering, 1999. 30(3): p. 257-266.

32. Farley, G.L., *Energy absorption of composite materials.* Journal of composite materials, 1983. 17: p. 267-279.

33. Solaimurugan, S. and R. Velmurugan, *Influence of fibre orientation and stacking sequence on petalling of glass/polyester composite cylindrical shells under axial compression*. International Journal of Solids and Structures, 2007. 44(21): p. 6999-7020.

34. Tao, W.H., R.E. Robertson, and P.H. Thornton, *How to apply advanced composites technology*, in *4th Conference on Advanced Composites*. 1988, ASM International: Dearborn, Michigan. p. 47-52.

35. Matthews, F.L. and R.D. Rawlings, *Fracture mechanics and toughening mechanisms*, in *Composite materials: Engineering and Science*. 1994, Chapman & Hall. p. 326-362.

36. Hadavinia, H. and H. Ghasemnejad, *Effects of Mode-I and Mode-II interlaminar fracture toughness on the energy absorption of CFRP twill/weave composite box sections.* Composite Structures, 2009. 89(2): p. 303-314.

37. Warrior, N.A., et al., *The effect of interlaminar toughening strategies on the energy absorption of composite tubes.* Composites Part A: Applied Science and Manufacturing, 2004. 35(4): p. 431-437.

38. Mouritz, A.P., K.H. Leong, and I. Herszberg, *A review of the effect of stitching on the in-plane mechanical properties of fibre-reinforced polymer composites.* Composites Part A: Applied Science and Manufacturing, 1997. 28(12): p. 979-991.

39. Mouritz, A.P. and B.N. Cox, *A mechanistic approach to the properties of stitched laminates.* Composites Part A: Applied Science and Manufacturing, 2000. 31(1): p. 1-27.

40. Dickinson, L.C., G.L. Farley, and M.K. Hinders, *Translaminar reinforced composites: a review.* Journal of Composites Technology & Research, 1999. 21(1): p. 3-15.

41. Watt, A., A.A. Goodwin, and A.P. Mouritz, *Thermal degradation of the mode I interlaminar fracture properties of stitched glass fibre vinyl ester composites.*

Journal of Materials Science, 1998. 33(10): p. 2629-2638.

42. Mouritz, A.P., C. Baini, and I. Herszberg, *Mode I interlaminar fracture toughness properties of advanced textile fibreglass composites.* Composites Part A: Applied Science and Manufacturing, 1999. 30(7): p. 859-870.

43. Dransfield, K.A., Y.-W. Mai, and L.K. Jain, *On the effects of stitching in CFRPs - I. Mode I delamination toughness.* Composites Science and Technology, 1998. 58(6): p. 815-827.

44. Sankar, B.V. and S.K. Sharma, *Mode II delamination toughness of stitched graphite/epoxy textile composites.* Composites Science and Technology, 1997. 57(7): p. 729-737.

45. Jain, L.K., K.A. Dransfield, and Y.-W. Mai, *On the effects of stitching in CFRPs - II. Mode II delamination toughness.* Composites Science and Technology, 1998. 58(6): p. 829-837.

46. Ogo, Y., *The effect of stitching on in-plane and interlaminar properties of carbon fibre/epoxy fabric laminates*. 1987, MSc thesis, University of Delaware.

47. Lavoie, J.A. and S. Kellas, *Dynamic crush tests of energy-absorbing laminated composite plates.* Composites Part A: Applied Science and Manufacturing, 1996. 27(6): p. 467-475.

48. Farley, G.L. and R.M. Jones, *Energy-absorption capability of composite tubes and beams.* NASA-TM-101634, AVSCOM-TR-89-B-003, 1989.

49. Mamalis, A.G., et al., *The static and dynamic axial collapse of fibreglass composite automotive frame rails.* Composite Structures, 1996. 34(1): p. 77-90.

50. Thornton, P.H., *The crush behavior of pultruded tubes at high strain rates.* Journal of Composite Materials, 1990. 24(6): p. 594-615.

51. Gu, B. and F.-K. Chang, *Energy absorption features of 3-D braided rectangular composite under different strain rates compressive loading.* Aerospace Science and Technology, 2007. 11(7-8): p. 535-545.

52. Schmueser, D.W. and L.E. Wickliffe, *Impact energy absorption of continuous fiber composite tubes.* Journal of Engineering Materials and Technology, Transactions of the ASME, 1987. 109(1): p. 72-77.

53. Mamalis, A.G., et al., *Axial collapse of thin-walled fibreglass composite tubular components at elevated strain rates.* Composites Engineering, 1994. 4(6): p. 653-677.

54. Lanzi, L., L.M.L. Castelletti, and M. Anghileri, *Multi-objective optimisation of composite absorber shape under crashworthiness requirements.* Composite Structures, 2004. 65(3-4): p. 433-441.

55. Mamalis, A.G., et al., *Experimental determination of splitting in axially collapsed thick-walled fibre-reinforced composite frusta.* Thin-Walled

Structures, 1997. 28(3-4): p. 279-296.

56. Alkateb, M., et al., *On the energy absorption capability of axially crushed composite elliptical cones.* Composite Structures, 2004. 66(1-4): p. 495-501.

57. Farley, G.L., *Effect of specimen geometry on the energy absorption capability of composite materials.* Journal of Composite Materials, 1986. 20(4): p. 390-400.

58. Farley, G.L., *Energy-absorption capability and scalability of square cross section composite tube specimens.* NASA-TM-89087, AVSCOM-TM-87-B-3, 1987.

59. Mamalis, A.G., D.E. Manolakos, and G.L. Viegelahn, *Crashworthy behaviour of thin-walled tubes of fibreglass composite materials subjected to axial loading.* Journal of Composite Materials, 1990. 24: p. 7391.

60. Palanivelu, S., et al., *Crushing and energy absorption performance of different geometrical shapes of small-scale glass/polyester composite tubes under quasi-static loading conditions.* Composite Structures, 2011. 93(2): p. 992-1007.

61. Hanagud, S., et al., *Energy absorption behavior of graphite epoxy composite sine webs.* Journal of Composite Materials, 1989. 23(5): p. 448-459.

62. Farley, G.L., *A method of predicting the energy-absorption capability of composite subfloor beams.* NASA-TM-89088, AVSCOM-TM-87-B-4, 1987.

63. Dubey, D.D. and A.J. Vizzini, *Energy absorption of composite plates and tubes.* Journal of Composite Materials, 1998. 32(2): p. 158-176.

64. *Sandwich concept, DIAB sandwich handbook.* Available from: www.diabgroup.com.

65. Woods, D.W. and I.M. Ward, *Study of the interlaminar shear strength of unidirectional high-modulus polyethylene fibre composites* Journal of Materials Science, 2004. 29(10): p. 2572-2578.

66. Tilbrook, M.T., et al., *Dynamic crushing of sandwich panels with prismatic lattice cores.* International Journal of Solids and Structures, 2007. 44(18-19): p. 6101-6123.

67. Yoo, S.H., S.H. Chang, and M.P.F. Sutcliffe, *Compressive characteristics of foam-filled composite egg-box sandwich panels as energy absorbing structures.* Composites Part A: Applied Science and Manufacturing, 2010. 41: p. 427-434.

68. Xue, Z. and J.W. Hutchinson, *Preliminary assessment of sandwich plates subject to blast loads.* International Journal of Mechanical Sciences, 2003. 45(4): p. 687-705.

69. Rathbun, H.J., et al., *Performance of metallic honeycomb-core sandwich beams under shock loading.* International Journal of Solids and Structures, 2006. 43(6): p. 1746-1763.

70. Hutchinson, J.W. and Z. Xue, *Metal sandwich plates optimized for pressure impulses.* International Journal of Mechanical Sciences, 2005. 47(4-5): p. 545-569.

71. Liang, S. and H.L. Chen, *Investigation on the square cell honeycomb structures under axial loading.* Composite Structures, 2006. 72(4): p. 446-454.

72. Davalos, J.F., et al., *Torsion of honeycomb FRP sandwich beams with a sinusoidal core configuration.* Composite Structures, 2009. 88(1): p. 97-111.

73. Hexcel Corporation, *Honeycomb attributes and properties*. TSB 120. 1999: CA, USA.

74. Wu, E. and W.-S. Jiang, *Axial crush of metallic honeycombs.* International Journal of Impact Engineering, 1997. 19(5-6): p. 439-456.

75. Wicks, N. and J.W. Hutchinson, *Optimal truss plates.* International Journal of Solids and Structures, 2001. 38(30-31): p. 5165-5183.

76. Xue, Z. and J.W. Hutchinson, *A comparative study of impulse-resistant metal sandwich plates.* International Journal of Impact Engineering, 2004. 30(10): p. 1283-1305.

77. Deshpande, V.S. and N.A. Fleck, *One-dimensional response of sandwich plates to underwater shock loading.* Journal of the mechanics and physics of solids, 2005. 53(11): p. 2347-2383.

78. Phadke, M.S., *Quality engineering using robust design*. 1989: AT&T Bell Laboratories.

79. Ross, P.J., *Taguchi techniques for quality engineering*. 1996: McGraw-Hill.

80. Park, S.H., *Robust design and analysis for quality engineering*. 1996: Chapman & Hall.

81. Taguchi, G. and S. Konishi, *Orthogonal arrays and linear graphs: tools for quality engineering*. 1987: ASI Press.

82. Genichi, T., C. Subir, and T. Shin, *Robust engineering*. 1999: McGraw Hill.

83. Dehnad, K., *Quality control, robust design, and the taguchi method*. 1989: AT&T.

84. Fisher, R., *Studies in Crop Variation. I. An examination of the yield of dressed grain from Broadbalk.* Journal of Agricultural Science, 1918. 11: p. 107-135.

85. Seemann, W.H., *Plastic transfer molding techniques for the production of fiber reinforced plastic structures*. 1990: U.S. Patent 4902215.

86. *Scott Bader co., ltd, Technical data sheet: Crystic® 489PA.* Technical Leaflet No. 172.7 SA. March 2001.

87. *Reichhold ltd, preliminary data sheet: Norpol DION 9102-500.*

88. *Huntsman International LLC, datasheet: warm-curing epoxy system based on Araldite® LY 564 / Hardener XB 3486 / Hardener XB 3487*. March 2004.

89. *Henkel AG & Co. KGaA, technical data sheet: LOCTITE® Hysol® 9460™*. December 2006.

90. Robinson, P. and J.M. Hodgkinson, *Interlaminar fracture toughness*, in *Mechanical Testing of Advanced Fibre Composites*, J.M. Hodgkinson, Editor. 2000, Woodhead Publishing Ltd. p. 170-210.

91. *ASTM D5528-01, standard test method for Mode I interlaminar fracture toughness of unidirectional fiber-reinforced polymer matrix composites.* Annual Book of ASTM standards, 2001. Vol. 15.03.

92. Caprino, G., *The use of thin DVB specimens for measuring Mode I interlaminar fracture toughness of composite materials.* Composite Science and Technology, 1990. 39(2): p. 147-158.

93. Schuecker, C. and B.D. Davidson, *Evaluation of the accuracy of the four-point bend end-notched flexure test for mode II delamination toughness determination.* Composites Science and Technology, 2000. 60(11): p. 2137-2146.

94. Martin, R.H. and B.D. Davidson, *Mode II fracture toughness evaluation using four point bend, end notched flexure test.* Plastics, Rubber and Composites, 1999. 28(8): p. 401-406.

95. Martin, R.H., T. Elms, and S. Bowron. *Characterisation of Mode II delamination using the 4-ENF*. in *Proceedings of 4 th European Conference on Composite Materials: Testing and Standardisation*. 1998. Lisbon, Portugal: Institute of Materials, IoM Communications Ltd, London.

96. *ASTM D790-02, Standard test methods for flexural properties of unreinforced and reinforced plastics and electrical insulating materials.* Annual Book of ASTM standards, 2002. Vol. 08.01.

97. *ASTM D3039/D3039M-00, Standard test method for tensile properties of polymer matrix composite materials.* Annual Book of ASTM standards, 2000. Vol. 15.03.

98. Hu, H.T. and W.L. Tzeng, *Buckling analysis of skew laminate plates subjected to uniaxial inplane loads.* Thin-Walled Structures, 2000. 38(1): p. 53-77.

99. *ABAQUS example problems manual, version 6.6*: Hibbitt, Karlsson, Sorensen, Inc.

100. *ABAQUS analysis user's manual, version 6.6*: Hibbitt, Karlsson, Sorensen, Inc.

101. Wang, X.W., et al., *Compressive failure of composite laminates containing multiple delaminations.* Composites Science and Technology, 2005. 65(2): p. 191-200.

102. Kutlu, Z. and F.-k. Chang, *Composites panels containing multiple through-the-width delaminations and subjected to compression. Part II: experiements & verification.* Composite Structures, 1995. 31(4): p. 297-314.

103. Hull, D., *An introduction to composite materials*. 1981: Cambridge University Press.

104. Gerard, G. and H. Becker, *Handbook of structural stability part I : buckling of flat plates.* . NACA TN 3781: Material advisory committee for aeronautics. 1957.

105. Kollár, L. and E. Dulácsska, *Buckling of shells for engineers*. 1984: John Wiley & Sons.

106. Daniel, L., P.J. Hogg, and P.T. Curtis, *The crush behaviour of carbon fibre angle-ply reinforcement and the effect of interlaminar shear strength on energy absorption capability.* Composites Part B: Engineering, 2000. 31(5): p. 435-440.

107. Mouritz, A.P., J. Gallagher, and A.A. Goodwin, *Flexural strength and interlaminar shear strength of stitched GRP laminates following repeated impacts.* Composites Science and Technology, 1997. 57(5): p. 509-522.

108. Gibson, R.F., *Principles of composite materials mechanics*. 1994: McGraw-Hill, Inc.

109. Megson, T.H.G., *Structural and stress analysis*. 2nd ed. 2005: Elsevier Butterworth-Heinemann.

110. Hagerty, W.W. and H.J. Plass, *Engineering mechanics*. 1967: D. Van Nostrand Company (Canada), Inc.

111. Adams, R.D. and M.R. Maheri, *Dynamic flexural properties of anisotropic fibrous composite beams.* Composites Science and Technology, 1994. 50(4): p. 497-514

112. Shibata, S., Y. Cao, and I. Fukumoto, *Flexural modulus of the unidirectional and random composites made from biodegradable resin and bamboo and kenaf fibres.* Composites Part A: Applied Science and Manufacturing, 2008. 39(4): p. 640-646.

113. Shibata, S., Y. Cao, and I. Fukumoto, *Study of the flexural modulus of aatural fiber/polypropylene composites by injection molding.* Journal of Applied Polymer Science, 2005. 100: p. 911-917.

114. Mouritz, A.P., *Flexural properties of stitched GRP laminates.* Composites Part A: Applied Science and Manufacturing, 1996. 27(7): p. 525-530.

115. Devitt, D.F., R.A. Schapery, and W.L. Bradley, *A method for determining the Mode I delamination fracture toughness of elastic and viscoeleastic composite materials.* Journal of Composite Materials, 1980. 14: p. 270.

116. Cauchi-Savona, S., C. Zhang, and P.J. Hogg, *Optimisation of crush energy*

absorption of non-crimp fabric laminates by through-thickness stitching. Composites Part A: Applied Science and Manufacturing, 2011. 42(7): p. 712-722.

117. Mouritz, A.P., *Review of z-pinned composite laminates.* Composites Part A: Applied Science and Manufacturing, 2007. 38(12): p. 2383-2397.

118. Potluri, P., et al. *Benchmarking of 3D preforming strategies*. in *CD-ROM Proceedings of The 17th International Conference on Composite Materials (ICCM-17)*. 2009. Edinburgh, UK.

119. Vinson, J.R. and R.L. Sierakowski, *The behavior of structures composed of composite materials*. 1986: Martinus Nijhoff Publishers.

120. Jones, R.M., *Mechanics of composite materials*. 1975, New York: Hemisphere Publishing Corporation.

121. Calcote, L.R., *The analysis of laminated composite structrues*. 1969, Van Nostrand Reinhold Company.

122. Daniel, I.M. and O. Ishai, *Engineering mechanics of composite materials*. 1994: Oxford University Press.